THÈSE

Présentée en vue de l'obtention du titre de

DOCTEUR de l'Université Bordeaux I

spécialité

Informatique

par

Pablo SALAS

Aspects numériques et physiques des instabilités thermoacoustiques dans les chambres de combustion annulaires

Soutenance prévue le 15 Novembre 2013 devant le jury :

M. SAAD, Yousef	Rapporteur
M. SCHULLER, Thierry	Rapporteur
M. GIRAUD, Luc	Directeur de thèse
M. VASSEUR, Xavier	Co-Directeur de thèse
M. POINSOT, Thierry	Examinateur
M. NICOUD, Franck	Examinateur
M. MEERBERGEN, Karl	Examinateur
M. LARROYA, Juan Carlos	Invité

Physical and numerical aspects of thermoacoustic instabilities in annular combustion chambers

Abstract: Modern pollutant emission regulation has led to the use of lean premixed combustion in gas turbine combustors, a technology which is prone to develop thermoacoustic instabilities. This phenomenon is the result of a resonant feedback between combustion, acoustic waves and flow dynamics in confined combustion chambers. In this work, combustion instabilities are studied using a Helmholtz equation with a reactive term that takes into account the coupling between combustion and acoustics. The discretization of the resulting Helmholtz equation on unstructured meshes leads to a large sparse non-symmetric complex nonlinear eigenvalue problem of size N (N is equal to the number of nodes in the mesh). Its solution provides the frequencies and growth rates (complex eigenvalues) and the structure (eigenvectors) of the resonant modes of the combustor. Since dangerous combustion instabilities occur mostly at low frequencies, the nonlinear eigenvalue problem must be solved in order to obtain the smallest magnitude eigenvalues. The nonlinear problem is linearized using a fixed point iteration procedure. This leads to a sequence of linear eigenproblems which must be solved iteratively in order to obtain one nonlinear eigenpair. Therefore, efficient and robust parallel eigensolvers for the solution of linear problems are investigated, and strategies to accelerate the solution of the sequence of linear eigenproblems are also proposed. In modern gas turbines with annular combustors, the most dangerous resonant modes often take the form of azimuthal waves, making their study of first importance. This work focuses on azimuthal modes in annular combustors: their stability and nature (standing, spinning or mixed) are investigated as a function of the symmetry of the configuration. Thanks to the efficiency of the algorithms for the solution of the thermoacoustic eigenproblem, the 3D Helmholtz solver AVSP is used for the study of combustion instabilities of an annular industrial combustor.

Keywords: Thermoacoustic instabilities, Annular combustion chambers, Azimuthal modes, Eigenvalue problems, Parallel eigensolvers, Block eigensolvers.

Aspects numériques et physiques des instabilités thermoacoustiques dans les chambres de combustion annulaires

Résumé: L'exigence croissante des régulations concernant les émissions de polluants a poussé les motoristes à concevoir des chambres de combustions fonctionnant en régime pauvre (prémélangé). Cependant cette technologie est particulièrement sujette au développement d'instabilités thermoacoustiques. Ce phénomène résulte d'une boucle rétroactive entre la combustion, l'acoustique, et la dynamique de l'écoulement dans les chambres de combustion confinées. Dans ce travail, les instabilités de combustion sont étudiées en utilisant l'équation de Helmholtz avec ajout d'un terme réactif qui permet de prendre en compte le couplage entre la combustion et l'acoustique. La discrétisation de l'équation de Helmholtz résultante sur un maillage non structuré mène à un problème aux valeurs propres non linéaire. La matrice associée à ce problème est complexe, non-symétrique, de taille N (N étant égal au nombre de noeuds du maillage). La solution du problème aux valeurs propres fournit les fréquences et les taux d'amplification (valeurs propres complexes) ainsi que les structures (vecteurs propres) des modes propres de la chambre de combustion. Les instabilités de combustion les plus dangereuses se produisant généralement aux fréquences les plus faibles, le problème non linéaire doit être résolu afin d'obtenir les valeurs propres de plus petit module. Pour cela il est d'abord linéarisé en utilisant une méthode de point fixe. On résout de facon itérative une séquence de problèmes aux valeurs propres linéaires qui converge vers une solution du problème non linéaire initial. Par conséquent, différents solveurs aux valeurs propres parallèles, robustes, et efficaces sont étudiés. Des strategies pour accélérer la résolution de la séquence de problèmes linéaires sont également proposées. Dans les turbines à gaz modernes présentant des chambres de combustion annulaires, les modes de résonance les plus dangereux prennent souvent la forme d'ondes azimutales. Ces travaux se focalisent donc sur l'analyse de ces modes, notamment l'effet de la symétrie de la configuration sur leur stabilité et leur nature (stationnaire, tournant, ou mixte). L'efficacité des algorithmes étudiés et implémentés dans le solveur de Helmholtz 3D AVSP, rend ainsi possible l'analyse des instabilités thermoacoustiques d'une chambre de combustion annulaire industrielle.

Mots clés: Instabilités thermoacoustiques, Chambres de combustion annulaires, Modes azimuthaux, Problèmes aux valeurs propres, Solveurs aux valeurs propres parallèles, Solveurs aux valeurs propres bloc.

Remerciements

Ça y est. La fin de la thèse. Le manuscrit est fini, corrigé, la soutenance réussie, le pot digéré. . . Il faut passer à autre chose. Il y a des personnes pour qui c'est facile de tourner la page, et d'autres, pour qui c'est un peu plus compliqué. Ceux qui me connaissent un peu savent dans quel groupe je me trouve.

Tout d'abord, je veux remercier Yousef Saad, que j'ai eu la chance de rencontrer en personne et qui m'a consacré du temps pour discuter sur mon travail. Quand une référence incontournable du monde de l'algèbre linéaire accepte de lire ton manuscrit, on ne peut pas s'empêcher d'avoir un peu peur, mais quand le retour est bon, la satisfaction est double. Merci à Thierry Schuller, mon deuxième rapporteur, qui a contribué avec ses remarques et ses critiques constructives. Je remercie également Karl Meerbergen et Juan Carlos Larroya-Huguet d'être venus pour ma soutenance et pour leurs questions pertinentes.

Je remercie mes encadrants. Merci Xavier Vasseur pour tes conseilles avisés et ta disponibilité pour m'aider quand j'en ai eu besoin. Je remercie mon directeur de thèse, Luc Giraud, pour tout ce qu'il a fait pour moi depuis le premier jour. J'ai eu la chance de découvrir une personne d'une intégrité hors du commun. Ça a été un plaisir de travailler avec toi et j'espère qu'on se croisera à nouveau.

Je veux remercier Thierry Poinsot pour son accueil au sein du Cerfacs, ce microcosme si particulier. Merci pour ton implication tout le long de ma thèse. J'ai appris énormément grâce à ton exigence. Merci aussi à Franck Nicoud, qui m'a toujours aidé avec sa vision scientifique et son pragmatisme. Avec Thierry vous formez un duo scientifique difficile à égaler.

Merci à toute l'équipe CSG (Fabrice, Gérard et Isabelle). J'ai énormément apprécié votre savoir faire et votre gentillesse. Et merci aux secrétaires et au service administratif pour leurs aides (mention spéciale pour Michèle).

Et bien sur, ce qui rend le CERFACS un endroit aussi particulier: les thésards, stagiaires et al. Tous différents, tous pareils (ou pas!). C'est tellement bien de pouvoir échanger! Merci aux anciens (Marlène, Elsa, Camilo, Emmanuel, Marta, Matthias, Philippe, Evelyn, JF Parmentier, . . .) pour les bons moments et pour leur héritage. Enfin, côté AVSP, l'héritage ça craint ! :p Un grand merci à 'l'autre Pablo', sans qui beaucoup de difficultées auraient été du genre insurmontables.

Merci aux contemporains et bonne chance pour la fin: Lucas, Corentin, Damien, Sandrine, Anthony, Michael (qui pond un papier tout les cinq minutes), . . . et bon courage à la nouvelle génération, en particulier Aïcha et Franchine qui vont bien galérer avec AVSP. Rappelez vous que la galère est toujours relative! Je ne t'oublie pas, Mowgli.

Un grand merci aux amis du CERFACS: Moff, qui va bientôt doubler son volume initial; Laure, la fille thésarde qui mérite un prix; Frichouille, qui aime les choses pas vielles (;p);

Jaravel aka JarJar ou l'homme qui se bourre la gueule au cognac; Abdulla Ghhhrrrani, l'afgano-allemand impatient (merci pour les cours d'allemand); Adrien 'Didi', l'homme aux outils infinis; Remy développeur Fransen Paraview; Nacho alias 'JFM' ou l'homme qui a étudié Physique Quantique en Espagne (me quito el sombrero); Greg, le dernier français que j'ai été capable de suivre dans son discours; Basti, pour son humour(?) allemand; Julie, la fille de Michèle :D, ...

On arrive ainsi aux Trois Mousquetaires et D'Artagnan (si D'Artagnan est le plus petit j'hésite entre David et P'tit Ju, mais je ne suis pas sûr): Thom aka 'le roux' "je n'ai pas d'outil de postraitemet alors je change le sujet de ma thèse", "pause BF, trimard", Pierre (aussi roux un peu carotte) "je me suis acheté quatre paires de chaussures sur internet", "j'ai mal au bide!", P'tit Ju alias 'Julien Richard' "je ne peux pas dormir il faut que je travaille", "mais elle a les yeux qui pétillent..." et David alias 'davidator', la petite peluche musclée "j'ai faite une putain de thèse mais personne est au courant!". Les soirées, les journées, les fêtes de Nöel, ...Je vais pas m'étendre avec vous parce que si je commence, j'en ai pour une deuxième thèse. Vous êtes géniaux!!!!

Merci aux amis non cerfacsiens: Tran, Tiphaine, Baptiste, Anne Flore, Alice, Marjo, Seb, ...Vous avez fait que l'aventure française soit devenue une expérience inoubliable. J'espère qu'on se perdra pas de vue.

Como no podía ser de otra manera, mil veces gracias a mi familia: mi padre, mi madre, mi hermano. Sin vosotros no sería quien soy. Gracias por vuestro apoyo infinito.

Et ma chère compagne, Marie ...

Contents

II Eigenvalue problem: algorithms and numerical aspects 55

3 Algorithms for the solution of the thermo-acoustic eigenproblem 57

III   Thermoacoutic instabilities in annular combustion chambers   143

Part I

Introduction: General context and theoretical framework

Introduction

"Ce que nous appelons progrès
est le remplacement d'un
inconvénient par un autre"

Henry Havelock Ellis

Contents

1.1   Gas turbines and pollution

1.1.1   Pollutant emissions and combustion

The United Nations population forecast foresees an increment of the current world population (around 7 billion people) to 9.6 billion people in 2050 and more than 10 billion in 2100 [165], following a medium-variant projection (Fig. 1.1). Consequently, since people need energy, the energy consumption is expected to grow accordingly from 13 terawatts (TW) today, to 28 TW in 2050 and 46 TW in 2100 [79]. Despite the development of alternative clean energies, fossil fuels provide the 85% of the world energy [57]. Nevertheless fossil fuels are limited and not evenly distributed over the world, leading to energy security problems and geopolitical tension. Moreover, they are associated with global warming and pollution [166]. In spite of these drawbacks, replacing fossil fuels today is impossible and, consequently, it is crucial to efficiently use them in the context of new technologies.
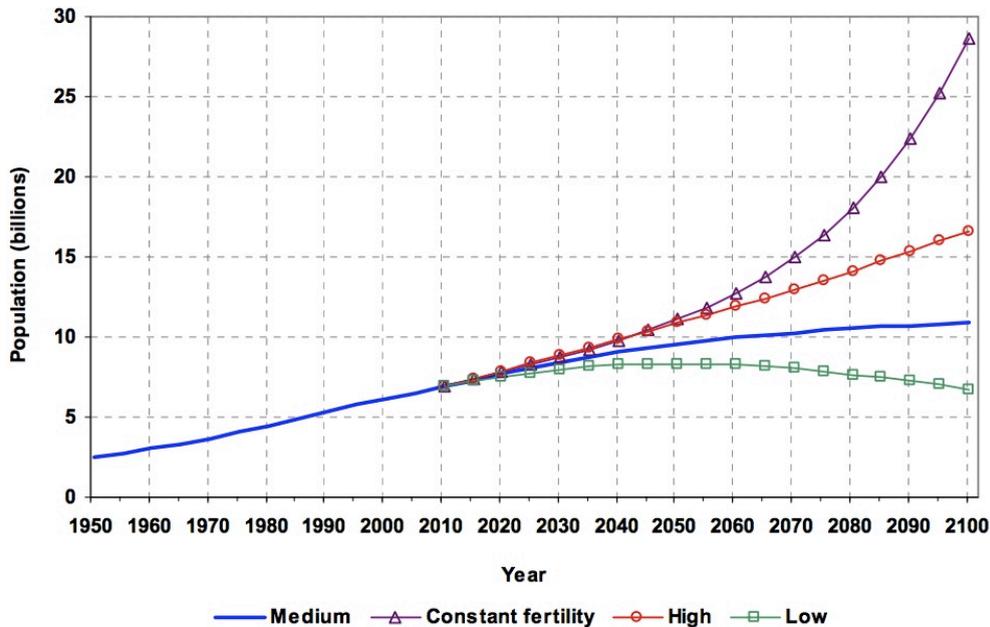
Figure 1.1: World's population (1950-2010) according to different projections [165].

As mentioned before, combustion produces a large amount of pollutants that affect the environment and that are harmful for the human health. Pollutant emissions come from the combustion of hydrocarbons present in fossil fuels, generating greenhouse gases like carbon dioxide (CO_2) and pollutants such as unburned hydrocarbons (UHC), nitrogen oxides (NO_x) and carbon monoxides (CO) as well as particles like soots [136] (Fig. 1.2).

Incomplete combustion results from insufficient oxidizer (oxygen) or from the quenching of the flame due to heat losses near the wall or due to a high strain rate. In order to avoid incomplete combustion, *lean combustion* can be employed, meaning that a quantity of oxygen larger than the one imposed by the stoichiometric condition is used. Nevertheless, the oxygen in excess promotes the oxygen-nitrogen reaction and therefore the formation of nitrogen oxides [23]. NO_x emissions from combustion are primarily NO. According to the Zeldovich mechanism [177], NO is generated to the limit of available oxygen (about 200,000
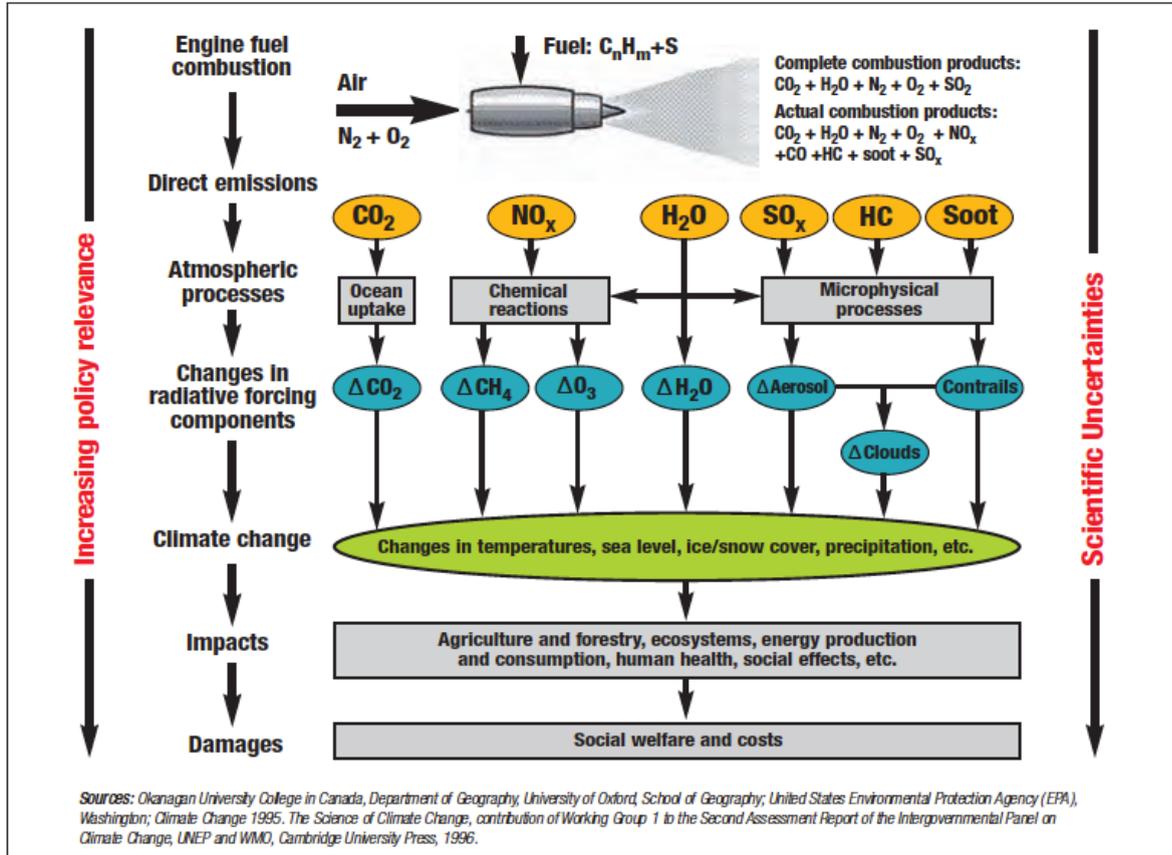
Figure 1.2: Aircraft pollutant emission and their potential impact on climate change [58].

ppm) in air at temperatures above $1300°C$. At temperatures below $760°C$, NO is either generated in much lower concentrations or not at all. Fig 1.3 summarizes the generation of main emissions as a function of the air/fuel ratio. For lean flames, CO and CO_2 production decreases strongly, although NO_x emissions are at first promoted by the excess of oxygen and then decrease for very lean regimes, due to the temperature drop (the heat release is maximum at stoichiometric condition and then it decreases for lean combustion and so does the temperature).

The impact of the pollutant emissions due to combustion has multiple aspects:

- Combustion and climate change: Among all pollutant emissions due to combustion, CO_2 and water vapor are the main "greenhouse" gas contributing to global warming [2]. The effects of global warming are numerous:

  – Physical impact: it refers to the effects on the rain fall and extreme weather with drought and cyclone activity, glacier retreat and disappearance, volcano activity, earthquakes, rise of the sea level and its temperature [160].

  – Regional effects: global warming changes the regional climate e.g. the forming and melting of ice, the current in oceans and air flows and the hydrological cycle. Coastal regions are heavily affected by the rising of the sea level [160].

  – Ecosystems: Plants and animals are responding (extinction or movement) to
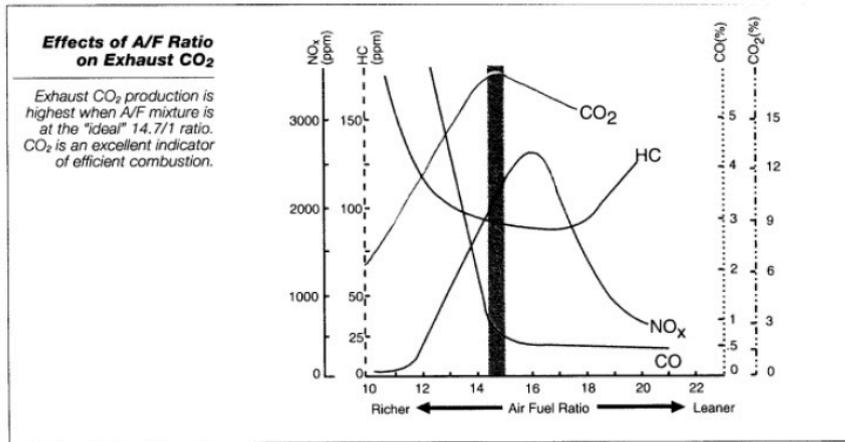
Figure 1.3: Evolution of pollutant emissions with the air/fuel ratio.

temperature changes, having strong effects on biological systems [112]

- Impact on human health: pollutant emissions induce hazardous effects on human health. Fig. 1.4 (extracted from [58]) summarizes symptoms due to every pollutant.

Therefore, nowadays it has become crucial to reduce pollutant emissions. This is the objective, for example, of the CAEP (Committee for Aviation Environmental Protection) [96], part of the ICAO, which has proposed to deal with both NO_x and CO_2 emissions. The increasingly demanding environmental policies have led engine manufacturers to use lean combustion, which represents a good compromise in order to have efficient systems with low emissions. However, lean combustion is subject to potential problems such as combustion instabilities (see Sec. 1.2), which are the topic of this PhD.

1.1.2 Gas turbine principles

The first known precursor of a gas turbine is the Hero's aeolipile around the year 50, which consists in a steam turbine used as a toy. In the 16th century Leonardo da Vinci drew the Chimmey Jack: hot air rises from a fire and passes through an axial turbine at the exhaust, which is connected to a roasting split and makes it turn. Another example is the Branca's jet turbine in the 17th century (Fig. 1.5). The first patent was given to John Barber. His gas turbine had most of the elements present in a modern gas turbine and was designed to power a horseless carriage. In 1903 the Norwegian Ægidius Elling built the first gas turbine producing more power than the one necessary to run its own components. A few years later, General Electric started its own production division and the first aeronautical design was patented in the 30's by Sir Franck Whittle.

Today, gas turbines are used in a broad range of applications such as power generation, compressor stations at gas pipelines, water and sewage pumping stations or engines for aircrafts and ships. An efficient design of gas turbines is imposed by the increasing demand of energy and fossil fuels and the associated pollutant emissions. For most aircraft and helicopters, gas turbines have become the only propulsion method. On the energy market,

Pollutant	Health Effect
CO – **Carbon Monoxide**	• Cardiovascular effects, especially in those persons with heart conditions
HC – **Unburned Hydrocarbons** (a primary component of Volatile Organic Compounds, or VOC)	• Eye and respiratory tract infection • Headaches • Dizziness • Visual disorders • Memory impairment
NO$_x$ – **Nitrogen Oxides**	• Lung irritation • Lower resistance to respiratory infections
O$_3$ – **Ozone** (HC is a precursor for ground-level O$_3$ formation)	• Lung function impairment • Effects on exercise performance • Increased airway responsiveness • Increased susceptibility to respiratory infection • Increased hospital admissions and emergency room visits • Pulmonary inflammation, lung structure damage
PM – **Particulate Matter** (smoke is a primary component of PM.)	• Premature mortality • Aggravation of respiratory and cardiovascular disease • Changes in lung function • Increased respiratory symptoms • Changes to lung tissues and structure • Altered respiratory defence mechanisms

Figure 1.4: Representative health effects from local air quality pollutants [58].
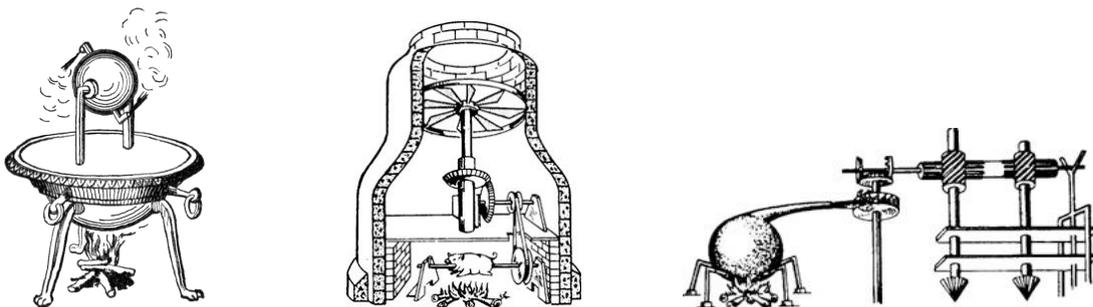
Figure 1.5: Hero's aeolipile (left); Da Vinci's Chimmey Jack (center) and Branca's jet gas turbine (right).

they are mandatory to complete other sources which are very slow to start up (such as nuclear plants) or unpredictable (sun or wind).

A gas turbine is an internal combustion engine that operates with rotary motion. Basically, it is composed of three main parts: a compressor, a combustion chamber and a turbine, as shown in Fig. 1.6. It works following the Brayton cycle of Fig. 1.7: Air passes
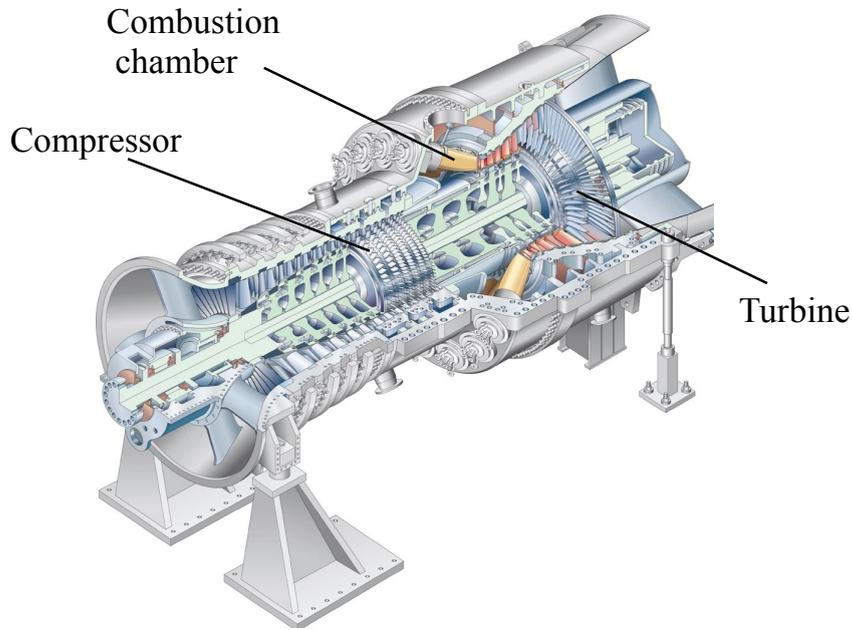
Figure 1.6: Siemens SGT5-8000H gas turbine reachs power outputs of up to 375 MW.

the compressor, where it is isentropically compressed, increasing the thermal efficiency (steps 1 – 2). Then it is mixed with fuel and burnt in the combustion chamber at constant pressure (steps 2 – 3). At the exit of the combustion chamber, the hot gases expand in the turbine back to the initial pressure (steps 3 – 4). Finally the hot gases are rejected in the atmosphere at constant pressure (steps 1 – 4). The recovered energy in the turbine is used to move the compressor, through a shaft. In the case of aircraft engines, the exhaust gases pass through a nozzle where the flow velocity is incremented to create thrust.
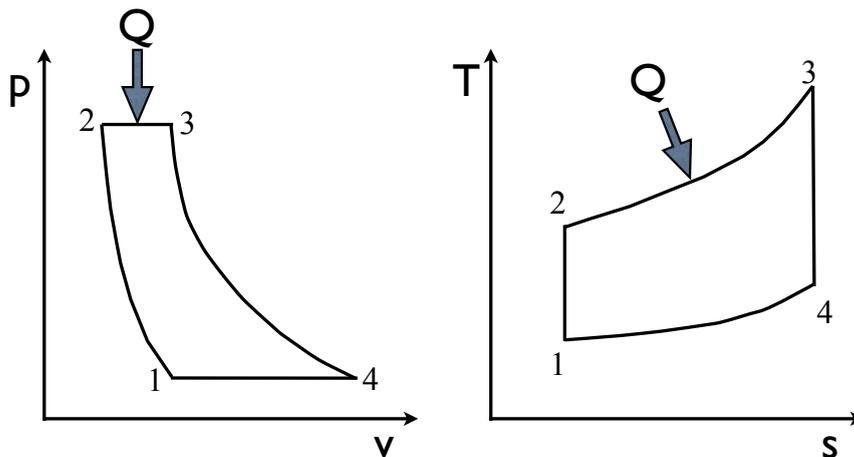
Figure 1.7: Brayton cycle in a gas turbine. p-v and T-s diagrams.

The combustion process is one of the key elements in a gas turbine. Most modern combustion chambers are of annular type (Fig. 1.8). In order to achieve a high efficiency, two aspects can be exploited:

- A higher combustion temperature leads to a higher performance engine. A lot of research work has ben invested in order to increase the thermal tolerance of the turbine blades, so that higher combustion temperatures can be reached.

- A higher compression rate, which can be obtained by adding compressor stages.
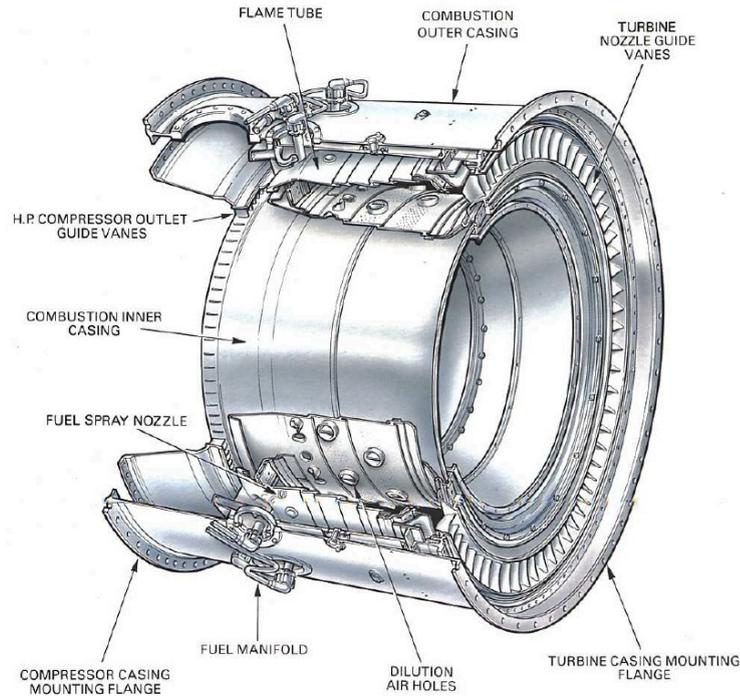
Figure 1.8: Annular combustion chamber (Source: The Jet Engine, Rolls-Royce plc.).

The regulation policies concerning pollutant emissions (such as NO_x, CO_2 and CO) are increasingly demanding. Therefore, the reduction of pollutant emissions has become a major issue during the design stage of gas turbines. It is a great challenge for engineers to reach high performance gas turbines while reducing the emissions, since both are conflicting goals. Indeed, as shown in Sec. 1.1.1, a higher temperature (good from an efficiency point of view) increases the NO_x emissions. Reducing the available oxygen reduces the NO_x but, on the other hand, increases the carbon monoxide CO and the unburnt hydrocarbon (UHC) emissions. The compromise reached by gas turbine manufacturers is the *lean premixed combustion*, which employs a low fuel-air mass flow ratio. This reduces the combustion temperature and the formation of hot spots, and therefore NO_x formation. The reduction of hot spots has the secondary benefit of reducing the indirect combustion noise (the noise coming from the expansion of these hot spots through the turbine). Nevertheless, using lean combustion can lead to thermoacoustic instabilities [74, 118], which are due to the coupling between the combustion and the acoustic modes of the combustion chamber. They are characterized by large pressure fluctuations and heat release oscillations that can lead to severe problems like noise emission, heat flux enhancement on duct lining, global extinction of the flame, structural vibrations or fatigue, ... The prediction of this phenomenon at en early design stage has become a very important task. Nevertheless, due to the complexity of the coupling mechanisms underlying this phenomenon, combustion instabilities remain a great challenge today and are not fully understood yet.

1.2 Combustion instabilities

1.2.1 Combustion instabilities overview

Combustion instabilities are the framework of the present work. The high efficiencies of modern gas turbines that allow to reach large power densities, along with the use of lean combustion to reduce pollutant emissions, lead to combustion instabilities. This phenomenon results from the coupling between the combustion in the flame zone and the acoustic modes of the combustion chamber. It leads to high pressure and heat release oscillations in the chamber the which can even provoke its destruction. This is the case of the picture in Fig. 1.9, which shows a rocket motor chamber with several damages caused by thermoacoustic instabilities [84].

Figure 1.9: Damaged rocket chamber from combustion instabilities.

The article by Raun et al. [122] constitutes an excellent review of thermoacoustic instabilities throughout the recent history. Combustion-driven acoustic oscillations were first observed by Higgins in 1777. Higgins found that placing a hydrogen diffusion flame inside a closed or a open-ended tube could produce a sound, depending on the tube and fuel supply line lengths. This phenomenon was called the *singing flame*. In 1858, LeConte [73] described the influence of sound produce by musical instrument on flames:

> "I happened to be one of a party of eight persons assembled after tea for the purpose of enjoying a private musical entertainment. Three instruments were employed in the performance of several of the grand trios of Beethoven, namely, the piano, violin and violoncello. Two 'fish-tail' gas burners projected from the brick wall near the piano. (...) Soon after the music commenced, I observed that the flame of the last-mentioned burner exhibited pulsations in height which were exactly synchronous with the audible beats. This phenomenon especially striking when the strong notes of the violoncello came in. It was exceedingly interesting to observe how perfectly even the trills of this instrument were reflected on the sheet of flame. A deaf man might have seen the harmony."

Rijke published in 1859 [124] his study of the so-called today Rijke tube: he found that sound was produced by placing a hot metal gauze in the lower half of open-ended vertical tubed. In 1878 Lord Rayleigh [123] offered an explanation to combustion instabilities.

Since then, combustion instabilities has been a known phenomenon, although it became the object of intense research with the development of high power density combustion systems that exhibit these undesired instabilities, specially in rockets [30]. Thermoacoustic instabilities are characterized by large pressure amplitude oscillations and heat release fluctuations, which have associated a series of undesirable consequences: noise emission, heat flux enhancement on duct linings, global extinction of the flame, structural vibrations or fatigue of burner and liner parts and even the failure of the turbine [161].

1.2.2 Instabilities mechanism
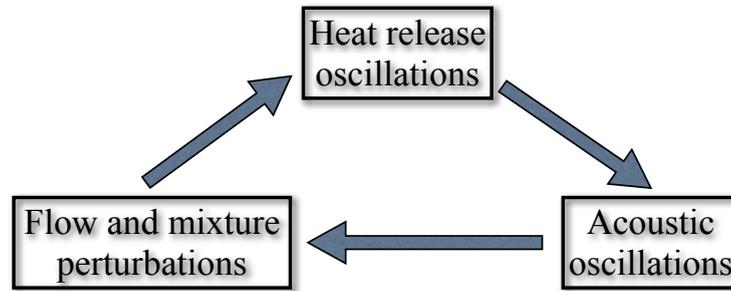
Figure 1.10: Feedback mechanism leading to combustion instabilities [82].

Thermoacoustic instabilities are the result of a resonant feedback between combustion, acoustic waves and flow dynamics [19, 33, 35] (Fig. 1.10). When the heat release fluctuates, the gases dilatation rate varies in time, acting as an unsteady local source of volume that pushes the surrounding gases, leading to an increment of the local pressure which propagates then as acoustic waves. These pressure waves propagate and are reflected at the combustion chamber walls, inlet and outlet (the reflection depends on the corresponding impedances), coming eventually back to the flame zone. The reflected acoustic waves perturb the flow and mixture, which leads to heat release fluctuations in the flame, closing a loop (Fig. 1.10) that can be potentially unstable if certain phase and gain conditions are satisfied. The heat release fluctuations are driven basically by two mechanisms [82]:

- Variation of the flame surface area: the perturbed flow is accelerated and decelerated in the flame zone, which changes the flame shape and leads to an overall flame surface area variation and consequently, to oscillations in the total heat release.

- Fluctuations of the local equivalence ratio: the acoustic waves can induce flow fluctuations through both the air and fuel inlets, which results in local mixture heterogeneities. These mixture variations are convected to the flame front, causing fluctuations in the heat release [135].

The Rayleigh criterion [98, 123] establishes the necessary condition to have a thermoacoustic instability, which depends on the phase between the pressure and the heat release oscillations:

> "If heat be given to the air at the moment of greatest condensation or be taken from it at the moment of greatest rarefaction, the vibration is encouraged."

Mathematically expressed, the instability condition reads as:

$$\int_T \int_V p'q'dV\,dt > 0, \tag{1.1}$$

where p' and q' denote the pressure and heat release fluctuations respectively, V is the volume of the domain and T is the period of the oscillation.
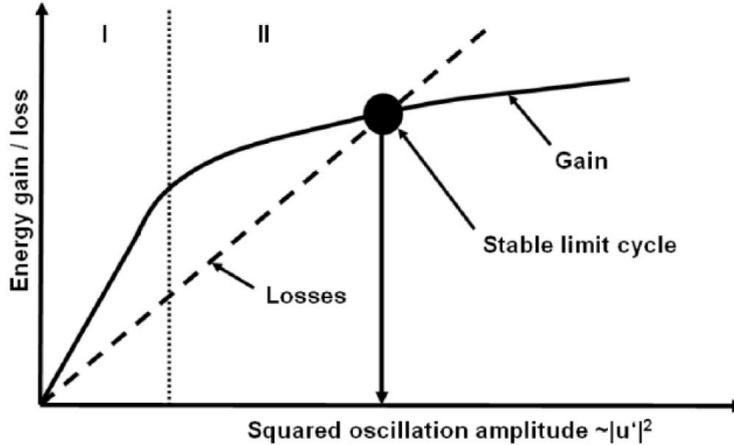
Figure 1.11: Evolution of energy gain and losses with the perturbation amplitude for a combustion instability [11].
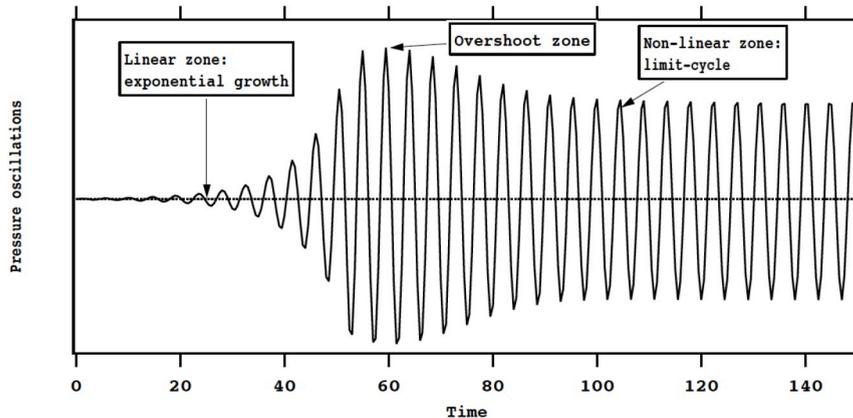
Figure 1.12: Typical time-evolution of a combustion instability: exponential grow of the acoustic pressure followed by an overshoot before reaching a limit cycle [117].

If the energy gain due to the coupling between acoustics and combustion is greater than losses (acoustic flow through boundaries and viscous dissipation), the amplitude of the fluctuations increases exponentially until a limit cycle is reached due to saturation, which is controlled by nonlinear effects [81]. This behavior is represented in Fig. 1.11 [11], which shows the energy gain and losses associated with a thermoacoustic instability as a function of the square of the acoustic velocity fluctuation u'^2. According to [34], the losses increase linearly with the perturbation amplitude, whereas the energy gain due to the coupling between flame and acoustics increases first linearly (region I) and then it saturates for

24

higher perturbation amplitudes (region II). The level of perturbation for which energy gain and losses are equal is known as limit cycle [95, 83], which is characterized by sustained oscillations. The time evolution of a typical combustion instability is displayed in Fig. 1.12: first, the pressure fluctuations increase exponentially in the linear zone. Then an overshot is often observed before the system reaches a limit cycle with a sustained level of oscillation, for which losses balance the energy gain. In the present work, we focus on tools which can predict the linear regime. Acoustics remains linear in most cases when $p'/\bar{p}$ is smaller than 1%, i.e., when the fluctuation over the mean value of the pressure remains small.

1.2.3 Control of combustion instabilities

Although thermoacoustic instabilities should preferably be avoided at an early design stage, it is important to be able to control and suppress instabilities when they appear a posteriori. We can distinguish mainly two methods for the control of thermoacoustic instabilities:

- Passive control techniques [12, 30, 40, 82, 111]:

  – Acoustic dampers: resonators can be used to damp acoustic modes. In the case of gas turbine combustors the unstable eigenfrequencies are generally low, so that large volumes would be needed to make this method effective. Since the space is very limited in most applications, the use of these resonators is limited.

  – Use of baffles in order avoid the acoustic flux [30].

  – Operating conditions: changes in the air/fuel mass flow rate, air temperature injection, fuel/oxidizer ratio, fuel staging [137], etc. will change the flame response, having an effect on the phase lag between pressure and heat release fluctuations [22].

  – Design changes: the geometry of the combustion chamber (swirler position, modifications of the burner outlet, etc.) can modify the flame time response and so the stability of the configuration [111].

  Although these techniques are relatively cheap and robust, they are not very flexible and they may be ineffective at very low frequencies [36] (under a few hundred Hertz).

- Active control techniques [88]: sensors are employed to detect the presence of an instability (pressure signal). They are connected by a closed feedback loop to actuators that act according to the signal from sensors to suppress the instability. Although many theoretical studies and experiments on academic chambers have been carried out showing their effectiveness [115, 116, 147], these methods can not provide enough robustness from an industrial point of view today, especially in terms of certification for aircraft or helicopters.

1.2.4 Study of combustion instabilities: several approaches

Many approaches are possible for the study of combustion instabilities: from theoretical models to full scale Large Eddy Simulations, passing by low-order network methods. The

modeling level required by these approaches decreases as the cost and complexity increases. In the following, the different options available today for the study of instabilities are briefly described.

- **Experimental works**: simplified configurations have been used in order to study thermoacoustic instabilities experimentally. Although for many years only longitudinal instabilities were studied [20, 21, 37, 101, 102, 113, 120, 141], more recently, simplified annular configurations have allowed the study of azimuthal modes. Moeck et al. [90] and Gelbert et al. [46] have studied azimuthal instabilities in an annular Rijke tube, using heating grids as unsteady heat source. Dawson et al. [173] and Worth et al. [172] have used an annular configuration with swirled premixed flames to study the interaction between flames and the effect of mean swirl on the stability and nature of azimuthal modes. Another recent interesting work concerning the experimental study of azimuthal instabilities can be found in [17].

- **Theoretical methods**: An important analytical research effort has been invested in order to understand the underlying phenomena governing the mutual interaction between combustion and acoustics, leading to combustion instabilities [26, 33, 35, 62, 86, 98, 118, 168]. The main drawback of analytical models is that a certain number of hypothesis must be considered to simplify the problem and hence only academic or highly simplified configurations can be studied.

- **Low-order network models**: low-order models are applied to simplified geometries, which allows to obtain fast responses and phenomenological interpretation [111]. One-dimensional schemes based on one-dimensional acoustic wave propagation in a network of ducts, are often studied [51], but also two-dimensional and three-dimensional simplified geometries [1, 15, 40]. In order to investigate complex geometries, network models are used, which decompose the real geometry in a set of constant density lumped acoustic elements. Each one of them is modeled by means of a transfer function matrix, which can be solved analytically [118, 119, 158]. This approach also allows taking into account the effect of the Mach number [33]. Recently, a semi-analytical approach using a 1D network model has been proposed for the study of azimuthal modes in a one-ring configuration [111], which has been extended to a 2D network for the study of two-ring configurations in [10]. The main drawback of this approach is the low level of geometric complexity that can be taken into account.

- **Three-dimensional numerical simulation**: of course, numerical tools are widely used for the study of combustion instabilities. Large Eddy Simulation (LES) [67, 152, 176] is a powerful numerical tool able to take into account all the mechanisms involved in the combustion-acoustics coupling, reproducing naturally combustion instabilities in complex geometries. Recently, LES has been successfully employed for the simulation of azimuthal instabilities in real gas turbine combustion chambers in [153, 169]. The very high computational cost of LES and the required heavy post-processing are the main drawbacks of this approach.

  A less expensive method is the use of acoustic solvers based on a finite element approach that solves the linearized reactive Euler equations in the frequency or time domain under the assumption of linear acoustics [33, 118]. This work focuses on

this kind of solver for the simulation of thermoacoustic instabilities. AVSP is the acoustic solver used and further developed during this thesis. Originally developed at CERFACS ("Centre Européen de Recherche et de Formation Avancée en Calcul Scientifique"), it solves a reactive Helmholtz equation in the frequency domain for unstructured meshes, using a finite volume discretization [97, 144]. Neglecting turbulence and viscous effects and assuming that the flow is frozen ($\bar{u} = 0$), it solves the wave equation in a non-isothermal flow, taking into account a distributed heat source and impedances of walls, inlet(s) and outlet(s).

1.2.5   Instabilities in annular combustion chambers
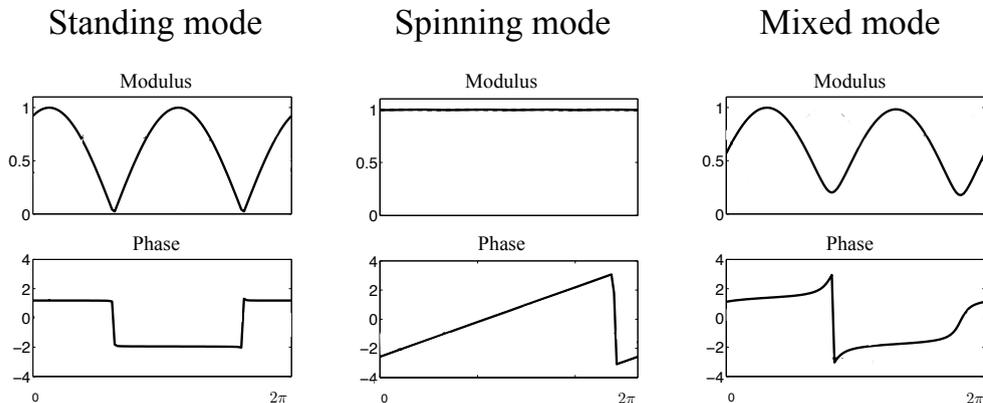
Figure 1.13: Pressure modulus and phase corresponding to standing, spinning and mixed modes.

Today, most modern gas turbines use annular combustion chambers. In annular configurations, combustion instabilities often appear as azimuthal waves [19, 27, 82, 118]. Since the radial and longitudinal directions are shorter than the azimuthal one, the lowest frequency modes correspond to azimuthal modes, which requires methods to identify these instabilities at an early design stage. This is the reason why, in the last years a lot of work has been invested in the research of azimuthal instabilities. Azimuthal modes can be standing, spinning or mixed, depending on the modulus and phase of the pressure waves (Fig. 1.13) [41, 140, 169, 90, 46, 171, 174]. A recent LES simulation of a full annular combustion [170] and experimental works [174, 17] suggest that swirlers induce an azimuthal mean flow that influences the occurrence of spinning and standing modes. The dynamic nature of azimuthal modes has also been studied theoretically [100, 103, 140, 111]. Sensiau [144, 145] and Noiray [100] have shown that purely spinning modes can appear only in perfectly symmetric configurations, while standing or mixed modes would appear otherwise. Nevertheless, the effect of the nature of azimuthal modes on instabilities is still an open issue.

1.3 From thermoacoustics to the parallel resolution of a large scale eigenvalue problem

In AVSP, the thermoacoustics code used in this study, the discretization of the Helmholtz equation on unstructured meshes leads to an eigenvalue problem [97] and its construction will be detailed in Chapter 2. When the flame is taken into account, and/or complex impedances are considered, the eigenvalue problem is actually a nonlinear eigenproblem. Its solution provides the frequencies (eigenvalues) and structures (eigenvectors) of the chamber eigenmodes, as well as their growth rate, which allows to know whether modes are stable or unstable. Solving the eigenproblem in AVSP is a challenging task from a numerical and a mathematical point of view for many reasons:

- The associated matrix is sparse complex non-symmetric and non-Hermitian. No particular simplifications leading to faster, simpler and more robust algorithms can be exploited, as it would be the case for symmetric (or hermitians) matrices, for example [72].

- It is known from experience that combustion instabilities happen at low frequencies. It means that the eigenvalue problem must be solved in order to obtain a few eigenvalues corresponding to those of smallest magnitude (the lowest frequencies). Unfortunately, the eigensolvers that can be found in literature are well adapted to the computation of largest magnitude eigenvalues. The computation of smallest magnitude eigenvalues remains a difficult problem.

- The size of the matrix associated with the corresponding eigenproblem is equal to the number of mesh nodes. The meshes employed for the discretization of real configurations have a very large number of elements (a few millions of nodes typically), which leads to a very large sparse eigenproblem. The consequences of facing very large problems are multiple:

  - The matrix is not built explicitly, since the necessary amount of memory needed for its storage would be prohibitive. Only the result of applying the matrix to a vector can be computed. Therefore, direct methods can not be used, and iterative methods become the only option in order to compute a few eigenvalues lying in a certain region of the spectrum [156].

  - Since the matrix is not explicitly available, the use of explicit preconditioners to accelerate the convergence is not possible, which would be very interesting for the use of shift-and-invert approaches [156].

  - Another important aspect is the parallelism of the algorithms. Indeed, in the framework of High Performance Computing (HPC), effective parallel algorithms with good scalability are needed, in order to handle real configurations within a reasonable elapsed time.

- As mentioned before, a nonlinear eigenproblem must be solved. Today, nonlinear eigensolvers of general purpose are not available in the literature. In order to handle this limitation, the eigenproblem is first linearized and then a sequence of linear

problems has to be solved to obtain one solution of the nonlinear problem, making the process long and expensive. This work investigates different ways of accelerating the said process.

Numerical linear algebra in general, and eigenvalue problems in particular, are very active fields of research, specially since the introduction of modern computers around 1950. The article by Golub and van der Vorst [48] constitutes an excellent review of the eigenvalue problem throughout the 20th century, and contains more than 150 references concerning eigenvalue computation. The eigenvalue problem for a square matrix A consists in the determination of nontrivial solution of

$$Ax = \lambda x$$

where λ represents an eigenvalue of A and x is an eigenvector. The question that summarizes the eigenvalue problem is: how can eigenvalues and eigenvectors be computed efficiently and how accurate are they? Many methods have answered this question, but only a few are of practical use today. One of the first and simplest methods is the so-called Power iteration. It is based on the idea that if a given vector is repeatedly applied to a matrix, and properly normalized, then it will eventually lay in the direction of the eigenvector associated with the largest magnitude eigenvalue. The Power method is not used directly today, but it is exploited (implicitly) by more efficient techniques, like Krylov methods, inverse iteration or the QR algorithm [129, 156, 167].

One thing is clear: a method for the calculation of the eigenvalues of any matrix of order n must be necessarily iterative. If it was possible to compute the eigenvalues of a nth order matrix A in a finite number of computation, depending only on n, it would be in contradiction with the fundamental theorem of Abel-Ruffini: no algorithm exists for the computation of the roots of a general polynomial of degree greater than 4.

Therefore, the methods used in AVSP and studied in this work are iterative. Traditionally, the solver used in AVSP for the computation of a few smallest magnitude eigenvalues was the Implicitly Restarted Arnoldi method [4, 78], implemented in the Fortran package ARPACK [75]. A basic version of the Jacobi-Davidson method [146, 149, 150, 151] was also available in AVSP. In this work, these and other methods are investigated for solving the eigenvalue problem from combustion instabilities in an effective fashion. Some of them showing promising features have been implemented in the acoustic solver.

1.4 Objectives and organization of the present work

1.4.1 Objectives

The present work is circumscribed by the framework of thermoacoustic instabilities. It develops along two well differentiated axes: on one hand, a physical study of thermoacoustic instabilities in annular combustion chambers via the acoustic solver AVSP; on the other hand, the study and development of efficient numerical algorithms necessary to the solution of the nonlinear eigenproblem that comes from the discretization of the Helmholtz

equation [144]. Indeed, AVSP has been widely used for the study of combustion instabilities [50, 97, 145, 148], using Flame Transfer Functions (FTF) for describing the flame-acoustics mutual interaction [28, 29, 38, 142]. The main objectives of this thesis can be summarized as follows:

- Study and development of fast and robust parallel eigensolvers adapted to the thermoacoustic context of AVSP.

- Accelerate the computation of eigenvalues and eigenvector of the nonlinear eigeproblem in AVSP. The nonlinear eigenvalue problem is handled by solving a sequence of linear eigenproblems. Techniques allowing the use of solutions previously computed in order to accelerate the solution of the next problem in the sequence are proposed.

- Today most modern gas turbine combustors are annular, which means that the most dangerous resonant modes often take the form of azimuthal waves. In this work, azimuthal modes in annular combustion chambers are investigated. The study of their nature (standing, spinning or mixed) and stability depending on the symmetry of the system is one of the objectives of this work. The effect of Flame Transfer Function parameters and the coupling between cavities is also investigated.

As a result, this work is a mixed study between two fields: thermoacoustics and numerical methods for the solution of large sparse eigenproblems. It is typical of many present research themes where the interaction between the physical and the numerical method used to solve it is very strong and requires specific attention.

1.4.2 Organization of the manuscript

Part I The current chapter is a description of the general framework of combustion instabilities. Growing energy demand and environmental issues have put gas turbine engine manufactures into a challenging situation. Combustors using lean combustion are particularly prone to develop combustion instabilities. The prevention of these instabilities at an early design stage has become of first importance. In Chapter 2, the basic equations and hypothesis that allow the study of thermoacoustic instabilities in this work are described. A wave equation with a reactive term is then obtained. Its discretization on unstructured meshes leads to a nonlinear eigenvalue problem whose solution provides the frequency, stability and structure of the resonant modes of the combustion chamber.

Part II This part is dedicated to the numerical aspects of the solution of the nonlinear eigenproblem, which is linearized using a fixed point method. In Chapter 3, algorithms for the solution of the resulting linear eigenproblems are described. The pertinence of these algorithms for the solution of the thermoacoustic eigenvalue problem is investigated in Chapter 4. Several strategies for accelerating the fixed point iteration method are proposed, showing good results.

Part III Today, most modern gas turbine combustors are of annular type, showing azimuthal instabilities. This part is dedicated to the study of azimuthal modes in annular chambers. In Chapter 5, an academic annular combustion chamber is studied using both an analytical model called ATACAMAC and the 3D Helmholtz solver AVSP, showing a very good agreement. The use of this analytical tool helps the analysis of the effect of symmetry breaking on the stability and nature of azimuthal modes is investigated. In Chapter 6, combustion instabilities in a real annular combustor are studied using AVSP.

Chapter **2**

Thermoacoustic model in AVSP

Contents

This chapter is dedicated to the description of the physical model used in this work for the study of thermoacoustic instabilities in combustion chambers. Starting from the Navier-Stokes equations, the hypotheses needed to construct a wave equation in reactive flows are first presented. The flame model that allows to link the flame response to acoustic fluctuations is described and extended to annular configurations that present many flames circumferentially-arranged in annular chambers, representative of modern gas turbine combustors.

33

Assuming harmonic fluctuations, the wave equation in the time domain can be written in the frequency domain, taking the form of a non homogeneous Helmholtz equation whose right-hand side term accounts for the coupling between combustion and acoustics.

The discretization of the Helmholtz equation on unstructured meshes, using a finite volume formulation, leads to a complex non-symmetric nonlinear eigenvalue problem. The matrices that define the eigenvalue problem are mostly determined by the mesh size and quality, as well as by the acoustic boundary conditions and the integration of the active flame effects. There is a direct link between the quality of the acoustic model (and its complexity) and the eigenproblem which will have to be solved later. For example, meshes with very large size variations between the smallest and the largest elements, will lead to ill-conditioned matrices. Similarly, using complex impedances at the boundaries or active flame formulation will lead to a nonlinear eigenvalue problem, which is more complicated to solve than a linear one. Throughout this work, we will point out the implications of modeling on the applied mathematical methods required to solve the problem.

2.1 From Navier-Stokes equations to a wave equation for reactive flows

The thermoacoustic instabilities mechanism is the result of complex interactions between turbulence, combustion and acoustic waves in the confined domain that is a combustion chamber. A certain number of hypothesis (described in the following) are often made [35, 97, 118] in order to simplify the problem: most of them are reasonable and allow to capture the main physical phenomena involved in thermoacoustic instabilities. The mixture is considered as a perfect gas where all species have the same molar weight and heat capacity. Then, starting from the general Navier-Stokes equations, within the context of linear acoustics, these hypothesis allow the derivation of a wave equation that takes into account the interaction between the flame and the acoustic waves.

2.1.1 The fundamental set of equations

As shown in [35], the mass conservation and momentum equations for a compressible viscous fluid, in absence of external forces (H1) read:

$$\frac{D\rho}{Dt} + \rho \nabla \cdot \vec{u} = 0, \tag{2.1}$$

$$\rho \frac{D\vec{u}}{Dt} = -\nabla p + \frac{\partial \sigma_{i,j}}{\partial x_j} \vec{e_i}, \tag{2.2}$$

where $\sigma_{i,j}$ is the viscous stress tensor and $\vec{e_i}$ is the unit vector in the direction of the coordinate i. From the energy equation, the following equation is obtained for the entropy:

$$\rho T \frac{DS}{Dt} = q + \nabla \cdot (k \nabla T) + \sigma_{i,j} \frac{\partial u_i}{\partial x_j}, \tag{2.3}$$

where k is the thermal conductivity and q is the rate of heat added by the combustion to the fluid. Viscosity can dissipate energy at high frequencies, but for the range of frequencies

at which thermoacoustic instabilities rise (low frequencies), the corresponding wave lengths are large so that it is commonly assumed that viscous terms can be neglected (H2), i.e., $\sigma_{i,j} = 0$ in Eqs. (2.2) and (2.3). Moreover, heat transfer by conduction is also neglected in Eq. (2.3).

From the First Principle of thermodynamics, the entropy equation can be written as

$$\frac{DS}{Dt} = \frac{C_v}{p}\frac{Dp}{Dt} - \frac{C_p}{\rho}\frac{D\rho}{Dt}.$$

Using the mass conservation equation (Eq. (2.1)), this equation can be recast as

$$\frac{1}{\gamma p}\frac{Dp}{Dt} + \nabla \cdot \vec{u} = \frac{\gamma - 1}{\gamma}\frac{q}{p}.$$

Hence, the fundamental set of equations is:

$$\boxed{\frac{1}{\gamma p}\frac{Dp}{Dt} + \nabla \cdot \vec{u} = \frac{\gamma - 1}{\gamma}\frac{q}{p}} \tag{2.4}$$

$$\boxed{\rho\frac{D\vec{u}}{Dt} + \nabla p = 0.} \tag{2.5}$$

2.1.2 Linearization of the fundamental set of equations

The fluid variables are decomposed into a mean value, denoted by the subscript 0, plus a fluctuation, denoted by the subscript 1,

$$p(\vec{x}, t) = p_0(\vec{x}) + p_1(\vec{x}, t),$$
$$\rho(\vec{x}, t) = \rho_0(\vec{x}) + \rho_1(\vec{x}, t),$$
$$\vec{u}(\vec{x}, t) = \vec{u}_0(\vec{x}) + \vec{u}_1(\vec{x}, t).$$

It is assumed, within the context of linear acoustics (H3), that fluctuations are small compared to the mean values: $p_1 \ll p_0, \rho_1 \ll \rho_0, u_1 \ll c_0$. Note that the reference velocity is the sound speed $c_0(\vec{x})$. The mean flow $\vec{u}_0$ is considered null (H4). This is a strong assumption that constraints the application of these equations to situations where the Mach number is small and its effect on acoustics can be neglected [97].

Considering this variable decomposition and neglecting second order terms, the fundamental set of equations (Eqs. (2.4–2.5)) is linearized, giving the following set of linearized equations:

$$\boxed{\frac{1}{\gamma p_0}\frac{\partial p_1}{\partial t} + \nabla \cdot \vec{u_1} = \frac{\gamma - 1}{\gamma p_0}q_1,} \tag{2.6}$$

$$\boxed{\frac{\partial}{\partial t}\vec{u}_1 + \frac{1}{\rho_0}\nabla p_1 = 0,} \tag{2.7}$$

where q_1 is the fluctuating part of the heat release. Note that Eqs. (2.6–2.7) are equivalent to the linearized Euler equations for non-reactive flows, except that the right-hand side term of Eq. (2.6) is non null. It takes into account the combustion effect on the acoustics.

2.1.3   A wave equation for reactive flows

As done in classic acoustics, the set of linearized equations can be combined in order to obtain the wave equation. Indeed, taking $[\partial/\partial t(\text{Eq. }(2.6)) - \nabla(\text{Eq. }(2.7))]$, it follows

$$\frac{1}{\gamma(\vec{x})p_0}\frac{\partial^2 p_1(\vec{x},t)}{\partial t^2} - \nabla \cdot \frac{1}{\rho_0(\vec{x})}\nabla p_1(\vec{x},t) = \frac{\gamma(\vec{x})-1}{\gamma(\vec{x})p_0}\frac{\partial q_1(\vec{x},t)}{\partial t}. \tag{2.8}$$

The left-hand side of Eq. (2.8) has the form of the classic wave equation in a variable sound speed flow, but in the present case, there is a non null right-hand side term that accounts for the flame effect on acoustics (active flame). The combustion is also present through temperature variations, which is the reason why the quantity $\rho_0(\vec{x})$ is not constant in space and it must be kept within the divergence (passive flame). If the molecular weights of all the species that compose the equivalent gas are considered constant (H5), it follows that $\gamma(\vec{x})$ is constant [118]. In this case, the wave equation reads as

$$\boxed{\frac{\partial^2 p_1(\vec{x},t)}{\partial t^2} - \nabla \cdot c_0^2(\vec{x})\nabla p_1(\vec{x},t) = (\gamma-1)\frac{\partial q_1(\vec{x},t)}{\partial t}.} \tag{2.9}$$

Within the framework of linear acoustics it is reasonable to assume that the pressure fluctuations have the form of an harmonic wave:

$$p_1(\vec{x},t) = \Re[\hat{p}(\vec{x})e^{-i\omega t}], \ \hat{p} \in \mathbb{C}, \omega \in \mathbb{C} \Rightarrow$$

$$\Rightarrow \ p_1(\vec{x},t) = e^{\omega_i t}\Re[\hat{p}(\vec{x})e^{-i\omega_r t}],$$

where $\omega_r = \Re(\omega)$ and $\omega_i = \Im(\omega)$. The acoustic pressure can be then viewed as an harmonic signal that oscillates with angular frequency ω_r and whose amplitude grows ($\omega_i > 0$) or decreases ($\omega_i < 0$). Analogously, the velocity fluctuation $\vec{u}_1$ and the heat release fluctuations q_1 can be written as

$$\vec{u}_1(\vec{x},t) = \Re[\hat{\vec{u}}(\vec{x})e^{-i\omega t}],$$
$$q_1(\vec{x},t) = \Re[\hat{q}(\vec{x})e^{-i\omega t}].$$

Alternatively, the imaginary part of the complex quantities $\hat{p}e^{-i\omega t}$, $\hat{\vec{u}}e^{-i\omega t}$, $\hat{q}e^{-i\omega t}$ can be taken instead. In either case, using the harmonic assumption for the fluctuating variables, the wave equation in the time domain becomes a Helmholtz equation in the frequency domain:

$$\boxed{\nabla \cdot c_0^2(\vec{x})\nabla \hat{p}(\vec{x}) + \omega^2 \hat{p}(\vec{x}) = i\omega(\gamma-1)\hat{q}(\vec{x}).} \tag{2.10}$$

The objective of AVSP is to solve Eq. (2.10) in a 3D field with the proper boundary conditions. Writing Eq. (2.7) in the frequency domain allows to express the acoustic velocity in terms of the pressure fluctuation gradient

$$-i\omega\hat{\vec{u}} + \frac{1}{\rho_0(\vec{x})}\nabla \hat{p}(\vec{x}) = 0. \tag{2.11}$$

In the context of the present work, three boundary conditions are usually considered:

- Rigid walls that impose zero normal acoustic velocity on the boundary, i.e., $\hat{\vec{u}} \cdot \vec{n}_{BC} = 0$. This condition can be rewritten as a Neumann condition for the acoustic pressure using Eq. (2.11):

$$\nabla \hat{p} \cdot \vec{n}_{BC} = 0 \text{ on } \partial\Omega_N. \tag{2.12}$$

- A Dirichlet condition for the acoustic pressure, imposing a null pressure on the corresponding boundary:

$$\hat{p} = 0 \text{ on } \partial\Omega_D. \tag{2.13}$$

- A reduced complex impedance $Z = \hat{p}/(\rho_0 c_0 \hat{\vec{u}} \cdot \vec{n}_{BC})$ establishing a general relation between $\hat{\vec{u}}$ and $\hat{p}$ on the corresponding patch (the concept of acoustic impedance is further developed in Sec. 2.3.1). This condition can be written as a Robin condition for the acoustic pressure using Eq. (2.11):

$$c_0 Z \nabla \hat{p} \cdot \vec{n}_{BC} - i\omega \hat{p} = 0 \text{ on } \partial\Omega_Z. \tag{2.14}$$

For a Dirichlet condition we have $Z = 0$, whereas for a wall $Z = \infty$.

2.2 Flame model

One of the difficult points of the present model for thermoacoustic instabilities, is the description of the fluctuating heat release term $\hat{q}$. The objective is to write this quantity in terms of acoustic variables $(\hat{\vec{u}}, \hat{p})$, so that Eq. (2.10) can be entirely expressed in acoustic variables $\hat{\vec{u}}, \hat{p}$. In this work, Flame Transfer Functions (FTF) are used to link the heat release fluctuation $\hat{q}$ to the acoustic velocity fluctuation $\hat{u}$. The idea behind FTF is simple: an acoustic perturbation is introduced to the flame and its response is analyzed by quantying $\hat{q}$ as a function of $\hat{u}$. This idea was first introduced by Crocco [28, 29] for compact flames. In the frequency domain, the global FTF is defined as the ratio between the relative heat release fluctuations integrated over the flame volume V_f ($\hat{Q}/\bar{Q}$) and the relative inlet velocity perturbation ($\hat{u}/\bar{u}$):

$$F(\omega) = \frac{\hat{Q}/\bar{Q}}{\hat{u}/\bar{u}} = N_3 e^{i\omega\tau}, \tag{2.15}$$

where ω is the angular frequency. The FTF is a function of the frequency ω and is determined by the gain $N_3 = |F(\omega)|$ and its phase $\tau = Arg(F(\omega)/(2\pi\omega))$. In Eq. (2.15) the interaction index N_3 is dimensionless. One can alternatively write

$$F(\omega) = \frac{\hat{Q}}{\hat{u}} = N_2 e^{i\omega\tau}, \tag{2.16}$$

where the interaction index N_2 has dimensions ($N_2 = \dfrac{\bar{Q}}{\bar{u}} N_3 \ [J/m]$)[1].

Flame Transfer Functions have been widely used in the literature for the study of thermoacoustic instabilities [80]. It has been shown that the FTF depends on the flame shape [66] as well as on operating conditions [68]. Flame Transfer Functions have been

---

[1]See Tab. 2.2 for notations

investigated for laminar and turbulent flames for which only axial velocity perturbations are considered. Examples of FTF for laminar conical flames can be found in [39, 65, 68] and laminar and turbulent V-flames in [142, 3], respectively. The effect of thermal boundary conditions and combustor confinement on perfectly premixed swirl flames is investigated in [162]. Recently, FTF formulations have been extended to FDF (Flame Describing Function) by EM2C [148] to include the effects of the amplitude of the acoustic velocity u_1 on the flame response. FDF will not be used here.

2.2.1 Local Flame Transfer Function

The FTF of Eq. (2.16) is a global formulation that links the heat release fluctuations integrated over the flame zone $\hat{Q} = \int_{V_f} \hat{q} dV$ to the velocity fluctuation $\hat{u}$ at a given reference point placed at the burner inlet. This model was extended to a local formulation by Nicoud et al. in [97], where the local response of the flame $q_1(\vec{x}, t)$ at the instant t is linked to the acoustic velocity fluctuations $\vec{u}_1(\vec{x}_{ref}, t - \tau)$ at the instant $t - \tau$ at a reference point $\vec{x}_{ref}$ suitably chosen (Fig. 2.1).
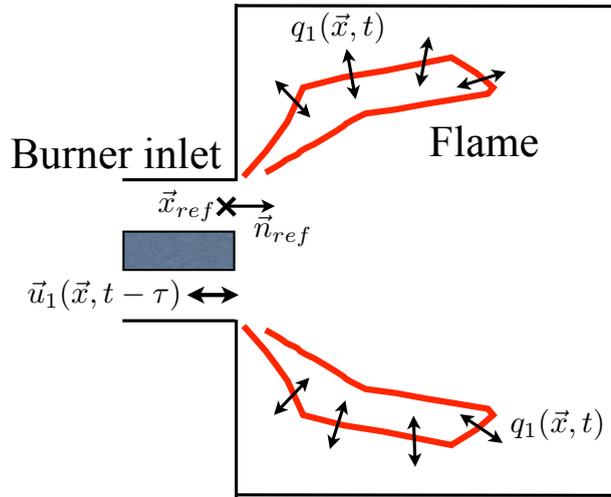
Figure 2.1: Scheme of a combustion chamber with a forced acoustic perturbation through the burner inlet: the velocity fluctuation $\vec{u}_1$ through the inlet is measured at the reference point $\vec{x}_{ref}$ and is responsible of the heat release fluctuations q_1 in the flame.

The extension to a local formulation of the global model of Eq. (2.16) allows to write the heat release fluctuation in the frequency domain $\hat{q}$ as:

$$\boxed{\hat{q}(\vec{x}) = n_{local}(\vec{x})\vec{\hat{u}}(\vec{x}_{ref}) \cdot \vec{n}_{ref} e^{i\omega \tau_{local}(\vec{x})}} \quad [W/m^3], \tag{2.17}$$

where $\vec{x}_{ref}$ is the reference point where the velocity fluctuation is considered along the direction $\vec{n}_{ref}$, which is taken in general normal to the inlet.

In Eq. (2.17), the local FTF parameters n_{local} $[W/m^4]$ and τ_{local} $[s]$ depend on the pulsation frequency ω. Note also that the choice of the reference point $\vec{x}_{ref}$ where the velocity fluctuations are measured plays an important role in this model. As shown by Truffin

in [164] it must be chosen close enough to the flame, so that $|\vec{x}_{ref} - \vec{x}_{flame}|$ remains small compared to the wavelength λ of the forced acoustic mode. Typically, the Helmholtz number He $= |\vec{x}_{flame} - \vec{x}_{ref}|\omega/c \ll 1$. When the flame is compact, the time delay τ_{local} is expected to be the same for all flame points and therefore equal to the global time delay τ of Eq. (2.15).

Although the response of the flame is linear for small amplitude velocity fluctuations, nonlinear effects appear [8, 11] when the velocity oscillation amplitude increases, until a limit cycle is reached, for which the the oscillation level is sustained. When the velocity fluctuations are of the same order than the mean flow, the FTF depends not only on the excitation frequency ω, but also on the amplitude of the velocity fluctuations $|\vec{u}_1|$. Then the FTF can be extended [34] to the so-called Flame Describing Function (FDF) defined as

$$F(\omega, |\hat{u}|) = \frac{\hat{q}/\bar{Q}}{\hat{u}/\bar{u}},$$

which takes into account nonlinear effects on the flame response. Linear thermoacoustic analysis provides a stability criterion, but the use of the FDF becomes necessary in order to study certain nonlinear phenomena such as limit cycles, mode switching or instability triggering [16, 63].

Generally the FTF can be determined experimentally, analytically and numerically. Experimentally, loudspeakers are used to excite the flow and velocity or pressure sensors allow to measure the unsteady velocity $\hat{u}$ in Eq. (2.17). The heat release fluctuations, on the other hand can be determined by chemiluminescense of radicals CH^* or OH^* [38, 154, 171]. Experimental studies for the determination of the FTF of laminar and turbulent flames include [56, 82]. Nevertheless, for complex industrial combustors, the experimental determination of the FTF is difficult and costly because it requires optical access to the combustion chamber. Concerning analytical determinations, Fleifil et al. introduced in [42] a model based on the kinematic analysis of the flame front evolution for conical flames. This model was extended in [38, 142] and recently Palies et al. [109] adapted it to premixed swirled flames. Finally, the FTF can be determined via Computational Fluid Dynamics (CFD) computations [53, 64, 25, 162]. In this approach the combustion chamber is excited with forced flow oscillations in order to perturb the flame, so that time series of unsteady velocity and heat release fluctuations are obtained. Then, the obtained data are post-processed in order to obtain the gain and the phase of the FTF.

2.2.2   From global to local Flame Transfer Functions

In certain cases, the local parameters $n_{local}(\vec{x})$ and $\tau_{local}(\vec{x})$ describing the point wise heat release $\hat{q}(\vec{x})$ can be obtained from numerical simulations, e.g. from LES. Nevertheless, in many other cases (experiments, analytical models, etc.), only the global value of the heat release $\hat{Q} = \int_V \hat{q}dV$ is available. Tab. 2.2 contains different definitions of the interaction index corresponding to global formulations of the FTF.

AVSP requires a local heat release $\hat{q}$ defined by n_{local} and τ_{local}. When these fields are not available, they must be obtained from the global values of Tab. 2.2. Knowing that

Type	Name	Definition	Units	Order of magnitude
Dimensional	$n_{local}(x)$	$\dfrac{\hat{q}}{\hat{u}(\mathbf{x}_{ref}) \cdot \mathbf{n}_{ref}}$	$[J/m^4]$	$\mathcal{O}(10^9)$

Table 2.1: Definition of the local interaction index $n_{local}(x)$ in AVSP.

Type	Name	Definition	Units	Order of magnitude
Crocco	N_1	$\dfrac{\hat{Q}}{\hat{u}(\mathbf{x}_{ref}) \cdot \mathbf{n}_{ref}} \dfrac{\gamma - 1}{S_f \gamma p_0}$	$[-]$	$\dfrac{T_{hot}}{T_{cold}} - 1$ (see [118])
Dimensional	N_2	$\dfrac{\hat{Q}}{\hat{u}(\mathbf{x}_{ref}) \cdot \mathbf{n}_{ref}}$	$[J/m]$	$\mathcal{O}(10^9)$
Non-dimensional	N_3	$\dfrac{\hat{Q}/\overline{Q}}{\hat{u}(\mathbf{x}_{ref}) \cdot \mathbf{n}_{ref}/\overline{u}}$	$[-]$	$\mathcal{O}(1)$

Table 2.2: Convention for global amplitude values N_1, N_2 and N_3 with fluctuations of the global heat release $\hat{Q}$ [W]. $\overline{Q}$ and $\overline{u}$ stand for scales of global heat release and velocity, usually taken as the time averaged volume integrated heat release and bulk velocity respectively. In the Crocco's formulation, S_f is a reference surface equal to the cross section area of the injector upstream of the region where the flame stands.

the global heat release $\hat{Q}$ must satisfy $\displaystyle\int_V \hat{q}dV$, the following relation must link the local interaction index n_{local} and time delay τ_{local} to the global quantities of Tab. 2.2:

$$\int_{V_f} n_{local}(\vec{x})e^{i\omega\tau_{local}(\vec{x})}dV = N_2 e^{i\omega\tau}. \tag{2.18}$$

Assuming that $\tau_{local}(\vec{x}) = \tau_{local}$ and $n_{local}(\vec{x}) = n_{local}$ are constant in the flame (which is consistent for compact flames) then, from Eq. (2.18) one simply obtain:

$$n_{local} = \frac{N_2}{V_f} \quad \text{and} \quad \tau_{local} = \tau \quad \text{within the flame,} \tag{2.19}$$

$$n_{local} = 0 \quad \text{and} \quad \tau_{local} = 0 \quad \text{outside the flame,} \tag{2.20}$$

with V_f is the flame volume.

Crocco's model

The Crocco's model [28, 29] is well adapted for analytical comparisons when the flames are compact. This one-dimensional formulation assumes that the heat release fluctuation
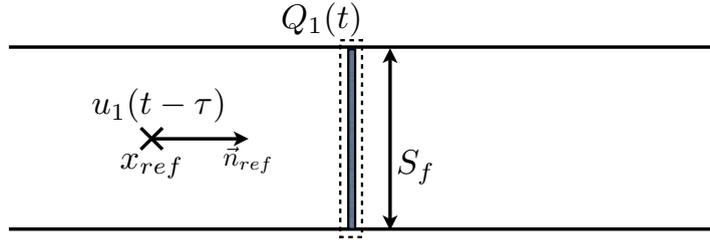
Figure 2.2: Scheme of Crocco's flame model.

integrated over the flow domain $\hat{Q}$ can be written as:

$$\hat{Q} = \int_V \hat{q}(\vec{x})dV = S_f \frac{\gamma p_0}{\gamma - 1} N_1 \vec{\hat{u}} \cdot \vec{n}_{ref} e^{i\omega\tau}, \tag{2.21}$$

where S_f is a reference surface representative of the section that occupies the flame (see Fig. 2.2).

The point wise FTF quantities n_{local} and τ_{local} required by AVSP can be obtained from the global Crocco's parameters considering, as before, that they are constant in the flame and zero everywhere else. From $\hat{Q} = \int_V \hat{q}(\vec{x})dV$, we have:

$$\int_{V_f} n_{local} e^{i\omega\tau_{local}}dV = S_f \frac{\gamma p_0}{\gamma - 1} N_1 e^{i\omega\tau}, \tag{2.22}$$

which yields to the following relation:

$$n_{local} = \frac{\gamma p_0}{(\gamma - 1)} \frac{S_f}{V_f} N_1 \quad \text{and} \quad \tau_{local} = \tau. \tag{2.23}$$

2.2.3 Flame model extension to multi-burner combustors

The classical model described in Sec. 2.2 links the heat release fluctuations in the flame zone to the velocity fluctuations in the burner and was basically designed for longitudinal acosutic modes in a single duct with a single flame. In annular combustors, which have many circumferentially-arranged burners (typically 15-24), it does not seem reasonable to relate the heat release fluctuations of each flame to the velocity through a single burner. Sensiau et al. propose in [145] an extension of the flame model of sec. 2.2 to multi-sector annular combustors which is based on the so-called *Independence Sector Assumption in Annular Combustors (ISAAC)*: Heat release fluctuations in a given sector are driven only by the velocity fluctuations through its own swirler (Fig. 2.3).

Therefore, the annular chamber is divided into N equals sectors and the heat release fluctuations in each sector are related to its own reference point:

$$\hat{q}(\vec{x}) = \begin{cases} n_{local}(\vec{x}, \omega)e^{i\omega\tau_{local}(\vec{x}, \omega)}\vec{\hat{u}}(\vec{x}_{ref_1}) \cdot \vec{n}_{ref_1} \text{ for } \vec{x} \in \text{ Sector 1,} \\ n_{local}(\vec{x}, \omega)e^{i\omega\tau_{local}(\vec{x}, \omega)}\vec{\hat{u}}(\vec{x}_{ref_2}) \cdot \vec{n}_{ref_2} \text{ for } \vec{x} \in \text{ Sector 2,} \\ \qquad\qquad\qquad\qquad\vdots \\ n_{local}(\vec{x}, \omega)e^{i\omega\tau_{local}(\vec{x}, \omega)}\vec{\hat{u}}(\vec{x}_{ref_N}) \cdot \vec{n}_{ref_N} \text{ for } \vec{x} \in \text{ Sector N.} \end{cases} \tag{2.24}$$
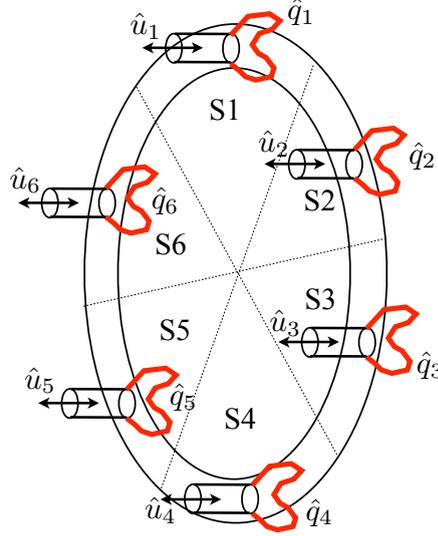
Figure 2.3: Scheme of an annular combustion chamber with 6 burners. ISAAC assumption: the heat release fluctuations in each burner $\hat{q}_i$ are driven by its own unsteady velocity fluctuations $\hat{u}_i$.

The ISAAC assumption is implicitly used in many annular combustor studies [69, 158, 140, 93] and remains valid as long as the interactions between neighboring flames can be neglected. This is acceptable for most gas turbine combustion chambers and it has been confirmed via Large Eddy Simulations of an helicopter combustion chamber composed of fifteen identical burners in [153, 170].[2] Moreover, the flame model of Eq. (2.24) can be still used for the study of azimuthal modes since the main effect of these modes is to introduce longitudinal pulsations of the flow rates through each burner [153, 170, 52, 14].

2.3 Acoustic energy and the Rayleigh criterion

Under the hypothesis previously considered, it is possible to define the following acoustic energy associated with the pressure and velocity fluctuations p_1 and $\vec{u}_1$ [118]:

$$e_1(\vec{x}, t) = \frac{1}{2}\left(\rho_0(\vec{x})u_1^2(\vec{x}, t) + \frac{p_1^2(\vec{x}, t)}{\gamma p_0}\right). \tag{2.25}$$

In [62] the authors provide other definitions of disturbance energy that account not only for acoustic waves, but also for entropy and vorticity waves convected by a mean flow $\vec{u}_0 \neq 0$, but we will limit this discussion to the classical acoustic from of Eq. (2.25).

The temporal evolution of e_1 can be obtained by combining the fundamental linearized equations as $p_1 \times$ [Eq. (2.6)] + $\rho_0 \vec{u}_1 \cdot$ [Eq. (2.7)], so that the following conservation equation for e_1 is obtained:

$$\frac{\partial}{\partial t}\left[\frac{1}{2}\left(\rho_0(\vec{x})u_1^2(\vec{x}, t) + \frac{p_1^2(\vec{x}, t)}{\gamma p_0}\right)\right] + \nabla \cdot p_1(\vec{x}, t)\vec{u}_1(\vec{x}, t) = \frac{\gamma - 1}{\gamma p_0}p_1(\vec{x}, t)q_1(\vec{x}, t). \tag{2.26}$$

---

[2]Nevertheless, there are cases where flame-to-flame interactions play an important role [174, 171] and can not be neglected, like rocket engines. They are not studied in this PhD.

Defining the source term:

$$r_1(\vec{x}, t) = \frac{\gamma - 1}{\gamma p_0} p_1(\vec{x}, t) q_1(\vec{x}, t),$$

and the acoustic flux:

$$\vec{f}_1(\vec{x}, t) = p_1(\vec{x}, t) \vec{u}_1(\vec{x}, t),$$

Eq. (2.26) is integrated over the domain Ω using the Green-Ortrogradsky theorem to obtain:

$$\frac{\partial}{\partial t} \int_\Omega e_1(\vec{x}, t) \; dV + \oint_{\partial \Omega} \vec{f}_1(\vec{x}, t) \cdot \vec{n}_{BC} \; dS = \int_\Omega r_1(\vec{x}, t) \; dV, \qquad (2.27)$$

where

$$E_1(t) = \int_\Omega e_1(\vec{x}, t) \; dV,$$

$$F_1(t) = \oint_{\partial \Omega} \vec{f}_1(\vec{x}, t) \cdot \vec{n}_{BC} \; dS \text{ and}$$

$$R_1(t) = \int_\Omega r_1(\vec{x}, t) \; dV.$$

The conservation equation for the total acoustic energy in the domain Ω is:

$$\frac{d}{dt} E_1(t) = R_1(t) - F_1(t). \qquad (2.28)$$

The meaning of Eq. (2.28) is clear: the evolution of the acoustic energy E_1 integrated over the domain Ω is controlled by the balance between the volumic term R_1 and the acoustic flux F_1 through the boundary $\partial \Omega$. The volumic term

$$r_1(\vec{x}, t) = \frac{\gamma - 1}{\gamma p_0} p_1(\vec{x}, t) q_1(\vec{x}, t)$$

results from the coupling between the pressure and the heat release fluctuations. If the boundary conditions are such that the acoustic flux $F_1(t) = 0$, then the acoustic energy E_1 depends only on the thermoacoustic volumic term R_1. If the last increases with time, then $\frac{dE_1}{dt} > 0$, which reveals the existence of a thermoacoustic instability. Depending on the phase between the pressure fluctuation p_1 and the heat release fluctuation q_1, the volumic term R_1 will appear either as an energy source or as an energy sink, as stated by Rayleigh in 1878 [123]: *"At the phase of greatest condensation heat received by the air, and at the phase of greatest rarefaction heat is given up from it, and thus there is a tendency to maintain the vibrations."* Note that in the present flame model, the phase between p_1 and q_1 is controlled by the FTF delay parameter τ:

$$R_1(t) = \int_\Omega \frac{\gamma - 1}{\gamma p_0} p_1 \frac{\bar{Q}}{\bar{U}} n u_1 e^{i\omega} dV = \frac{\gamma - 1}{\gamma p_0} \frac{\bar{Q}}{\bar{U}} \int_\Omega p_1 u_1 e^{i\omega\tau} dV.$$

The Rayleigh criterion depends directly on the field of τ and on the phase between p_1 and u_1 which is controlled by the impedances on boundaries and can not be changed easily. As

a consequence R_1 depends mainly on τ. In [111], the stability of azimuthal modes in an academic annular configuration is investigated as a function of τ. In [170], a compressible LES of a real combustion chamber allows to demonstrate that changing the kinetics of the combustion reaction (i.e., modifying the delay τ) can be enough to damp the thermoacoustic instability installed in the chamber.

In general, the flux $p_1\vec{u}_1$ is associated with acoustic losses through the boundaries $\partial\Omega$ of the domain. In this case, the Rayleigh criterion is only a necessary condition for thermoacosutic instabilities to occur. More generally, the acoustic energy E_1 integrated over the domain Ω will increase (the thermoacoustic instability will occur) if the gain due to R_1 is larger than the losses at the boundaries:

$$\int_\Omega \frac{\gamma-1}{\gamma p_0} p_1 q_1 \ dV > \oint_{\partial\Omega} p_1 \vec{u}.\vec{n}_{BC} \ dS.$$

2.3.1 Acoustic impedance

The concept of impedance appears first in the field of electricity. The electric impedance Z allows to link the current I to the potential difference V in the case of sinusoidal power, following the Ohm's law $V = Z\,I$. Under the assumption of harmonics oscillations, we can introduce an acoustic impedance Z analogous to the electric impedance, where the role of the potential difference V is played by the pressure oscillation $\hat{p}$ and the role of the current I is played by the velocity $\hat{\vec{u}}$. Hence we can write :

$$Z = \frac{\hat{p}(\vec{x})}{\rho_0 c_0 \ \hat{\vec{u}}(\vec{x}) \cdot \vec{n}}, \tag{2.29}$$

where $\vec{n}$ is the domain boundary normal. In Eq. (2.29), Z is a complex reduced acoustic impedance, whose argument represent the phase between pressure and velocity fluctuations along the direction $\vec{n}$ at point $\vec{x}$. Note that, in general, the impedance is a function of the frequency ω, i.e., $Z = Z(\omega)$.

In many low-order models for thermoacoustics, the configuration is modeled as a 1D network of acoustic elements [47, 139, 33], and the acoustic impedance is used in transfer matrices that link pressure and velocity signals, replacing elements with a complex geometry by the equivalent impedance [141, 121, 164]. A famous example in the literature is the equivalent complex impedance $Z(\omega)$ of the Helmholtz resonator [13]:

$$Z(\omega) = \frac{\rho c k^2}{2\pi} + j\left(\omega\frac{\rho\ell}{S} - \frac{\rho c^2}{\omega V}\right),$$

where k is the wavenumber ($k = \omega/c$), ℓ is the length of the small tube, S is its section and V is the volume of the big cavity.

Reflection coefficient and impedance

A very intuitive way of expressing boundary conditions for acoustic problems is to use the reflection coefficient R, which is equal to the ratio between the amplitudes of the reflected (A^-) and incident (A^+) waves at the point $\vec{x}_w$ (Fig. 2.4):

$$R = \frac{A^- e^{-i\vec{k}\cdot\vec{x}_w}}{A^+ e^{i\vec{k}\cdot\vec{x}_w}}. \tag{2.30}$$

Intuitively, $|R| < 1$ implies that fluctuations are damped at the boundary, which translates into an acoustic flux leaving the domain, leading to a net loss of acoustic energy. On the contrary, $|R| > 1$ means that the oscillations are amplified at the wall and a net acoustic flux enters the domain.
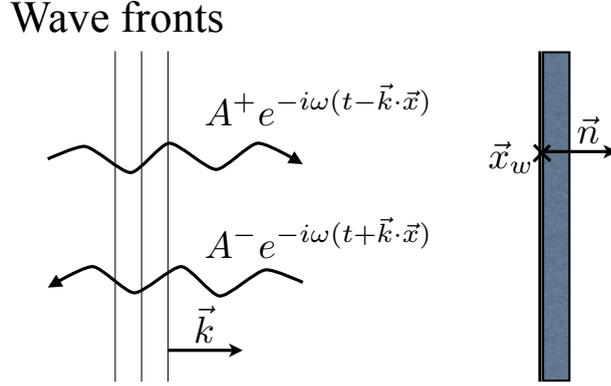
Figure 2.4: Incident and reflected waves traveling along the direction $\vec{k}$.

The pressure $\hat{p}$ and the velocity $\hat{\vec{u}}$ at the point $\vec{x}_w$ can be written as the superposition of two traveling planar waves, propagating in opposite directions along $\vec{k}$, as

$$\hat{p}(\vec{x}_w) = A^+ e^{i\vec{k}\cdot\vec{x}_w} + A^- e^{-i\vec{k}\cdot\vec{x}_w},$$

$$\hat{\vec{u}}(\vec{x}_w) = \frac{A^+}{\rho c} e^{i\vec{k}\cdot\vec{x}_w} - \frac{A^-}{\rho c} e^{-i\vec{k}\cdot\vec{x}_w}. \tag{2.31}$$

From the definition of impedance (Eq. (2.29)) at the point $\vec{x}_w$, the impedance can be written in terms of reflected and incident waves

$$Z_w = \frac{\hat{p}(\vec{x}_w)}{\rho c \hat{\vec{u}}(\vec{x}_w) \cdot \vec{n}} = \frac{A^+ e^{i\vec{k}\cdot\vec{x}_w} + A^- e^{-i\vec{k}\cdot\vec{x}_w}}{A^+ e^{i\vec{k}\cdot\vec{x}_w} - A^- e^{-i\vec{k}\cdot\vec{x}_w}}.$$

The relation between impedance and reflection coefficient is straighforward[3]:

$$Z_w = \frac{1+R}{1-R} \Leftrightarrow R = \frac{Z_w - 1}{Z_w + 1}. \tag{2.32}$$

---

[3]Note however that the link between Z and R depends on the sign convention used for the normal vector $\vec{n}$ at boundaries: in AVSP, all normal vectors $\vec{n}$ are considered entering the domain

2.4 From the Helmholtz equation to a nonlinear eigenvalue problem

Using Eq. (2.11), the heat release fluctuation $\hat{q}(\vec{x})$ from Eq. (2.17) can be written in terms of the pressure gradient at the reference point:

$$\hat{q} = n_{local}e^{i\omega\tau_{local}}\underbrace{\frac{1}{i\omega\rho_0}\nabla\hat{p}(\vec{x}_{ref})}_{\hat{u}(\vec{x}_{ref})}\cdot\vec{n}_{ref}, \tag{2.33}$$

which allows to obtain, using Eq. (2.33) in Eq. (2.10), the Helmholtz equation for reactive flows entirely written in terms of the acoustic pressure oscillation $\hat{p}$

$$\boxed{\nabla \cdot c_0^2(\vec{x})\nabla\hat{p}(\vec{x}) + \omega^2\hat{p}(\vec{x}) = \frac{(\gamma-1)}{\rho_0(\vec{x})}n_{local}(\vec{x},\omega)e^{i\omega\tau_{local}(\vec{x},\omega)}\nabla\hat{p}(\vec{x}_{ref}) \cdot \vec{n}_{ref}.} \tag{2.34}$$

This section shows how the discretization of Eq. (2.34) with boundary conditions defined by Eqs. (2.12–2.14), using a finite volume formulation on unstructured tetrahedral meshes, leads to a nonlinear complex eigenvalue problem. The underlying numerical aspects in AVSP are inherited from AVBP [126, 138] and they have been developed to offer excellent parallel performances. The subsequent developments are extracted from the PhD of C. Sensiau [144], where one can additionally find the equivalent finite element formulation obtained from the finite volume formulation used in AVSP. The resulting discretization matrices are never stored, since the necessary machine memory when dealing with very large meshes can become unaffordable. In this formulation, called "matrix free", matrices are never formed explicitly and only the output vector, resulting of applying the associated linear operator to a given input vector, can be computed.

In AVSP, the discrete values of the acoustic pressure and the sound speed are stored at the mesh nodes, while the pressure gradient is evaluated at the center of the cells and it is constant for each cell. For the sake of simplicity, the developments and schemes presented here correspond to 2D meshes, but the extension to 3D cases is straightforward. In Fig. 2.5, a cell corresponding to a 2D mesh composed of triangular elements is displayed. The cell is noted Ω_j and its three edges have lengths L_{e_1}, L_{e_2} and L_{e_3}, with normals $\vec{n}_{e_1}$, $\vec{n}_{e_2}$ and $\vec{n}_{e_3}$, respectively. The index used for the edges is the index of their opposite nodes. It is useful to note that, for a triangular element, we have

$$L_1\vec{n}_{L_1} + L_2\vec{n}_{L_2} + L_3\vec{n}_{L_3} = 0. \tag{2.35}$$

2.4.1 Discretization of the $\nabla \cdot c_0^2\nabla p$ operator

The calculation of the $\nabla\cdot c_0^2\nabla p$ operator at the node j requires knowing the pressure gradient ∇p for the adjacent elements Ω_j. The pressure gradient at the element Ω_j is noted $\nabla p|_{\Omega_j}$ and it is computed as the mean value over the cell

$$\nabla p|_{\Omega_j} = \frac{1}{S_{\Omega_j}}\int_{\Omega_j}\nabla p \ dS.$$
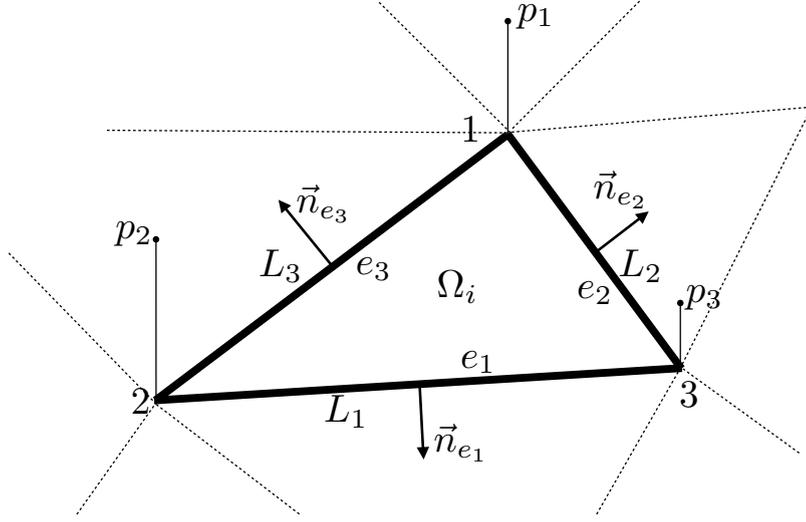
Figure 2.5: Ω_j is one cell of a 2D unstructured (or regular) mesh. The discrete values of the pressure $\hat{p}(\vec{x})$ from Eq. (2.34) are stored at the nodes of the elemet, noted p_1, p_2 and p_3 respectively, as well as the discrete values of the sound speed field $c_0(\vec{x})$, c_{0_1}, c_{0_2} and c_{0_3}. The edges of the element are noted e_1, e_2 and e_3 and the corresponding exterior normals are $\vec{n}_{e_1}$, $\vec{n}_{e_2}$ and $\vec{n}_{e_3}$. The area of the cell is S_{Ω_i} (V_{Ω_i} is the corresponding volume in the 3D case).

Using the Green-Ostrogradsky theorem, it can be recast as

$$\nabla p|_{\Omega_j} = \frac{1}{S_{\Omega_j}} \oint_{\partial \Omega_j} p \, \vec{n} \, dL = \frac{1}{S_{\Omega_j}} \left[\int_{e_1} p \, \vec{n}_{e_1} \, dL + \int_{e_2} p \, \vec{n}_{e_2} \, dL + \int_{e_3} p \, \vec{n}_{e_3} \, dL \right].$$

Having the discrete values of the pressure stored at nodes and considering a linear evolution of the pressure along the element edges, it follows

$$\nabla p|_{\Omega_j} = \frac{1}{S_{\Omega_j}} \left[\frac{(p_2 + p_3)L_{e_1}}{2} \vec{n}_{e_1} + \frac{(p_1 + p_3)L_{e_2}}{2} \vec{n}_{e_2} + \frac{(p_1 + p_2)L_{e_3}}{2} \vec{n}_{e_3} \right].$$

Reordering terms and using Eq. (2.35), one can finally write

$$\boxed{\nabla p|_{\Omega_j} = \frac{1}{2S_{\Omega_j}} \left[p_1 L_{e_1} \vec{n}_{e_1} + p_2 L_{e_2} \vec{n}_{e_2} + p_3 L_{e_3} \vec{n}_{e_3} \right].} \tag{2.36}$$

On the other hand, the sound speed evaluated at the elements adjacent to the node j, noted $c_0|_{\Omega_j}$ is also needed for the discretization of $\nabla \cdot c_0^2 \nabla p$ at node j. The sound speed at the center of the element Ω_j is simply evaluated as the mean of the node values

$$c_0|_{\Omega_j} = \frac{c_{0_1} + c_{0_2} + c_{0_3}}{3}. \tag{2.37}$$

2.4.1.1 Computation of $\nabla \cdot c_0^2 \nabla p\big|_j$ for interior nodes

An interior node of a 2D triangular mesh is represented in Fig. 2.6, where the notations of the geometric elements used in the following are described. With the orientation of the
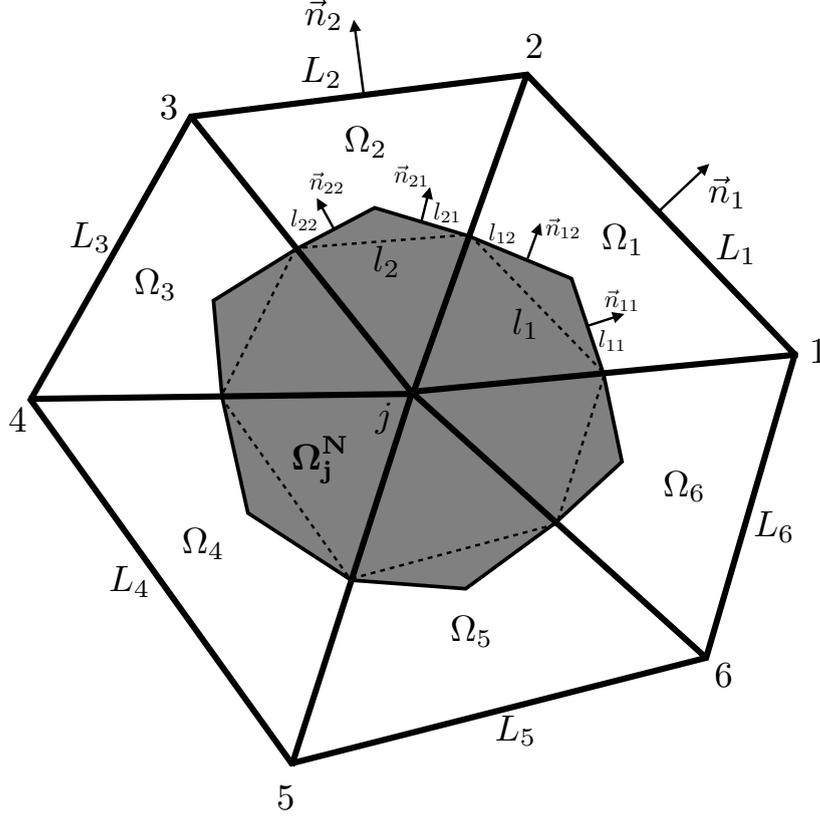
Figure 2.6: Representation of an interior node, noted j for a 2D triangular mesh, shared by the elements Ω_i, for $i = 1, \ldots, 6$. The dual cell noted Ω_j^N associated with the node j is represented by the shaded area. It is delimited by the segments (of length l_{i1} and l_{i2}) linking the center of each element Ω_i (medians intersection) to the middle of the corresponding edge. The normals $\vec{n}_{i1}$, $\vec{n}_{i1}$ are external to the dual cell. The segments l_i (dashed-lines) link the middle of two consecutive edges and, from Thales' theorem, $l_i = L_i/2$.

normals Fig. 2.6, and using Thales' theorem, we have, for the element Ω_1

$$l_11\vec{n}_{11} + l_12\vec{n}_{12} = l_1\vec{n}_1 = \frac{L_1}{2}\vec{n}_1. \tag{2.38}$$

The discrete value of $\nabla \cdot c_0^2 \nabla p$ at node j, noted $\nabla \cdot c_0^2 \nabla p|_j$, is computed as the mean value of $\nabla \cdot c_0^2 \nabla p$ over the dual cell Ω_j^N:

$$\nabla \cdot c_0^2 \nabla p\big|_j = \frac{1}{S_{\Omega_j^N}} \int_{\Omega_j^N} \nabla \cdot c_0^2 \nabla p \, dS = \frac{1}{S_{\Omega_j^N}} \oint_{\partial \Omega_j^N} c_0^2 \nabla p \cdot \vec{n} \, dL.$$

As mentioned before, the values $c_0|_{\Omega_i}$ and $\nabla p|_{\Omega_i}$ are assumed constant over the element Ω_i. Consequently they are constant along the corresponding segments l_{i1} and l_{i2}, and the integral over the border of the dual cell gives

$$\nabla \cdot c_0^2 \nabla p\big|_j = \frac{1}{S_{\Omega_j^N}} \left[c_0^2|_{\Omega_1} \nabla p|_{\Omega_1} \cdot (l_{11}\vec{n}_{11} + l_{12}\vec{n}_{12}) + \cdots + c_0^2|_{\Omega_6} \nabla p|_{\Omega_6} \cdot (l_{61}\vec{n}_{61} + l_{62}\vec{n}_{62}) \right].$$

Finally, using Eq. (2.38) one obtains

$$\nabla \cdot c_0^2 \nabla p \big|_j = \frac{1}{S_{\Omega_j^N}} \sum_{i=1}^{6} c_0^2 \big|_{\Omega_i} \nabla p \big|_{\Omega_i} \cdot \frac{L_i}{2} \vec{n}_i, \tag{2.39}$$

where $\nabla p|_{\Omega_i}$ and $c_0^2|_{\Omega_i}$ are given by Eqs. (2.36) and (2.37), respectively.

In matrix notation, the discrete pressure values can be arranged in a vector $\bar{p}$, whose j component is $\hat{p}|_j$, i.e., the pressure at node j. On the other hand, the discretized operator $\nabla \cdot c_0^2 \nabla$ can be written as a sparse matrix, noted $\mathbf{A}$, whose (i, j) entry a_{ij} can be determined from Eq. (2.39). The matrix $\mathbf{A}$ is symmetric up to scaling, that is,

$$S_{\Omega_i^N} a_{ij} = S_{\Omega_j^N} a_{ji}.$$

The position of the non-zero entries of the matrix $\mathbf{A}$ depends on the nodes numbering while its number depends on the mesh itself (2D, 3D, structured, unstructured, etc.)

2.4.1.2   Computation of $\nabla \cdot c_0^2 \nabla p \big|_j$ for nodes located at the domain border
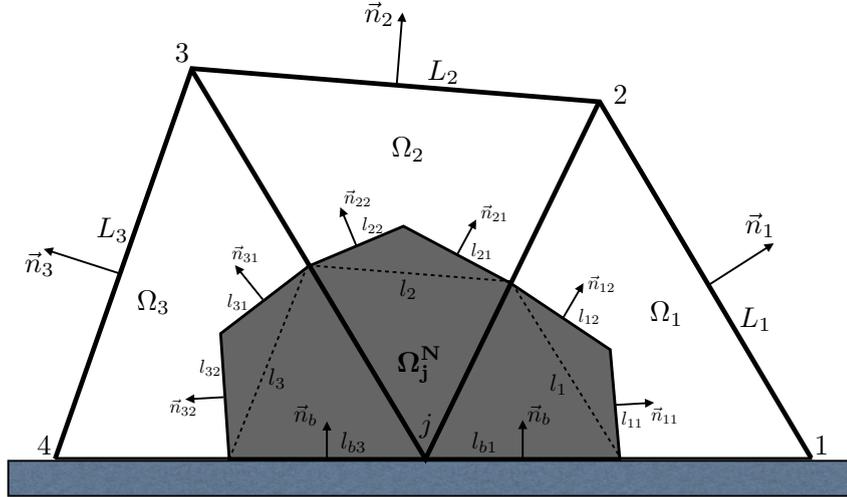
Figure 2.7: Representation of node, noted j, located at the border of a 2D triangular mesh. $\vec{n}_b$ is the interior normal of the domain border.

As for an interior node, for a node j located at the domain border (Fig. 2.7) it is possible to write

$$\nabla \cdot c_0^2 \nabla p \big|_j = \frac{1}{S_{\Omega_j^N}} \big[c_0^2 \big|_{\Omega_1} \nabla p \big|_{\Omega_1} \cdot (l_{11} \vec{n}_{11} + l_{12} \vec{n}_{12} - l_{b1} \vec{n}_b) +$$

$$c_0^2 \big|_{\Omega_2} \nabla p \big|_{\Omega_2} \cdot (l_{21} \vec{n}_{21} + l_{62} \vec{n}_{22}) + c_0^2 \big|_{\Omega_3} \nabla p \big|_{\Omega_3} \cdot (l_{31} \vec{n}_{31} + l_{32} \vec{n}_{32} - l_{b3} \vec{n}_b) \big],$$

which using Eq. 2.38 reads as

$$\nabla \cdot c_0^2 \nabla p\big|_j = \frac{1}{S_{\Omega_j^N}} \left[c_0^2|_{\Omega_1} \nabla p|_{\Omega_1} \cdot \frac{L_1}{2}\vec{n}_1 + c_0^2|_{\Omega_2} \nabla p|_{\Omega_2} \cdot \frac{L_2}{2}\vec{n}_2 + c_0^2|_{\Omega_3} \nabla p|_{\Omega_3} \cdot \frac{L_3}{2}\vec{n}_3 \right.$$
$$\left. \boxed{-c_0^2|_{\Omega_1} \nabla p|_{\Omega_1} \cdot l_{b1}\vec{n}_b - c_0^2|_{\Omega_3} \nabla p|_{\Omega_3} \cdot l_{b3}\vec{n}_b} \right].$$

The only difference with respect to Eq. (2.39) is the term within the box. This term is defined by the type of boundary condition associated with the node j. The Robin condition allows to write the pressure gradient at node j as

$$\nabla p \cdot \vec{n}\big|_j = i\frac{\omega}{c_{0_j} Z_j} p_j,$$

where Z_j is the complex acoustic impedance. On the other hand, for the Neumann condition, we have

$$\nabla p \cdot \vec{n}\big|_j = 0.$$

The normal gradients to the border are expressed hence in terms of the impedance at node j:

$$\left(c_0^2|_{\Omega_1} \nabla p|_{\Omega_1} l_{b1} + c_0^2|_{\Omega_3} \nabla p|_{\Omega_3} l_{b3} \right) \cdot \vec{n}_b = i\frac{c_{0_j}\omega}{Z_j}(l_{b1} + l_{b3})p_j.$$

Note that here, the acoustic impedance Z_j is defined using a normal vector $\vec{n}_b$ pointing into the domain.

Therefore, for a boundary node, we have

$$\nabla \cdot c_0^2 \nabla p\big|_j = \frac{1}{S_{\Omega_j^N}} \left[c_0^2|_{\Omega_1} \nabla p|_{\Omega_1} \cdot \frac{L_1}{2}\vec{n}_1 + c_0^2|_{\Omega_2} \nabla p|_{\Omega_2} \cdot \frac{L_2}{2}\vec{n}_2 + c_0^2|_{\Omega_3} \nabla p|_{\Omega_3} \cdot \frac{L_3}{2}\vec{n}_3 \right.$$
$$\left. - \boxed{i\frac{c_{0_j}\omega}{Z_j}(l_{b1} + l_{b3})p_j} \right]. \tag{2.40}$$

Eq. (2.40) shows that the discretization of $\nabla \cdot c_0^2 \nabla p\big|_j$ for a node placed at the border is the same as the one for an interior node, except that it is necessary to add the boundary condition term

$$- i\frac{c_{0_j}\omega}{Z_j}(l_{b1} + l_{b3})p_j. \tag{2.41}$$

This term is null for a Neumann condition ($Z_j = \infty$) and it does not appear either for a Dirichlet condition, which is taken into account by imposing $p_j = 0$ to the concerned nodes. For all other cases, the term of Eq. (2.41) depends on ω. The dependency on the frequency ω is not only due to the explicit presence of ω in Eq. (2.41), but also through the complex impedance Z_j, whose value depends generally on the frequency ω.

The nodes affected by a Robin boundary condition, have associated a diagonal matrix $\mathbf{B}$, whose non-null entries b_{jj} (being j the index of the concerned boundary nodes) are (leaving ω outside)

$$b_{jj} = \frac{-i}{S_{\Omega_j^N}} \frac{c_{0_j}}{Z_j}(l_{b1} + l_{b3}).$$

In summary, for a mesh composed of N nodes, the discretized term $\nabla \cdot c_0^2 \nabla \hat{p}(\vec{x})$ of Eq. (2.34) can be written as:

$$\nabla \cdot c_0^2 \nabla \hat{p}(\vec{x}) \rightarrow \text{ finite volume discretization } \rightarrow \mathbf{A}\,\bar{p} + \underbrace{\omega \mathbf{B}(\omega)\,\bar{p}}_{Robin\ B.C.}, \qquad (2.42)$$

where $\bar{p} \in \mathbb{C}^N$ is the vector of discrete pressure node values, $\mathbf{B} \in \mathbb{C}^{N \times N}$ is a complex diagonal associated with the boundary conditions and $\mathbf{A} \in \mathbb{R}^{N \times N}$ is a sparse real matrix.

2.4.2 Discretization of the right-hand side term

The right-hand side term of Eq. (2.34) has the form

$$\frac{(\gamma - 1)}{\rho_0(\vec{x})} n_{local}(\vec{x}, \omega) e^{i\omega \tau_{local}(\vec{x}, \omega)} \nabla \hat{p}(\vec{x}_{ref}) \cdot \vec{n}_{ref}.$$

Once the geometry has been discretized, the discrete values of $\rho_0(\vec{x})$, $n_{local}(\vec{x})$ and $\tau_{local}(\vec{x})$ can be arranged in a vector $\bar{q}$, whose element q_j is defined by the discrete nodal values of the discretized variables

$$q_j = \frac{(\gamma - 1)}{\rho_{0_j}} \frac{\bar{Q}}{\bar{U}} n_{local_j} e^{i\omega \tau_{local_j}}.$$

Only the nodes within the flame zone have $q_j \neq 0$, so that the number of non-zero entries of $\bar{q}$ is equal to the number of nodes placed in the flame zone.

The pressure gradient at node j_{ref} is computed as the mean of the pressure gradient of the dual cell $\Omega_{j_{ref}}^N$:

$$\nabla p|_{j_{ref}} = \frac{1}{S_{\Omega_{j_{ref}}^N}} \int_{\Omega_{j_{ref}}^N} \nabla p \; dS.$$

Since the pressure gradient is constant over each element surrounding the node j_{ref}, and the dual cell $\Omega_{j_{ref}}^N$ takes exactly $\frac{1}{3}$ of the surface ($\frac{1}{4}$ of the volume for 3D tetrahedral meshes) of each one of them, the integral can be computed as

$$\int_{\Omega_{j_{ref}}^N} \nabla p \; dS = \sum_{i=1}^{6} \frac{S_{\Omega_i}}{3} \nabla p|_{\Omega_i}.$$

Therefore, the discretization of the term $\nabla \hat{p}(\vec{x}_{ref}) \cdot \vec{n}_{ref}$ leads to (from Fig. 2.6)

$$\boxed{\nabla p|_{j_{ref}} = \frac{1}{S_{\Omega_{j_{ref}}^N}} \sum_{i=1}^{6} \frac{S_{\Omega_i}}{3} \nabla p|_{\Omega_i} \cdot \vec{n}_{ref}.} \qquad (2.43)$$

Consequently, the discretized right-hand side term of Eq. (2.34), in matrix notation, can be written as

$$\frac{(\gamma - 1)}{\rho_0(\vec{x})} n_{local}(\vec{x}, \omega) e^{i\omega \tau_{local}(\vec{x}, \omega)} \nabla \hat{p}(\vec{x}_{ref}) \cdot \vec{n}_{ref} \rightarrow \text{ discretization } \rightarrow \mathbf{C}\,\bar{p} = \bar{n}\bar{r}^T\bar{p}.$$

The values of the entries of the vector $\bar{r}^T$ are given by Eq. (2.43). Hence, only the entries corresponding to the nodes surrounding the reference point $\vec{x}_{ref}$ are non-zero. Thus the row index of the non-null elements of the matrix $\mathbf{C} = \bar{n}\bar{r}^T$ are the index of the nodes located in the flame zone and the column index of its non-null entries are the indices of the nodes surrounding the reference point $\vec{x}_{ref}$.

2.5 The nonlinear eigenvalue problem
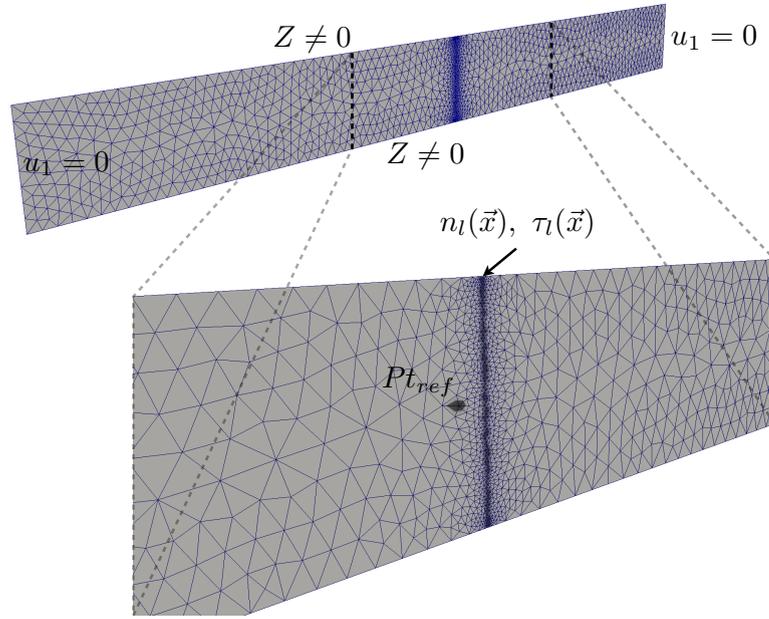
Figure 2.8: 2D tetrahedral mesh (1489 nodes) of a tube with a flame placed at the middle and an impedance $Z \neq 0$ at the top and bottom sides. Zoom of the flame zone, showing the reference point Pt_{ref} and the point within the flame ($n_l \neq 0, \tau_l \neq 0$).

From the previous section, it has been obtained that the discretized Helmholtz equation (Eq. (2.34)) becomes

$$\mathbf{A}\bar{p} + \omega\mathbf{B}\bar{p} + \omega^2\bar{p} = \mathbf{C}(\omega)\bar{p}, \qquad (2.44)$$

where:

- **A** is a $N \times N$ sparse real matrix (being N the size of the associated mesh) that is structurally symmetric. It comes form the discretization of the operator $\nabla c_0^2(\vec{x})\nabla$.

- **B** is a $N \times N$ complex diagonal matrix. Its non-null entries correspond to the external domain nodes that are concerned by a Robin condition. The term $\omega\mathbf{B}$ does not appear if only Neumann and/or Dirichlet boundary conditions are used.

- **C** is a rectangular sparse complex matrix coming from the discretization of the right-hand side term of Eq. (2.34). The row index of its non-null entries are equal to the nodes index that are in the flame zone, the associated column indices are those of the

nodes surrounding the reference point node j_{ref}. It appears when the **active flame** is considered in the thermoacoustic simulation.

The structure of the matrices **A**, **B** and **C** are shown in Fig. 2.9 for a simple case displayed in Fig. 2.8. It consists in a 2D tube with a flame placed at the middle. The left and right sides are rigid walls ($u_1 = 0$), whereas the top and bottom sides have an impedance $Z \neq 0$.

Matrix **A**

Matrix **B**

Matrix **C**
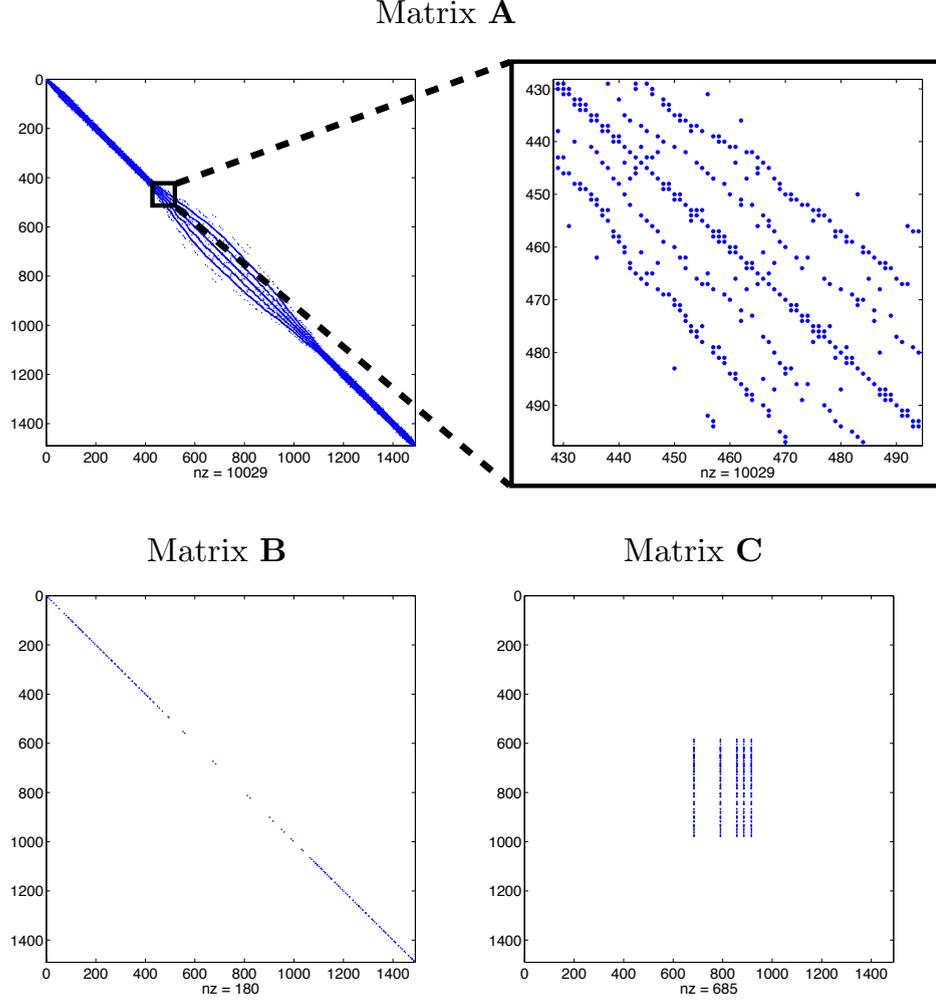
Figure 2.9: Structure of the sparse matrices **A**, **B** and **C** issued from the discretization of the Helmholtz equation of the 2D unstructured mesh of Fig. 2.8.

Eq. (2.44) is a nonlinear eigenvalue problem. As exposed in Chapter 4, there are no standard methods for the solution of such a problem. Therefore, Eq. (2.44) is handled by solving a sequence of linear eigenproblems obtained when the value of ω is set to a constant ω^* in $\omega^* \mathbf{B}(\omega^*)$ and $\mathbf{C}(\omega^*)$, so the nonlinear dependency from ω disappears. The resulting linear eigenvalue problem

$$\left[\mathbf{A} + \omega^*\mathbf{B}(\omega^*) - \mathbf{C}(\omega^*)\right]\bar{p} = -\omega^2\bar{p} \;\Rightarrow\; \mathbf{OP}(\omega^*)\bar{p} = -\omega^2\bar{p}, \tag{2.45}$$

where $\mathbf{OP}(\omega^*) \in \mathbb{C}^{N \times N} = \mathbf{A} + \omega^*\mathbf{B}(\omega^*) - \mathbf{C}(\omega^*)$ (being N the number of the mesh nodes) is a non-symmetric complex matrix. In the following, Chapter 3 is dedicated to the description

of algorithms for the solution of general large non-symmetric sparse eigenproblems, while in Chapter 4 the use of these algorithms for the solution of $\mathbf{OP}\bar{p} = -\omega^2\bar{p}$ is investigated.

Part II

Eigenvalue problem: algorithms and numerical aspects

Chapter 3

Algorithms for the solution of the thermo-acoustic eigenproblem

Contents

When we deal with very large matrices, such as the one obtained in Eq. (2.45), the computation of its complete spectrum is out of question, due to the limited amount of available computing resources. For example, for a dense matrix A of order $n = 10^6$, even its storage is not feasible: if double precision is chosen to represent a real number, it will take 10^{12} numbers $\times$ 8 bytes, i.e., 8000 gigabytes to store the matrix A, what obviously is not of any practical use. The size of the matrix to solve in this work is determined by the mesh size (the number of nodes), which can lead to matrices of order $n \approx \mathcal{O}(10^7)$ for real geometries. Besides, in complex arithmetic the needed amount of memory is even doubled. Fortunately, very large matrices that arise in most applications (structural mechanics, electronic, chemistry, ...) are sparse, what reduces the memory requirements drastically. This is also the case for the matrix **OP** obtained from the discretization of the Helmholtz equation, as seen in Chapter 2.

Direct methods for the computation of the complete spectrum of dense matrices, like the *QR algorithm* [156, Chapter 2] are based on similarity transformations. In general, applying a similarity transformation causes fill-in, so after a few transformations, an initially sparse matrix becomes a dense matrix and then, as mentioned above, solving it directly is not an option when its size is large. On the other hand, in most applications, it is not necessary to compute the whole spectrum of the matrix, but only a few eigenvalues within a region of interest (largest magnitude, smallest real part, ...). The study of thermoacoustic instabilities in combustion chambers requires the computation of the lowest eigenfrequencies, which correspond to the smallest magnitude eigenvalues of the matrix **OP**. Hence the algorithms presented in this chapter are used for computing the part of the spectrum nearest zero.

The alternative to direct eigensolvers is the use of iterative methods. These methods build subspaces with suitable properties that eventually contain good approximations of an invariant subspace of the matrix in question. In addition, they allow to compute a given region of the spectrum using only matrix-vector products, which is well adapted to the matrix-free formalism employed in AVSP.

This chapter describes the algorithms dedicated to the solution of the large complex sparse eigenproblems that appear in AVSP. It is organized as follows: The first section introduces Krylov subspaces and Rayleigh-Ritz extraction, which are the main ingredients of more complex algorithms. The second and the third sections are dedicated to the description of two algorithms based on Krylov subspaces: The *implicitly restarted Arnoldi method* and the *Krylov-Schur method*, respectively. The fourth section introduces block algorithms, which might be an interesting alternative to to recycle invariant subspaces previously computed, since they can start from a set of vectors. The fifth section introduces the Jacobi-Davidson algorithm, one of the most important alternatives to the Krylov-based methods. In the last section, the stopping criterion used to decide if the approximated eigenpairs can be accepted as solution of the problem, is briefly described.

3.1 Krylov subspaces and Rayleigh-Ritz extraction

Probably the most basic method for the computation of eigenvalues of a matrix A is the *Power method* [156, Chapter 2][129, Chapter 4]. Its use as an explicit method for the computation of the dominant (largest magnitude) eigenpair goes back at least to 1913 [94]. Let us assume that the matrix A is nondefective and that (λ_i, x_i) $(i = 1, \ldots, n)$ is the complete set of its eigenpairs such that $|\lambda_1| > |\lambda_2| > \cdots > |\lambda_n|$. Then, since x_i are linearly independent, any vector u_1 can be written as a linear combination of them

$$u_1 = \gamma_1 x_1 + \cdots + \gamma_n x_n.$$

Now, if a power k of the matrix A is applied to the vector u_1, from $A^k x_i = \lambda^k x_i$, it follows that

$$A^k u_1 = \gamma_1 \lambda_1^k x_1 + \gamma_2 \lambda_2^k x_2 + \cdots + \gamma_n \lambda_n^k x_n.$$

Therefore, if $|\lambda_1| > |\lambda_i|$ $(i > 2)$ and $\gamma_1 \neq 0$, then when $k \to \infty$ the first term $\gamma_1 \lambda_1 x_1$ dominates, so that $A^k u_1$ becomes an increasingly accurate multiple of the dominant eigenvector x_1.

In spite of its simplicity, the Power method is at the basis of more sophisticated methods that are going to be presented in this chapter. It is also closely connected to the *QR algorithm* [156, Chapter 2][167, Chapter 4], one of the greatest success of modern matrix computations. The QR algorithm and its variants can be used to: compute the whole spectrum of a general matrix, its singular value decomposition, the generalized Schur form of a matrix pencil and many other applications.

The sequence of vectors generated by the Power method u_1, Au_1, $A^2 u_1$, ..., $A^{k-1} u_1$ spans a particular subspace with interesting features. The Power method uses only the vector $u_k = A^{k-1} u_0$ of the current iteration, throwing away the information contained in the previously computed vectors. It turns out that the subspace spanned by the sequence of vectors generated by the Power method can contain precious information, as the following example taken from [156, Chapter 4] shows.

Let A be a diagonal matrix of order 100 whose eigenvalues are 1, 0.95, 0.95^2,..., 0.95^{99}. Starting from a random vector u_1, the solid line in Fig. 3.1 plots the tangent of the angle between the k-vector $u_k = A^{k-1} u_1$ and the dominant eigenvector x_1 of A. Since the ratio between the dominant and the subdominant eigenvalue of A is 0.95, the convergence is very slow as expected. The dashed line plots the angle between x_1 and the subspace spanned by the sequence u_1, Au_1, $A^2 u_1$, ..., $A^{k-1} u_1$. Finally, the dash-dot line shows the convergence of the subdominant vector x_2.

This example shows that the sequence u_1, Au_1, $A^2 u_1$, ..., $A^{k-1} u_1$ span a subspace that contains information about the eigenspace of the matrix A and it contains more information than only the vector u_k of the Power method iteration k. This kind of sequence is called a Krylov sequence.
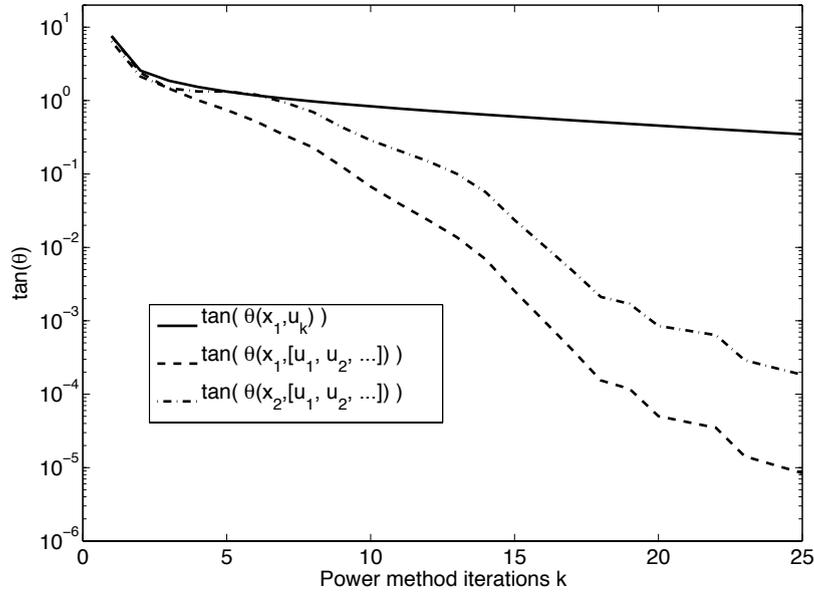
Figure 3.1: Power method convergence. Taking into account the previous vectors generated by the Power method improves the convergence rate and they can contain valuable information about the next eigenvectors.

3.1.1 Krylov sequences and Krylov subspaces: definitions and properties

Definition Let A be of order $n \neq 0$ and let $u \neq 0$ be a vector in $\mathbb{C}^n$. Then the sequence

$$u, Au, A^2u, A^3u, \dots$$

is a *Krylov sequence based on A and u*. The matrix

$$K_k(A, u) = [u \ Au \ A^2u \ \dots \ A^{k-1}u]$$

is called the kth *Krylov matrix*. Finally, the subspace

$$\mathcal{K}_k(A, u) = \mathcal{R}[K_k(A, u)]$$

is called the kth *Krylov subspace*, where $\mathcal{R}(v_1, \dots, v_k)$ denotes the space spanned by $(v_1, \dots, v_k)$.

Krylov subspaces have the following properties:

1. the sequence of Krylov subspaces satisfies

$$\mathcal{K}_k(A, u) \subset \mathcal{K}_{k+1}(A, u)$$

and

$$A\mathcal{K}_k(A, u) \subset \mathcal{K}_{k+1}(A, u).$$

2. If $\sigma \neq 0, \sigma \in \mathbb{C}$,
$$\mathcal{K}_k(A, u) = \mathcal{K}_k(\sigma A, u) = \mathcal{K}_k(A, \sigma u).$$

3. For any κ, $\kappa \in \mathbb{C}$,
$$\mathcal{K}_k(A, u) = \mathcal{K}_k(A + \kappa I, u).$$

4. If $W \in \mathbb{C}^{n \times n}$ is nonsingular, then
$$\mathcal{K}_k(W^{-1}AW, W^{-1}u) = W^{-1}\mathcal{K}_k(A, u).$$

We say that a Krylov sequence *terminates* at ℓ if ℓ is the smallest integer such that
$$\mathcal{K}_{\ell+1}(A, u) = \mathcal{K}_\ell(A, u). \tag{3.1}$$

Theorem 3.1 presents some important facts about termination of Krylov sequences.

Theorem 3.1 *A Krylov subsequence based on A and u terminates at ℓ if and only if ℓ is the smallest integer for which*
$$dim[\mathcal{K}_{\ell+1}] = dim[\mathcal{K}_\ell]. \tag{3.2}$$
If the Krylov sequence terminates at ℓ, $\mathcal{K}_\ell$ is an eigenspace of A of dimension ℓ. On the other hand, if u lies in an eigenspace of dimension m, then for some $\ell \leq m$, the sequence terminates at ℓ.[1]

As the former example shows (Fig. 3.1), Krylov subspaces contain increasingly accurate approximations to certain eigenvectors of the matrix in question, more precisely, those eigenvectors that have eigenvalues lying on the periphery of the spectrum of the matrix. More details about convergence of Krylov sequences can be found for instance in [156].

3.1.2 Rayleigh-Ritz extraction

The most commonly used method for extracting spectral information of a given subspace is called the *Rayleigh-Ritz method*. The starting point is the matrix A and a subspace $\mathcal{U}$ containing an approximate eigenspace of it. Note that $\mathcal{U}$ is chosen as a Krylov subspace associated with the matrix A, but this is not a necessary condition to carry out the Rayleigh-Ritz procedure. The basis of the method is given in the following theorem:

Theorem 3.2 *Let $\mathcal{U}$ be a subspace and let U be a basis for $\mathcal{U}$. Let V^H be a left inverse of U and set*
$$B = V^H AU.$$
If $\mathcal{X} \subset \mathcal{U}$ is an eigenspace of A, then there is an eigenpair (L, W) of B such that (L, UW) is an eigenpair of A with $\mathcal{R}(UW) = \mathcal{X}$.

---

[1]See [156, page 271] for the proof.

Proof We suppose that (L, UW) is an eigenpair of A. Then

$$AUW = UWL.$$

If we multiply this relation on the left by V^H, we obtain

$$BW = V^H AUW = V^H UWL = WL,$$

so that (L, W) is an eigenpair of B. ∎

Theorem 3.2 says that it is possible to find exact eigenspaces of the $n \times n$ matrix A contained in $\mathcal{U}$ by computing eigenpairs of the $k \times k$ (with $k << n$) Rayleigh quotient B, which is much cheaper. Obviously, in practice, we will not have a subspace $\mathcal{U}$ containing an exact eigenspace $\mathcal{X}$ of A, but an approximation $\tilde{\mathcal{X}}$. By continuity, it is reasonable to think that there would be an eigenpair $(\tilde{L}, \tilde{W})$ of B such that $(\tilde{L}, U\tilde{W})$ is an approximate eigenpair of A with $\mathcal{R}(U\tilde{W}) \cong \tilde{\mathcal{X}}$. Therefore, the following procedure allows to compute an approximate eigenspace $\tilde{\mathcal{X}}$ of A:

1. Let U be a basis for $\mathcal{U}$ and let V^H be a left inverse of U.

2. Form the Rayleigh quotient $B = V^H AU$.

3. Compute a suitable eigenpair (M, W) of B .

4. Then the pair (M, UW) is an approximate eigenpair of A.

This procedure is known as a *Rayleigh-Ritz procedure*. The pair (M, UW) is called a *Ritz pair*, being M its *Ritz block* and UW its *Ritz basis*. W is the *primitive Ritz basis* and the space $\mathcal{R}(UW)$ is called the *Ritz space*. When it comes to the computation of single eigenpairs, then the Ritz pair can be written as $(\lambda, U\omega)$ and λ is called a *Ritz value*, $U\omega$ a *Ritz vector* and ω a *primitive Ritz vector*.

In its general form, described over these lines, the Rayleigh-Ritz method uses two different basis U and V, spanning different subspaces, to form the Rayleigh quotient B. It is called then an *oblique Rayleigh-Ritz method*[2]. A very important particular case is when U is chosen orthonormal and V equal to U. In this case we talk of the *orthogonal Rayleigh-Ritz method*. In addition the primitive Ritz basis W is also taken orthonormal so that the Ritz basis $\hat{X} = UW$ is orthonormal as well. Unless the contrary is specified, the methods used in this work uses the orthogonal Rayleigh-Ritz method. The first advantage of this choice is given by the following theorem[3]:

---

[2]In the context of linear systems, the Rayleigh-Ritz method is also known as Galerkin method (if $\mathcal{V} = \mathcal{U}$) or Galerkin-Petrov method (if $\mathcal{V} \neq \mathcal{U}$). These methods try to solve the equation $Ax = b$, choosing x to satisfy

1. $x \in \mathcal{U}$

2. $Ax - b \perp \mathcal{V}$.

[3]Proof in [156, page 286]

Theorem 3.3 *If* $(M, \hat{X})$ *is an orthonormal Rayleigh-Ritz pair with respect to U, then*

$$R = A\hat{X} - \hat{X}M$$

is minimal in any unitarily invariant norm.

The other positive aspect is that working with unitary matrices has evident advantages within the context of finite precision arithmetic.

Any Ritz pair (λ, ω) satisfies

1. $x \in \mathcal{U}$

2. $Ax - \lambda x \perp \mathcal{V}$.

The Rayleigh-Ritz method is also called a projection method because a Ritz pair (μ, x) is an eigenpair of the matrix $P_\mathcal{V} A P_\mathcal{U}$, where $P_\mathcal{V}$ and $P_\mathcal{U}$ are orthogonal projectors onto $\mathcal{U}$ and $\mathcal{V}$, respectively.

3.1.3   The shift-and-invert transformation

Let us recall that in the thermoacoustic problem the concern is about the lowest resonant frequencies of the system, i.e., those corresponding to the smallest magnitude eigenvalues. Nevertheless, it has been already pointed out that due to the link between Krylov subspaces and the Power method, these subspace converge naturally toward eigenspaces associated with eigenvalues lying on the periphery of the spectrum of the matrix. This difficulty can be overcome thanks to the *shift-and-invert enhancement*. This technique can be used to make the interior eigenvalues of the matrix A dominant, so they are naturally approached by a Krylov subspace. Consider that $\lambda_1, \lambda_2, \ldots, \lambda_n$ are the eigenvalues of A (in no particular order). If a good approximation κ to λ_1 is available, then, the eigenvalues of the matrix $(A - \kappa I)^{-1}$ are

$$\mu_1 = \frac{1}{\lambda_1 - \kappa}, \ \mu_2 = \frac{1}{\lambda_2 - \kappa}, \ \ldots, \mu_n = \frac{1}{\lambda_n - \kappa}.$$

As $\kappa \to \lambda_1$, $\mu_1 \to \infty$ and for $i > 1$, the μ_i approach $(\lambda_i - \lambda)^{-1}$, which are finite quantities. Therefore, if κ is chosen close enough to λ_1, the shift-and-invert procedure makes μ_1 the dominant eigenvalue of the transformed matrix $(A - \kappa I)^{-1}$. Then the original eigenvalue of A can be computed from μ_1 as $\lambda_1 = \frac{1}{\mu_1} + \kappa$. More generally, if one is interested in the closest eigenvalues to a particular target κ, computing the dominant eigenvalues of the transformed matrix $(A - \kappa I)^{-1}$ allows to find the eigenvalues of A closest to the given target κ.

In our case, computing the smallest magnitude eigenvalues (those closest to zero) of the matrix **OP** is equivalent to compute the largest magnitude eigenvalues of the inverse matrix **OP**$^{-1}$. Therefore, in order to use the shift-and-invert enhancement the operator **OP**$^{-1}$ is thus needed or, alternatively, the result of applying it to a given vector $x = $ **OP**^{-1}y. This is equivalent to solve a large sparse non-symmetric linear system **OP**$x = y$ each time that the operator **OP** has to be applied to an input vector y. If preconditioning techniques are

not available or it is not possible to use them, solving these linear systems is a challenging problem that would require a study apart itself, which is the reason why this technique has not been retained in this work.

3.2 The Implicitly Restarted Arnoldi algorithm

The Arnoldi method is an efficient procedure for approximating a suitably chosen subset of the spectrum of a large sparse matrix A of order n. Its origin can be found in the work of Arnoldi, back in the 50's [4]. It is a generalization of the Lanczos algorithm designed for symmetric matrices [72]. After k steps, the method produces a Hessenberg matrix H_k of order k. The idea is to use the eigenvalues of the small matrix H_k to approximate a subset of the eigenvalues of the large matrix A, using the Rayleigh-Ritz procedure.

There are some difficulties inherent to the Arnodi (or Lanczos) method. As k increases, some of the Ritz pairs of H_k will hopefully approach eigenpairs of A. But, for memory reasons, we cannot keep increasing the size of the factorization until we reach the convergence. Therefore, when k becomes too large, the process needs to be restarted. The *Implicitly Restarted Arnoldi method*, developed by Sorensen and Lehoucq in [78], is a powerful method to restart the Arnoldi iteration.

3.2.1 The Arnoldi factorization

After k steps, the Arnoldi process computes the following factorization of the n matrix A:

$$AV_k = V_k H_k + f_k e_k^T, \tag{3.3}$$

where $V_k^H V_k = I_k$. The vector f_k is the residual and is orthogonal to the columns of V_k and e_k is the last column of the k order identity matrix I_k. The $k \times k$ matrix H_k is an upper Hessenberg matrix, which can be seen as the orthogonal projection of A onto $\mathcal{R}(V_k) = \mathcal{K}_k(A, v_1)$. The factorization (3.3) can be also written as follows:

$$AV_k = V_{k+1} \hat{H}_k, \text{ with } \hat{H}_{k+1} = \begin{pmatrix} H_k \\ h_{k+1,k} e_k^T \end{pmatrix}.$$

In this more compact form, h_{k+1} is the norm of the residual f_k and the last column v_{k+1} of V_{k+1} is the normalized residual. Let us set $\beta = h_{k+1,k}$, then dropping subscripts, the Arnoldi decomposition can be written as $AV = VH + \beta v e^T$ or $AV = \hat{V} \hat{H}$, where the hats over the matrices V and H represent an augmentation by a column and a row respectively.

Algorithm 3.1 implements the *Arnoldi process*, which builds an Arnoldi decomposition starting from a given initial vector v_1.

Let us introduce two important properties of the Arnoldi factorization:

Uniqueness   There exists a one-to-one correspondence between a non-terminating Krylov sequence $K_{k+1}(A, v_1)$ and the corresponding Arnoldi decomposition. In other words, if the

---

Algorithm 3.1 $[V_{k+1}, \hat{H}_k] = ARL\_reortho(A, v_1, k)$

Given a n matrix A and an initial vector v_1, construct an Arnoldi decomposition of order $k < n$, $AV_k = V_k H_k + \beta v_{k+1} e_k^T = V_{k+1} \hat{H}_k$ with selective re-orthogonalization, using Classical Gram Schmidt.

>   Set $V(:, 1) = v_1 / norm(v_1)$
>   **for** $j = 1, 2, \ldots, k$ **do**
> $w = AV(:, j)$
> $wnorm1 = norm(w)$
> $H(1 : j, j) = V(:, 1 : j)^H w$
> $w = w - V(:, 1 : j)H(1 : j, j)$
> $wnorm = norm(w)$
>   **if** $wnorm < \sqrt{2}wnorm1$ **then**
> $s = V(:, 1 : j)^H w$
> $H(1 : j, j) = H(1 : j, j) + s$
> $w = w - V(:, 1 : j)s$
> $wnorm = norm(w)$
>   **end if**
> $\beta = wnorm$
>   **if** $\beta \neq 0$ **then**
> $H(j + 1, j) = \beta$
> $V(:, j + 1) = w/\beta$
>   **end if**
>   **end for**

Krylov sequence $K_{k+1}(A, v_1)$ does not terminate, its associated Arnoldi decomposition is *unique* up to scaling of the columns of V_{k+1}.

Reduced Arnoldi decompositions and invariant subspaces   We will say that an *Arnoldi decomposition is unreduced* if its associated Hessenberg matrix $\hat{H}_k$ is unreduced, i.e., $h_{i+1,i} \neq 0$, for $i = 1, \ldots, k$. If this is not the case, we say that the Arnoldi factorization is *reduced*. The following theorem establishes the condition under which an Arnoldi decomposition $AV_k = V_{k+1}\hat{H}_k$ is reduced:

Theorem 3.4 *Let the orthonormal matrix V_{k+1} satisfy*

$$AV_k = V_{k+1}\hat{H}_k,$$

where $\hat{H}_k$ is Hessenberg. Then $\hat{H}_k$ is reduced if and only if $\mathcal{R}(V_k)$ contains an eigenspace of A.[4]

3.2.2   The implicitly restarted Arnoldi method

The amount of memory is usually limited, which means that it is not possible to expand the Arnoldi factorization as far as necessary until the convergence of the desired eigenpairs

---

[4]Proof in [156, page 306]

is reached. Then let us assume that m is the maximum size of the Arnoldi factorization that we can afford:

$$AV_m = V_m H_m + \beta v_{m+1} e_m^T.$$

Once the factorization has been computed, the Ritz procedure is used in order to evaluate a set of eigenvalues of interest. If these eigenvalues are not approximated well enough, then the process has to be restarted. In order to do that, the idea is to improve the starting vector, using a filter polynomial. A particular case of filter polynomial, is the very natural choice of a linear combination of Ritz vectors that we are interested in. As presented in [78], the QR algorithm can be used to form a filter polynomial which will be applied implicitly to the starting vector v_1. But first, we will explain further the motivation of this procedure.

3.2.2.1 Filter polynomials

In order to explain in a simple manner why the process does work, let us assume that A has a complete set of eigenpairs (λ_i, x_i). Then any vector can be written as a linear combination of eigenvectors of A and, particularly, the starting vector of the Arnoldi factorization. If we are interested in the first k eigenvalues of A, then v_1 can be expanded in the form

$$v_1 = \sum_{i=1}^{k} \gamma_i x_i + \sum_{i=k+1}^{n} \gamma_i x_i,$$

from which follows that, if p is any polynomial

$$p(A)v_1 = \sum_{i=1}^{k} \gamma_i p(\lambda_i) x_i + \sum_{i=k+1}^{n} \gamma_i p(\lambda_i) x_i.$$

It seems clear that if we have a polynomial p so that the values $p(\lambda_i)(i = k+1, \ldots, n)$ are small compared to those $p(\lambda_i)(i = 1, \ldots, k)$, then v_1 will be rich in the components of the wanted vectors and deficient in the ones not wanted. The polynomial p is called a *filter polynomial*. If the Arnoldi factorization is of size m and we are interested in k eigenpairs, the degree of p is $m-k$. The cost of calculating $p(A)v_1$, being p of degree $m-k$, is expensive ($m - k$ matrix-vector products) if it is done directly. In the following section, an elegant and economic way of computing the Krylov decomposition of $\mathcal{K}_k[p(A)v_1]$ using shifted QR steps is introduced. This procedure is known as *implicit restarting*.

3.2.2.2 Implicit Restarted Arnoldi method

The method will work in the following manner:

1. Start with an Arnoldi decomposition of size k

$$AV_k = V_k H_k + \beta_k v_{k+1} e_k^T.$$

2. Expansion phase: the decomposition is expanded to one of order m, with m suitable chosen so that it fits in the available memory:

$$AV_m = V_m H_m + \beta_m v_{m+1} e_m^T.$$

3. Contraction phase: apply a filter polynomial p of degree $m - k$ to reduce the decomposition to one of size k, using the implicit restarting process, to obtain

$$A\tilde{V}_k = \tilde{V}_k\tilde{H}_k + \tilde{\beta}_k\tilde{v}_{k+1}e_k^T.$$

4. Repeat steps 2–3 until the desired Ritz values have converged.

The process allowing to apply the filter polynomial p (in its factored form)

$$p(t) = (t - \kappa_1)(t - \kappa_2)\cdots(t - \kappa_{m-k}),$$

to the decomposition $AV_m = V_mH_m + \beta v_{m+1}e_m^T$ in an implicit way, which will be analogous to a basic QR algorithm step, is explained in the following.

Let us start by shifting the decomposition

$$(A - \kappa_1 I)V_m = V_m(H_m - \kappa_1 I) + \beta v_{m+1}e_m^T.$$

If $H_m - \kappa_1 I = Q_1R_1$ is the QR factorization of the shifted Hessenberg matrix, then

$$(A - \kappa_1 I)V_m = V_mQ_1R_1 + \beta v_{m+1}e_m^T. \tag{3.4}$$

Multiplying on the right by Q_1 we have

$$(A - \kappa_1 I)(V_mQ_1) = (V_mQ_1)(R_1Q_1) + \beta v_{m+1}(e_m^TQ_1),$$

which can be recast into

$$AV_m^{(1)} = V_m^{(1)}H_m^{(1)} + \beta v_{m+1}b_m^{(1)H}, \tag{3.5}$$

with

$$V_m^{(1)} = V_mQ_1, H_m^{(1)} = R_1Q_1 + \kappa_1 I, \text{ and } b_m^{(1)H} = e_m^TQ_1.$$

One can see that $H_m^{(1)}$ is actually the result from one QR step with shift κ_1 applied to H_m.

Let us analyze more carefully the properties of the factorization from Eq. (3.5):

1. Since the QR algorithm preserves the Hessenberg form, the matrix $H_m^{(1)}$ is also of Hessenberg form. Besides, at most its last subdiagonal element is zero.

2. The matrix $V_m^{(1)}$ is orthonormal.

3. The matrix Q_1 is upper Hessenberg and so the vector $b_m^{(1)H} = e_m^TQ_1$ is the last row of Q_1, which means that only the last two components of $b_m^{(1)}$ are nonzero.

Now these three facts allow to say that expression (3.5) is almost an Arnoldi factorization. Almost because the last two components of $b_m^{(1)}$ are nonzero and thus it cannot be written as $b_m^{(1)} \propto e_m$. But if we equate the first $(m-1)$ colums of Eq. (3.5), then we have an Arnoldi factorization of order $(m-1)$, i.e., its order has been reduced by one.

And this is not all. Indeed, what is maybe the most important feature of this method has not been shown yet. Let us recall that what it is sought is to filter the initial vector

v_1 with a filter polynomial that makes the initial vector richer in the wanted directions, attenuating the components of the unwanted ones. If Eq. (3.4) is post-multiplied by e_1, as R_1 is upper triangular, we get

$$(A - \kappa_1 I)v_1 = r_{11}^{(1)} v_1.$$

Since $(H_m - \kappa_1 I)$ is unreduced, $r_{11}^{(1)}$ is nonzero. This means that the first column of $V_m^{(1)}$ is a multiple of $(A - \kappa_1 I)v_1$. One can already begin to realize the power and elegance of the method.

If we repeat this process with $\kappa_2, \ldots, \kappa_{m-k}$ we end up obtaining the following decomposition:

$$AV_m^{(m-k)} = V_m^{(m-k)} H_m^{(m-k)} + \beta v_{m+1} b_m^{(m-k)H}. \tag{3.6}$$

As done before, let us analyze the different terms in Eq. (3.6):

1. $H_m^{(m-k)}$ is upper Hessenberg. At most its last $m - k$ subdiagonal elements are zero.

2. $V_m^{(m-k)}$ is orthonormal.

3. $Q = Q_1 Q_2 \ldots Q_{m-k}$ is zero below its $(m - k)$ subdiagonal. This can be seen in the following Wilkinson diagram for $k = 3$ and $m = 6$

$$Q = Q_1 Q_2 Q_3 = \begin{pmatrix} q & q & q & q & q & q \\ q & q & q & q & q & q \\ q & q & q & q & q & q \\ \hline q & q & q & q & q & q \\ 0 & q & q & q & q & q \\ 0 & 0 & q & q & q & q \end{pmatrix},$$

which means that $b_m^{(m-k)H}$ is the last row of Q, and hence its first $k - 1$ components are zero.

4. The first column of $V_m^{(m-k)}$ is a multiple of $(A - \kappa_1 I)(A - \kappa_2 I) \cdots (A - \kappa_{m-k} I)v_1$. The initial vector v_1 has been filtered with $p(A)$.

Fig. 3.2 displays a scheme of this restart process, showing the Arnoldi decomposition before and after applying the $m - k$ shifts. The k first columns of Eq. (3.6) can be written in the form

$$AV_m^{(m-k)} = V_m^{(m-k)} H_k^{(m-k)} + h_{k+1}^{(m-k)} v_{k+1}^{(m-k)} e_k^T + \beta q_{mk} v_{m+1} e_k^T,$$

where $V_k^{(m-k)}$ consists of the first k columns of $V_m^{(m-k)}$, $H_k^{(m-k)}$ is the leading principal submatrix of order k of $H_m^{(m-k)}$, and q_{mk} is the last row of the matrix $Q = Q_1 Q_2 \ldots Q_{m-k}$.

Therefore, setting

$$\tilde{V}_k = V_k^{(m-k)}, \tag{3.7}$$

$$\tilde{H}_k = H_k^{(m-k)}, \tag{3.8}$$

$$\tilde{\beta}_k = \|h_{k+1}^{(m-k)} v_{k+1}^{(m-k)} + \beta q_{mk} v_{m+1}\|_2, \tag{3.9}$$

$$\tilde{v}_{k+1} = \tilde{\beta}_k^{-1}(h_{k+1}^{(m-k)} v_{k+1}^{(m-k)} + \beta q_{mk} v_{m+1}), \tag{3.10}$$
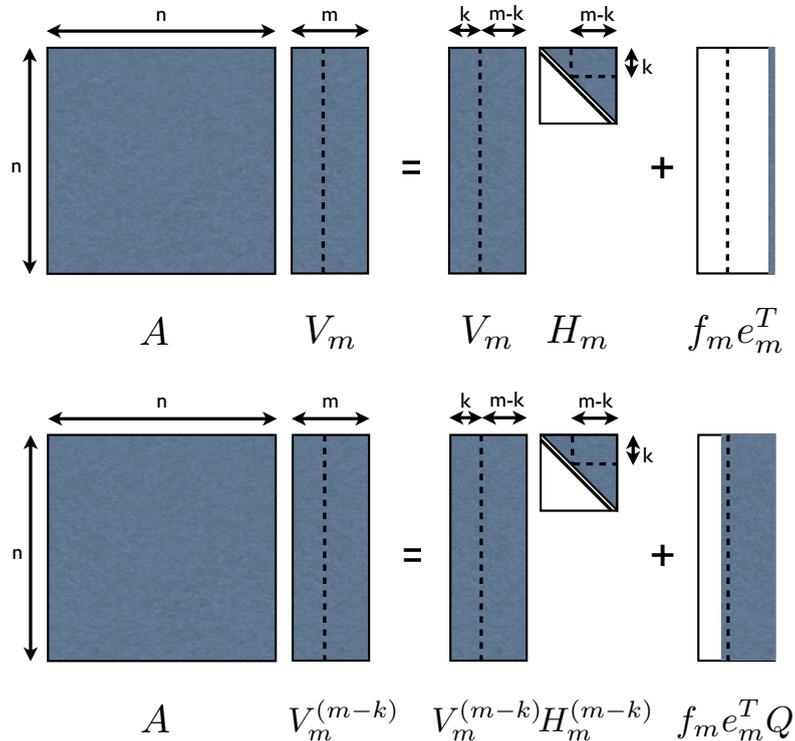
Figure 3.2: Scheme of an the implicit restart process m.

we retrieve an Arnoldi decomposition of order k

$$A\tilde{V}_k = \tilde{V}_k \tilde{H}_k + \tilde{\beta}\tilde{v}_{k+1}e_k^T$$

whose starting vector is proportional to $(A - \kappa_1)\cdots(A - \kappa_{m-k})v_1$, i.e., it has been filtered by $p(A)$. The economy of the method is outstanding: no matrix-vector multiplications involving A are needed to form the new starting vector, and its Arnoldi factorization of order k is obtained for free. Implementation issues, as well as an algorithm implementing a single implicit QR step and its inclusion in a whole restarted Arnoldi cycle can be found in [156].

This method has been used with great success for the solution of large eigenvalue problems by the scientific community. ARPACK is the name of its definitive FORTRAN implementation developed by Lehoucq, Sorensen and Yang[5], which is used in AVSP. More details can be found in the ARPACK's user guide [75].

Exact shifts and Forward Instability

The Implicitly Restarted Arnoldi method offers to the user the possibility of choosing the shift to be applied. If the Ritz values are chosen as shifts, it is called exact shifts. In this case, the Rayleigh quotient assumes a particular form where the discarded Ritz values appear on the diagonal of the unwanted part of the Rayleigh quotient. To see this

---

[5]http://www.caam.rice.edu/software/ARPACK/

more clearly, let us consider the unreduced Hessenberg matrix H, and let μ be a Ritz value (eigenvalue of H). Then, it can be proved that [156, p. 329], after one QR step with shift μ, the resulting matrix $\tilde{H}$ has the form

$$\tilde{H} = \begin{pmatrix} \tilde{H}_{11} & \tilde{h}_{12} \\ 0 & \mu \end{pmatrix}, \tag{3.11}$$

where $\tilde{H}_{11}$ is unreduced. Now, if k QR steps are applied, using as shifts the eigenvalues of H (μ_m, ..., μ_{k+1}), then the final matrix H_m^{m-k} (from Eq. 3.6) has the form

$$H_m^{(m-k)} = \begin{pmatrix} \tilde{H}_k & H_{12}^{(m-k)} \\ 0 & T^{(m-k)} \end{pmatrix}$$

where $T^{(m-k)}$ is an upper triangular matrix with the Ritz values μ_{k+1}, ..., μ_m (in this order when they are applied on the inverse order)on its diagonal.

Because $H_m^{(m-k)}$ is diagonal by blocks, $\tilde{H}_k$ must contain the Ritz values that were not used as shifts during the contraction phase. The consequences of this is that one can choose the Ritz values that are kept and those that are discarded: after the expansion phase, the eigenvalues of the Hessenberg quotient are computed and those wanted to be discarded can be used as shifts in the contraction phase. This way of restarting the process will be used to steer the Arnoldi algorithm to regions of interest (smallest magnitude eigenvalues in the present case).

Eq. (3.11) remains true in exact arithmetic. Unfortunately, in the presence of rounding error, it can happen that given an exact shift, the computed matrix can fail to deflate – i.e., its $(m, m-1)$-element can be far from zero. This phenomenon is known as *forward instability* of the QR step, and it can prevent eventually the purge of undesirable Ritz values. In fact, an unwanted Ritz value can become permanently locked into the decomposition.

Despite its name, forward instability cannot generate instability in the Arnoldi process itself, and the relation $AV = VH + \beta u e^T$ will continue to hold to working accuracy. At worst it can only delay its progress.

3.3   The Krylov-Schur method

General orthonormal Krylov decompositions were first introduced by Stewart in [155]. They are a generalization of Arnoldi decompositions, and they constitute an elegant way to overcome the limitations imposed by the need to preserve the restrictive form of an Arnoldi factorization. Indeed, the two defects of the implicitly restarted Arnoldi procedure – the forward instability and the difficulty to deflate converged Ritz pairs – come from the commitment to maintaining the Hessenberg structure of its Rayleigh quotient. Therefore, deflation and purging can be treated in a natural and efficient way by relaxing the definition of an Arnoldi decomposition, to obtain a decomposition based on Krylov subspaces that is closed under certain transformations. Because the method is based on Schur decompositions of the Rayleigh quotient, Stewart called it the Krylov-Schur method. The concepts and notations used here come from [155, 156].

3.3.1 Krylov decompositions

The Krylov decomposition is introduced here by its definition:

Definition A Krylov decomposition of order k is a relation of the form

$$AU_k = U_k B_k + u_{k+1} b_{k+1}^H, \tag{3.12}$$

where B_k is of order k and the columns of $(U_k \quad u_{k+1})$ are independent. Equivalently, it is possible to write

$$AU_{k+1} = U_{k+1} \hat{B}_k,$$

with $U_{k+1} = (U_k \quad u_{k+1})$ and

$$\hat{B}_k = \begin{pmatrix} B_k \\ b_{k+1}^H \end{pmatrix}.$$

If U_{k+1} is orthonormal, the Krylov decomposition is orthonormal. The space $\mathcal{R}(U_{k+1})$ is called the space spanned by the decomposition and U_{k+1} the basis of the decomposition. If two Krylov decompositions span the same space they are said to be equivalent.

Eq. (3.12) has the same form as an Arnoldi decomposition, but the vectors of the basis U_{k+1} are not required to be orthonormal. In addition, the matrix $\hat{B}_k$ is not assumed to have any particular form, being uniquely determined by the basis U_{k+1}. If $(V \quad v)^H$ is any left inverse of U_{k+1} then, from Eq. (3.12), it follows that $B_k = V^H A U_k$ and $b_{k+1}^H = v^H A U_k$, i.e., B_k is a Rayleigh quotient of A. For an orthonormal Krylov decomposition, $U_{k+1}^H U_{k+1} = I$, so that $B_k = U_k^H A U_k$. In the following, only orthonormal Krylov decompositions are considered.

Krylov decompositions are closed under two types of transformations: similarity and translation. The first transformation allows to transform the pair (B_k, U_k) along with the vector b_{k+1}^H. The second one changes the vector u_{k+1}.

3.3.1.1 Similarity transformations

Dropping subscripts, let us start with a Krylov decomposition

$$AU = UB + ub^H,$$

and let Q be nonsingular. Then by post-multiplying by Q, we obtain the equivalent Krylov decomposition

$$\begin{aligned} A(UQ) &= (UQ)(Q^{-1}BQ) + u(b^H Q) \\ &\equiv A\tilde{U} = \tilde{U}\tilde{B} + u\tilde{b}_{k+1}^H. \end{aligned} \tag{3.13}$$

Both Krylov decompositions are *similar*. This transformation allows to reduce the Rayleigh quotient to any convenient form. For example, if the Rayleigh quotient is reduced to Jordan form, then we can talk about a Krylov-Jordan decompositions. From this point of view, an Arnoldi decomposition could be called a Krylov-Hessenberg decomposition. Precisely, the name of Krylov-Schur method comes from the fact that it uses the Schur form S of the

Rayleigh quotient B. Indeed, as exposed later, similarity transformations are at the heart of the Krylov-Schur method, since they are used not only to reduce the Rayleigh quotient to an upper triangular matrix, but also in order to sort the eigenvalues appearing in its diagonal attending to any prescription.

3.3.1.2 Translation

To introduce the operation of translation, let

$$\gamma \tilde{u} = u - Ug,$$

where $\gamma \neq 0$. Then it is easily verified that

$$AU = U(B + gb^H) + \tilde{u}\tilde{b}^H,$$

with $\tilde{b}^H = \gamma b^H$, is a Krylov decomposition with the same space as the original. Note that translation cannot produce any arbitrary vector $\tilde{u}$ since $\gamma \neq 0$. The new vector $\tilde{u}$ will always contain the original vector u, so that the two decompositions span the same space.

These two transformations allow to establish an important result: every Krylov decomposition is equivalent (i.e., it spans the same space) to a (possibly unreduced) Arnoldi decomposition. If the Arnoldi decomposition in unreduced, then it is essentially unique, and the original Krylov decompositions must come from a non-degenerate Krylov subspace.

3.3.1.3 Equivalence between Krylov and Arnoldi decompositions

The following theorem states that every Krylov decomposition has an equivalent Arnoldi decomposition.

Theorem 3.5 *Let*

$$AU = UB + ub^H$$

be a Krylov decomposition of order k. Then it is equivalent to an Arnoldi decomposition. If the Hessenberg matrix of the Arnoldi decomposition is unreduced, the Arnoldi decomposition is essentially unique.

In [156] a detailed algorithm to obtain the Arnoldi decomposition equivalent to a given Krylov decomposition is presented. Here, following [155], only the main steps to obtain the Arnoldi decomposition starting for the Krylov decomposition are described. They constitute the sketch of the proof for Theorem 3.5.

1. By similarity transformation, orthogonalize the columns of U.

2. Use a translation in order to make u of norm one and orthogonal to $\mathcal{U}$.

3. By a unitary similarity transformation, reduce b to a multiple of e_k.

4. Finally, using an unitary similarity transformation reduce B to Hessenberg form. The reduction must be done rowwise by Householder transformations beginning with the last row, so that not nonzero elements are introduced into the first $k-1$ components of b.

3.3.2 The Krylov-Schur method as an alternative to the implicitly restarted Arnoldi method

The method is called Krylov-Schur because it uses the Schur form of the Rayleigh quotient matrix B. Purging unwanted Ritz values and deflating (locking) converged ones in the implicitly restarted Arnoldi algorithm are awkward tasks because of the structure of the Arnoldi decomposition. Krylov-Schur decompositions offer an elegant way of dealing with these two aspects. First, it is easier to move eigenvalues around in a triangular matrix (the Schur form of the Rayleigh quotient) than in a Hessenberg matrix. Second, if the Krylov decomposition can be partitioned in the form

$$A(U_1 \; U_2) = (U_1 \; U_2) \begin{pmatrix} B_{11} & B_{12} \\ 0 & B_{22} \end{pmatrix} + u(b_1^H \; b_2^H),$$

then $AU_1 = U_1 B_{11} + ub_1^H$ is also a Krylov decomposition, which means that the decomposition can be truncated at any position without additional operations. This suggests a very natural restarting algorithm: compute the Schur decomposition of the Rayleigh quotient B and move the desired eigenvalues into the leading block using unitary similarity transformation. Once this has been done the unwanted Ritz values are purged just by throwing away the rest of the decomposition. These are the main ingredients of the *Krylov-Schur restart technique*, a natural, effective and elegant alternative to the implicitly restarted Arnoldi method.

3.3.2.1 Sorting eigenvalues in a Schur form

The Krylov-Schur method requires being able to move eigenvalues around in a triangular matrix. To avoid dealing with 2×2 diagonal blocks, the complex Schur form is considered here. If one has to re-order eigenvalues in a real Schur form, then first it is transformed into its complex form. In [156] some general notions about exchanging eigenvalues around in a triangular (or block-triangular) matrix are exposed.

For the implementation of the Krylov-Schur algorithm proposed in this work (see sec. 3.3.2.3), two different (although based on the same concepts) algorithms have been retained for exchanging eigenvalues in the Rayleigh quotient's diagonal. The first one is inspired from the algorithm used by Sleijpen et al. in their MATLAB implementation of the Jacobi-Davidson style QR algorithm [44][6]. A permutation vector coming from sorting the diagonal elements in any prescribed order is given to the re-ordering routine together with the triangular matrix and the corresponding Schur vectors matrix. The output is the triangular matrix with the diagonal elements sorted and the matrix of Schur vectors updated consequently. The flexibility of this option is obvious, allowing the user to move eigenvalues around with total freedom. More details about this algorithm for the re-ordering of the diagonal elements of a triangular matrix using Given rotations can be found in [43, Ch.6]. The second algoritm is based on LAPACK routines. There is not a single LAPACK routine that allows to re-order all the diagonal elements of an upper triangular matrix in a prescribed order at once, but it is possible to use a combination of subroutine to achieve

---

[6]http://www.math.uu.nl/~sleij101/

the objective. For more details on these algorithms, see the LAPACK subroutine xLAEXC (http://www.netlib.org/lapack/).

Algorithm 3.2 [Q,S]=SortSchur(A,σ,k)

Given a complex matrix $A \in \mathbb{C}^{n \times n}$, compute the Schur decomposition $AQ = QS$, with the k leading elements of $diag(S)$ sorted according to the order prescribed by σ.

  $[Q, S]$=Schur(A) ! Compute the complex Schur form of A
  $perm =$ SortEig($diag(S)$,σ) ! Sort the eigenvalues of S according to σ
  $[Q, S] =$ SwapSchur($Q, S, perm(1 : k)$) ! Reorder the Schur form

---

Algorithm 3.2 is a general description of the re-ordering algorithm. As input it takes a complex matrix A of order n whose ordered Schur decomposition is going to be computed, a parameter σ and an integer k. The outputs are the matrices Q and S so that

$$AQ = QS,$$

where Q is an unitary transformation matrix and S is the ordered Schur form. The k leading elements of $diag(S)$ are sorted according to σ. The parameter σ can be:

- A chain of characters. For example: 'SM', $diag(S)$ are sorted from smallest to largest magnitude; or 'LM', from largest to smallest magnitude.

- A complex scalar: $diag(S)$ are sorted with increasing distance from σ.

- A vector of scalars: let us assume that the length of σ is ℓ, with $\ell <= n$. Then the first k elements of $diag(S)$ are component-wise the closest to σ. If $k > \ell$ the remaining elements of $diag(S)$ are sorted with increasing distance from $\sigma(\ell)$.

3.3.2.2 The Krylov-Schur restart technique

As it is the case for the implicitly restarted Arnoldi method, a cycle of the Krylov-Schur method has an expansion phase that ends up with the computation of the eigenvalues of the Rayleigh quotient of order m and a contraction phase that reduces the order of the decomposition to k, keeping the k wanted Ritz values and throwing away the rest. Thus, the Krylov-Schur cycle begins with an order k Krylov-Schur decomposition

$$AU_k = U_k S_k + u_{k+1} b_{k+1}^H = U_{k+1} \hat{S}_k,$$

where U_{k+1} is orthonormal and S_k is upper triangular. To get this decomposition an Arnoldi decomposition is built starting from an initial vector and then, using an unitary similarity transformation, the Hessenberg matrix is reduced to its complex Schur form. The expansion phase is done analogously to the expansion phase of the Arnoldi method, using Algorithm 3.3.

Note that Algorithm 3.3 uses Classical Gram-Schmidt (CGS) with selective re-orthogonalization in order to orthogonalize the new direction w against the existing Krylov

basis U_{j+1}. It is chosen over the Modified Gram-Schmidt (MGS) method because it is better suited for parallel computing and it is the choice done in ARPACK as well, whose stability is out of question and can be considered as a reference. In [130] one can find different implementations of the Arnoldi process using either CGS, MGS or Householder transformations, as well as the computational cost of each implementation.

Before performing the expansion of the Krylov-Schur decomposition, the expanded Rayleigh quotient $\hat{S}_k$, for $k = 4$ has the form

$$
\begin{pmatrix}
s & s & s & s \\
0 & s & s & s \\
0 & 0 & s & s \\
0 & 0 & 0 & s \\
b & b & b & b
\end{pmatrix}.
$$

At the end of the expansion phase, for $m = 8$, $\hat{S}_m$ has been updated to

---

Algorithm 3.3 $[U_{m+1}, \hat{B}_m] = contARL\_reortho(k, m, A, U_{k+1}, \hat{B}_k)$

Given the orthonormal matrix U_{k+1} and the Rayleigh quotient $\hat{B}_k$ of the Krylov decomposition $AU_k = U_k B_k + u_{k+1} b_{k+1}^H = U_{k+1} \hat{B}_k$ of order k, $contARL\_reortho$ extend it to a Krylov decomposition $AU_m = U_m S_m + u_{m+1} b_{m+1}^H = U_{m+1} \hat{S}_m$ of order m, using the Arnoldi process.

    for j=k+1,...,m **do**
      $w = AU(:, j)$
      $wnorm1 = norm(w)$
      !First CGS iteration
      $B(1:j, j) = U(:, 1:j)^H w$
      $w = w - U(:, j)B(1:j, j)$
      $wnorm = norm(w)$
      !Re-orthogonalization
      if $wnorm < \sqrt{2}wnorm1$ **then**
        $s = U(:, 1:j)^H w$
        $S(1:j, j) = S(1:j, j) + s$
        $w = w - U(:, 1:j)s$
        $wnorm = norm(w)$
      end if
      $S(j+1, j) = wnorm$
      $U(:, j+1) = w/wnorm$
    end for

$$\begin{pmatrix} s & s & s & s & h & h & h & h \\ 0 & s & s & s & h & h & h & h \\ 0 & 0 & s & s & h & h & h & h \\ 0 & 0 & 0 & s & h & h & h & h \\ b & b & b & b & h & h & h & h \\ 0 & 0 & 0 & 0 & h & h & h & h \\ 0 & 0 & 0 & 0 & 0 & h & h & h \\ 0 & 0 & 0 & 0 & 0 & h & h & h \\ 0 & 0 & 0 & 0 & 0 & 0 & h & h \\ 0 & 0 & 0 & 0 & 0 & 0 & 0 & h \end{pmatrix},$$

where h has been chosen by analogy to the Hessenberg form. The expanded Krylov decomposition of order m reads as

$$AU_m = U_m B_m + \beta u_{m+1} e_m^T. \tag{3.14}$$

Finally, an unitary similarity transformation is applied to Eq. (3.14) using Algorithm 3.2 in order to compute the ordered Schur form of the Rayleigh quotient B_m, $\tilde{S}_m = Q^H B_m Q$, putting the k wanted Ritz values in the leading block of $\tilde{S}_m$, to obtain the equivalent decomposition

$$A\tilde{U}_m = \tilde{U}_m \tilde{S}_m + u_{m+1} \tilde{b}_{m+1}^H, \tag{3.15}$$

where $\tilde{U}_m = U_m Q$ and $\tilde{b}_{m+1} = \beta e_m^T Q$. Then we have just to truncate the resulting decomposition (3.15) to reduce its order to k. Since the Schur form $\tilde{S}_m$ has the k wanted eigenvalues in its leading block, truncating the decomposition is equivalent to keep the wanted Ritz values, and throwing away the unwanted ones. Although the proof is not straightforward (see [156] for the proof), this simple procedure is equivalent to apply $m - k$ shifts to the Rayleigh quotient in the implicitly restarted Arnoldi algorithm, using the unwanted Ritz values as shifts. At this point, the process can continue with the expansion phase again.

3.3.2.3   Final algorithm

The algorithm presented in this section implements the Krylov-Schur method for the computation of *nev* approximate eigenpairs (μ_j, x_j) of the large sparse complex matrix A of order n, corresponding to those of smallest magnitude. It starts with an initial vector u_0 and it computes the Krylov decomposition of order m

$$AU_m = U_m B_m + u_{m+1} b_{m+1}^H = U_{m+1} \hat{B}_m.$$

Then the Krylov-Schur restart technique is used to reduce the Krylov decomposition to a Krylov-Schur decomposition

$$A\tilde{U}_k = \tilde{U}_k S_k + u_{k+1} \tilde{b}_{k+1}^H = \tilde{U}_{k+1} \hat{S}_k$$

of order k, where the k wanted Ritz values appear on the diagonal of S_k, and then it is expanded again to a m order Krylov decomposition. This procedure is repeated until the residual $r_j = Ax_j - \mu_j x_j$ is small enough for the *nev* wanted eigenvalues respect to a prescribed tolerance *tol* or the maximum number of iterations *maxiter* is reached. The convergence criteria will be treated more precisely later in this chapter. Note that it exists an inexpensive way of evaluating the norm of the residual r_j. Indeed, starting from

$$A\tilde{U}_k = \tilde{U}_k S_k + u_{k+1}\tilde{b}_{k+1}^H,$$

let (μ_j, x_j) be the approximate eigenpair of A associated to the Ritz pair (μ_j, p_j), such that $x_j = U_k p_j$, being p_j the j-eigenvector of the Rayleigh quotient $S_k p_j = \mu_j p_j$. Then the norm of the residual r_j can be written as

$$\|r_j\| = \|AU_k p_j - \mu_j U_k p_j\| = \|(AU_k p_j - U_k S_k)p_j\| = \|u_{k+1}b^H p_j\| = |b^H p_j|. \qquad (3.16)$$

As soon as a certain number *nconv* of Ritz values has converged, the size k of the reduced Krylov-Schur decomposition is set to $k = k_0 + nconv$, where k_0 is the initial size chosen for the reduced Krylov-Schur decomposition. This strategy has been taken from ARPACK, where it is used to avoid an eventual stagnation in the expansion-contraction process. Algorithm 3.4 implements the Krylov-Schur method, taking into account these considerations.

The parameter k_0 must be at least equal to the number of wanted eiganvalues *nev*. When using the implicitly restarted Arnoldi method or the Krylov-Schur method, there is not a general rule to choose k_0 and m optimally (the size of the restarted Krylov space and the size of the biggest Krylov space we can afford, respectively). The common advice is to choose $m = 2k_0$ at least. The parameter k_0 can affect the convergence of the method. Even is we are interested only in very few eigenvalues, if k_0 is chosen too small, it may penalize the convergence. The advise given here is not to choose k_0 smaller than 5. Of course, these observations are not written in stone and they can be extremely case-dependent.

3.3.3 Harmonic Ritz pairs computation

Harmonic Ritz vectors were introduced by Morgan in [91] for symmetric matrices as good approximations of interior eigenvectors. The goal of harmonic Ritz pairs is to emulate the effect of the shift-and-invert transformation, but avoiding the inverted operator $(A - \kappa I)^{-1}$ when computing eigenpairs nearest to κ. This is achieved by working with two bases, one that spans the subspace of an approximate eigenspace of the matrix A, U, and another that is defined as

$$V := (A - \kappa I)U. \qquad (3.17)$$

The following definition of of harmonic Ritz pair is given in [156]:

Definition Let $\mathcal{U}$ be a subspace and U an orthonormal basis of it. Then $(\delta + \kappa, Uw)$ is a harmonic Ritz pair with shift κ if

$$U^H(A - \kappa I)^H(A - \kappa I)U = \delta U^H(A - \kappa I)Uw. \qquad (3.18)$$

Algorithm 3.4 $[eigval, eigvec]=KS\_solver(k_0, m, A, u_0, nev, tol, maxiter)$

Given the initial vector u_0, KS_solver computes the nev approximate eigenvalues $eigval$ of the n non-symmetric complex matrix A corresponding to those of smallest magnitude, and the nev corresponding eigenvectors $eigvec$. The user must provide the reduced Krylov decomposition of size k_0 and the extended Krylov decomposition size m as well; the tolerance tol used for the convergence test; and the maximum number of Krylov-Schur restarts allowed $maxiter$.

> S(1:m+1,1:m) = 0
> $k_{bef} = k_0$
> [U(:,1:k+1),S(1:k+1,1:k)]=ARL_reortho(A,u_0,k_0)
> **for** i=1,...,maxiter **do**
> $k = k_0 + nconv$
> $[U(:, 1 : m + 1), S(1 : m + 1, 1 : m)] = contARL\_reortho(k_{bef}, m, A, U, S)$
> $[Q, S(1 : m, 1 : m)] = SortSchur(S(1 : m, 1 : m),' SM', k)$
>   U(:,1:k) = U(:,1:m)Q(:,1:k)
> $b = (S(m + 1, m)Q(m, 1 : k))^H$
>   Compute the eigenvectors of the Schur matrix $S(1 : k, 1 : k)$:
> $S(1 : k, 1 : k)V = DV$
> $eigS = diag(S(1 : k, 1 : k))$
> $nconv = 0$
>   **for** $j = 1, \ldots, nev$ **do**
> $res = |b^H V(:, j)|$
>   **if** $res \leq tol * |eigS(j)|$ **then**
> $nconv = nconv + 1$
>   **end if**
>   **end for**
>   **if** $nconv = nev$ **then**
> $eigval(1 : nev) = eigS(1 : nev)$
> $eigvec(:, 1 : nev) = U(:, 1 : k)V(:, 1 : nev)$
>   **return**
>   **else if** $i = maxiter$ **then**
>   'Max. number of iteration reached without convergence'
>   **return**
>   **end if**
> $k_{bef} = k$
> $S(1 : k + 1, 1 : k) = [S(1 : k, 1 : k); b^H]$
> $U(:, 1 : k + 1) = [U(:, 1 : k)U(:, m + 1)]$
> **end for**

When the Rayleigh-Ritz method is used for computing harmonic Ritz pairs, it is referred as the harmonic Rayleigh-Ritz method.

In [157], Stewart extends the Krylov-Schur method to the computation of harmonic Ritz values (actually to any Rayleigh quotient with the form $(V^H U)^{-1} V^H AU$). It is done by

showing that the Rayleigh quotient

$$\hat{B} = (V^H U)^{-1} V^H A U$$

can be written as a translation of the classical Rayleigh quotient B of a Krylov decomposition $AU = UB + ub^H$

$$\hat{B} = B + gb^H,$$

where $g = (V^H U)^{-1} V^H u$. Therefore, if the starting point is the Krylov decomposition

$$AU = UB + ub^H,$$

then using a translation transformation defined by the vector $g = (V^H U)^{-1} V^H u$,

$$AU = U\hat{B} + \hat{u}b^H$$

is an equivalent Krylov decomposition, with $\hat{B} = B + gb^H$ and $\hat{u} = u - Ug$, and the Rayleigh quotient $\hat{B} = (V^H U)^{-1} V^H A U$.

For the computation of harmonic Ritz pairs V is chosen as $V = (A - \kappa I)U$. From Eq. (3.18) and considering the Krylov decomposition $(A - \kappa I)U = U(B - \kappa I) + ub^H$, it is found

$$[(B - \kappa I)^H (B - \kappa I) + bb^H]w = \delta(B - \kappa I)^H w. \tag{3.19}$$

Then the computation of harmonic Ritz pair is done by solving the small generalized eigenvalue problem (3.19). If $(B - \kappa I)^{-H}$ is well conditioned, then it is possible to solve the equivalent standard eigenproblem

$$[(B - \kappa I) + (B - \kappa I)^{-H} bb^H]w = \delta w.$$

For $V = (A - \kappa I)U$, the matrix $\hat{B} = B - gb^H$ resulting from a translation is precisely equal to $[(B - \kappa I) + (B - \kappa I)^{-H} bb^H]$. In this case, g takes the form

$$g = (B - \kappa I)^{-H} b.$$

This suggests the following procedure to compute the harmonic Ritz values $(\delta + \kappa, Uw)$ using the Krylov-Schur method:

1. The starting point is the Krylov decomposition $AU = UB + ub^H$ of order m.

2. Apply a translation transformation to $(B - \kappa I)$ using $g = (B - \kappa I)^{-H} b$, so that

$$\hat{B} = B + gb^H = (B - \kappa I) + (B - \kappa I)^{-H} bb^H.$$

   The matrix $\hat{B}$ includes the shift κ. Note that solving the eigenproblem $\hat{B}w = \delta w$ is equivalent to solve Eq. (3.19). To preserve the Krylov decomposition equality the translation is applied to u consequently: $\hat{u} = u - Ug$. At this point the Krylov decomposition reads

$$(A - \kappa I)U = U\hat{B} + \hat{u}b^H.$$

3. Compute the Schur form of $\hat{B}$

$$\hat{B}Q = Q\hat{S},$$

   with its diagonal elements sorted in increasing magnitude order and apply the unitary similarity transformations $\tilde{U} = UQ$ and $\tilde{b}^H = b^H Q$, so that

$$(A - \kappa I)\tilde{U} = \tilde{U}\hat{S} + \hat{u}\tilde{b}^H.$$

4. Use the harmonic Rayleigh-Ritz extraction to compute the harmonic Ritz pairs $(\delta + \kappa, Uw)$ and check for convergence.

5. In order to restart the process, reduce the decomposition to order k by simply truncating it and remove the shift κ from $\hat{S}$. Before the decomposition can be extended again, it is necessary to orthonormalize the last vector $\hat{u}$ against $\tilde{U}$, using a translation transformation again.

3.4 Block methods

Block methods for the solution of eigenproblems allow to build a search basis starting from an initial block of vectors, contrary to the single vector methods that start from a single vector. Block methods have their place in the development of modern numerical linear algebra. Advantages of using block methods are:

- It is the natural choice when more than one good initial vector is available.

- They are well adapted for the computation of multiple or clustered eigenvalues.

- They do better use of the memory hierarchy, what can yield to significant gain for large dense matrix vector products (BLAS 3 efficiency). This is also in the case of sparse matrix.

As explained in Chapter 4, the interest here is in exploiting multiple initial vectors, since we are not concerned by multiple (clustered) eigenvalues and in AVSP the matrix-vector products are coded without using storage schemes and one can only perform one matrix-vector product at once, so that the cache advantage can not be exploited.

In [76, 175] block versions of the implicitly restarted Arnoldi method are proposed, but the fact is that due to the difficulties inherent to the method (deflation of converged Ritz values, forward instability) it can not be extended naturally to its block variant. The reason resides mainly in the use of the implicit shifted QR method for restarting. A genuine implicitly restarted block Arnoldi method would require block implicit shifted QR decomposition to filter out the unwanted Ritz values, but unfortunately currently there are not known efficient methods performing a block implicit shifted QR decomposition. Note that the IRBL method presented in [6, 5] is actually based on explicit shifted QR decomposition, which is not as stable as the implicit shift QR decomposition. For this reason, the Krylov-Schur method presented formerly is a better candidate for the implementation of a block method for the solution of eigenproblems, since it does not use implicit shifted QR

decompositions and its flexibility allows a natural extension to its block variant. Therefore, in this section an implementation of a block Krylov-Schur method is presented, while the option of an implicitly restarted block Arnoldi method is not considered. More details about block methods can be found in [6, 7, 45, 49, 128, 132, 133, 134].

The block Krylov-Schur algorithm for the solution of general non-symmetric complex eigenproblems presented in what follows, is an extension of the algorithm in [178], where a block Krylov-Schur method for the solution of symmetric eigenproblems is proposed. The main difficulty of block methods arises when vectors in a new block become linearly dependent. This is known as the *rank deficient case*. A more detailed description of this phenomena and its cure can be found in [45]. In [178] rank revealing pivoted thin QR decompositions are proposed as a solution to deal with this concern. An additional advantage of the block Krylov-Schur method is that the block size has not to be constant and it can be adapted during the process, what is implemented in [178] as well. Here, since there are no reasons to modify the block size and for the sake of simplicity it is going to be kept constant. The *rank deficient case* is treated simply by using a vector-wise construction of the block Krylov decomposition, as will be shown. Before presenting the block algorithm, the block Arnoldi procedure to obtain orthonormal Krylov basis is described.

The subspace iteration method is another block method that allows to start from an initial set of vectors. This method consists basically in applying repeatedly a matrix A to the search subspace and then using the Rayleigh-Ritz extraction in order to obtain approximated eigenpairs of A. It is often used along with acceleration techniques (such Chebyshev filter polynomials) that enhances the convergence of the method toward a given region of the spectrum of A.

In Sec. 3.4.1 the Arnoldi algorithm is extended to the block version, which is used in Sec. 3.4.2 within the proposed algorithm implementing the block version of the Krylov-Schur method. Finally, in Sec. 3.4.3, we detail an implementation of the subspace iteration method with Chebyshev acceleration.

3.4.1   The block Arnoldi procedure

Block versions of the Arnoldi algorithm for the construction of an orthonormal Krylov basis based on an initial $p - size$ block V_1 are given in [130]. There are mainly two versions: block Arnoldi and the Ruhe's variant. Given a matrix A, with V_p being the initial block of p orthonormal vectors, both algorithms end up with the following decomposition:

$$AV_m = V_m H_m + v_p h_{m:p,1:m} E_m^T, \tag{3.20}$$

where $[V_m \ v_p]$ is an orthonormal $(m + p) - size$ Krylov basis; E_m is the matrix of the last p columns of the identity matrix of size m and H_m is a band Hessenberg matrix, with p non zero subdiagonal elements, instead of only one. In its compact form, Eq. (3.20) reads as

$$AV_m = V_{m+p} \hat{H}_m,$$

where $V_{m+p} = [V_m \ v_p]$ and $\hat{H}_m = \begin{pmatrix} H_m \\ h_{m:p,1:m} \end{pmatrix}$, whose Wilkinson diagram for $p = 3$ and $m = 9$ is

$$\hat{H}_m = \begin{pmatrix} * & * & * & * & * & * & * & * & * \\ * & * & * & * & * & * & * & * & * \\ * & * & * & * & * & * & * & * & * \\ * & * & * & * & * & * & * & * & * \\ 0 & * & * & * & * & * & * & * & * \\ 0 & 0 & * & * & * & * & * & * & * \\ 0 & 0 & 0 & * & * & * & * & * & * \\ 0 & 0 & 0 & 0 & * & * & * & * & * \\ 0 & 0 & 0 & 0 & 0 & * & * & * & * \\ 0 & 0 & 0 & 0 & 0 & 0 & * & * & * \\ 0 & 0 & 0 & 0 & 0 & 0 & 0 & * & * \\ 0 & 0 & 0 & 0 & 0 & 0 & 0 & 0 & * \end{pmatrix}.$$

Note that using this notation, and considering the block size p fixed, the size m of the block Arnoldi factorization must be a multiple of p, i.e., *block steps* $= m/p$. Algorithm 3.5 implements the block Arnoldi procedure. It is a straightforward block analogue of the sequential Algorithm 3.1.

Algorithm 3.5 $[V_{m+p}, \hat{H}_m] = Bl\_ARL(m, p, A, V_p)$

Given the orthonormal matrix $n \times p$ V_p, build a m-size p-block Arnoldi factorization $AV_m = V_{m+p}\hat{H}_m$.

  $k = 0$
  while $k + p \leq m$ **do**
    $W = AV(:, k+1 : k+p)$
    $H(1 : k+p, k+1 : k+p) = V(:, 1 : k+p)^H W$
    $W = W - V(:, 1 : k+p)H(1 : k+p, k+1 : k+p)$
    $k = k + p$
    Compute the thin QR factorization of W:
    $W = V(:, k+1 : k+p)H(k+1 : k+p, k-p+1 : k)$
  end while

Algorithm 3.5 can include a re-orthogonalization phase. The main advantage of using this block variant of the Arnoldi algorithm is that it allows to take advantage of the BLAS-3 performance. On the other hand, it needs detection and treatment of the rank deficient case. Since the matrix-free formalism implemented in AVSP can only perform one matrix-vector product at once, using Algoritm 3.5 is not of practical use. A vector-wise version, known as the Ruhe's variant [127] is considered instead. It is implemented in Algorithm 3.6. Since each new vector $w = Av_k$ is orthogonalized against the whole current Krylov basis, the rank deficient case is taken into account naturally, without requiring any special treatment.

Note that Algorithm 3.6 uses selective re-orthogonalization like Algorithms 3.1 and 3.3.

Algorithm 3.6 $[V_{m+p}, \hat{H}_m] = ARL\_Ruhe(k_0, k_f, A, V_{k_0+p}, \hat{H}_{k_0})$

Given the $k_0 - size$ block Arnoldi decomposition $AV_{k_0} = V_{k_0}H_{k_0} + v_{k_0+1,p}H_{k_0+p,k}E_{k_0}^T = V_{k_0+p}\hat{H}_{k_0}$, ARL_ruhe extends it to the $k_f - size$ decomposition $AV_{k_f} = V_{k_f+p}\hat{H}_{k_f}$. It assumes that k_0 and k_f are multiple of the block size p.

   for $i = k_0, \ldots, k_f + p - 1$ **do**
      Set $j = i - p + 1$
      $w = AV(:, j)$
      $wnorm1 = norm(w)$
      $H(1 : i, j) = V(:, 1 : i)^H w$
      $w = w - V(:, 1 : i)H(1 : i, j)$
      $wnorm = norm(w)$
      if $(wnorm < \sqrt{2}wnorm1)$ **then**
         $h = V(:, 1 : i)^H w$
         $H(1 : i, j) = H(1 : i, j) + h$
         $w = w - H(:, 1 : i)h$
         $wnorm = norm(w)$
      end if
      $H(i + 1, j) = wnorm$
      $V(:, i + 1) = w/wnorm$
   end for

At most one re-orthogonalization step is done. In ARPACK, the DGKS method [31] is used instead, which employs the same test for re-orthogonalization, but the process can be iterated more than once, until the desired precision or a given number of iterations are reached.

3.4.2 A block Krylov-Schur algorithm

The extension of the Krylov-Schur method to its block version is straightforward. Let k and m (both set to be multiple of the block size p) be the size of the restarted and the extended block Krylov decompositions, respectively. The method has the following main steps:

1. Given an initial orthonormal $n \times p$ matrix V_p, Algorithm 3.6 is used to compute the block Arnoldi decomposition

$$AV_m = V_m H_m + v_p h_{m:p,1:p}E_m^T.$$

2. An unitary similarity transformation is used to compute the equivalent block Krylov-Schur decomposition. This is done using Algorithm 3.2. Then we have

$$A(V_m Q) = (V_m Q)S_m + v_p h_{m:p,1:m}E_m^T Q \equiv$$
$$AU_m = U_m S_m + u_p B^H,$$

where $U_m = V_m Q$, $u_p = v_p$, $B^H = h_{m:p,1:m} E_m^T Q$ and S_m is the complex Schur form of the band Hessenberg matrix H_m, with the k wanted Ritz values in the leading block. The compact form is

$$AU_m = U_{m+p}\hat{S}_m,$$

being $U_{m+p} = [U_m \; u_p]$ and $\hat{S}_m = \begin{pmatrix} S_m \\ u_p B^H \end{pmatrix}$.

3. Use Ritz extraction to compute approximate eigenpairs and test for convergence. Then the decomposition is reduced to size k, just by truncating the decomposition and keeping only the first k columns:

$$AU_k = U_k S_k + u_p B^H = U_{k+p}\hat{S}_k.$$

4. The $k - size$ decomposition is extended to size m using Algorithm 3.6 again.

Steps 2 to 4 are repeated until the wanted eigenvalues have converged or the maximum number of restarted iterations is reached. This procedure is completely equivalent to the sequential Krylov-Schur method. Only the algorithm for the computation of the block Krylov decomposition changes and k and m have to be kept multiples of the block size p. Algorithm 3.7 implements this method. As said before, contrary to what is done in [178], here the block size is kept constant, since we are not concerned *a priori* by multiple or clustered eigenvalues, what reduces the complexity of the algorithm.

In Algorithm 3.7, the number of wanted eigenvalues *nev* must be at least equal to k, although it is recommended to use a value of $k > nev$.

As explained before, a single vector Krylov method applies a filter polynomial of degree K_{deg} which is equal to $m - k$, i.e., the size of the extended Krylov decomposition minus the size of the restarted one. On the other hand, if k and m are kept the same, the block method applies a filter polynomial of degree $K_{block} = K_{deg}/p$, being p the block size, which can penalize the efficiency of the method. This rises another concern: the equivalence between the block Krylov-Schur method and the implicitly restarted block Arnoldi method. In the case of their sequential versions, both methods are equivalent if the IRA algorithm uses as shifts the same Ritz values that are discarded when the Krylov-Schur decomposition is truncated. This is true because the number of shifts to apply $(m - k)$ in the first case is equal to the number of Ritz values that are thrown away in the second case. In the block version of the IRA algorithm, there will be $m - k$ unwanted Ritz values as well, but now it is possible to apply only $(m - k)/p$ shifts, since every shift reduces the size of the decomposition by p. It means that one has to choose which Ritz values are used as shift among all the unwanted ones and this choice will modify the resultant restarted Krylov subspace. In the block Krylov-Schur method, the restart is doing just by keeping the k wanted Ritz values. Therefore, there is no guarantee that both restarted Krylov subspace are equivalent.

Algorithm 3.7 $[eigval, eigvec]$=block_KSmethod(k,m,p,A,initblock,nev,tol,maxiter)

Given an initial matrix $n \times p$ of linear independent vectors *initblock*, *block_KSsolver* computes the *nev* approximate eigenvalues *eigval* of the n non-symmetric complex matrix A corresponding to those of smallest magnitude, and the *nev* corresponding eigenvectors *eigvec*. User must enter k and m corresponds to the size of the restarted and the extended block Krylov decompositions, respectively; the tolerance *tol* used for the convergence test; and the maximum allowed number of Krylov-Schur restarts *maxiter*.

   Orthogonalize the initial block:
      $initblock = V(:, 1 : p)R$, where $V(:, 1 : p)^H V(:, 1 : p) = I$
   If k and m are nor multiple of p, modify them so that:
      $mod(\tilde{m}, p) = 0$ and $mod(\tilde{k}, p) = 0$, with $\tilde{m} \leq m$ and $\tilde{k} \leq k$
   Set $k = \tilde{k}$ and $m = \tilde{m}$
   $S(1 : m + p, 1 : m) = 0$
   $[V(:, 1 : k + p), S(1 : k + p, 1 : k)] = ARL\_Ruhe(0, k, A, V, S)$
   for $i = 1, \ldots, maxiter$ **do**
     $[V(:, 1 : m + p), S(1 : m + p, 1 : m)] = ARL\_Ruhe(k, m, A, V, S)$
     $[Q, S(1 : m, 1 : m)] = SortSchur(S(1 : m, 1 : m),' SM', k)$
     $U(:, 1 : k) = U(:, 1 : m)Q(:, 1 : k)$
     $B^H = S(m + 1 : m + p, m - p + 1 : m)Q(m - p + 1 : m, 1 : k)$
     Compute the eigenvectors of the Schur matrix $S(1 : k, 1 : k)$:
       $S(1 : k, 1 : k)V = DV$
     $eigS = diag(S(1 : k, 1 : k))$
     $nconv = 0$
     for $j = 1, \ldots, nev$ **do**
       $res = \|B^H V(:, j)\|_2$
       if $res \leq tol * |eigS(j)|$ **then**
         $nconv = nconv + 1$
       end if
     end for
     if $nconv = nev$ **then**
       $eigval(1 : nev) = eigS(1 : nev)$
       $eigvec(:, 1 : nev) = U(:, 1 : k)V(:, 1 : nev)$
       return
     else if $i = maxiter$ **then**
       'Max. number of iteration reached without convergence'
       return
     end if
     Truncate the factorization for restart:
       $S(1 : k + p, 1 : k) = [S(1 : k, 1 : k); B^H]$
       $U(:, 1 : k + p) = [U(:, 1 : k) \; U(:, m + 1 : m + p)]$
   end for

3.4.3 Subspace iteration with Chebyshev acceleration

The simplest version of the subspace iteration method is a block version of the power method, first introduced by Bauer under the name of *Treppeniteration* (staircase iteration) [9]. Starting with an initial block of m vectors arranged in the $n \times m$ matrix $X_0 = [x_1, \ldots, x_m]$ the matrix $X_k = A^k X_0$ is computed for a certain power k. The columns in X_k will loose their linear independency for increasing values of k, so that the idea is to re-establish their linear independency using, for instance, the QR factorization. Under a certain number of assumptions [129], the columns of X_k will converge to the Schur vectors associated with the m dominant eigenvalues of A: $|\lambda_1| > |\lambda_2| > \cdots > |\lambda_m|$. Instead of using the columns of X_k as approximations to the Schur vectors, using them in a Rayleigh-Ritz procedure will produce in general better approximations, which yields to the Algorithm 3.8

Algorithm 3.8 Basic Subspace Iteration

Given the $n \times m$ matrix $X_0 = [x_1, \ldots, x_m]$, iterate until an invariant subspace of $A \in \mathbb{C}^{n \times n}$ is found.

1: Orthonormalize the initial block: $X = qr(X_0)$.
2: **for** $i = 1, \ldots$ until convergence **do**
3:     Compute $\hat{X} = AX$.
4:     Orthonormalization of $\hat{X}$: $X = qr(\hat{X})$.
5:     Form the Rayleigh quotient $B = X^H A X$ and compute its eigenvectors $V = [v_1, \ldots, v_m]$.
6:     Update X with the Ritz vectors: $X \leftarrow XV$.
7:     Test for convergence.
8: **end for**

This algorithm is well suited for the computation of largest magnitude eigenpairs, but the interest in this work is on smallest magnitude eigenvalues. Therefore, preconditioning techniques must be used in order to make the method converged toward the zone of interest. Two classic options are:

- Shift-and-invert. As seen before in this chapter, it consists in working with the matrix $(A - \sigma I)^{-1}$, with $\sigma \in \mathbb{C}$. In this case, the eigenvalues near σ will converge fast. The problem is that this option needs the solution of linear systems involving the matrix A, which can be a difficult problem itself, as mentioned before.

- Polynomial acceleration. Instead of using the polynomial A^k which enhances the convergence of largest magnitude eigenvalues, the idea is to use the polynomial $T_m[(A - \sigma I)\rho]$, being T_m the Chebyshev polynomial of the first kind of degree m.

The second option is retained here. In the following, some details about Chebyshev polynomials and their properties are given.

3.4.3.1 Chebyshev polynomials

Chebyshev polynomials are very important in the study of iterative methods in linear algebra, as is the case of the conjugate gradient method. In practice they are used to accelerate

single vector iterations or projection processes. In **real arithmetic**, the Chebyshev polynomial of the first kind of degree k is defined as:

$$C_k(t) = \begin{cases} cos(k \ cos^{-1}t), & |t| < 1, \\ cosh(k \ cosh^{-1}t), & |t| > 1. \end{cases} \tag{3.21}$$

The Chebyshev polynomial of degree k can be computed using the following three-term recurrence:

$$C_0(t) = 1,$$
$$C_1(t) = t,$$
$$C_{k+1}(t) = 2tC_k(t) - C_{k-1}(t), \ k = 1, 2, \dots$$

The following theorem from [129] establishes an important result concerning Chebyshev polynomials that justifies their use as filter polynomials.

Theorem 3.6 *Let $[\alpha, \beta]$ be a non-empty interval in $\mathbb{R}$ and let γ be any real scalar such with $\gamma \geq \beta$. Then the minimum*

$$\min_{p \in \mathbb{P}_k, p(\gamma)=1} \ \max_{t \in [\alpha, \beta]} \ |p(t)|$$

is reached by the polynomial

$$\hat{C}_k \equiv \frac{C_k \left(1 + 2\frac{t-\beta}{\beta-\alpha}\right)}{C_k \left(1 + 2\frac{\gamma-\beta}{\beta-\alpha}\right)}.$$

For the proof see [24]. In other words, Theorem 3.6 says that among all the possible polynomials of degree k, $\hat{C}_k$ reaches the smallest possible absolute values in the interval $[\alpha, \beta]$, such that $\hat{C}_k(\gamma) = 1$.

The definition of Chebyshev polynomials can be extended naturally to **complex arithmetic** [129]. The Chebyshev polynomial of degree k can still be computed using the three-term recurrence

$$C_0(z) = 1,$$
$$C_1(z) = z,$$
$$C_{k+1}(z) = 2zC_k(z) - C_{k-1}(z), \ k = 1, 2, \dots$$

The segment $[\alpha, \beta]$ in real arithmetic becomes an ellipse E in the complex plane which is symmetric with respect to the real axis, i.e., its center is on the real axis and its foci are either pure real or pure imaginary numbers (Fig. 3.3).

3.4.3.2 Subspace iteration with Chebyshev acceleration

This algorithm consists in using Chebyshev polynomials during the subspace iterations to accelerate the convergence of the method. As exposed in [129], if the ellipse $E(c, a, e)$
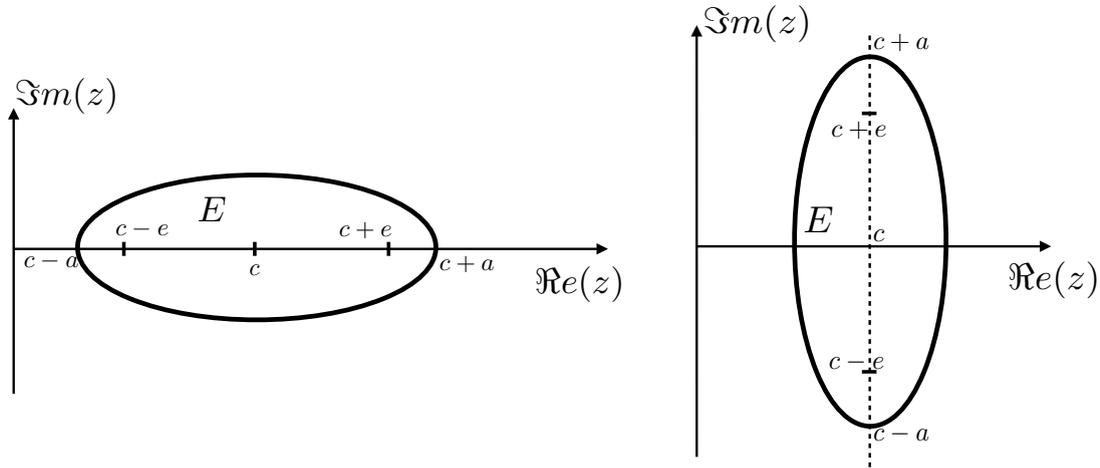
Figure 3.3: Ellipses in the complex plane defined by their center c, foci $c-e$ and $c+e$ and major semi-axis a.

(Fig. 3.3) encloses the unwanted part of the spectrum of A, then the asymptotically best min-max polynomial is the polynomial

$$p_k(\lambda) = \frac{C_k[(\lambda - c)/e]}{C_k[(\lambda_1 - c)/e]}, \tag{3.22}$$

where C_k is the Chebyshev polynomial of degree k of the first kind and λ_1 is an approximation of the first wanted eigenvalue that is not enclosed by the ellipse E. Therefore, the successive applications of the polynomial defined by Eq. (3.22) to a set of vectors U during the subspace iterations, will make U converge to an invariant subspace corresponding to the eigenvalues that lay out the ellipse E.

The computation of $z_k = p_k(A)z_0$ is performed iteratively thanks to the three-term recurrence for Chebyshev polynomials [129] as:

1. Given the initial vector z_0, compute

$$\sigma_1 = \frac{e}{\lambda_1 - c},$$

$$z_1 = \frac{\sigma_1}{e}(A - cI)z_0.$$

2. Iterate for $i = 1, \ldots, k-1$:

$$\sigma_{i+1} = \frac{1}{2/\sigma_1 - \sigma_i},$$

$$z_{i+1} = 2\frac{\sigma_{i+1}}{e}(A - cI)z_i - \sigma_i\sigma_{i+1}z_{i-1}.$$

Algorithm 3.9 implements the Subspace iteration method with Chebyshev acceleration.

Algorithm 3.9 Chebyshev Subspace Iteration

Given the $n \times m$ matrix $X_0 = [x_1, \ldots, x_m]$, iterate until an invariant subspace of $A \in \mathbb{C}^{n \times n}$ corresponding to the k smallest magnitude eigenvalues is found. The parameters c, a and e are defined by the ellipse E that encloses the unwanted part of the spectrum of A. λ_1 is an approximation of the smallest magnitude eigenvalue which is used only for a normalization purpose.

    Orthonormalize the initial block: $X = qr(X_0)$.
    for $i = 1, \ldots$ until convergence **do**
        $Z_0 = X$
        $\sigma_1 = \frac{e}{\lambda_1 - c}$
        $Z_1 = \frac{\sigma_1}{e}(A - cI)X$
        for i=2,...,k **do**
            $\sigma_i = \frac{1}{2/\sigma_1 - \sigma_{i-1}}$
            $Z_i = 2\frac{\sigma_i}{e}(A - cI)Z_{i-1} - \sigma_{i-1}\sigma_i Z_{i-2}$
        end for
        $\hat{X} \leftarrow Z_k$
        Orthonormalization of $\hat{X}$: $X = qr(\hat{X})$.
        Form the Rayleigh quotient $B = X^H A X$ and compute its eigenvectors $V = [v_1, \ldots, v_m]$.

        Update X with the Ritz vectors: $X \leftarrow XV$.
        Test for convergence.
    end for

3.5   The Jacobi-Davidson method

The Jacobi-Davidson method is probably the main alternative to Krylov-based methods for the solution of very large eigenproblems. Its origin can be found in the Davidson's algorithm [87] for the computation of a few eigenvalues of symmetric matrices. In 1990 Olsen et al. [106] proposed a new algorithm that can be seen as the Davidson's method with an approximate Newton correction. The final Jacobi-Davidson algorithm presented here was first proposed by Sleijpen, van der Vorst and their colleagues in 1996 [150] and further developed in [44, 149, 151] for harmonic Ritz vectors and generalized eigenvalue problems. They derived it by considering an algorithm of Jacobi [59]. Since then, it has been successfully used for many different applications. The developments presented here are taken from [156], where more details can be found.

3.5.1   Approximate Newton methods for eigenproblems

The Jacobi-Davidson can be seen as a Newton method for the solution of eigenproblems. In order to clarify this link with the Newton method, let us assume that (μ, z) is an approximate eigenpair of the matrix A. The objective is then to determine corrections η and v so that $(\mu + \eta, z + v)$ is a better approximation to the actual eigenpair (λ, u)

$$(A - \lambda I)u = 0.$$

For a reason elucidated later in Sec. 3.5.2, the subsequent relations are written in terms of an approximation $\tilde{A} = A + E$, where E is small, instead of the actual matrix A. If $(\mu + \hat{\eta}, z + \hat{v})$ is an exact eigenpair of A, then

$$[(\tilde{A} - E) - (\mu + \hat{\eta})](z + \hat{v}) = 0.$$

Developing products and dropping the second order terms ($E\hat{v}$ and $\hat{\eta}\hat{v}$), it can be written as

$$(\tilde{A} - \mu I)\hat{v} - \hat{\eta}z \cong -(A - \mu I)z.$$

Hence, approximate corrections η and v are defined as the solutions of the equation

$$(\tilde{A} - \mu I)v - \eta z = -(A - \mu I)z \equiv -r.$$

This equation offers only n relations, whereas the number of unknowns are $n + 1$ (the n components of v and the scalar η). In order to close the problem, the additional condition

$$\omega^H v = 0,$$

where ω is a suitably chosen vector, is considered. In matrix notation, it reads as

$$\begin{pmatrix} \tilde{A} - \mu I & -z \\ \omega^H & 0 \end{pmatrix} \begin{pmatrix} v \\ \eta \end{pmatrix} = \begin{pmatrix} -r \\ 0 \end{pmatrix},$$

which can be recast as the following triangular system:

$$\begin{pmatrix} \tilde{A} - \mu I & -z \\ 0 & \omega^H(\tilde{A} - \mu I)^{-1}z \end{pmatrix} \begin{pmatrix} v \\ \eta \end{pmatrix} = \begin{pmatrix} -r \\ \omega^H(\tilde{A} - \mu I)^{-1}r \end{pmatrix}.$$

Hence, we obtain the *approximate Newton correction formula*:

$$v = -(\tilde{A} - \mu I)^{-1}(r - \eta z), \quad \text{where} \quad \eta = \frac{\omega^H(\tilde{A} - \mu I)^{-1}r}{\omega^H(\tilde{A} - \mu I)^{-1}z}. \tag{3.23}$$

As shown later, ω is chosen as z in the Jacobi-Davidson method. In this case, Eq. (3.23) becomes

$$v = -(\tilde{A} - \mu I)^{-1}(r - \eta z), \quad \text{where} \quad \eta = \frac{z^H(\tilde{A} - \mu I)^{-1}r}{z^H(\tilde{A} - \mu I)^{-1}z}. \tag{3.24}$$

This solution was proposed by Olsen et al. [106] and it is sometimes known as Olsen's method.

Let us consider now for a moment, the implications of working with the exact matrix A. In this case, $\tilde{A} = A$ and the equation for the *exact corrections* $\hat{\eta}$ and $\hat{v}$ is

$$(A - \mu I)\hat{v} - \hat{\eta}z = -(Az - \mu I)z \equiv -r.$$

Again, the additional condition $\omega^H \hat{v} = 0$, being ω a suitably chosen vector, is considered to close the problem. Eq. (3.24) becomes

$$\hat{v} = -(A - \mu I)^{-1}(r - \hat{\eta}z), \quad \text{where} \quad \hat{\eta} = \frac{\omega^H(A - \mu I)^{-1}r}{\omega^H(A - \mu I)^{-1}z}. \tag{3.25}$$

Eq. (3.25) is called the *Newton correction formula*. It implies that, starting from an approximate eigenpair (μ, z), if Eq. (3.25) can be solved exactly, then the exact eigensolution $(\mu + \hat{\eta}, z + \hat{v})$ is found. Note that the cost of the exact solution is thus solving 2 linear systems, which can be prohibitive for very large problems.

At this point, the link with the Newton method can be shown easily considering one step of Newton's method for solving following the nonlinear system of equations

$$\begin{cases} (A - \lambda I)u &= 0 \\ \frac{1}{2}u^T u - 1 &= 0 \end{cases}.$$

If an approximation (μ, z) is available, such that

$$\begin{cases} (A - \mu I)z &= r \\ \frac{1}{2}z^T z - 1 &= 0 \end{cases},$$

then one step of the Newton's method is given by

$$\begin{pmatrix} z_{new} \\ \mu_{new} \end{pmatrix} = \begin{pmatrix} z \\ \mu \end{pmatrix} - \begin{pmatrix} (A - \mu I) & -z \\ z^T & 0 \end{pmatrix}^{-1} \begin{pmatrix} r \\ 0 \end{pmatrix}.$$

Finally if $\tilde{A}$ is put in the place of A and $z_{new} = z + v$ and $\mu_{new} = \mu + \eta$, then Eq. (3.24) is retrieved, showing the equivalence between the Olsen's method and using an approximate Newton step.

3.5.2 The correction equation

Now the concern is about the correction equation and its solution. The first thing to do is find an equivalent formula to Eq. (3.23) involving only v, which is of theoretical and practical use. In order to derivate it, Eq. (3.23) is written in the form

$$(\tilde{A} - \mu I)v = -r + \eta z. \tag{3.26}$$

Oblique projectors

In order to get rid of η, oblique projectors can be used. An oblique projector

$$P_{z,r_{\perp}} = I - \frac{z r_{\perp}^H}{r_{\perp}^H z}$$

applied to a vector u, projects it onto the orthogonal complement of $r_{\perp}$ along z. In particular, $P_{z,r_{\perp}} z = 0$ and $P_{z,r_{\perp}} r = r$. Thus, If we multiply Eq. (3.26) on the left by $P_{z,r_{\perp}}$ we obtain

$$P_{z,r_{\perp}}(\tilde{A} - \mu I)v = -r. \tag{3.27}$$

This equation can be viewed as a singular system of equations which has infinitely many solutions. More particularly, any solution v satisfying the relation

$$(\tilde{A} - \mu I)v = -r + \eta z \quad \text{for} \quad \eta \in \mathbb{C} \tag{3.28}$$

is solution of the system (3.27), as can be verified multiplying (3.28) by $P_{z,r_\perp}$. We have ignored so far the constraint $\omega^H v = 0$. This condition can be taken into account if we introduce the projector

$$P_{z,\omega} = I - \frac{z\omega^H}{\omega^H z}.$$

Then, the constraint $v \perp \omega$ can be replaced by the relation $P_{z,\omega} v = v$. Hence, Eq. (3.27) can be replaced by

$$P_{z,r_\perp}(\tilde{A} - \mu I)P_{z,\omega} v = -r, \qquad v \perp \omega. \tag{3.29}$$

In terms of solutions of the system of equations, this relation involving both projectors can be viewed in the following way: among all the solutions of the system (3.27), the unique solution that is orthogonal to ω is given by (3.29) and it is the unique solution $v = P_{z,\omega} v$. Eq. (3.29) is called the *approximate Newton correction equation* and it characterizes the vector v [156, p. 404].

Orthogonal projectors

The previous relations involve oblique projectors, which can be arbitrarily large and can show an undesirable numerical behavior in finite precision on a computer. So it would be desirable to replace the projections $P_{z,r_\perp}$ and $P_{z,\omega}$ by a single orthogonal projection. Concerning $P_{z,\omega}$, a simple geometrical picture shows that it seems natural to take $\omega = z$. Indeed, for if $v \perp z$ and v is small, then $\|v\|_2$ is very close to the minimum distance between z and $\text{span}(z + v)$. In other words, v is close to the smallest possible correction. Taking $\omega = z$, the oblique projector $P_{z,\omega}$ becomes the orthogonal projector

$$P_\perp = I - \frac{zz^H}{z^H z}.$$

On the other hand, $P_{z,r_\perp}$ can be taken equal to $P_\perp$ only if $z \perp r$. Theorem 3.7, which is the single vector version which Theorem 3.2 is based on (see proof in [156, page 63]), shows that if μ is taken as the Rayleigh quotient

$$\mu = \frac{z^H A z}{z^H z},$$

then z is, indeed, orthogonal to r.

Theorem 3.7 *Let $z \neq 0$ and for any μ set $r_\mu = Az - \mu z$. Then $\|r_\mu\|_2$ is minimized when*

$$\mu = \frac{z^H A z}{z^H z}.$$

In this case $r_\mu \perp z$.

Therefore, using orthogonal projectors, the (approximate) correction equation becomes

$$P_\perp(\tilde{A} - \mu I)P_\perp v = -r, \qquad v \perp z.$$

All the facts exposed so far about the correction equation are summarized by the following theorem [156, page 404].

Theorem 3.8 *Let (μ, z) be an approximate normalized eigenpair of A where*

$$\mu = z^H A z$$

and let

$$r = Az - \mu z.$$

Let

$$\tilde{A} = A + E$$

and assume that $(\tilde{A} - \mu I)$ is nonsingular. Then the Newton-based correction v that is orthogonal to z is given by the correction formula

$$v = -(\tilde{A} - \mu I)^{-1}(r - \mu z), \quad where \quad \eta = -\frac{z^H(\tilde{A} - \mu I)^{-1}r}{z^H(\tilde{A} - \mu I)^{-1}z}. \tag{3.30}$$

Equivalently, v is the unique solution of the correction equation

$$(I - zz^H)(\tilde{A} - \mu I)(I - zz^H)v = -r, \quad v \perp z. \tag{3.31}$$

In Theorem 3.8, the vector v is called the *orthogonal (approximate Newton) correction*, equation (3.30) is the *orthogonal correction formula* and equation (3.31) is the *orthogonal correction equation*. From now on, only orthogonal correction will be considered, dropping the qualifier "orthogonal". When dealing with $\tilde{A} = A$ "approximate" does not apply.

In the following we explain the reason why $\tilde{A} = A + E$ is considered instead of working directly with A. Note that if $\tilde{A}$ is taken equal to A the method would converge quadratically. It is possible to cite three situations in which it is desirable to take $\tilde{A} \neq A$:

- Natural approximations: This case arises when A can be written as $A = \tilde{A} - E$ and $\tilde{A}$ is easier to invert than A (in the sense of being easy to solve system involving $(\tilde{A} - \mu_k I)$), being E small. For example, if A is diagonally dominant, then it can be split as $A = D - E$, which allows to implement the approximate Newton method solving only diagonal systems. This situation is closely related to the Jacobi's method [59].

- Constant shift approximations: At each iteration of the Newton method, a system involving the matrix $(A - \mu_k I)$ must be solved. Assuming that is possible to obtain a matrix factorization, since μ_k changes at every iteration, it would be necessary to obtain a new factorization for each new value of μ_k. This can be avoided if the matrix $(A - \tau I)$ is considered instead, where τ is the center of a focal region containing the eigenvalues we are interested in. If

$$\tilde{A} = A + E_k, \quad where \quad E_k = (\mu_k - \tau)I, \quad then \quad \tilde{A} - \mu_k I = A - \tau I.$$

In this case the remainder E_k varies at each iteration.

- Inexact solution: When dealing with large general matrices, it is often impossible to solve the correction equation directly, and the use of iterative linear solvers is the

only alternative. In general, we will stop the iterative solver (referred to as the inner iterations) when the residual

$$s = -r - (I - zz^H)(A - \mu I)(I - zz^H)v \tag{3.32}$$

is small enough. Quantifying the effect of the linear solution accuracy (inner iteration) on the convergence of the approximate Newton method (the outer iteration) is a capital issue in the analysis of the Jacobi-Davidson method. Using the backward error theorem (Theorem 3.9) is is possible to relate s and E, showing that the error associated with the inexact solution of the correction equation can be "absorbed" naturally by the perturbation E.

Theorem 3.9 *Let* $r = Au - \mu u$. *Then there is a matrix*

$$E = \frac{ru^H}{\|u\|_2^2}$$

such that

$$\frac{\|E\|_p}{\|A\|_p} = \frac{\|r\|_2}{\|A\|_p \|u\|_2}, \quad p = 2, F,$$

and

$$(A - E)u = \mu u.$$

Therefore, from Theorem 3.9, there is a matrix

$$E = -\frac{sv^H}{\|v\|_2^2}$$

such that

$$[(I - zz^H)(A - \mu I)(I - zz^H) + E]v = -r. \tag{3.33}$$

The last step is to show that E can be moved inside the brackets with A. First, since $(I - zz^H)r = r$ and $P_\perp^2 = P_\perp$, from (3.32) it follows that $(I - zz^H)s = s$. Moreover, the iterative method should produce a solution v orthogonal to z and then $(I - zz^H)v = v$, so that

$$(I - zz^H)(A + E - \mu I)(I - zz^H)v = -r.$$

Therefore, terminating the inner iteration with a residual s is equivalent to perform the outer iteration with an approximate $\tilde{A}$ for which $\|E\|_2 = \|s\|_2$. More details about convergence of the method can be found in [156, p. 406-410]

Concerning iterative linear solvers for the solution of the correction equation, the ones based on Krylov subspaces are the best suited to easily ensure that the computed solution v is orthogonal to z as is established in the following proposition.

Proposition 3.10 *For the sake of simplicity, let us denote* $B = (I - zz^H)(A - \mu I)(I - zz^H)$ *the matrix associated with the correction equation. Because* $Bz = 0$ *and so* $B^H z = 0$, *starting from an initial guess* $v_0 = 0$ *using a Krylov linear solver, ensures that the solution* v *of the system* $Bv = -r$ *is always orthogonal to* z.

Proof Starting from an initial guess v_0, any Krylov linear solver searches for a solution in the space $v_0 + span(w_0, Bw_0, \ldots, B^k w_0)$ where $w_0 = -r - Bv_0$. Now, $Bz = 0$ because $(I - zz^H)z = 0$, and taking into account that $(I - zz^H)^H = (I - zz^H)$, it follows that $B^H z = 0$ as well. Thus, if $v_0 = 0$, since $z^H r = 0$ and z is in the null space of B^H, each direction of the Krylov space $span(r, Br, \ldots, B^k r)$ is orthogonal to z, as it is shown:

1. $v_0 = 0$ so that $\omega_0 = -r$. Then, the first direction of the Krylov space $\omega_0 \perp z$;

2. and for any $\ell \leq k$, $z^H B^\ell r = (B^H z)^H B^{\ell-1} r = 0$, because $B^H z = 0$.

Consequently any solution v in that space will be orthogonal to z. ∎

In this work we are concerned by the constant shift approximation and the inexact solution of the correction equation cases. Concerning the constant shift approximation, it can be interesting to solve the correction equation for $(A - \tau I)$ rather than for $(A - \mu_k I)$ in order to reach a faster convergence: at the beginning of the process, μ_k will be in general a very poor approximation and using the target τ would lead to a faster convergence. On the other hand, due to the size of the problem, an iterative solver has to be use to obtain an approximate solution of the correction equation.

3.5.3 The Jacobi-Davidson algorithm

The Jacobi-Davidson method is the result of combining the approximate Newton method described in the former section with a Rayleigh-Ritz approximation for the computation of the approximate eigensolutions. The first advantage of combining both techniques is that the Rayleigh-Ritz procedure can focus the Newton iteration on the region that we are interested in. Other advantage is that, as shown previously for the Power method, while the algorithm tries to converge a given eigenpair, it produces information that later speeds up convergence to other eigenpairs in the area [156]. This is because it does not only focus in a single vector, but it works with subspaces that contain information about other eigensolutions within a region. Concerning the first point, if the Newton process does not start close enough to an eigenpair, there is no real control over what eigenvalue the method will converge to. On the other hand, using the Newton method alone, means that the correction vector v_k is applied once to the current approximate eigenvector z_k and then is discarded. This is equivalent to say that, z_{k+1} is chosen (up to normalization) as

$$z_{k+1} = z_0 + v_0 + v_1 + \cdots + v_k. \tag{3.34}$$

Now, if every new correction vector is saved, then it is possible that another vector in the subspace spanned by $(z_0, v_0, v_1, \ldots, v_k)$ provides a better approximate eigenvector than (3.34). In particular, the chosen linear combination is that given by the Rayleigh-Ritz procedure:

$$V_k \text{ is an orthonormal basis of } span(z_0, v_0, v_1, \ldots, v_k).$$

Then form the Rayleigh quotient

$$C_k = V_k^H A V_k.$$

The eigenpairs of C_k are computed, and the closest one (μ_k, p_k) to a given target τ is selected. Finally, the new approximate eigenvector of A is given by

$$z_{k+1} = V_k p_k. \tag{3.35}$$

Hence, the Ritz pair (μ_k, z_{k+1}) is the approximation to the eigenpairs given by the Rayleigh-Ritz procedure.

Algorithm 3.10 The basic Jacobi-Davidson algorithm

Given a normalized vector z, the algorithm attempts to compute an eigenpair whose eigenvalue is near a focal point τ.

1: Set $V_1 = [z]$
2: **for** $k = 1, \ldots, k_{max}$ **do**
3:     Using V_k compute a normalized Ritz pair (μ_k, z_k) such that μ is the closest to τ
4:     $r_k = Az_k - \mu_k z_k$
5:     **if** r_k is sufficiently small **then**
6:         return (μ_k, z_k)
7:     **end if**
8:     Choose a shift σ near μ_k or τ
9:     Solve the linear system

$$(I - z_k z_k^H)(\tilde{A} - \sigma I)(I - z_k z_k^H)v = -r_k, \text{ so that } v \perp z_k$$

10:     Compute w by orthonormalizing v against V_k
11:     Set $V_{k+1} = [V_k, w]$
12: **end for**

Algorithm 3.10 implements this procedure, a basic Jacobi-Davidson method. In the following, this algorithm is enhanced to be able of computing a set of eigenpairs in a region of interest, taking into account aspects such as deflation and restarting.

Deflation

Once the method has converged to one eigenpair and starts seeking for a new one, a strategy avoiding the convergence to a vector that has already been found is needed. This can be done by constraining the iterations to proceed outside the space spanned by the already converged eigenvectors, for instance in spaces orthogonal to the found invariant subspace. This is possible by considering the Schur vectors associated with the converged eigenvalues. If $U = [u_1, u_2, \ldots, u_p]$ is the set of Schur vectors associated with the converged invariant subspace, then the other Schur vectors lie in the orthogonal complement of span(U). Consider an existing partial Schur decomposition

$$AU = UT, \tag{3.36}$$

where T is an $p \times p$ upper triangular matrix. It is possible to extend Eq. (3.36) by mimicking the reduction to Schur form. Let $(U \ \ U_\perp)$ be unitary, and write

$$\begin{pmatrix} U^H \\ U_\perp^H \end{pmatrix} A \begin{pmatrix} U & U_\perp \end{pmatrix} = \begin{pmatrix} T & H \\ 0 & B \end{pmatrix}.$$

Now suppose that (μ, z) is a normalized eigenpair of B, and let $(z \ \ Z_\perp)$ be unitary. Then

$$\begin{pmatrix} z^H \\ Z_\perp^H \end{pmatrix} B \begin{pmatrix} z & Z_\perp \end{pmatrix} = \begin{pmatrix} \mu & g^H \\ 0 & C \end{pmatrix}.$$

is upper triangular form and it is possible to write

$$\begin{pmatrix} U^H \\ z^H U_\perp^H \\ Z_\perp^H U_\perp^H \end{pmatrix} A \begin{pmatrix} U & U_\perp z & U_\perp Z_\perp \end{pmatrix} = \begin{pmatrix} T & Hz & HZ_\perp \\ 0 & \mu & g^H \\ 0 & 0 & C \end{pmatrix}.$$

Hence,

$$A \begin{pmatrix} U & U_\perp z \end{pmatrix} = \begin{pmatrix} U & U_\perp z \end{pmatrix} \begin{pmatrix} T & Hz \\ 0 & \mu \end{pmatrix} \tag{3.37}$$

is a partial Schur decomposition of A of order one higher than the one given in Eq. (3.36). Because it requires the construction of $U_\perp$, Eq. (3.37) is not well adapted for large sparse problems, which are the interest of this work. However, it is possible to recast the algorithm in terms of the matrix A. Let

$$P_\perp = U_\perp U_\perp^H = I - UU^H \equiv I - P$$

be the orthogonal projector onto the column space of $U_\perp$. Then, since $B = U_\perp^H A U_\perp$,

$$A_\perp = P_\perp A P_\perp = U_\perp U_\perp^H A U_\perp U_\perp^H = U_\perp B U_\perp^H.$$

If (μ, z) is an eigenpair of B such, and let $y = U_\perp z$, then (μ, y) satisfies

$$\begin{aligned} &1. \quad A_\perp y = \mu y, \\ &2. \quad y \perp U. \end{aligned} \tag{3.38}$$

And vice-versa, if y satisfies (3.38) and let $z = U_\perp^H y$, then $Bz = \mu z$. Therefore, there is a one-to-one correspondence between the eigenvectors of $A_\perp$ lying in $\mathcal{R}(U_\perp)$ and the eigenvectors of B, what implies that the knowledge of the eigenvector y is all that is necessary to extend the partial Schur decomposition. Thus, from (3.37), the extended Schur decomposition is given by

$$A \begin{pmatrix} U & y \end{pmatrix} = \begin{pmatrix} U & y \end{pmatrix} \begin{pmatrix} T & t \\ 0 & \mu \end{pmatrix}, \quad \text{where } t = U^H A y. \tag{3.39}$$

Now, consider the residual

$$r = A_\perp z - \mu z.$$

It must be tested if it is small enough to accept the associated pair as an eigenpair of A. Taking a look to Eq. (3.39) (and putting z instead of y) what is actually wanted is to get a satisfactorily small residual

$$s = Az - Ut - \mu z.$$

In [156, page 415] is shown that $\|r\|_2 = \|s\|_2$, so the convergence can be based on r. In practice, the residual r is not computed directly. First $Az - \mu z$ is computed and then the resulting residual is orthogonalized against U.

Suppose that we have the Schur vectors U and the matrix V of orthonormalized corrections which is assumed to be orthogonal to $\mathcal{R}(U)$, and the new correction vector v. Then the Jacobi-Davidson algorithm can be used in order to extend the partial Schur decomposition, following these steps:

1. The new correction vector v is orthogonalized against V and incorporated into it. A priori it will be already orthogonal to U, but if during the orthogonalization process against V there is cancellation, it could be no longer orthogonal to U. Therefore, orthogonalization of v against U is required as well.

2. Extend the Rayleigh quotient $B = V_\perp^H A_\perp V$. Observe that since $V \perp U$, it is possible to compute simply $B = V^H AV$.

3. Compute the Ritz pairs of B and choose the closest one to the target τ, (μ, z).

4. Test the convergence of the new Ritz pair using $r = A_\perp z - \mu z$.

5. If the residual is not small enough, then solve the correction equation

   $$(I - zz^H)(A - \kappa I)(I - zz^H)v = -r$$

   in order to obtain the new correction v.

6. Repeat the process from step 1 until the convergence of the Ritz pair (μ, z) is achieved.

This process builds incrementally a partial Schur decomposition where each new Schur direction is computed using the Jacobi-Davidson method in spaces orthogonal to the already computed invariant subspace associated with the Schur vectors. Once a subspace of the desired dimension has been computed, the eigenvector of A are recovered from the computed Schur vectors. Note that in general, this process can not be carried out indefinitely until all the wanted eigenpairs have been converged, since for machine memory reasons, the size of the subspace V that one can store is limited. A restart procedure is thus necessary.

Restarting

In practice, basis of the subspaces V and $W = AV$ have to be stored. The affordable corresponding dimensions will be constrained by the storage capacity of the computer. As it occurs with the IRA and the Krylov-Schur methods, to overcome this constraint, a restart mechanism is required. It must allow to shrink the most valuable spectral information contained in V in a lower dimension space that before it is extended again. The advantage

of the Jacobi-Davidson method versus both previously mentioned ones is that it does not require to preserve neither any special relation in the new basis nor any particular structure in the new Rayleigh quotient, what makes the task easier. If m is the maximum dimension of the basis V_m that can be afforded, once this dimension is reached the process has to be restarted from a basis V_ℓ of size $\ell < m$ (typically ℓ is chosen at least equal to the number of desired eigenpairs) containing as much useful information as possible. The following procedure allows to restart the iteration with the basis V_ℓ, whose Ritz subspace corresponds to the ℓ Ritz values of $C_m = V_m^H A V_m$ that are closest to the chosen focal point τ.

1. Compute the Schur decomposition $C_m = QTQ^H$, where the diagonal elements of T are ordered so that $|t_{ii} - \tau| \leq |t_{i+1,i+1} - \tau|$.

2. $V_\ell = V_m Q(:, 1 : \ell)$

3. $W_\ell = W_m Q(:, 1 : \ell)$

4. $C_\ell = T(1 : \ell, 1 : \ell)$

The implementation of these aspects (deflation and restart) within the Jacobi-Davidson procedure corresponds to the *Jacobi-Davidson style QR algorithm* presented in [44], where the authors extend the method to the solution of generalized eigenproblems and the computation of Harmonic Ritz pairs as well.

3.5.4 JDQR: a practical Jacobi-Davidson algorithm implementation

The Jacobi-Davidson algorithm implemented in AVSP (see Algorithm 3.11) is similar to the implementation of the method given in [44], referred to by the authors as JDQR. Algorithm 3.11 extends a partial Schur decomposition of the matrix A using the Jacobi-Davidson method. It includes a tracking strategy that produces a smoother convergence: when the current approximation (μ, z) has an associated residual which is larger than a given threshold ϵ_{thres} (which is chosen larger than the one used to decided the convergence), the Ritz values are sorted in increasing distance from a target value τ_0. If at the iteration k, $\|r\| < \epsilon_{thres}$, then the target for the next iteration is set to $\tau = \mu_k$ instead of τ_0. When the tracked eigenpair is converged, the target is set again to be τ_0 before converging the next one. Algorithm 3.11 is conceived to be used by a higher level routine that decides the number of wanted eigenpairs nev, the focal point τ, the maximum and the minimum size of the basis V, etc.

Inputs for the algorithm are the existing converged Schur vectors U_{conv} of A, the current size k of the basis V_k and $W_k = AV_k$ and the Rayleigh quotient C_k, the focal point τ_0, the threshold value for tracking ϵ_{thres}, the maximum size m affordable for V and the size of the restarted basis ℓ and the maximum number of restarted allowed. Outputs are μ, u and t, such that

$$A(U\ u) = (U\ u) \begin{pmatrix} T & t \\ 0 & \mu \end{pmatrix}$$

Algorithm 3.11

$[\mu, u, t]$=JDQR($U(:,1{:}nconv)$,$V(:,1{:}k)$,$W(:,1{:}k)$,C(1:k,1:k),τ_0,ϵ_{thres},ℓ,m,$maxiter$)

    Set $iter = 0$; $k_{init} = k$; $\tau = \tau_0$; $tr = 0$
    while iter<maxiter **do**
      $iter = iter + 1$
      for $k = k_{init}, \ldots, m$ **do**
        [Q,T]=SortSchur(C(1:k,1:k),τ,k)
        Choose $\mu = T(1, 1)$ and $p = Q(:, 1)$, the Ritz pair closest to τ
        Approximate eigenvector of A: $z = V(:, 1 : k)p$, and Az: $y = W(:, 1 : k)p$
        Compute the residual $r = y - \mu z$, orthogonalize it against $U(:,1{:}nconv)$ and compute
        its norm: $rnorm$=norm(r)
        if $tr = 1$ and $rnorm_{bef} < rnorm$ **then**
          $\tau = \mu$
        else if $tr = 0$ and $rnorm < \epsilon_{thres}$ **then**
          $\tau = \mu$, $tr = 1$
        end if
        Convergence test:
        if $rnorm$ is small enough **then**
          $nconv = nconv + 1$
          Prepare outputs and deflate: $u = z$; $t = U^H y$; $V = V(:, 1 : k)Q(:, 2 : k)$;
          $W = W(:, 1 : k)Q(:, 2 : k)$; $C = T(2 : k, 2 : k)$

          return
        else if $k = m$ **then**
          Restart:
          $V(:, 1 : \ell) = V(:, 1 : m)Q(:, 1 : \ell)$;
          $W(:, 1 : \ell) = W(:, 1 : m)Q(:, 1 : \ell)$;
          $C(1 : \ell, 1 : \ell) = T(1 : \ell, 1 : \ell)$;
          $k_{init} = \ell$
        end if
        No convergence reached and $k < m$. Solve the correction equation:

$$(I - zz^H)(A_\perp - \tau I)(I - zz^H)v = -r$$

        Orthogonalize v against $V(:, 1 : k)$ and $U(:, 1 : nconv)$
        Extend the Rayleigh basis and the Rayleigh quotient:
        $V(:, k + 1) = v$, $W(:, k + 1) = Av$, $C(k + 1,1{:}k)$=$v^H W(:,1{:}k)$,
        $C(1{:}k,k + 1)$=$V(:,1{:}k)^H W(:,k + 1)$, $C(k + 1,k + 1)$=$v^H W(:,k + 1)$
        $rnorm_{bef} = rnorm$
      end for
    end while

is a partial Schur decomposition of one higher dimension.

The higher level routine must furnish Algorithm 3.11 with the necessary inputs. If the process starts from the beginning, then there are two situations. The first one corresponds to the case when the computation starts from a single random vector. Then the higher level routine computes an Arnoldi decomposition of size ℓ

$$AV_\ell = V_\ell H_\ell + \beta v_{\ell+1} e_\ell^T,$$

and the Jacobi-Davidson starts with $U = [\ ]$, $V = V_\ell$, $W = AV$ and $C = H_\ell$. The second case is when the process starts from a given number k of initial vectors. The initial block of vectors is then orthonormalized to obtain V_k and the process can start as indicated previously, with $U = [\ ]$, $V = V_k$, $W = AV_k$ and $C = V_k^H A V_k^H = V_k^H W$.

Once the partial Schur decomposition

$$AU_{nev} = U_{nev} T_{nev}$$

of the matrix A of size nev equal to the number of desired eigenpairs has been obtained using repeatedly Algorithm 3.11, the corresponding eigenvalues and eigenvectors are obtained using the Rayleigh-Ritz procedure.

3.6 Stopping criterion for convergence

All the iterative methods need condition to decide when the process can be stopped when the quality of the approximation is satisfactory. The problem is that since the exact solution is unknown, one can not compare the current eigenvector approximation x_k with the actual solution x and stop when the angle $\phi(x_k, x)$ is small enough. An alternative is to compute the residual

$$r_k = Ax_k - \lambda_k x_k,$$

where λ_k is a suitable approximation of λ, and stop when $\|r_k\|$ is sufficiently small. But, how small? A criterion based on the backward error can offer an answer to this question. Assuming that $\|x_k\| = 1$, Theorem 3.9 establishes that the approximation (λ_k, x_k) is the exact solution of a perturbed problem $(A + E_k)$

$$(A + E_k)x_k = \lambda_k x_k,$$

with $\|E_k\|_2/\|A\|_2 = \|r_k\|_2/\|A\|_2$. Therefore the iterative method can be stopped when

$$\frac{\|Ax_k - \lambda_k x_k\|_2}{\|A\|_2} \le tol, \tag{3.40}$$

where tol is a level of accuracy that is considered as satisfactory for a given problem. In practice, computing $\|A\|_2$ is too expensive, so a cheaper lower bound is used, what is even more restrictive in terms of backward error than Eq. (3.40). Since $|\lambda_k| \le \|B_k\|_2 \le \|A\|_2$, where B_k is the corresponding Rayleigh quotient obtained by the iterative method, in this work an eigenpair is considered as converged when

$$\frac{\|Ax_k - \lambda_k x_k\|\|_2}{|\lambda_k|} \le tol,$$

what ensures a small backward error associated with the pair (λ_k, x_k). This stopping criterion is widely used in other libraries for the solution of large eigenproblems, such as ARPACK [75] or SLEPC[7].

In [77] a study about determining stopping criteria for general sparse matrices is carried out. More details about convergence can be found in [110] for symmetric matrices. The non-hermitian case is analyzed in [129, 156]. In [18] one can find information about defectiveness and non-normality.

---

[7]http://www.grycap.upv.es/slepc/

Chapter 4

Numerical aspects of the solution of the thermoacoustic nonlinear eigenproblem

Contents

As seen in Chapter 2, the solution of the Helmholtz equation

$$\frac{\partial^2 p_1}{\partial t^2} - \nabla \cdot c_0^2 \nabla p_1 = \Phi(p_1)$$

on unstructured meshes using a finite volume discretization leads to the nonlinear eigenproblem

$$\underbrace{\mathbf{A}\bar{p}}_{\nabla \cdot c_0^2 \nabla p_1} + \underbrace{\omega \mathbf{B}(\omega)\bar{p}}_{Complex\ B.C} + \underbrace{\omega^2 \bar{p}}_{\partial^2 p_1/\partial t^2} = \underbrace{\mathbf{C}(\omega)\bar{p}}_{\Phi(p_1)}. \tag{4.1}$$

Every nonlinear eigenpair $(\omega, \bar{p})$ of Eq. (4.1) represents an eigenfrequency and the structure of the corresponding acoustic mode, respectively. Because thermoacoustic instabilities arise at low frequencies, Eq. (4.1) must be solved in order to obtain a few *nev* smallest magnitude nonlinear eigenvalues and the associated eigenvectors. Since there are no eigensolvers for the solution of general nonlinear eigenproblems, the problem is linearized by fixing a value $\tilde{\omega}$ for the nonlinear eigenvalue ω, so that the nonlinear terms $\mathbf{C}(\omega)$ and $\omega \mathbf{B}(\omega)$ become constant. Then, the Eq. (4.1) can be written as

$$\mathbf{OP}(\tilde{\omega})\bar{p} = -\omega^2 \bar{p}, \tag{4.2}$$

where $\mathbf{OP}(\tilde{\omega}) = \mathbf{A} + \tilde{\omega}\mathbf{B}(\tilde{\omega}) - \mathbf{C}(\tilde{\omega})$. Eq. (4.2) is a linear eigenproblem that is solved using any of the available solvers in AVSP. Its solution is then used as a new linearization value $\tilde{\omega}$ to obtain a new linear eigenproblem. The process is repeated until the successive solutions of the sequence of linear eigenproblems converge to the sought nonlinear eigenvalue ω of Eq. (4.1). This procedure is referred to as fixed point iterative method.

Therefore, the nonlinear eigenproblem (4.1) is handled by solving a sequence of linear eigenproblems $\mathbf{OP}\bar{p} = -\omega^2 \bar{p}$. The algorithms for the solution of linear eigenproblems described in Chap. 3 are used in this chapter for solving $\mathbf{OP}\bar{p} = -\omega^2 \bar{p}$. The influence of their numerical parameters associated with each method is analyzed. Three test cases are used for this purpose, two of them small enough ($N \approx \mathcal{O}(10^3)$) so that computing the whole spectrum with MATLAB is possible. Although they are academic cases, they contain the main ingredients of more realistic problems, and particularly, the presence of the active flame taken into account through the combustion matrix $\mathbf{C}$. This means that the operator $\mathbf{OP}$ is a sparse complex non-symmetric matrix, for which computing a few smallest magnitude eigenpairs constitutes a challenging problem from a numerical point of view. Strategies for accelerating the fixed point method are also discussed: during the sequence of linear eigenproblems solved at each fixed point iteration, the solution of previously solved linear eigenproblems can be a good approximation of the solution of the next one. Being able to reuse this information can reduce significantly the computational cost of each fixed point iteration, and consequently the overall solution time.

The chapter is organized as follows: the test cases are described in sec. 4.1. In sec. 4.2, the different eigensolvers are studied and the influence of their numerical parameters is analyzed. Sec. 4.3 is dedicated to the solution of the nonlinear eigenproblem. The effect of the mesh quality on the eigensolver is treated in sec. 4.4. The parallel implementation of the algorithms is discussed in Sec. 4.5, before concluding with some general remarks in sec. 4.6.

4.1 Test cases description

The numerical experiments presented in this chapter are performed for three different academic configurations. Although their size and their geometry can differ from those of actual industrial problems, they contain all the essential ingredients that can pose a difficult problem from a mathematical point of view. This will allow to analyze the available methods and determine which are best suited to solve the eigenproblem obtained from the discretization of the Helmholtz equation described in Chapter 2.

4.1.1 Test case A

It consists in a 2D rectangle of dimensions $0.5 \times 0.05m$ with temperature jump and a flame placed at the middle (Fig. 4.1) of the tube. The mesh is composed by 1489 nodes and 2782 cells, refined at the flame zone (Fig. 4.2). Boundary conditions are $u' = 0$ for left, top and bottom sides and $p' = 0$ for the right side of the tube, which means that the term $\omega \mathbf{B}(\omega)$ is null. Tab. 4.1 contains the values of the physical quantities.
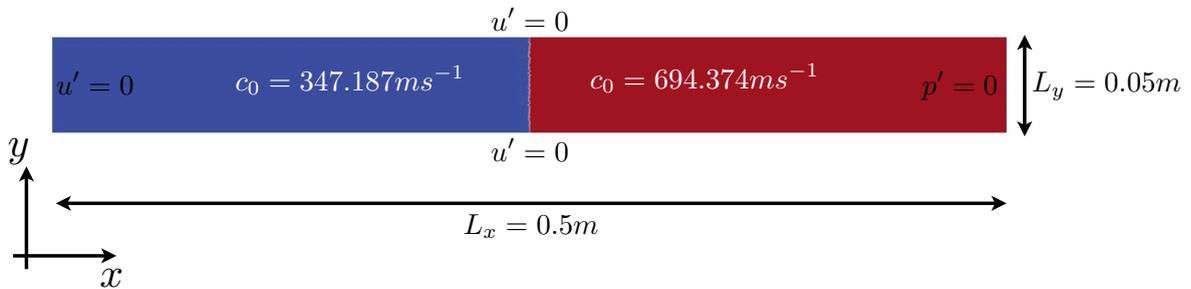
Figure 4.1: 2D rectangle with temperature jump.
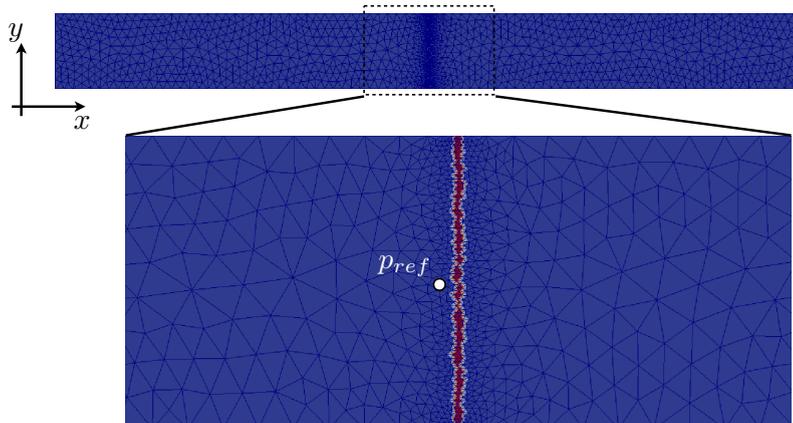
Figure 4.2: The mesh is refined in the flame zone. The reference point is placed right before the flame.

When the active flame is taken into account, the matrix $\mathbf{OP}(\omega) = \mathbf{A} - \mathbf{C}(\omega)$ has the structure shown in Fig. 4.3. Although the matrix $\mathbf{A}$ is real symmetric (up to a row scaling

Fresh gases	Hot gases
$\gamma = 1.4$	$\gamma = 1.4$
T = 300K	T=1200K
W = 0.02897 kg/mol	W = 0.02897 kg/mol

Table 4.1: Test case A: gas properties.

of its elements), the matrix **OP** is complex non-symmetric due to the combustion matrix **C**, which is complex non-symmetric.
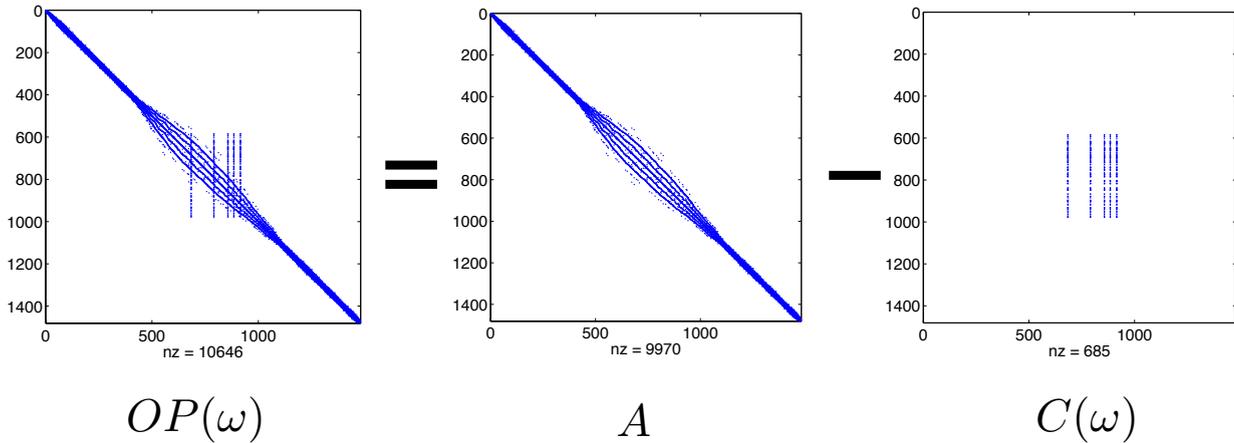
Figure 4.3: Portrait of the matrix **OP**, showing the structure of each one of the matrices **A** and **C**(ω) corresponding to the 2D tube.

The 10 smallest magnitude eigenfrequencies without active flame corresponding to the solution of the linear problem $\mathbf{A}\bar{p} = -\omega^2\bar{p}$ appear in Tab. 4.2 and the structures of the first 2 modes are shown in Fig. 4.4.

$Mode\ 1\ (272.3Hz)$ $Mode\ 2\ (694.3Hz)$
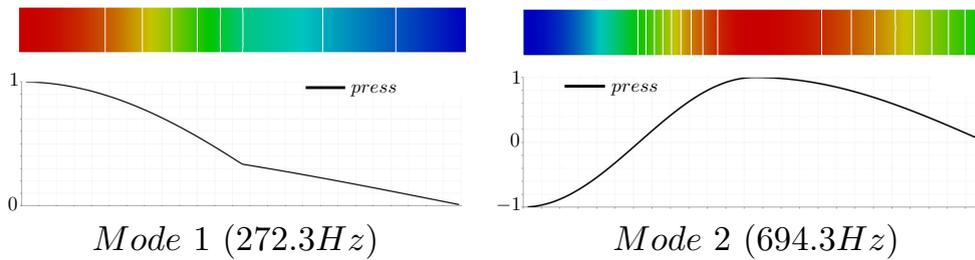
Figure 4.4: Structure of the first and second longitudinal modes of the 2D tube with temperature jump without active flame.

4.1.2 Test case B

This test case is an annular duct divided into 8 identical sectors, with a flame placed at the middle of each sector. The inner radius $R_{min} = 1.5\ m$ and the outer radius $R_{max} =$

	Frequencies (Hz)
ω_1	272.3
ω_2	694.3
ω_3	1117.0
ω_4	1160.8
ω_5	2080.8
ω_6	2503.1
ω_7	3043.6
ω_8	3461.7
ω_9	3470.4
ω_{10}	3600.0

Table 4.2: 10 smallest magnitude eigenfrequencies of the 2D tube with temperature jump without active flame ($\mathbf{C} = \mathbf{0}$).

1.7 m (Fig. 4.5). The mesh is composed by 5560 nodes and 22056 cells. All the boundary conditions corresponds to rigid acoustic walls ($u' = 0$), so that $\mathbf{B}$ is still zero. The properties of the gas are specified in Tab. 4.3.
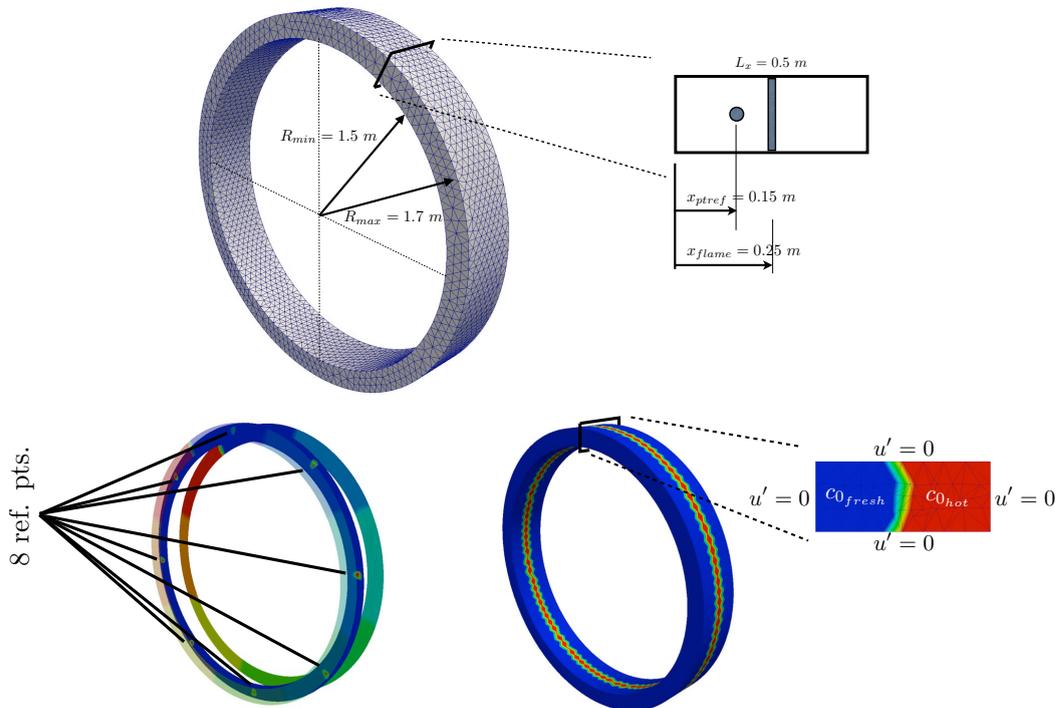
Figure 4.5: Annular duct with temperature jump and flame. Top: A view of the 5560 node mesh; the flame is placed at $x = 0.25m$ and the reference points at $x = 0.15m$. Bottom: the annular duct is divided into 8 sectors with the reference points located in each. The boundary conditions are $u' = 0$ for all patches.

Fresh gases	Hot gases
$\gamma = 1.4$	$\gamma = 1.4$
T = 504K	T= 2015K
W = 0.02897 kg/mol	W = 0.02897 kg/mol
$c_0 = 450 \ ms^{-1}$	$c_0 = 900 \ ms^{-1}$

Table 4.3: Test case B: gas properties.

The structure of the matrix $\mathbf{OP}(\omega) = \mathbf{A} - \mathbf{C}(\omega)$ corresponding to this case is displayed in Fig. 4.6. The combustion matrix $\mathbf{C}$ shows eight groups of non-null elements corresponding to each one of the eight sectors considered by the multi-burner combustion model introduced in Chapter 2.
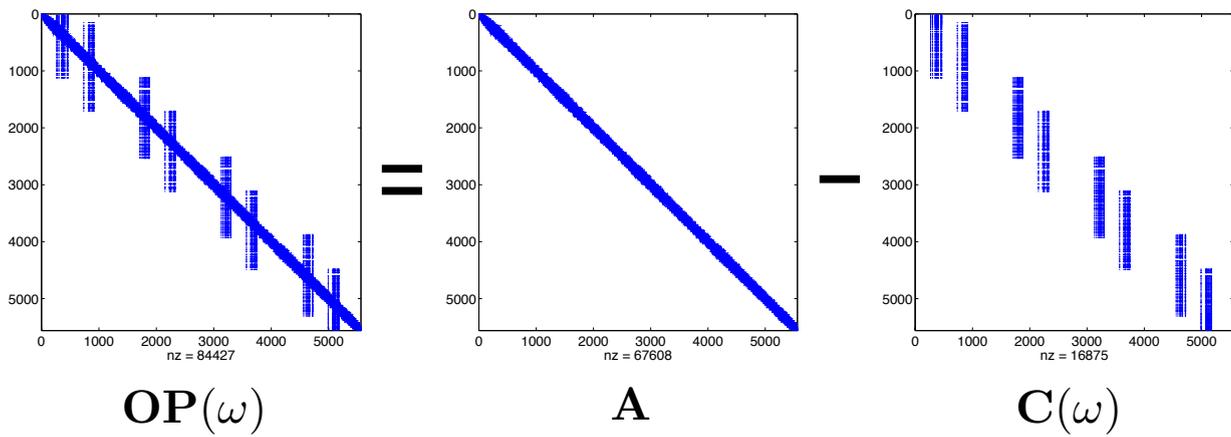

Figure 4.6: Test case B: structure of the matrix $\mathbf{OP}$, showing the structure of each one of the matrices $\mathbf{A}$ and $\mathbf{C}(\omega)$.

The first 10 smallest magnitude eigenfrequencies of test case B with temperature jump and without flame are shown in Tab. 4.4, while the structure of the first 2 modes are displayed in Fig. 4.7. The first eigenfrequency is null (rigid body mode) because $u' = 0$ is used as boundary condition for all the patches. The double frequencies correspond to azimuthal modes.

4.1.3 Test case C

This configuration is a simplified model of an annular combustor with six tubular burners. The properties of the fresh (in the burners) and hot (in the annular chamber) gases are the same as for case B (see Tab. 4.3). The flames are placed at each burner/chamber junction. The mesh is composed of 36510 cells and 173556 cells. Concerning boundary conditions, $p' = 0$ at the burners inlet and the rest of patches are rigid walls ($u' = 0$) (Fig. 4.8). This test case is considered because of its larger size. With respect to the previous cases (which are solved on one processor), the results presented in what follows concerning the test case

	Frequencies (Hz)
ω_1	0
ω_2	80.0
ω_3	80.0
ω_4	141.2
ω_5	141.2
ω_6	209.6
ω_7	209.6
ω_8	274.4
ω_9	276.5
ω_{10}	337.7

Table 4.4: Test case B: 10 smallest magnitude eigenfrequencies of the annular duct with temperature jump and no active flame ($\mathbf{C} = \mathbf{0}$).
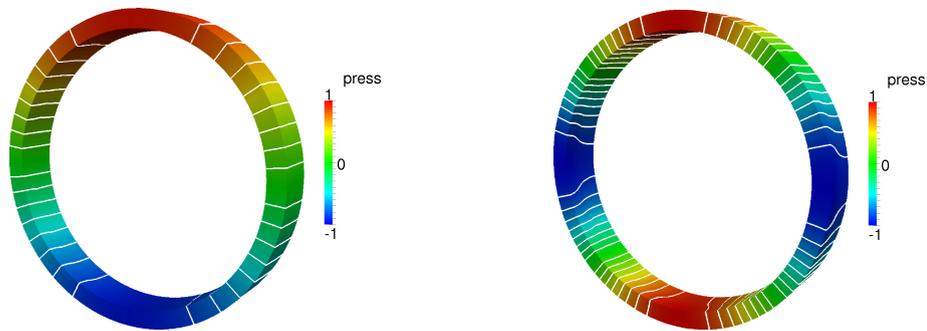
Figure 4.7: Structure of the first (80 Hz) and second (141.2 Hz) azimuthal modes of the annular duct with temperature jump without active flame ($\mathbf{C} = \mathbf{0}$).

C, have been obtained using many processors, showing that the algorithms implemented in AVSP have been implemented in a parallel computational context.
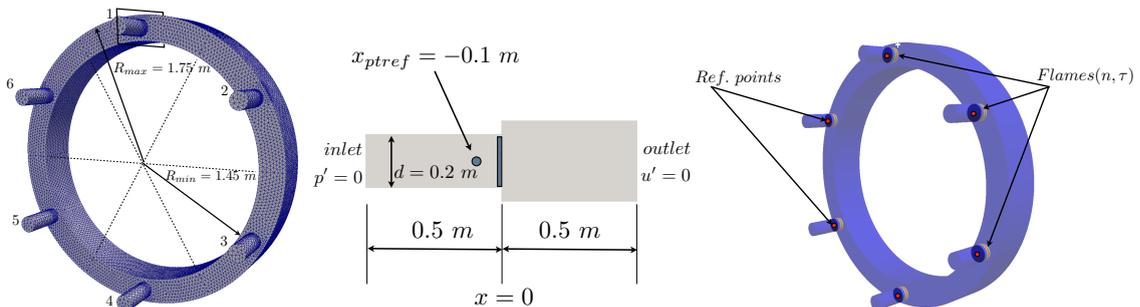
Figure 4.8: Test case C: simplified annular combustion chamber with 6 identical burners. The flames are places right at the interface between the tubes and the annular chamber at $x = 0m$. At the inlet of the tubes and the walls $u' = 0$ is imposed; $p' = 0$ is imposed at the outlet of the annular chamber.

The 10 smallest magnitude eigenfrequencies without active flame appear in Tab. 4.5 and the structure of the first 2 modes are displayed in Fig. 4.9.

	Frequencies (Hz)
ω_1	34.8
ω_2	95.4
ω_3	95.4
ω_4	180.9
ω_5	180.9
ω_6	266.2
ω_6	269.5
ω_6	353.4
ω_6	353.4
ω_6	422.9

Table 4.5: Test case C: 10 smallest magnitude eigenfrequencies obtained with temperature jump without active flame ($\mathbf{C} = \mathbf{0}$).
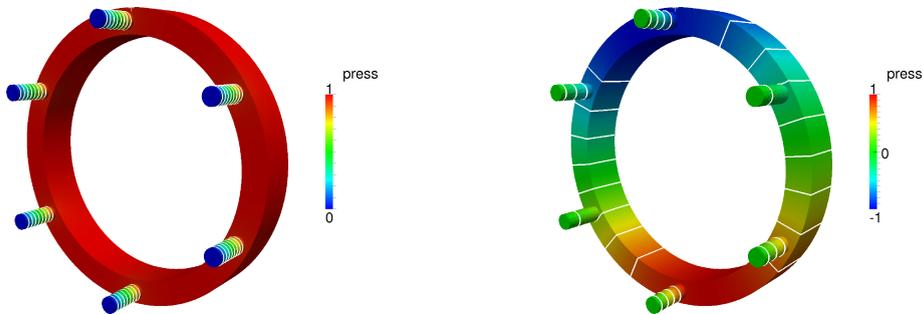
Figure 4.9: Test case C: structure of the first mode (34.8 Hz) which is the longitudinal mode of the burners and second mode (95.4 Hz) which is the first azimuthal mode of the chamber with temperature jump and no active flame ($\mathbf{C} = \mathbf{0}$).

4.2 Parametric study and comparison of eigensolvers

In this section the influence of the main numerical parameters of the different solvers implemented in AVSP is investigated. In order to analyze the numerical behavior of the different eigensolvers, the considered quantities are: computational time, number of matrix/vectors products (matvec) and number of iterations (implicit restarts or Jacobi-Davidson steps) needed for the computation of the desired eigenpairs.

4.2.1   Influence of convergence threshold *tol*

A given eigenpair (λ, x) is considered solution of $Ax = \lambda x$ when the associated normalized residual norm satisfies

$$\frac{\|Ax - \lambda x\|_2}{|\lambda|} \leq tol.$$

If the eigenvalues have to be computed more accurately, there is obviously a prize to pay: the computational cost increases in general when *tol* gets smaller. The chosen value for *tol* must be small enough to ensure an acceptable level of accuracy and reduce the chances of missing eigenvalues; but asking for a very high accuracy will just increase the computational cost unnecessarily.

The whole spectrum of the test case A without active flame is computed with the function *eig* of MATLAB. Then, using ARPACK, we ask for the 10 smallest magnitude (SM) eigenvalues, for different values of *tol*. In Tab. 4.6 appear the eigenfrequencies obtained in each case.

EIG (MATLAB)	ARPACK ($tol = 10^{-2}$)	ARPACK ($tol = 10^{-4}$)
272.25828	272.25820	272.25828
694.28538	694.28540	694.28538
1117.02961	1117.02961	1117.02961
1660.77236	1660.77237	1660.77236
2080.78000	2080.78002	2080.78000
2503.09511	2503.09487	2503.09510
3043.55136	3043.52788	3043.55136
3461.64601	3470.36046	3461.64872
3470.37628	3600.06698	3470.37629
3600.04314	3846.20832	3600.04314

Table 4.6: Test case A without active flame: smallest eigenfrequencies (Hz) obtained with MATLAB (considered as the reference) and with ARPACK for different values of *tol*.

This example illustrates what happens if the value of *tol* is not small enough: the eigensolver can skip one or more eigenvalues if they are very close to each other. For $tol = 10^{-2}$ ARPACK finds $\omega_8 = 3470.36 Hz$ and then $\omega_{10} = 3600.07 Hz$, skipping $\omega_9 = 3470.38 Hz$. A tolerance $tol = 10^{-4}$ is enough for ARPACK to find all the smallest magnitude eigenvalues without missing any of them. On the other hand, for the problem considered in this work, computing eigenfrequencies with two correct decimal digits is enough. Therefore, it does not make sense asking for an accuracy higher than $tol = 10^{-4}$ if there are no "physical" reasons to think that some eigenvalues could have been missed by the eigensolver.

Fig. 4.10 shows the computational time, number of matrix/vector products and restarts for ARPACK, the Krylov-Schur solver (KS) and the Jacobi-Davidson solver (JDQR). These are obtained for test case A (without active flame), when 10 eigenvalues are computed
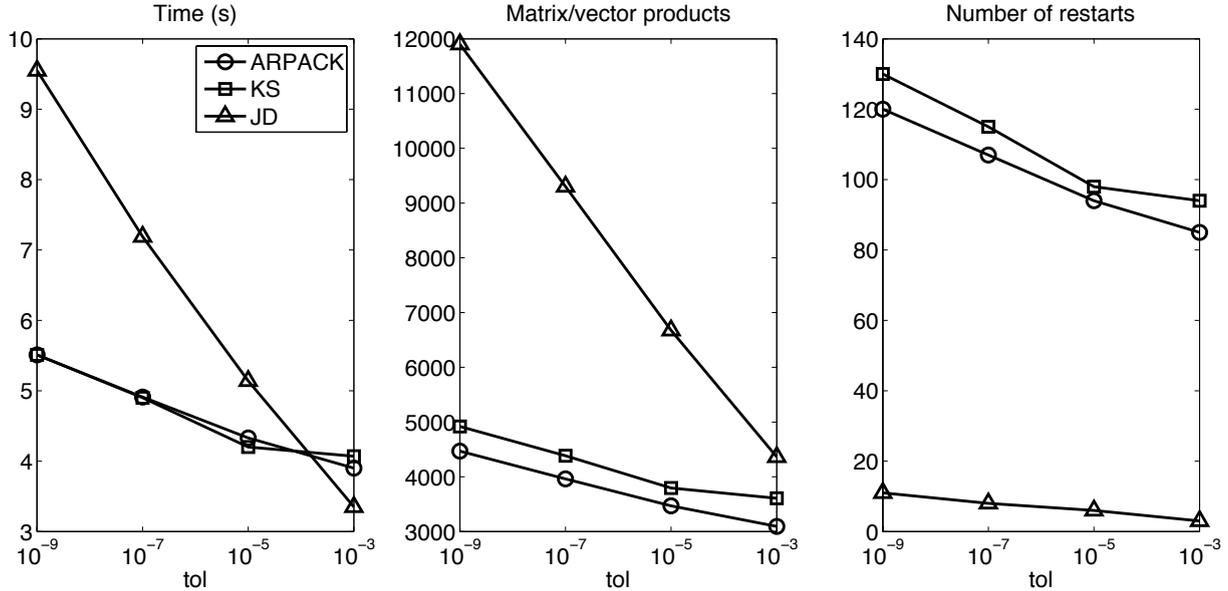
Figure 4.10: Computational cost as a function of the asked tolerance when computing the 10 first eigenvalues of case A without active flame.

with a search subspace of size $m = 50$. As expected, the overall cost increases when the convergence threshold decreases, for all the three solvers. Nevertheless, the JDQR solver is the most penalized. The reason is that Krylov-based solvers improve the quality of all the asked eigenpairs simultaneously, while the Jacobi-Davidson solver converges one approximate eigenpair at once. Therefore, if a large number of eigenpairs must be found with high accuracy, the JDQR solver is probably not the best option.

4.2.1.1 Accuracy and degenerate eigenvalues

The accuracy of the approximate eigenpairs, plays an important in the computation of eigenvalues with algebraic multiplicity larger than one, referred to as degenerate eigenvalues. If the matrix **OP** is non-defective then the algebraic and geometric multiplicity of degenerate eigenvalues are equal. In the context of this work, degenerate eigenvalues are often found due to the symmetry of the problem but they are not defective: they have associated a number of linearly independent eigenvectors equal to their algebraic multiplicity. This is the case of an azimuthal mode given by a couple of eigenvalues which are equal and have associated two linearly independent eigenvectors (see Chapter 5). In the following it is shown that computing eigenvalues with a higher level of accuracy can prevent skipping degenerate eigenvalues.

Let us consider the test case C without active flame, which has degenerate eigenvalues corresponding to azimuthal modes. When the first 5 eigenpairs are sought, Tab. 4.7 shows the eigenfrequencies computed by the different solvers for $tol = 10^{-4}$, $tol = 10^{-6}$ and $tol = 10^{-8}$. The results in Tab. 4.7 show that a small value of tol is required for the solvers to capture the doublets associated with azimuthal modes. In the case of ARPACK and KS, a value of $tol = 10^{-8}$ is enougth. For JDQR, a value $tol = 10^{-9}$ is needed to compute the

Freq. (Hz)		1	2	3	4	5
$tol = 10^{-4}$	ARPACK	34.82	95.41	180.85	266.23	269.46
	KS	34.82	95.41	180.85	266.23	269.46
	JD	34.82	95.41	180.85	266.23	269.46
$tol = 10^{-6}$	ARPACK	34.82	95.41	180.85	266.23	269.46
	KS	34.82	95.41	180.85	266.23	269.46
	JD	34.82	95.41	180.85	266.23	269.46
$tol = 10^{-8}$	ARPACK	34.82	95.41	95.41	180.85	180.85
	KS	34.82	95.41	95.41	180.85	180.85
	JD	34.82	95.41	95.41	180.85	266.23

Table 4.7: Test case C without active flame: 5 smallest eigenfrequencies obtained with ARPACK, KS and JDQR for different values of *tol*.

5 smallest eigenfrequencies correctly.

Concerning the JDQR solver, there is an interesting result regarding convergence of degenerate eigenvalues. As the following example shows, for a fixed value of *tol*, the level of accuracy chosen for the solution of the correction equation can play a role in the order in which eigenvalues are found. The 10 smallest magnitude eigenvalues of the test case B without active flame are computed for $tol = 10^{-4}$. The parameter that is investigated is the number of GMRES iterations used for solving approximately the correction equation. Ideally, the JDQR should converge first the two eigenvectors associated with the first doublet (the degenerate eigenvalue corresponding to the azimuthal mode), then those corresponding to the second azimuthal doublet and so on. Instead, the order in which eigenvectors are found depends on the accuracy of the correction equation solution (Tab. 4.8). This example shows that for a fixed value of *tol*, the obtained eigenvalues using the Jacobi-Davidson algorithm can be different depending on the accuracy of the correction equation solution (the convergence threshold of the inner iteration). In [44] the authors investigate the convergence of degenerate eigenvalues as well. Although the convergence seems to be delayed in the presence of doublets or triplets, the eigenvalues are found in the correct order. The reason is probably that the value of *tol* chosen by the authors is much more restrictive than the one used here ($tol = 10^{-9}$ instead of $tol = 10^{-4}$). Indeed, if the same problem is solved again with $tol = 10^{-10}$, JDQR finds the doublets one after the other in the correct order.

4.2.2 Influence of the search subspace maximum size m

The role played by the maximum size m of the search subspace is more important in the case of Krylov methods than in the case of the Jacobi-Davidson algorithm. The reason is the way these methods work: Krylov–based methods aim at converging a given eigenspace of size *nev* equal to the number of demanded eigenvalues, while the Jacobi-Davidson algorithm converges eigenpairs sequentially one after the other. In general, for reasonable values of m the Krylov methods restart several times before an approximate eigenspace is found. On

5 GMRES it		15 GMRES it		25 GMRES it	
1.	71.00	1.	71.00	1.	71.00
2.	141.16	2.	141.16	2.	141.16
3.	209.61	3.	209.61	3.	209.61
4.	274.41	4.	274.41	4.	274.41
5.	276.48	5.	276.48	5.	276.48
6.	337.73	6.	337.73	6.	337.73
7.	395.77	7.	395.77	7.	71.00
8.	449.29	8.	449.29	8.	141.16
9.	498.20	9.	71.00	9.	209.61
10.	71.00	10.	141.16	10.	337.73

Table 4.8: Case B without active flame: order of convergence for the first 10 eigenfrequencies computed with JDQR for $tol = 10^{-4}$ depending on the number of inner iterations used for the solution of the correction equation.

the other hand, it can happen that the Jacobi-Davidson method finds all the demanded eigenpairs before the search subspace reaches the maximal allowed size m. In this case, increasing the value of m does not change the behavior of the Jacobi-Davidson solver.

Fig. 4.11 displays the computational cost (in terms of run time, matrix/vector products and restarts) for ARPACK, KS and JDQR solvers when the first 10 eigenvalues are computed with $tol = 10^{-4}$ for test case A and B.

From the results in Fig. 4.11, three conclusions raise:

1. JDQR solver is barely affected by the maximum size of the search subspace m, whereas the Krylov-based solvers are very sensitive to this parameter. Choosing m equal to 2 or 3 times the number of wanted eigenvalues (nev) seems to be a reasonable choice.

2. For both ARPACK and KS solvers there exists an optimal size m that minimizes the computational cost.

3. The behavior of the Krylov-based solvers is similar (as it could be expected since there are mathematically equivalent). The KS solver seems though slightly faster than ARPACK, specially for larger values of m.

Concerning the ARPACK and KS solvers, when m increases the number of restarts decreases. Nevertheless the computation time is not monotonically decreasing with m: it decreases first and then it increases, existing an optimal value of m. The reason is that when m increases, the time spent per restart (extension of the base and computation of the eigenpairs of the Rayleigh quotient matrix) becomes larger and it becomes dominant, increasing the overall computational time.

One could wonder if there is a general rule to choose m optimally (that minimizes the run time), depending on the number of wanted eigenpairs nev. In the literature there is

(a) TEST CASE A

(b) TEST CASE B
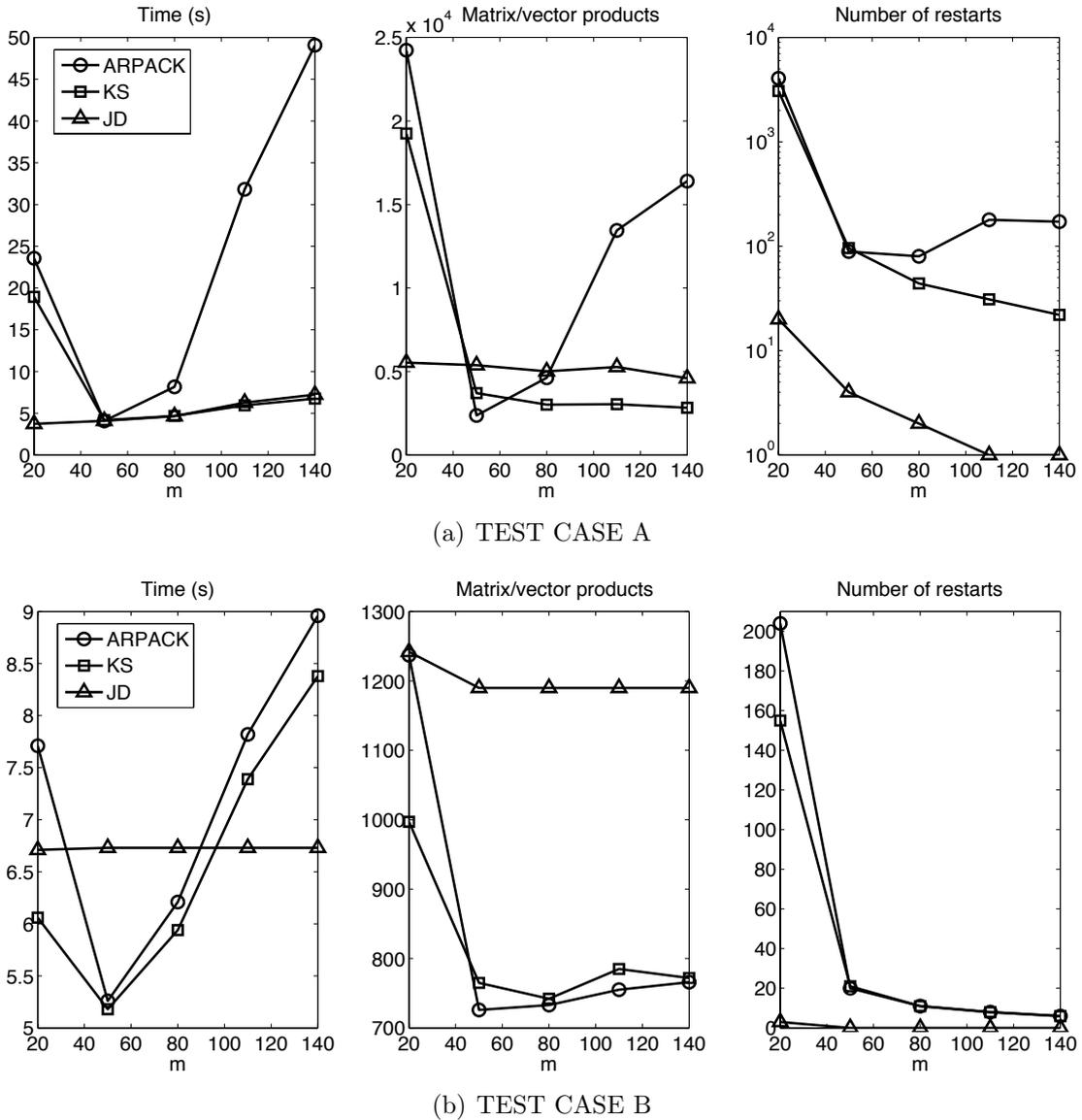
Figure 4.11: Influence of the maximum search subspace size m on the computational cost of 10 smallest magnitude eigenvalues with $tol = 10^{-4}$ for ARPACK, KS and JDQR solvers.

not a general recipe for this tuning. Although there is no general answer, it is possible to give an idea of the optimal choice, seeking an optimal ratio between m and nev. Fig. 4.12 plots computational time as a function of m for different number of asked eigenvalues nev for test cases A and C without active flame. The curves are normalized by the maximum computational time obtained for each value of nev. The minimum of each curve is marked with the corresponding ration m/nev. The tolerance for case A is $tol = 10^{-4}$ while for case C is chosen equal to $(tol = 10^{-8})$ in order to ensure that degenerate eigenvalues are not missed.

The results show that the optimal ratio m/nev (from the computational time point of view) depends on the number of wanted eigenvalues. However both cases exhibit the same trends: the optimal ratio decreases when the number of wanted eigenpairs increases. If the
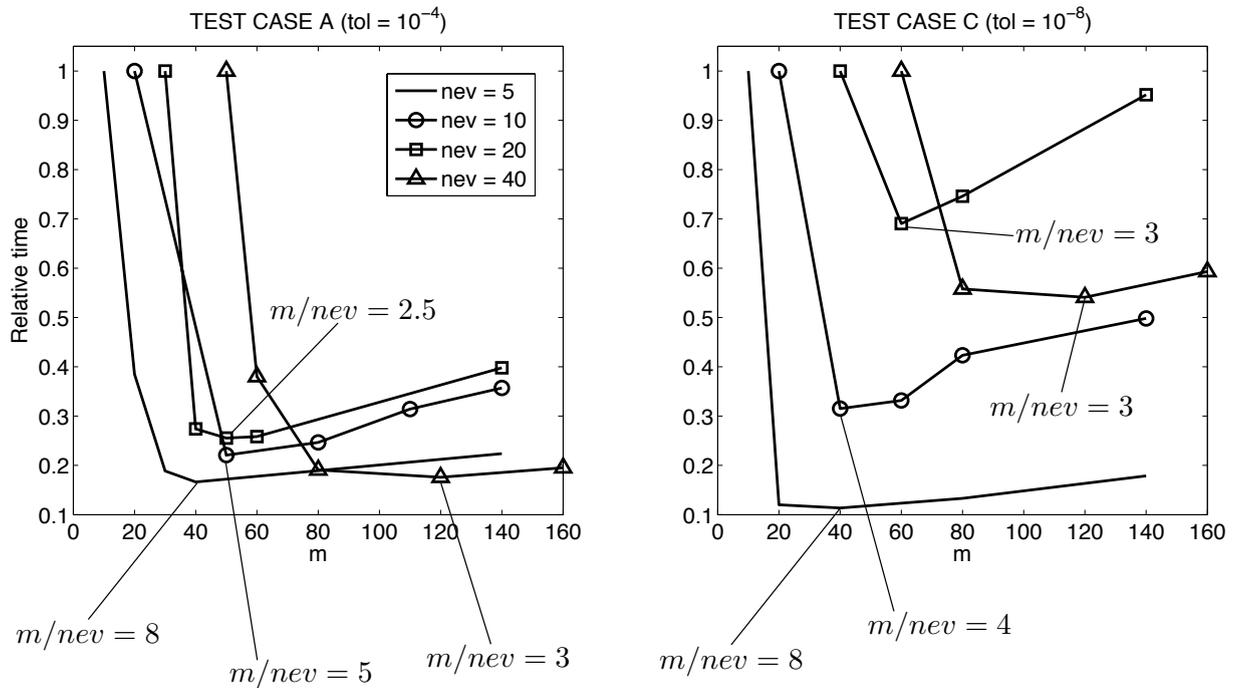
Figure 4.12: Influence of the ratio m/nev on the computation time for test cases A and C.

number of eigenpairs to compute is typically more than 10 and there is enough available memory, it does not seem appropriate to choose m smaller than $3 \times nev$ for problems of these sizes. However, from experience, for real cases with $N \approx \mathcal{O}(10^6)$, the ratio m/nev must be chosen larger to make the solver converge. The conclusion is that the optimal ratio m/nev is extremely case dependent.

4.2.3 Jacobi-Davidson: influence of the correction equation solution accuracy

As exposed in Chapter 3, the Jacobi-Davidson algorithm is a class of iterative subspace method for which every iteration consists of two main steps: (i) enlarge the so-called search subspace by adding a new basis vector and (ii) extract an approximate eigenpair from the said search space by using the Rayleigh-Ritz procedure. These two steps are the key points of the *outer* iteration that is called here a JD step. To obtain a new basis vector at each *outer* iteration, it is necessary to solve approximately the correction equation using an iterative solver, which constitutes the *inner* iterations. Since the most part of the time of the outer iteration is spent performing the inner iterations, the solution of the correction equation is the bottleneck of the Jacobi-Davidson method. This topic has been discussed in a large number of works [44, 54, 55, 150, 151], specially the matter of how to include preconditioning for the correction equation solution.

In the present work, a Generalized Minimal Residual Method (GMRES) [131] is used to obtain the approximate solution of the correction equation at each JD step. No preconditioning is used since the explicit operator is unavailable and the stopping criterion for

the approximate solution of the correction equation is established by fixing a given number of GMRES iterations (the inner iterations). As the theoretical results presented in [54] show, it is possible to link the optimal level of accuracy of the correction equation to the residual of the associated approximate eigenpair. The authors demonstrate that solving the correction equation beyond a certain level of accuracy does not improve the convergence of the outer iteration and it is a waste of resources.

The three test cases without active flame are used in order to try to extrapolate an optimal value for the number of full GMRES iterations. Fig. 4.13 shows the effect of the number of GMRES iterations (that is, the stopping criterion for the correction equation solution) on the computational time, number of matrix/vector products and JD steps when computing the 10 smallest magnitude eigenfrequencies with $tol = 10^{-6}$ (which ensures finding all the doublets for cases B and C). Looking at the number of JD steps in Fig. 4.13
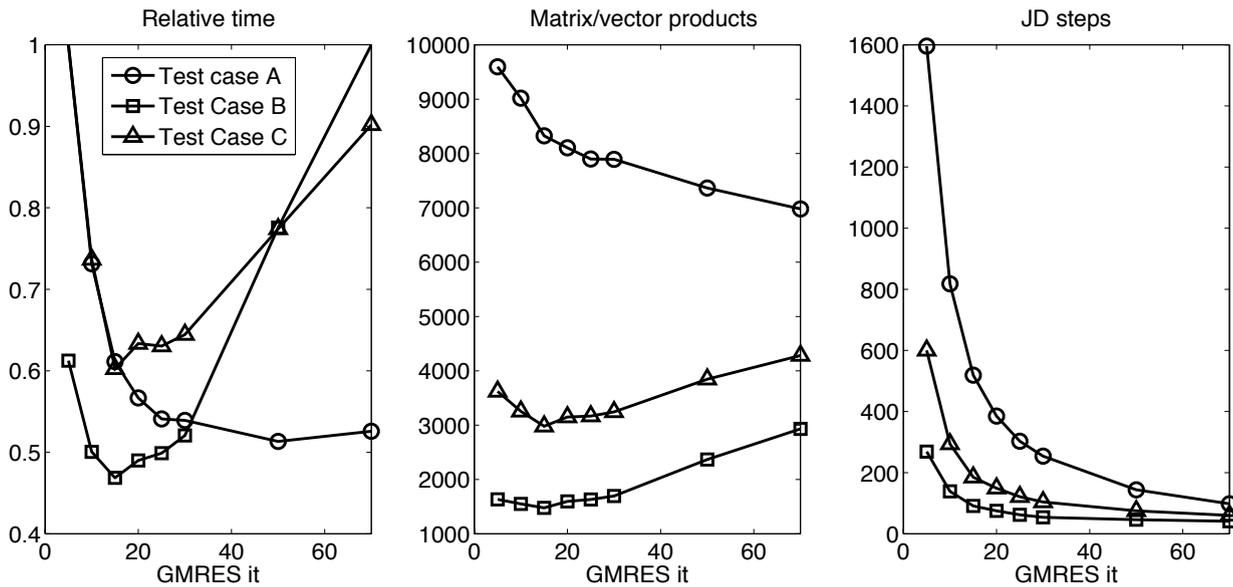
Figure 4.13: For test case A, B and C, effect of the number of inner iterations (full GMRES iterations here) on the performance of the JD solver.

one sees that, at first, it decreases fast with the number of GMRES iterations but then it reaches a limit. This behavior illustrates well what has already been mentioned: solving the correction equation beyond a certain level of accuracy does not improve the performance of the outer iterations and it just increases the time spent per iteration. The number of GMRES iterations for which this limit is reached seems to be larger for the test case A than for B and C. Extrapolating these results to other cases, since it is not of practical use to tune this parameter for every case, it seems a good compromise choosing the number of GMRES iterations equal to 25.

4.2.4 Harmonic extraction

Harmonic Ritz values are considered in literature [91, 92, 107] as a good alternative to the shift-and-invert spectral transformation that avoids the need of "inverting" matrices. They

appear as a good alternative for the computation of eigenvalues nearest to a given target τ, specially when the interest is in eigenvalues laying in the interior of the spectrum. For example, in [125] the authors show the efficiency of performing harmonic extraction in a Krylov-Schur solver compared to considering spectral transformations such as shift-and-invert.

Imposed by the physics of the problems, the matrices to deal with in this work have spectra that lay along the negative part of the real axis (although sometimes they may have some eigenvalues with positive real part), and in general the magnitude of the imaginary part of the eigenvalues are significantly smaller than the magnitude of the corresponding real part. The objective is to compute a few smallest magnitude eigenvalues: although they are not interior eigenvalues (see Fig. 4.14), smallest magnitude eigenvalues are more difficult to capture than the largest magnitude ones, and the harmonic extraction may be a good option. For this reason harmonic Ritz values have been implemented in the Krylov-Schur solver (see Chapter 3).
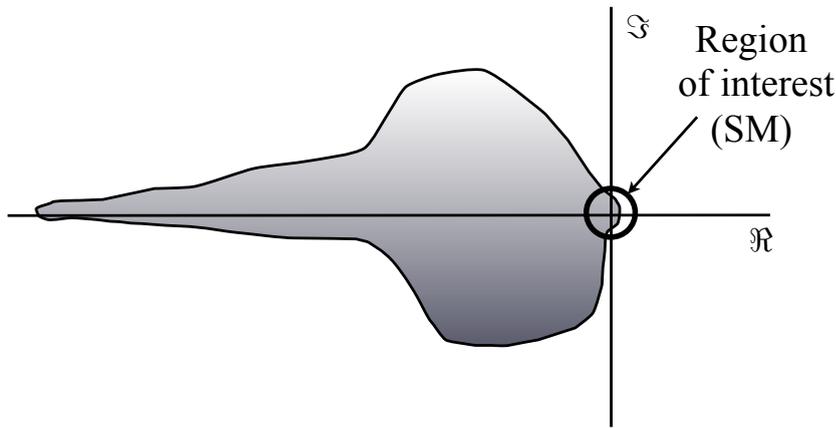
Figure 4.14: Scheme of the periphery of a typical spectrum from a matrix issued from the discretization of the Helmholtz equation.

The KS solver is used with classic and harmonic extraction in order to compute the 10 smallest magnitude eigenvalues of the test cases A, B and C without active flame with $tol = 10^{-6}$. The harmonic shift τ is set to a value near 0 in order to capture the smallest magnitude eigenvalues. The run time and the number of implicit restarts needed by the KS solver in each case appear in Tab. 4.9 for both extraction techniques.

The results of Tab. 4.9 suggest that using harmonic Ritz values does not really improve the convergence of the method when computing the smallest magnitude eigenvalues in these cases. Nevertheless, it might still be useful for the computation of a few interior eigenvalues, which is necessary in cases where the first tens of smallest magnitude eigenvalues are not of interest and the target is around the 50th or the 100th eigenfrequency, for example. For test case A, a few eigenvalues around a given target τ are computed in two different ways:

1. Using harmonic extraction, which must return those eigenvalues of the matrix **A** closest to the harmonic shift τ.

2. Computing the smallest magnitude eigenvalues δ of the shifted matrix $(\mathbf{A} - \tau I)$ using

		Time(s)	Restarts	Matvec
CASE A	Classical Ritz	4.77	108	4136
	Harmonic Ritz	4.76	106	4110
CASE B	Classical Ritz	5.82	21	776
	Harmonic Ritz	5.41	21	784
CASE C	Classical Ritz	14.68	55	2007
	Harmonic Ritz	13.54	52	1887

Table 4.9: Computational cost of classical Ritz values and harmonic Ritz values corresponding to the calculation of the $nev = 10$ SM eigenvalues of cases A, B and C without active flame with $tol = 10^{-6}$ ($m = 70$).

classical Rayleigh-Ritz extraction. Then, the original eigenvalues ω of the matrix $\mathbf{A}$ are simply $\omega = \tau + \delta$.
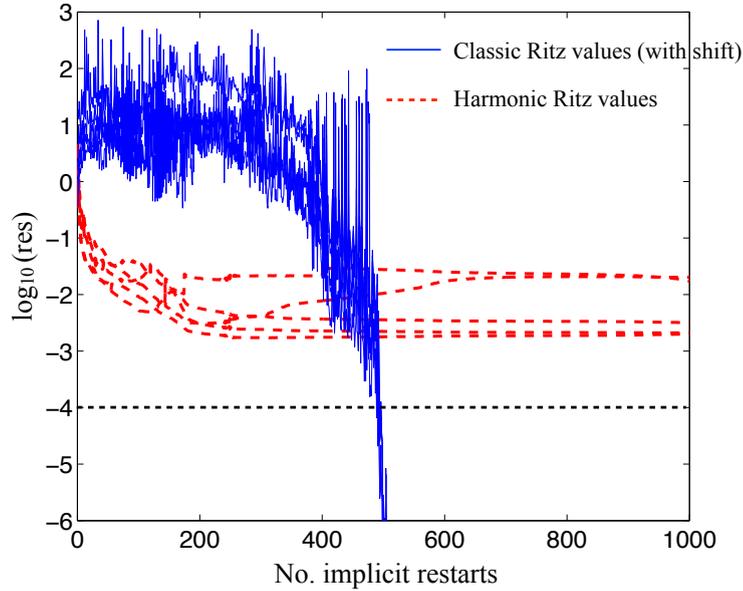
Figure 4.15: Convergence history of the harmonic Ritz values ($- -$) and the classic Ritz values ($-\!\!-$) when computing $nev = 5$ eigenvalues closest to 15000 Hz of the test case A ($tol = 10^{-4}$ and $m = 100$).

Let us suppose that, for the test case A without active flame, the 5 eigenvalues closest to 15000 Hz are wanted. Then the proper shift ($\tau = -((2\pi)15000)^2$) is used to compute the harmonic Ritz values nearest τ, in the case of harmonic extraction, and the smallest eigenvalues of the shifted matrix ($\mathbf{A} - \tau I$) are computed using classical Ritz extraction. The residual ($res = |Ax - \lambda x|/|\lambda|$) curves obtained for both strategies are plotted in Fig. 4.15. After 2000 implicitly restarted iterations, the KS solver with harmonic extraction did not converge, whereas the classic Ritz extraction did after 522 iterations. The eigenfrequencies ($\omega = \tau + \delta$) obtained in the last case appear in Tab. 4.10.

14940.7 Hz
14972.7 Hz
15012.0 Hz
15058.2 Hz
15098.1 Hz

Table 4.10: Eigenfrequencies closest to 15000 Hz of the test case A without active flame.

This example shows that even for the computation of a few interior eigenvalues (those calculated here correspond to the 128th–132th smallest magnitude eigenvalues of the matrix **A**), a shift transformation gives better results than harmonic extraction. The stagnation of the residuals corresponding to the harmonic Ritz values is due to the fact that the harmonic shift τ is chosen too close to an actual eigenvalue. This inherent problem to harmonic extraction is difficult to overcome, since it is impossible to know a priori whether the chosen shift is very close or not to an actual eigenvalue. And even if this was possible (for this example it is the case since the whole spectrum is known), it may happen that the eigenvalues are too close to each other, so that is impossible to choose a shift that will not produce such a stagnation in practice.

Harmonic Ritz values can be computed using the Jacobi-Davidson method as well [156]. In [44] the authors show how the Jacobi-Davidson method for the solution of generalized eigenproblems (Jacobi-Davidson method style QZ) can be used for the calculation of harmonic Ritz pairs. A Matlab implementation of this algorithm (reffered to as JDQZ in [44]), downloaded from G.L.G. Sleijpen's web site[1], has been compared to a Matlab implementation of the JDQR algorithm described in Chapter 3 and no significant differences concerning the convergence have been found.

4.3 Strategies for the solution of the nonlinear eigenproblem

One of the difficulties of the thermoacoustic model considered in this work is the need to solve the nonlinear eigenvalue problem

$$\mathbf{A}\bar{p} + \omega\mathbf{B}(\omega)\bar{p} + \omega^2\bar{p} = \mathbf{C}(\omega)\bar{p} \tag{4.3}$$

in order to compute the *nev* smallest magnitude *nonlinear* eigenvalues

$$|\omega_1| \leq |\omega_2| \leq \cdots \leq |\omega_{nev}|.$$

As in other works treating nonlinear eigenproblems [55, 89], since there exists no general methods for the solution of such problems, Eq. (4.3) is linearized in order to obtain a problem that can be solved using one of the available methods for the solution of linear

---

[1]http://www.math.uu.nl/~sleij101/

eigenproblems. Depending of its nature, the problem can be linearized in many ways [163]. Here, a Fixed Point (FP) iterative procedure is chosen in order to linearize Eq. (4.3). Basically, it consists in fixing a given value $\tilde{\omega}^{(j)}$, called here *linearization value*, to the nonlinear terms of Eq. (4.3), so that they become constant and they can be added to the linear part **A**, in order to obtain the linear eigenproblem

$$[\mathbf{A} + \tilde{\omega}^{(j)}\mathbf{B}(\tilde{\omega}^{(j)}) - \mathbf{C}(\tilde{\omega}^{(j)})]\bar{p} + \omega^{(j)^2}\bar{p} = 0, \tag{4.4}$$

which can be written simply as

$$\mathbf{OP}^{(j)}\bar{p} = -\omega^{(j)^2}\bar{p}, \tag{4.5}$$

where $\mathbf{OP}^{(j)} = \mathbf{A} + \tilde{\omega}^{(j)}\mathbf{B}(\tilde{\omega}^{(j)}) - \mathbf{C}(\tilde{\omega}^{(j)})$.

Unless the solution of Eq. (4.5) $\omega^{(j)}$ is equal to the used linearization value $\tilde{\omega}^{(j)}$ (which means that $\omega^{(j)}$ is a solution ω of Eq. (4.3)), the method proceeds using $\omega^{(j)}$ as the new linearization value, that is, $\tilde{\omega}^{(j+1)} = \omega^{(j)}$, so that a new linear eigenvalue problem

$$\mathbf{OP}^{(j+1)}\bar{p} = -\omega^{(j+1)^2}\bar{p}$$

has to be solved. This procedure is repeated in order to make $\omega^{(j)}$ converge to a nonlinear eigenvalue ω solution of Eq. (4.3). The convergence is stated when the distance $|\tilde{\omega}^{(j)} - \omega^{(j)}|$ is smaller than a certain threshold ϵ.

The solution of each linear eigenproblem (Eq. (4.5)) is referred to as nonlinear iteration or FP iteration, and the set of nonlinear iterations performed until reaching the convergence is called the nonlinear loop. During the nonlinear loop only one nonlinear eigenvalue ω_i (and the corresponding eigenvector $\bar{p}_i$) of Eq. (4.3) can be tracked. If many nonlinear eigenpairs have to be computed, the whole procedure has to be repeated as many times as desired nonlinear eigenpairs $(\omega_i, \bar{p}_i)$ $(i = 1, \dots, nev)$.

In summary, the fixed point procedure, in its simplest form, proceeds as follows:

1. At the jth FP iteration the approximation $\tilde{\omega}^{(j)}$ to ω is used to linearize Eq. (4.3). The resulting problem

$$\mathbf{OP}^{(j)}\bar{p} = -\omega^{(j)^2}\bar{p}$$

   has to be solved in order to obtain $\omega^{(j)}$.

2. The solution $\omega^{(j)}$ is used as a new linearization value, i.e., $\tilde{\omega}^{(j+1)} = \omega^{(j)}$ and a new linear eigenproblem

$$\mathbf{OP}^{(j+1)}\bar{p} = -\omega^{(j+1)^2}\bar{p}$$

   has to be solved, whose solution $\omega^{(j+1)}$ will constitute the next linearization value.

3. Step 2 is repeated until two successive values $\omega^{(\ell-1)}$, $\omega^{(\ell)}$ are close enough. The value $\omega^{(\ell)}$ is accepted as a solution of Eq. (4.3) when the distance $|\omega^{(\ell)} - \tilde{\omega}^{(\ell)}|$ is smaller than a chosen threshold ϵ.

In practice, at the jth FP iteration iteration, a few *nev* linear eigenvalues of

$$\mathbf{OP}^{(j)}\bar{p} = -\omega^{(j)^2}\bar{p}$$

are computed

$$|\omega_1^{(j)}| \leq |\omega_2^{(j)}| \leq \cdots \leq |\omega_k^{(j)}| \leq \cdots \leq |\omega_{nev}^{(j)}|$$

sorted from smallest to largest magnitude. In order to preserve the convergence of the nonlinear loop, the linear eigenvalue $\omega_k^{(j)}$ closest to the current linearization value $\tilde{\omega}^{(j)}$ must be chosen as the $(j+1)^{th}$ linearization value $\tilde{\omega}^{(j+1)} = \omega_k^{(j)}$. That is, the output $\omega^{(j)}$ of the jth nonlinear iteration is the linear eigenvalue $\omega_k^{(j)}$ closest to $\tilde{\omega}^{(j)}$.

On the other hand, let us suppose that the nonlinear eigenvalue ω_i has just converged after ℓ FP iterations, and the next nonlinear eigenvalue ω_{i+1} has to be computed. Then, the linear eigenvalues

$$\omega_1^{(\ell)}, \omega_2^{(\ell)}, \ldots, \omega_k^{(\ell)}, \ldots$$

obtained at the ℓth nonlinear iteration for the computation of ω_i can provide a good initial guess to start a new nonlinear loop in order to compute the next nonlinear eigenvalue ω_{i+1}.

If the nonlinear problem is stiff, it may happen that the sequence $\omega^{(0)}, \omega^{(1)}, \omega^{(2)}, \ldots$ of values obtained at each FP iteration does not converge. In this case the FP method can be used with a relaxation parameter α ($0 \leq \alpha < 1$): the next linearization value $\tilde{\omega}^{(j+1)}$ is chosen now as a convex combination of the current one $\tilde{\omega}^{(j)}$, and the last obtained solution $\omega^{(j)}$:

$$\tilde{\omega}^{(j+1)} = (1 - \alpha)\omega^{(j)} + \alpha\tilde{\omega}^{(j)}.$$

Algorithm 4.1 implements the relaxed FP procedure to compute a nonlinear eigenpair $(\omega_i, \bar{p}_i)$ of Eq. (4.3).

Algorithm 4.1 ω_i, $\bar{p}_i]=FP\_relax(\omega^{(0)}, \alpha, \epsilon)$

Given the relaxation parameter α ($0 \leq \alpha < 1$) an the initial guess $\omega^{(0)}$, FP_relax returns the approximate eigenpair $(\omega_i, \bar{p}_i)$ of Eq. (4.3). The nonlinear eigenvalue ω_i is converged when $|\tilde{\omega}^{(j)} - \omega^{(j)}| \leq \epsilon$.

   Set $\tilde{\omega}^{(1)} = \omega^{(0)}$

  for $j = 1, 2, \ldots$ **do**

     Solve $\mathbf{OP}^{(j)}\bar{p} = -\omega^{(j)^2}\bar{p}$ to obtain *nev* eigenvalues:

       $|\omega_1^{(j)}| \leq \cdots |\omega_k^{(j)}| \cdots \leq |\omega_{nev}^{(j)}|$

     and the corresponding eigenvectors.

     Select the linear eigenvalue $\omega_k^{(j)}$ closest to $\tilde{\omega}^{(j)}$: Set $\omega^{(j)} \leftarrow \omega_k^{(j)}$.

     Convergence test:

    if $|\tilde{\omega}^{(j)} - \omega^{(j)}| \leq \epsilon$ **then**

      Return $\omega_i = \omega^{(j)}$ and the corresponding eigenvector $\bar{p}_i$.

    else

      Compute the next FP value $\tilde{\omega}^{(j+1)}$ as:

      $\tilde{\omega}^{(j+1)} = (1 - \alpha)\omega^{(j)} + \alpha\tilde{\omega}^{(j)}$

    end if

  end for

4.3.1 Acceleration techniques: recycling solutions between fixed point iterations

The linear eigenproblems at each nonlinear iteration can be solved one after the other considering each one of them as a new linear eigenproblem independent from the previous ones. But the fact is that the solution obtained during the previous nonlinear iteration can be a good approximation for the solution of the next one, so that exploiting this information can accelerate the convergence of the next linear eigenproblem. To support this idea, the sequence of solutions obtained during the computation of one mode of the test case B with active flame ($\mathbf{C}(\omega) \neq 0$) is analyzed. Starting from the solution of the problem without active flame (see Tab. 4.4), the mode with active flame closest to the 7th (209.6 Hz) mode without combustion is computed, using Algorithm 4.1 without relaxation ($\alpha = 0$). The nonlinear eigenproblem corresponding to this case is

$$\mathbf{A}\bar{p} + \omega^2 \bar{p} = \mathbf{C}(\omega)\bar{p},$$

since $\mathbf{B} = 0$ due to the Neumann boundary conditions. At each FP iteration, the following quantities are calculated, which are summarized in Tab. 4.11:

- The relative Frobenius norm of the difference between two consecutive matrices

$$\Delta_F = \frac{\|\mathbf{OP}^{(j-1)} - \mathbf{OP}^{(j)}\|_F}{\|\mathbf{OP}^{(j)}\|_F}.$$

- The relative distance between the outputs of two consecutive nonlinear iterations

$$\delta(\%) = \frac{|\omega^{(j-1)} - \omega^{(j)}|}{|\omega^{(j)}|} \times 100.$$

- The angle between the subspaces $P^{(j)} = span\{\bar{p}_1^{(j)} \cdots \bar{p}_{nev}^{(j)}\}$ formed by the eigenvectors obtained for two consecutive FP iterations and denoted $\angle(P^{(j-1)}, P^{(j)})$.

# FP it.	$\omega_7^{(j)}$ (Hz)	Δ_F	$\delta(\%)$	$\angle(P^{(j-1)}, P^{(j)})$ (degrees)
0	209.6000	–	–	
1	219.7025 - i3.9021	0.0404	4.92	48.82
2	219.8656 - i2.5189	0.0051	0.63	0.28
3	219.8675 - i2.5046	8.04e-5	6.58e-3	4.3e-3
4	219.8676 - i2.5044	1.06e-6	8.69e-5	5.72e-5

Table 4.11: Results obtained using the FP procedure (with $\alpha = 0$) when converging the 7th eigenfrequency with active flame of the test case B.

The FP procedure exhibits a quick convergence. Looking at the quantity Δ_F, one realizes that the matrix $\mathbf{OP}^{(j)}$ can be seen as the matrix $\mathbf{OP}^{(j-1)}$ corresponding to the previous
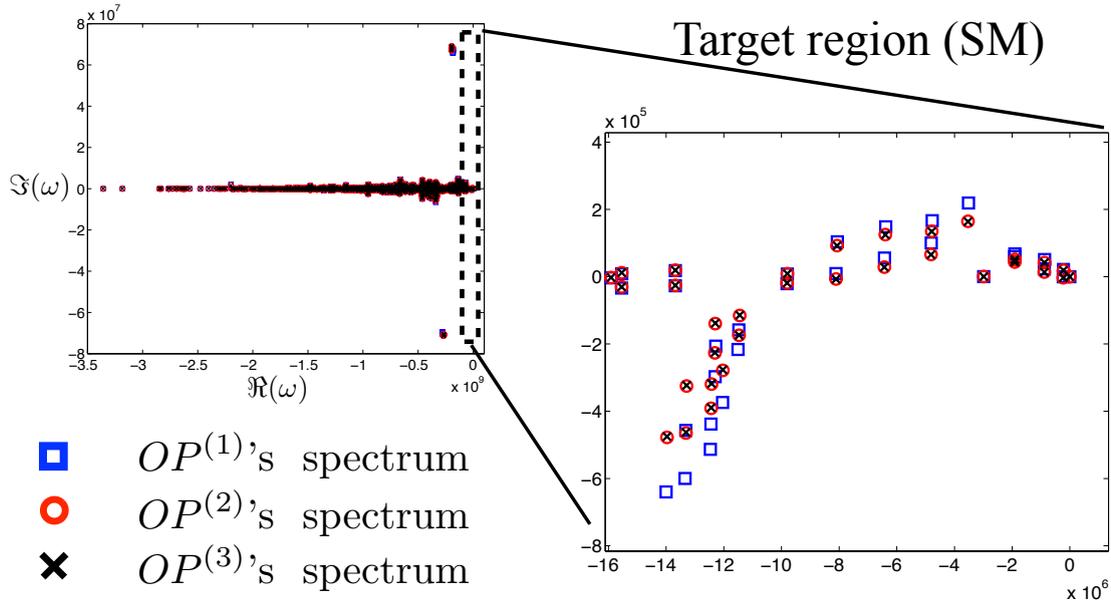
Figure 4.16: For test case B, spectra of the matrices $\mathbf{OP}^{(1)}$, $\mathbf{OP}^{(2)}$ and $\mathbf{OP}^{(3)}$ obtained during the FP procedure.

nonlinear iteration plus a small perturbation Δ, i.e., $\mathbf{OP}^{(j)} = \mathbf{OP}^{(j-1)} + \Delta$. Moreover, the small angle between the linear eigenvectors of two consecutive linear eigenproblems suggests that the subspace $P^{(j-1)}$ is a good approximation of $P^{(j)}$. The spectra of the matrices $\mathbf{OP}^{(1)}$, $\mathbf{OP}^{(2)}$ and $\mathbf{OP}^{(3)}$ (Fig. 4.16) shows that the sequence of linear solutions computed during the nonlinear loop are very close to each other. Therefore, it would be very advantageous being able to recycle the eigensolutions between successive nonlinear iterations in order to accelerate the solution of the next linear eigenproblem.

Depending on the eigensolver, four strategies aiming at reusing the linear solutions of a previous nonlinear iteration, are investigated:

- Using a block Krylov method: it starts from a block of vectors instead of just one direction. The idea is to choose as initial block the linear eigenvectors $P^{(j-1)}$ of $\mathbf{OP}^{(j-1)}$ to solve the problem $\mathbf{OP}^{(j)}\bar{p} = -\omega^{(j)2}\bar{p}$. The block-size p is then equal to the number *nev* of wanted eigenpairs.

- Using ARPACK or the KS solver: these methods can only start from a single vector. The way proposed here to take into account the *nev* available directions from the previous FP iteration consists in choosing the initial vector u_0 for the solution of $\mathbf{OP}^{(j)}\bar{p} = -\omega^{(j)2}\bar{p}$ as a linear combination of the eigenvectors $P^{(j-1)}$.

- Using JD solver offers a natural way of recycling the eigenvectors $P^{(j-1)}$ for the solution $\mathbf{OP}^{(j)}\bar{p} = -\omega^{(j)2}\bar{p}$: an orthonormal basis U of $P^{(j-1)}$ and the corresponding Rayleigh-quotient $C = U^H\mathbf{OP}^{(j)}U$ are computed. Then, since the Jacobi-Davidson algorithm does not require any particular form of C, it can be used to extend the search subspace and carry on the process.

- Using a Subspace iteration with Chebyshev acceleration: starting from subspace formed by the *nev* linear eigenvectors $P^{(j-1)}$ of $\mathbf{OP}^{(j-1)}$ (which can be eventually completed with random vectors), subspace iterations are performed to obtain the solution of $\mathbf{OP}^{(j)}\bar{p} = -\omega^{(j)^2}\bar{p}$.

4.3.2   Block Krylov methods for recycling eigenspaces

At the end of each FP step, *nev* eigenvectors corresponding to the *nev* smallest magnitude eigenvalues have been computed. Since we want to reuse the obtained solution, the block method must be used with a block size p equal to *nev*, so that it can start from an initial set of vectors corresponding to the *nev* eigenvectors computed during the last FP iteration.

In the case of a single vector (SV) Krylov method, if m is the maximum allowed size of the search subspace and k is the size of the restarted subspace, then the degree of the filter polynomial applied at each implicit restart is $(m-k)$. On the other hand, for a block Krylov method, the degree of the filter polynomial is divided by the block size p, being $(m-k)/p$. Consequently, if m and k are kept the same for both the single vector and the block solvers, the efficiency of the filter polynomial is reduced in the case of the block solver [76, 178]. Therefore, using the same dimension for the search subspace (i.e., the same amount of memory) the convergence rate of the block method is expected to be inferior compared to the one of the single vector solver. The question is: is the approximation of the solution provided by the initial block good enough to make the use of the block method advantageous, despite the expected lower convergence rate? To answer this question two successive FP iterations from Tab. 4.11 are considered: the problem $\mathbf{OP}^{(2)}\bar{p} = \omega^{(2)^2}\bar{p}$ is solved using the solution from $\mathbf{OP}^{(1)}$ (with an accuracy $tol = 10^{-6}$ for the eigensolver). Although, in general, the block size must be equal to the number of wanted eigenpairs, in order to see the effect of the block size p, *nev* is set to 3 while the block size p takes the values 3, 5, 7 and 9 (the first 3 vectors of each block correspond to the previously computed linear eigenvectors and then, when necessary, they are completed with random vectors). The computational cost is plotted in Fig. 4.17: from left to right, the normalized run time (denoted relative time), the number of matrix/vector products (matvec) and the number of restarts for the different block sizes. As expected, keeping $m = 70$ the same for the different block sizes, the efficiency of the method deteriorates when the size block p increases.

A comparison with the single vector KS method is performed: the same problem $(\mathbf{OP}^{(1)} \rightarrow \mathbf{OP}^{(2)})$ is solved keeping the same maximum search space size m for both solvers. The single vector method starts from a random vector, so no *a priori* information is exploited, while the block solver starts from the solution of $\mathbf{OP}^{(1)}$. In Tab. 4.12 are summarized the ratios of runtime, number of matvec, and number of implicit restarts between the block and the single vector methods. For the comparison, the block size p is set equal to *nev* in each case. The results show that, even for small block sizes, using the block method is not a good strategy in the context of this work.

In order to illustrate how the convergence rate of the block method is penalized due to the lower degree of the filter polynomial compared to the single vector method, Fig. 4.18 plots the convergence history of the residuals obtained for both methods, for *nev* = 5 ($p = 5$) when solving $\mathbf{OP}^{(3)}\bar{p} = -\omega^{(3)^2}\bar{p}$. The solution $P^{(2)}$ is used as initial set of vectors
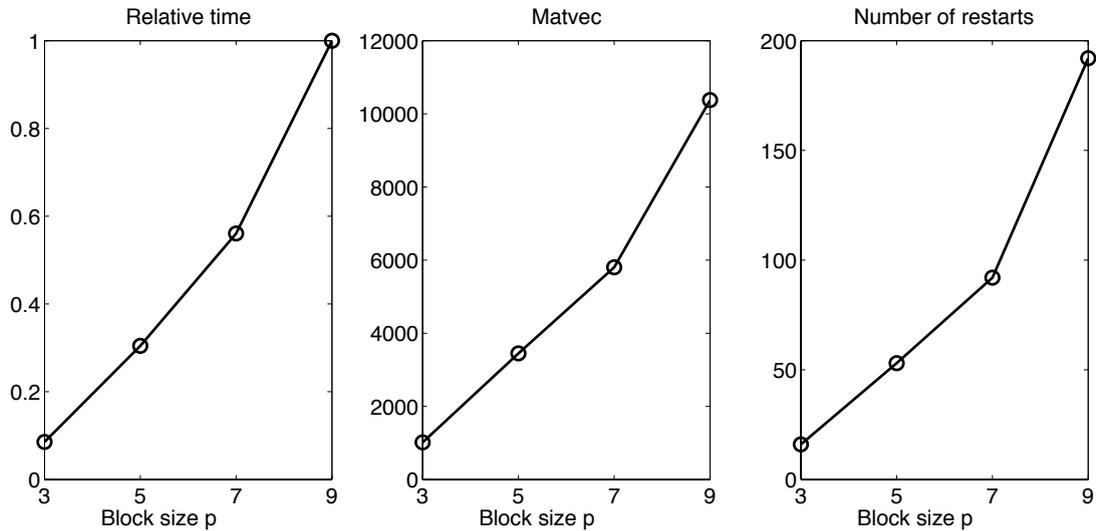
Figure 4.17: Computational cost of computing the $nev = 3$ smallest magnitude eigenvalues of the test case B for increasing block size p.

nev (p)	$\dfrac{\text{Time block}}{\text{Time SV}}$	$\dfrac{\text{Matvec block}}{\text{Matvec SV}}$	$\dfrac{\text{Restarsts block}}{\text{Restarts SV}}$
3	1.66	1.46	1.46
5	5.02	4.42	4.41
7	8.38	7.12	7.07
9	17.88	13.74	13.71

Table 4.12: Comparison of block and single vector Krylov-Schur methods when solving $\mathbf{OP}^{(2)}\bar{p} = -\omega^{(2)^2}\bar{p}$ for the test case B, with the initial block given by the eigenvectors of $\mathbf{OP}^{(1)}$ (for the block solver).

in the block solver, whereas the single vector solver starts from a single random vector. Although the residuals corresponding to the first iteration of the block method are smaller, the superior convergence rate of the single vector outperforms the block method very quickly.

Similar results to the ones in Tab. 4.12 are obtained for the other nonlinear iterations of Tab. 4.11 and for any other case. The poor convergence of the method might be balance by the higher computing performance of matrix/matrix products. For instance, according to the computation time in Tab. 4.12 required for the calculation of 3 eigenpairs, the BLAS-3 performance should be 1.66 times faster than the sequence of BLAS-2 operations applied to each set of 3 vectors, which seems not probable. Anyway, this feature can not be exploited in AVSP since only one matrix/vector product can be performed at once. Moreover, when a few tens of eigenvectors have to be recycled, the block size p is too large to expect a reasonable convergence rate, which makes the use of block methods unpractical. Nevertheless, the block-Krylov algorithm can be interesting for other problems, e.g. where the multiplicity of eigenvalues is known *a priori* and choosing a size block equal to it can improve the convergence, provide the block size remains small (2 or 3) [178].
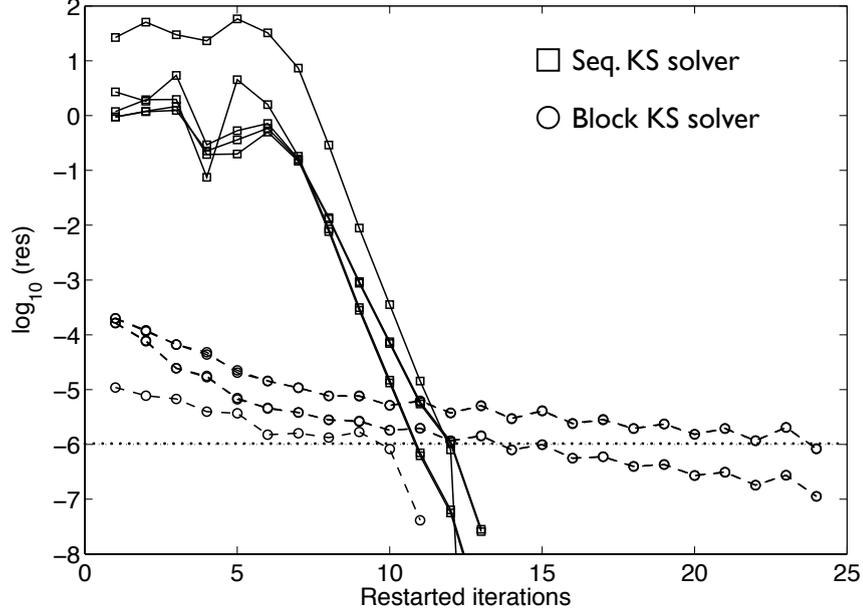
Figure 4.18: Test case B: residuals corresponding to the first 5 eigenpairs of $\mathbf{OP}^{(3)}\bar{p} = -\omega^{(3)}\bar{p}$, solved with the block and the SV versions of the KS solver.

4.3.3 Using linear combinations of previous eigensolutions

As explained in Chapter 3, if the initial vector u_0 of a Krylov subspace can be written as a linear combination of k eigenvectors of the matrix A

$$u_0 = \gamma_1 v_1 + \gamma_2 v_2 + \cdots + \gamma_k v_k,$$

with $\gamma_j \neq 0, j = 1, \ldots, k$, then the Krylov sequence terminates at step k, and the Krylov subspace $\mathcal{K}_k(u_0, A)$ is an eigenspace of dimension k of the matrix A. In our case, this means that if the vector $u_0 = \bar{p}_1^{(j)} + \bar{p}_2^{(j)} + \cdots + \bar{p}_{nev}^{(j)}$ is used as initial vector for ARPACK or the KS solver to compute the *nev* smallest magnitude eigenvalues of $\mathbf{OP}^{(j)}$, the methods are expected to converge within the first restarted iteration, since the initial vector is a linear combination of the solution eigenvectors. By continuity, since the subspace $P^{(j-1)}$ is close to the one spanned by $P^{(j)}$, one can expect that starting the Krylov solver from $u_0 = \bar{p}_1^{(j-1)} + \bar{p}_2^{(j-1)} + \cdots + \bar{p}_{nev}^{(j-1)}$ will improve the convergence for the eigensolution of $\mathbf{OP}^{(j)}$, compared to starting from a random vector. Note that the coefficients of the linear combination are all equal to one, since no a priori reason makes believe that there is any optimal combination[2]. The following simple procedure is considered:

1. The problem $\mathbf{OP}^{(j-1)}\bar{p} = -\omega^{(j-1)^2}\bar{p}$ corresponding to the $(j-1)^{th}$ FP iteration was solved and *nev* eigenpairs $(\omega^{(j-1)}, \bar{p}^{(j-1)})$ were computed.

2. Form the vector $u_0 = \bar{p}_1^{(j-1)} + \bar{p}_2^{(j-1)} + \cdots + \bar{p}_{nev}^{(j-1)}$.

---

[2]The optimal tuning of the linear combination coefficients is case dependent and it is not of practical use.

3. Using ARPACK or the KS solver, solve the problem $\mathbf{OP}^{(j)}\bar{p} = -\omega^{(j)2}\bar{p}$ using u_0 as initial vector.

This strategy is tested for test case A. The FP procedure is used without relaxation ($\alpha = 0$) to compute the smallest magnitude nonlinear eigenvalue of the problem with active flame. At every nonlinear iteration $nev = 5$ linear eigenvalues are computed (see Tab. 4.13), using ARPACK and KS with $tol = 10^{-4}$. As before, the iteration 0 corresponds to the solution of the problem without active flame ($\mathbf{C}(\omega) = 0$), which is a linear eigenproblem.

# FP it.	$\omega_1^{(j)}$ (Hz)	Δ_F	$\delta(\%)$	$\angle(P^{(j-1)}, P^{(j)})$ (degrees)
0	272.3000	–	–	–
1	159.6988 - i9.2850	6.7317e-2	70.6	13.72
2	159.6703 - i5.4399	4.7616e-3	2.41	0.3368
3	159.6703 - i5.4390	1.2049e-6	6.08e-4	8.5048e-5

Table 4.13: Results obtained using the FP procedure (with $\alpha = 0$) when converging the 1st nonlinear eigenfrequency with active flame of the test case A.

Fig. 4.19 plots the convergence history of the residual norms for the 5 smallest magnitude eigenpairs of $\mathbf{OP}^{(1)}$, $\mathbf{OP}^{(2)}$ and $\mathbf{OP}^{(3)}$ computed with ARPACK and KS. Each problem was solved 1) starting from a random vector (— line) and 2) using the linear combination of the eigenvectors obtained at the previous FP iteration as initial vector (–◦– line). Although both algorithms are mathematically equivalent, their numerical implementations yield to different convergence behaviors, which is not surprising. The residuals plotted in Fig. 4.19 show how the number of iterations needed for the solution of each linear eigenproblem is reduced by simply starting from a linear combination of previous eigenvectors. Logically, the savings become more important as the FP iterations converge, since the starting vector contains increasingly accurate information about the invariant subspace to be computed. In Tab. 4.14 appear the total time taken by ARPACK and KS to perform the 3 FP iterations with and without the recycling strategy. At the end of the 3rd FP iteration, when the nonlinear eigenfrequency ω_1 can be considered as converged, savings of around 40% in time are obtained thanks to this simple recycling procedure.

	without recycling	with recycling	Time savings (%)
ARPACK	18.24 s	11.09 s	39.2
KS	17.46 s	11.06 s	36.7

Table 4.14: Test case A: Total time spent by ARPACK and KS during the 3 FP iterations corresponding to Fig. 4.19 for the computation of the first nonlinear eigenfrequecny ω_1, with and without the recycling strategy.
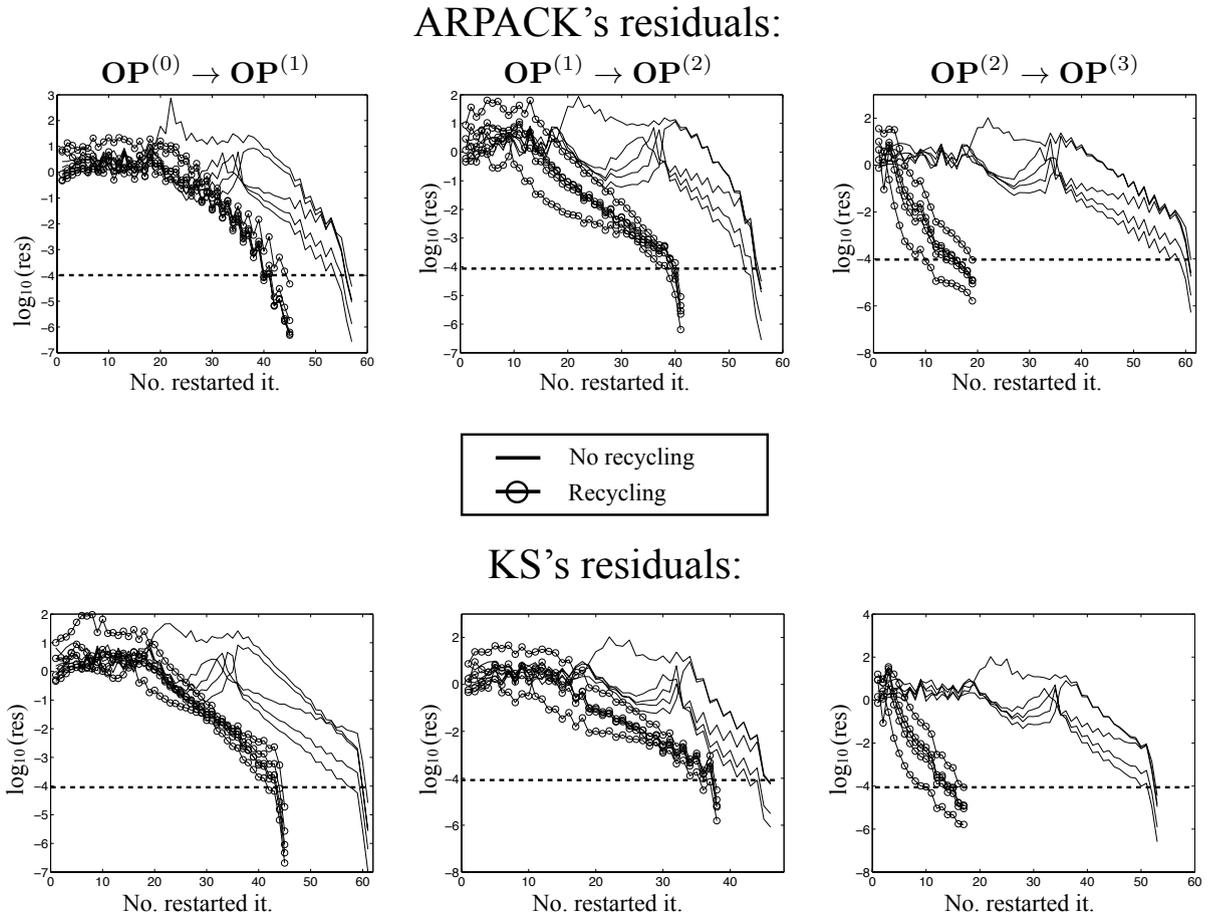
Figure 4.19: Test case A: Residuals corresponding to the $nev = 5$ smallest magnitude eigenpairs of the sequence of linear problems $\mathbf{OP}^{(1)}$, $\mathbf{OP}^{(2)}$ and $\mathbf{OP}^{(3)}$ solved with $tol = 10^{-4}$ for the computation of the smallest magnitude nonlinear eigenfrequency ω_1. ($-\circ-$): with recycling strategy; ($-\!\!-$) without recycling strategy.

4.3.4 Jacobi-Davidson method for recycling eigensolutions

Starting from a single vector, the Jacobi-Davidson method can be used to build the search space solving iteratively the correction equation. Nevertheless, if the initial vector does not contain any particular information on the solution (which is the case in general), the convergence of the method can be very erratic at the beginning, until the method is able to "focus" on the region of interest around the target τ. In practice, certain Jacobi-Davidson algorithm implementations use the initial vector to build first an Arnoldi basis of a given size k and then the Jacobi-Davidson method is used to go on with the process and extend the search subspace up to a size m, before restarting. In general, this improves the convergence of the method. In our case, within the context of the FP procedure, the solution of the previous FP iteration offers something better than an Arnoldi basis built from a random vector. Thus, to solve the linear problem $\mathbf{OP}^{(j)}\bar{p} = -\omega^{(j)^2}\bar{p}$, the following procedure is proposed in order to initialize the JDQR solver, taking advantage of the eigenvectors $P^{(j-1)}$ obtained at the previous FP iteration:

1. The problem $\mathbf{OP}^{(j-1)}\bar{p} = -\omega^{(j-1)2}\bar{p}$ corresponding to the $(j-1)^{th}$ FP iteration was solved and *nev* eigenpairs $(\omega^{(j-1)}, \bar{p}^{(j-1)})$ were computed.

2. An orthonormal basis U_{nev} of $P^{(j-1)} = [\bar{p}_1^{(j-1)}, ..., \bar{p}_{nev}^{(j-1)}]$ is computed with its associated Rayleigh quotient $C_{nev} = U_{nev}^H \mathbf{OP}^{(j)} U_{nev}$. Then the Rayleigh-Ritz procedure extracts an approximate eigenpair $(\tilde{\omega}, \tilde{p})$ closest to the target τ.

3. The JDQR algorithm is then used to extend C_{nev}, U_{nev} until *nev* eigenpairs have converged.

JD's residuals:
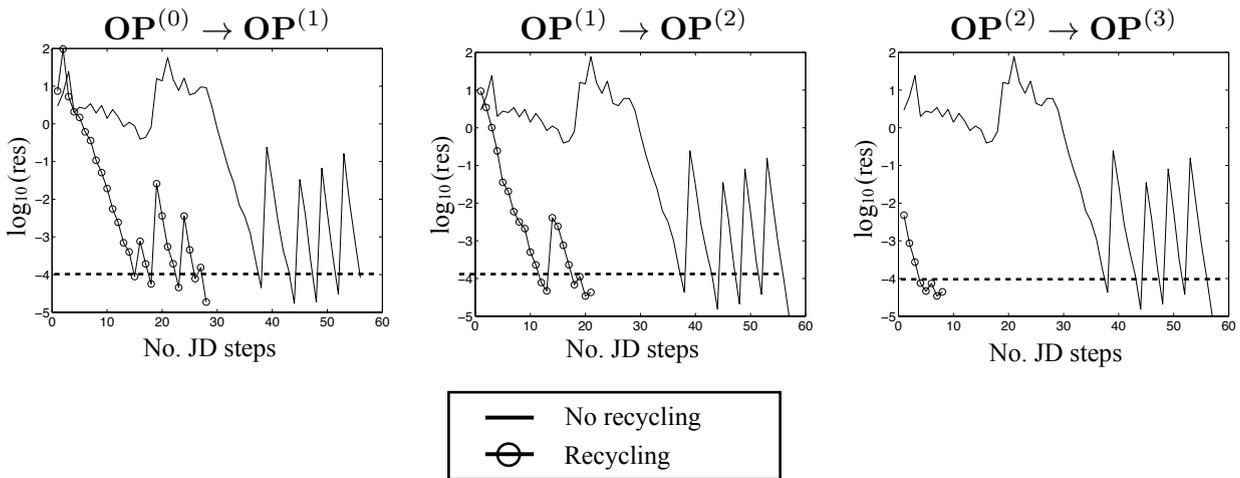
Figure 4.20: Test case A: Residual curves corresponding to the computation of the *nev* = 5 smallest magnitude eigenpairs of the linear problems $\mathbf{OP}^{(1)}$, $\mathbf{OP}^{(2)}$ and $\mathbf{OP}^{(3)}$ solved with *tol* = 10^{-4} for the computation of the smallest magnitude nonlinear eigenfrequency ω_1. (–∘–): with recycling strategy; (——) without recycling strategy.

The smallest magnitude nonlinear eigenvalue ω_1 of test case A with active flame is computed the with JDQR solver, with and without the recycling strategy. Again, the 5 smallest magnitude linear eigenvalues are computed at every FP iteration with *tol* = 10^{-4}. Fig. 4.20 plots the convergence history of the residual norm (normalized by the magnitude of the corresponding eigenvalue) for every FP iteration (starting from the solution of the problem without active flame). Without recycling, each linear eigenproblem requires almost 60 JD steps to converge to the 5 smallest magnitude eigenvalues. On the other hand, when the previous solutions are exploited, the number of required JD steps is reduced drastically, with a progressive gain as the FP procedure converges to the nonlinear eigenpair ω_1.

The savings obtained thanks to the recycling strategy are remarkable, specially at the latest FP iterations. Tab. 4.15 contains the cumulated time for the 3 FP iterations computed with JDQR solver with and without recycling. The results show that, in this particular case, 70% of the total time can be saved by exploiting previous eigensolutions.

A potential advantage of JD algorithm respect with the Krylov methods is that, in order to compute the ith nonlinear eigenpair of Eq. (4.3), it is not necessary to compute (at least)

	without recycling	with recycling	Time savings (%)
JD solver	13.0 s	3.9 s	70

Table 4.15: Test case A: Total time spent by JDQR during the 3 FP iterations of Fig. 4.20 for the computation of the smallest magnitude nonlinear eigenvalue ω_1, starting from a random vector and taking advantage of the solutions previously computed.

i linear eigenpairs at each FP iteration, as it would be the case when using a Krylov solver. Instead, only a few eigenpairs $nev < i$ closest to the target τ can be computed at each nonlinear iteration, saving an important amount of work. Note, however, that when the target τ is interior to the spectrum (what happens when the wanted nonlinear eigenpair $(\omega_i, \bar{p}_i)$ has a corresponding index i equal to a few tens), the convergence of the JD solver can deteriorate so that computing only a few ($k < i$) eigenpairs nearest the target τ with JD becomes more expensive than using a Krylov method for computing a larger number ($nev \geq i$) of eigenpairs. In any case, it is not possible to give general rules to use the eigensolvers optimally, which comes with experience.

4.3.5 Chebyshev subspace iteration

The last strategy investigated here for recycling eigenspaces, is the use of the subspace iteration method with Chebyshev acceleration. As exposed in Chapter 3, this method is a subspace iteration accelerated by using Chebychev filter polynomials of degree k. In practice this means that a certain amount of information about the spectrum is needed in order to build the "optimal" ellipse associated with the Chebyshev filter polynomial.

The procedure proposed here to compute a nonlinear eigenpair using the Chebyshev subspace iteration during the FP procedure is the following: construct an ellipse based on the spectrum of $OP^{(1)}$ and, since the spectrum between successive linearized matrix does not change drastically (e.g., Fig. 4.16 and Fig. 4.21), use this ellipse for the rest of the FP iterations. In order to compute the Chebyshev filter polynomial, the semi-axis a, b of the associated ellipse, and an estimation λ_1 of the smallest magnitude eigenvalue for normalization purposes (see Chapter 3) are needed. In order to obtain these quantities, some previous computations are performed:

1. The first fixed point iteration ($\mathbf{OP}^{(1)}$) is solved using any other solver (ARPACK, KS or JD) in order to obtain the nev smallest magnitude eigenvalues. This provides the necessary right-side limit of the ellipse.[3]

2. Compute the largest magnitude eigenvalue and the eigenvalue with the largest magnitude imaginary part of $\mathbf{OP}^{(1)}$, which provides the left-side limit and a lower bound of the semi-axis b. These eigenvalues lay in the periphery of the spectrum, so their computation is expected to be cheap.

---

[3]As it is shown later in this section, the right-side limit of the ellipse (the one closest to zero in the present work) does not play a very important role for the convergence of the method. It can be then roughly estimated, for example, from the solution of $OP^{(0)}$.

Test case A is used in the following in order to evaluate the pertinence of this approach to recycle previous solutions during the nonlinear iterations for the computation of the smallest nonlinear eigenvalue ω_1. At every FP iteration, 10 smallest magnitude eigenpairs of the linear eigenproblem $\mathbf{OP}^{(j)}\bar{p} = -\omega^{(j)2}\bar{p}$ are computed. Fig. 4.21 shows the spectrum
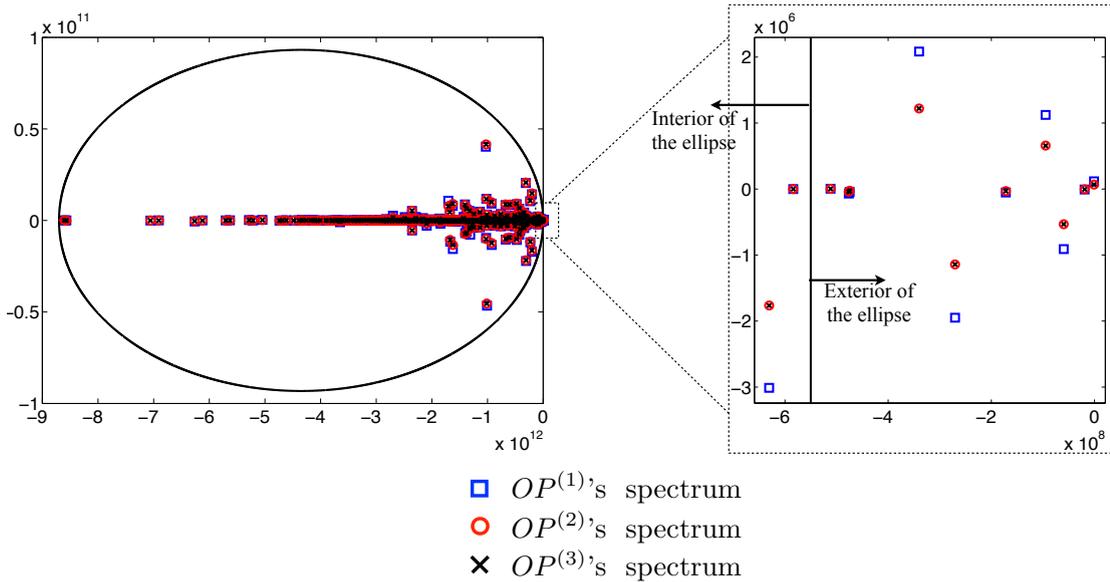

Figure 4.21: Spectrum of the matrices $\mathbf{OP}^{(1)}$, $\mathbf{OP}^{(2)}$ and $\mathbf{OP}^{(3)}$ obtained from the successive fixed point iterations when converging the smallest non linear eigenvalue ω_1. In black the ellipse used for the Chebyshev filter polynomial, containing the unwanted part of the spectrum.

of the matrices $\mathbf{OP}^{(1)}$, $\mathbf{OP}^{(2)}$ and $\mathbf{OP}^{(3)}$ for test case A. The spectra of the successive linearized operators are very similar to each other, so that the ellipse obtained considering the spectrum of $\mathbf{OP}^{(1)}$ is used for the other FP steps as well. The Chebyshev subspace iteration method is used for solving each linearized eigenproblem, starting from an initial subspace $U_m^{(0)}$ of size $m > nev$ that contains the $nev = 10$ eigenvectors obtained at the previous FP iteration and which is completed with random vectors.

4.3.5.1 Influence of the subspace size m and the polynomial degree k

The 10 smallest magnitude eigenvalues of the matrices $\mathbf{OP}^{(1)}$, $\mathbf{OP}^{(2)}$ and $\mathbf{OP}^{(3)}$ are computed using the solution of the previous FP iteration in each case. The influence of the search subspace size m and the degree of the Chebyshev filter polynomial k are studied. It is recommended when using a subspace iteration method, taking the size of the search subspace $m > nev$, which improves the convergence in general [129]. In order to solve $\mathbf{OP}^{(j)}\bar{p} = -\omega^{(j)2}\bar{p}$, the initial subspace U_m^0 is formed with the $nev = 10$ eigenvectors $P^{(j-1)}$ of the previous FP step and it is completed with random vectors up to m. The computational costs of each FP iteration (number of subspace iterations, number of matrix/vector products and runtime in seconds) are plotted in Fig. 4.22.

The runtime gets smaller as the FP method proceeds, showing that the recycling strategy gets more effective i.e., the better the initial approximation to the solution is (as it is the

case for the other recycling strategies). The curves in Fig. 4.22 show that, in general, taking the subspace size m too large makes the computation longer, which means that the optimal value of m, for this particular case, must be taken closer to the number of wanted eigenvalues ($nev = 10$). Concerning the polynomial degree k, the results plotted in Fig. 4.22 suggests that the degree polynomial must be taken large ($k \approx \mathcal{O}(100)$), although there is an optimal value of k beyond which the performance will be penalized. This conclusion is also valid for the subspace size m. It must be notice the large amount of matrix/vector products performed in each case (matvec $\approx \mathcal{O}(10^4 - 10^5)$).
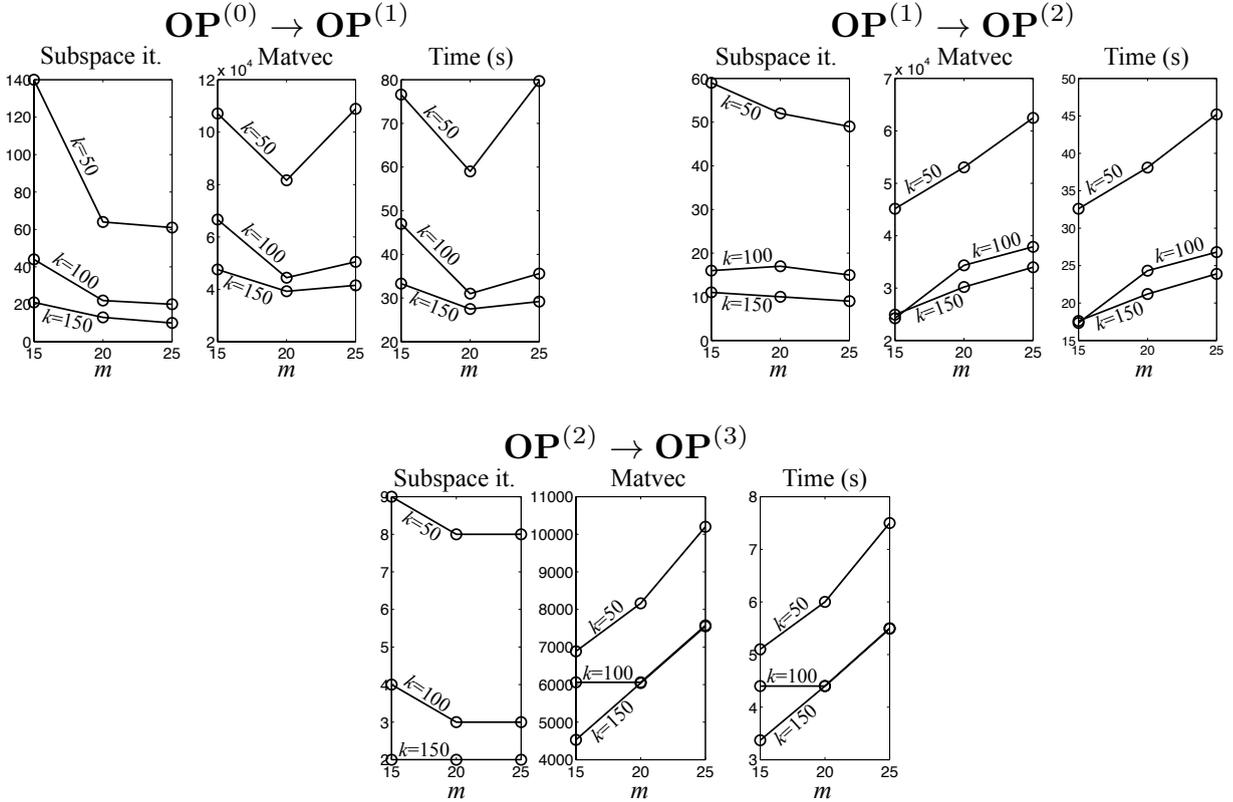
Figure 4.22: Test case A: Computational cost (number of restarted iteration, matrix/vector products and runtime) of the computation of 10 smallest magnitude eigenvalues associated with the sequence of linear problems $\mathbf{OP}^{(1)}$, $\mathbf{OP}^{(2)}$ and $\mathbf{OP}^{(3)}$ obtained during the computation of the smallest magnitude nonlinear eigenvalue ω_1 (k: degree of the Chebyshev polynomial; m: size of the subspace).

4.3.5.2 Influence of the ellipse

The influence of the chosen Chebyshev ellipse on the convergence of the method is investigated in the following. The ellipse of Fig. 4.21 is kept as the reference case. Respect to the reference ellipse four variations are considered:

1. Ellipse 1: the right-side limit of the ellipse as well as its semi-axis b are kept constant while the left side is moved further to the left. With respect to the reference case,

although the unwanted part of the spectrum is the same, the area of the ellipse is incremented.

2. Ellipse 2: keeping constant the other limits, the right-side limit is moved to the right, so that many wanted eigenvalues get into the ellipse.

3. Ellipse 3: as ellipse 2 but the right-side is displaced to the left instead, leaving outside the ellipse some unwanted eigenvalues.

4. Ellipse 4: the semi-axis b is increased. The unwanted eigenvalues remain in the ellipse but the area of the ellipse is incremented.

The linear problem $\mathbf{OP}^{(2)}\bar{p} = -\omega^{(2)2}\bar{p}$ is solved starting from the eigenvectors $P^{(1)}$ (and completing the subspace with random vectors up to $m = 25$) using the four ellipses of Fig. 4.23 to computed the Chebyshev filter polynomial in each case.
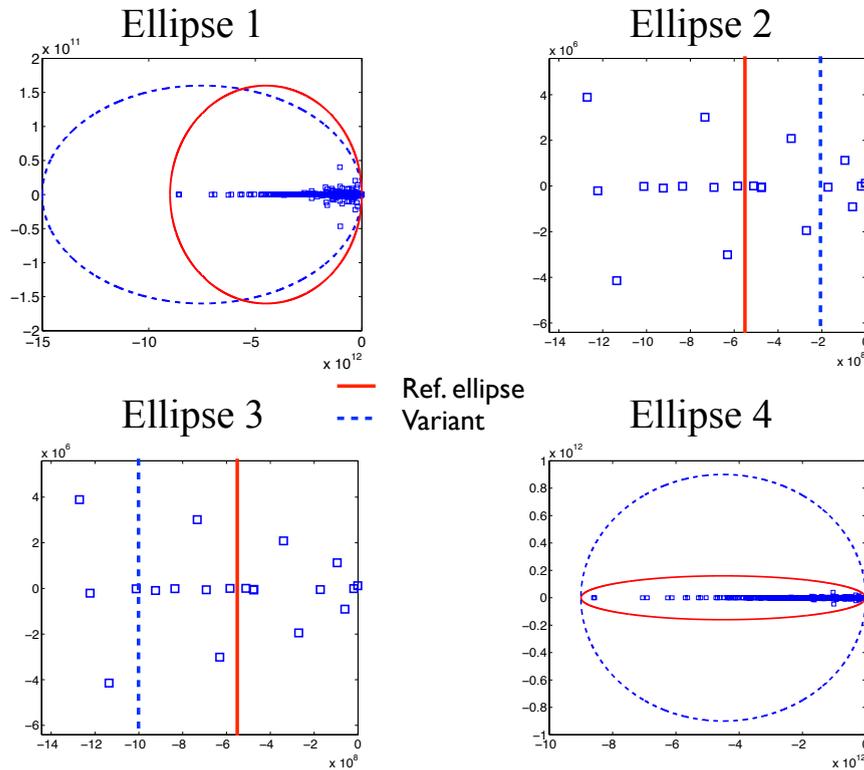
Figure 4.23: Four variations $(--)$ with respect to the reference ellipse $(—)$ used to investigate the influence of the quality of the ellipse on the method's convergence.

The normalized residual norms corresponding to computation of the $nev = 10$ smallest magnitude linear eigenvalues of $\mathbf{OP}^{(2)}$ are plotted in Fig. 4.24, for $m = 25$ and $k = 150$. In each case, the residual curves are plotted for the reference ellipse and the variant one. The tolerance is set to $tol = 10^{-6}$. The results in Fig. 4.24 show that the area of the ellipse plays an important role on convergence: the ellipse must be chosen the smallest as possible as long as it encloses the unwanted part of the spectrum, which is in agreement with the theoretical observations in [129]. In the context of this work, choosing an optimal ellipse
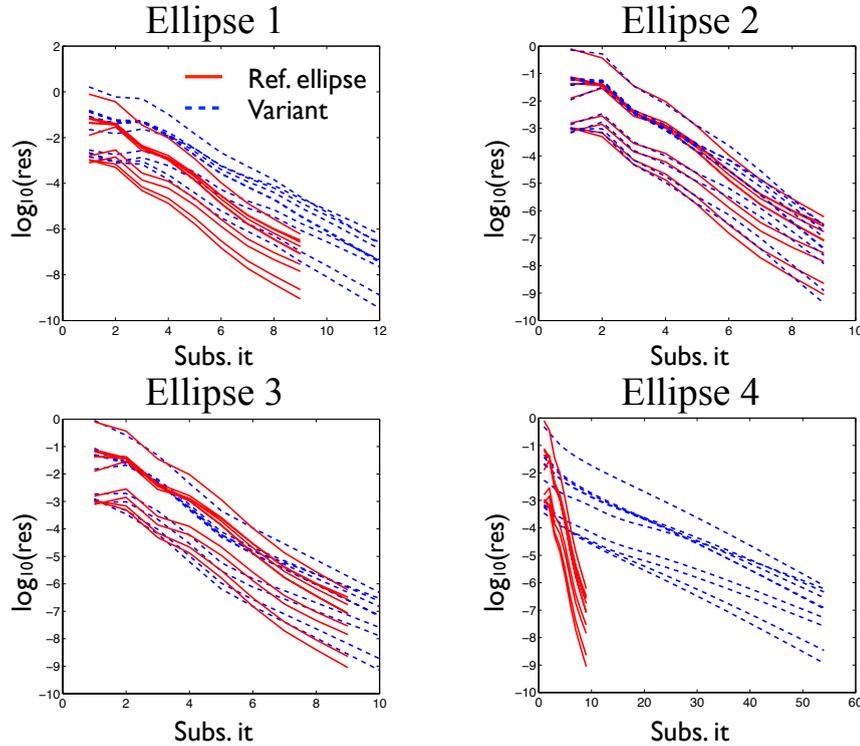
Figure 4.24: Residuals corresponding to the four different ellipses considered before for the computation of the corresponding Chebyshev polynomials. (– –) Residuals of the modified ellipse. (—) Residuals of the reference ellipse.

is not possible, since no accurate information about the complete spectrum is available in general. For example, the semi-axis b is chosen conservatively larger than the imaginary magnitude of the eigenvalue with the largest imaginary part in order to be sure that the ellipse encloses the unwanted eigenvalues. On the other hand, the right limit of the ellipse does not play an important role on the convergence rate, as far as it cuts the real axis around the area of interest.

4.3.5.3 Comparison with the Krylov-Schur solver

The comparison between the Chebyshev subspace iteration method and the KS solver is done for two implementations: a Fortran implementation in AVSP (for which the former results have been obtained) and a Matlab version of both solvers.

The second iteration of the FP iteration $\mathbf{OP}^{(2)}\bar{p} = -\omega^{(2)^2}\bar{p}$ is solved with both methods, recycling in each case the solution of the previous FP step in order to compute $nev = 10$ linear eigenpairs. The search subspace maximum size m is set to 60 for the KS solver, and 15 in the case of the Chebyshev subspace iteration method[4] (referred to as SI). The comparison is not performed keeping constant the search subspace size m, but choosing an optimal value for each one of the solvers, so that they are both working in their respective

---

[4]The initial subspace is formed by 10 eigenvectors obtained for $\mathbf{OP}^{(1)}$ and completed with 5 random vectors.

"comfort zones". The convergence threshold *tol* is set to 10^{-4} for both solvers, and the polynomial degree $k = 150$ for the SI solver.

|	Fortran		Matlab	
	KS	SI	KS	SI
Restarted it. / Subspace it.	45	11	45	13
Matvec.	2237	24915	2237	29445
$\frac{Time(KS)}{Time(SI)}$	$\frac{3.50}{17.48} = 0.2$		$\frac{22.9}{4.32} = 5.3$	

Table 4.16: Computational cost of computing 10 smallest magnitude linear eigepairs of $\mathbf{OP}^{(2)}\bar{p} = -\omega^{(2)^2}\bar{p}$ with KS and SI solvers for both the Fortran and the Matlab implementations. Both solvers reuse the solution of the previous FP iteration.

The results are shown in Tab. 4.16. The difference in terms of number of subspace iterations between the Fortran and the Matlab implementation of SI are due to the fact that the random vectors used in each case are different, leading to different convergence behaviors. The number of required matrix-vector products in the case of the Chebyshev subspace iteration method is about 11-12 times the number of matrix-vector products required by the KS solver. This explains the opposite behaviors in terms of runtime between the two implementations: for the SI solver, when the filter polynomial is applied to the vectors U_m of the search basis, in the case of the Fortran implementation (within the AVSP code), only one matrix-vector product can be performed at a time (BLAS 2 type implementation); while the Matlab implementation allows to perform sparse matrix-matrix products (BLAS 3 efficiency) so that the filter polynomial can be applied simultaneously to all the m vectors U_m. Consequently, in Matlab the matrix-vector products are very effective and less time consuming, so that the SI solver is more efficient than the KS solver. On the other hand, concerning the Fortran implementation of both methods, the KS method is faster than the SI solver since the matrix-vector product is much more expensive than in Matlab. In conclusion, due to the current matrix-free implementation in AVSP, the Chebyshev subspace iteration algorithm is not competitive compared to other methods (such as the KS solver). Nevertheless, if performing matrix-matrix products in a efficient fashion becomes possible in AVSP, the Chebyshev subspace iteration algorithm appears as a very interesting alternative to recycling solutions during the FP procedure.

4.4 Mesh quality and convergence

The value of the non zero elements of the matrix $\mathbf{A}$ arising from the discretization of the operator $\nabla \cdot c_0^2 \nabla$ depends on the discrete nodal values of c_0 and on the mesh geometrical parameters, notably the volume V_j of the dual cells associated with each node j (see Chapter 2). As far as the employed mesh allows the correct discretization of the geometry in order to capture the smallest required wavelength, the obtained eigenfrequencies and the corresponding eigenmodes of the configuration in question are practically independent of

the mesh. Nevertheless, since the mesh determines the entries of the matrix $\mathbf{A}$, it plays a role in the computation of the acoustic modes associated with the lowest frequencies.
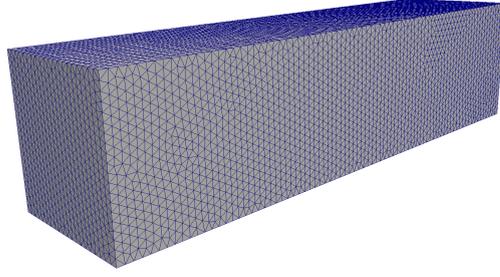
M1: 222857 cells

41944 nodes

$$\frac{V_{cell}{}^{max}}{V_{cell}{}^{min}} = 9.69$$
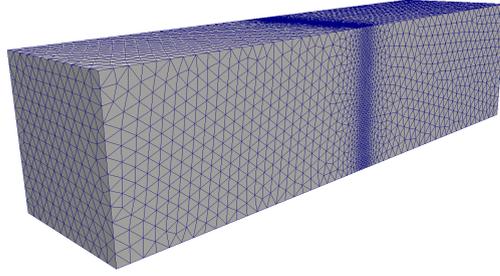
M2: 242387 cells

44463 nodes

$$\frac{V_{cell}{}^{max}}{V_{cell}{}^{min}} = 1806.13$$
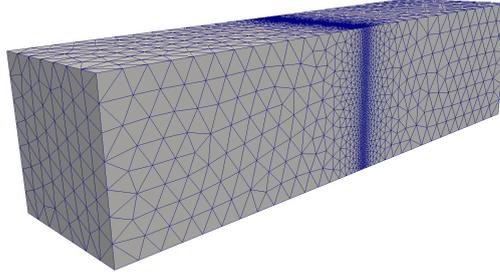
M3: 209385 cells

38092 nodes

$$\frac{V_{cell}{}^{max}}{V_{cell}{}^{min}} = 15440.54$$

Figure 4.25: Three meshes M1, M2, M3 with increasing maximum/minimum volume cell ratio.

The quality of the mesh plays an important role on the convergence of the linear eigensolver for the solution of $\mathbf{OP}\bar{p} = -\omega^2\bar{p}$. In the present context, the quality of the mesh depends on the volume ratio between the biggest and the smallest cells. To investigate this behavior a very simple geometry consisting in a 3D rectangular box $(0.25 \times 0.25 \times 1 \; m)$ is used. It is discretized using 3 different meshes (Fig. 4.25): M1, M2 and M3. Since the mesh size determines the eigenproblem size, the three meshes have roughly a similar number of elements, so that the comparison between them can be considered independent of the problem size N. The ratio

$$R_v = \frac{V_{cell}{}^{max}}{V_{cell}{}^{min}}$$

becomes larger from M1 to M3, so that M1 is the most homogeneous (better quality) and M3 is the most heterogeneous (worst quality). The soundspeed field $c_0(\vec{x})$ is constant in space $(c_0 = 2347m/s)$ so it does not play any role on the scaling of the matrix $\mathbf{A}$. For the sake of simplicity, the boundary conditions are set to $u' = 0$ ($\mathbf{B}(\omega) = 0$), and no active flame is considered. The 10 smallest magnitude eigenpairs of the associated linear eigenproblem

$$\mathbf{A}\bar{p} = -\omega^2\bar{p}$$

are computed for the three meshes using the KS and the JDQR solvers with $tol = 10^{-6}$ and $m = 60$. The values of the first 10 eigenfrequencies obtained for each mesh appear in Tab. 4.17. The discrepancies between the values get larger for higher frequencies, due to the poor discretization of transverse directions associated to these frequencies for the meshes M2 and M3. The runtime and the number of matvec are plotted in Fig. 4.26

ω_i (Hz)	M1	M2	M3
1.	≈ 0	≈ 0	≈ 0
2.	173.59	173.59	173.58
3.	347.13	346.97	346.59
4.	520.58	520.44	519.75
5.	693.89	692.68	690.46
6.	693.89	692.87	690. 52
7.	693.90	692.94	690.73
8.	715.22	713.84	711.06
9.	715.22	713.96	711.08
10.	775.67	774.66	772.12

Table 4.17: 10 smallest magnitude eigenfrequencies obtained using the meshes M1, M2 and M3. Since the rigid wall B.C. $u' = 0$ is used for all the patches, the first frequency is null (rigid body mode).
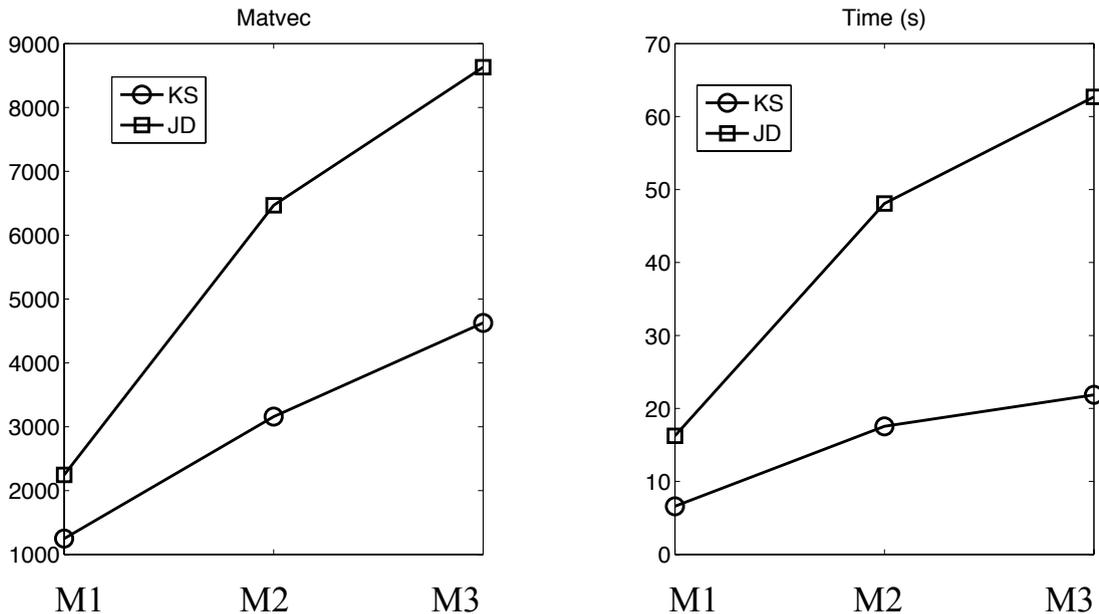

Figure 4.26: Runtime and matvec when computing the 10 smallest magnitude eigenvalues for the rectangular box, using KS and JD solvers ($tol = 10^{-6}$ and $m = 60$) for meshes M1, M2 and M3.

The results are very clear: using a mesh as homogeneous as possible improves the convergence speed of the eigensolver. In this particular case, KS is faster than JD, but the convergence of both methods are penalized in a similar way depending on the used mesh. From the eigensolver point of view, it is faster solving a larger problem using a homogeneous mesh rather than solving a small problem using a heterogeneous mesh.

4.5 Parallel implementation of the algorithms

The AVSP code is designed to perform simulations on real combustion chambers with complex geometries whose discretization leads to large meshes (the number of nodes $N \approx \mathcal{O}(10^6)$). In this context, using large parallel platforms becomes mandatory. The parallel implementation strategy followed in this work is based on the partitioning of the mesh, since it defines the size of the problem and governs most of the calculation. Therefore, in the present context, the parallel approach consists in splitting the complete mesh into sub-meshes so that each processor is in charge of one sub-mesh.

The most computationally intensive building boxes of all the eigensolvers considered in this work are the numerical kernels working on large vectors (of size N) defined on the complete mesh. Namely, the sparse matrix-vector product and the dot product calculations are the kernels parallelized here. The computations involving smaller matrices, e.g. the Hessenberg or Rayleigh quotient matrices, are replicated on all the processors and the required operations are performed redundantly on each processor. The motivation for these redundant calculations is actually to reduce the communication volume, which constitutes a well-known performance bottleneck on high performance computers.

Based on the mesh partitioning, the parallel matrix-vector product $y = \mathbf{OP}x$ is implemented in two steps. First, all processor exchange the values of x along their interfaces with the other neighboring processors and second, a local sparse matrix-vector product is performed. This computational kernel involves neighbor to neighbor communication using two-sided MPI routines. It is implemented using subroutines inherited from AVBP [126, 138].

The dot product calculation is also performed classically: all processors compute a dot product on their local entries of the vectors and then a MPI reduction is used to compute the final result. Because it involves a global synchronization among all the processors, the dot product calculation (and norm calculations as a particular case of dot products) is a well known bottleneck on high performance computers. This is the reason why, when orthogonalization schemes need to be implemented, the choice here is using the classical Gram-Schmidt with selective re-orthogonalization, which exhibits the best trade-off between numerical quality and parallel performance. When the QR factorization of a tall and skinny matrix is required, such as in block Krylov or subspace iteration methods, we still use this Gram-Schmidt variant, while a QR avoiding-communication algorithm [32] might have been worth considering.

In order to illustrate the parallel implementation in AVSP of the algorithms described in Chapter 3, a scalability study has been performed, using (P)ARPACK (which is considered the reference) and the implemented versions of the Krylov-Schur and the Jacobi-Davidson solvers. The test case corresponds to the industrial case described in Chapter 6. No active

flame or complex boundary conditions are considered. Therefore, a linear eigenproblem of size $n = 1,782,384$ is solved using the three eigensolvers in order to compute $nev = 10$ smallest magnitude eigenvalues. The maximum size of the search subspace is chosen equal to $m = 120$ for the three solvers, so that the study is roughly iso-memory[5]. The convergence threshold is set equal to $tol = 10^{-4}$ for the three solvers.
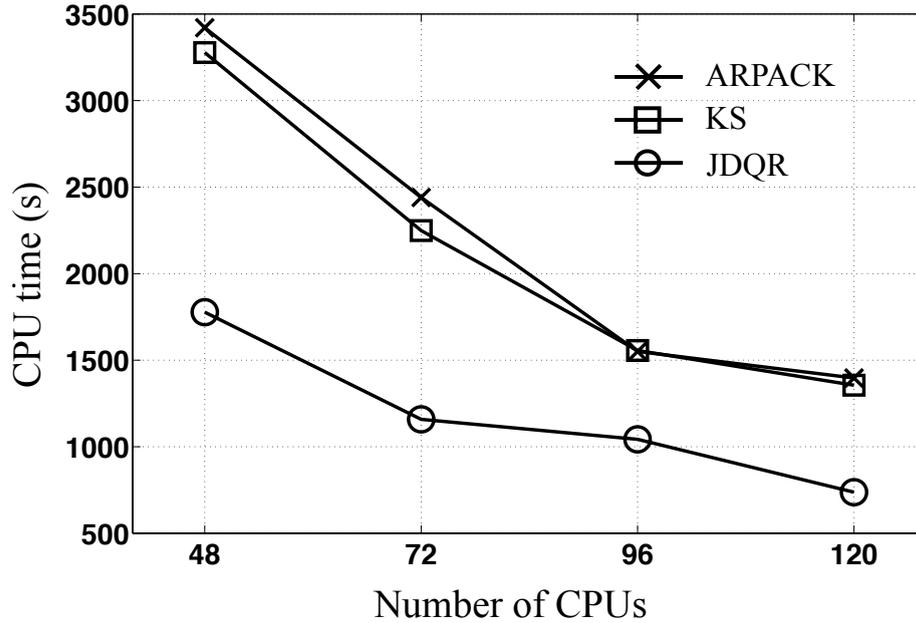

Figure 4.27: Scalability study: for the case described in Chapter 6, evolution of the computational cost as a function of the number of processors for (P)ARPACK, KS and JDQR solvers ($nev = 10$, $m = 120$ and $tol = 10^{-4}$ for the three eigensolvers).

Fig. 4.27 displays the runtime required by the three eigensolvers for the computation of 10 smallest magnitude eigenvalues, for different number of processors (48, 72, 96 and 120). Taking ARPACK as the reference, the results of Fig. 4.27 shows that the implementations of the KS solver is slightly faster than ARPACK while the JDQR solver is much faster.

Concerning the scalability of the different algorithms, Tab. 4.18 displays the efficiency for each number of processors (taking 48 processors as the reference), computed as:

$$\text{Efficiency} = \frac{\text{time (48 procs)}}{\text{time (}p\text{ procs)}} \frac{48}{p}. \tag{4.6}$$

In the ideal case where the algorithms scale perfectly, Eq. (4.6) gives 1. The results displayed in Tab. 4.18 shows that the parallel implementations of the three algorithms present very good scalability. Scalability efficiencies greater than 1 are probably due to memory hierarchy effects.

---

[5]The memory needed by both ARPACK and KS solvers is ideally the same whereas the amount of required memory is slightly larger in the case of the JDQR solver due to the memory allocation required by GMRES for the solution of the correction equation.

	72 procs	96 procs	120 procs
ARPACK	0.93	1.1	0.98
KS	0.97	1.05	0.97
JDQR	1.02	0.85	0.96

Table 4.18: Scalability efficiency computed using Eq. (4.6) for the three algorithms (ARPACK, KS and JDQR) for each number of processors.

4.6   Some comments

Three small test cases have been used in this chapter to investigates the use of the available solvers in AVSP for the solution of the nonlinear eigenproblem Eq. (4.3). This has allowed to establish some trends on how to use optimally these numerical tools. During this work an important number of cases has been solved using AVSP and the experience shows that there does not exist a "best for everything" eigensolver and that the optimal strategy depends on each particular case. Nevertheless, from experience, it is possible to give some general advice:

- If the number of wanted eigenvalues *nev* is larger than 5-10, in general, choosing a Krylov solver is the best option, since they intend to converge the wanted eigenpairs simultaneously. On the other hand, the Jacobi-Davidson algorithm finds eigenpairs one after the other, so that if *nev* is large it will take longer in general, specially if the requested tolerance *tol* is low (e.g. $tol \leq 10^{-6}$).

- For the computation of a nonlinear eigenvalue, a standard procedure would be: 1) solving the associated linear problem (without active flame and/or complex boundary conditions) in order to obtain a good initial guess; 2) then apply any of the recycling strategies during the FP procedure for solving the nonlinear problem (with combustion and/or complex boundary conditions), starting from the solutions of the linear problem.

- For computing interior eigenvalues, two options are available: 1) using JD to find the eigenvalues closest to the target τ or 2) using a Krylov solver to find the smallest magnitude eigenvalues of the shifted matrix $(\mathbf{OP} - \tau I)$. In either case, the convergence can be difficult to reach if τ is "very interior". A third option consists in using the KS solver with harmonic extraction considering the harmonic shift τ. As seen, the convergence of this method is subject to choosing τ far enough from an actual eigenvalue (which is obviously not known a priori).

Part III

Thermoacoutic instabilities in annular combustion chambers

Chapter 5

Stability and nature of azimuthal modes in annular combustion chambers

Contents

Today, most modern gas turbines have annular combustion chambers. Low frequency thermoacoustic modes very often take the form of azimuthal modes in annular combustors

since the azimuthal direction is often associated to a larger spatial dimension than the radial direction. Therefore, the study of azimuthal modes is of first importance.

In this chapter, azimuthal modes in an annular academic configuration are investigated, and more precisely, the effect of the azimuthal symmetry of the configuration on the stability and nature of azimuthal modes. Although this work is focused on the 3D Helmholtz solver AVPS, in this chapter an analytical tool called ATACAMAC for the study of azimuthal modes is also introduced: this analytical method has been developed at CERFACS by Parmentier et al. [111, 10]. The reason for this is that the results obtained using AVSP may be difficult to analyze to extract phenomenological conclusions. The analytical expressions provided by ATACAMAC constitute an excellent tool that provides, on one hand, fast results and on the other hand, a theoretical interpretation of the results obtained with AVSP.

Sec. 5.1 introduces previous works concerning the study of azimuthal modes and the motivation of the study performed in this chapter. Sec. 5.2 describes the $N = 24$ burners academic annular combustor used for the study of azimuthal modes with AVSP and ATA-CAMAC. In Sec. 5.3, the main aspects of the analytical tool ATACAMAC for the study of general non-symmetric annular configurations are introduced. More details concerning the obtaining of the analytical expressions can be found in the Appendix. Sec. 5.4 constitutes a phenomenological analysis of the effect of the configuration symmetry on the nature of azimuthal modes. The academic $N = 24$ burners configuration is studied in Sec. 5.5 using both AVSP and ATACAMAC, showing a very good agreement. Symmetry braking is performed and its effect on azimuthal modes stability and nature is investigated in order to illustrate the concepts previously introduced in the chapter. Some concluding remarks are given in Sec. 5.6.

5.1 Background

In modern gas turbine combustion chambers, azimuthal modes appear at low frequencies and often couple with unsteady heat release fluctuations, leading to thermoacoustic instabilities which can be dangerous. Therefore the study of azimuthal modes in annular combustion chambers has become a very active research topic in the last years [158, 70, 71, 174, 171, 90, 46, 40]. Azimuthal modes can be standing, spinning or mixed and they can be seen as the combination of two traveling waves, traveling in clockwise A^+ and counter clockwise direction A^-. The ratio of the amplitudes of the turning waves A^+/A^- determines the nature of the corresponding azimuthal mode [111].

The azimuthal symmetry of the configuration can play a role in the stability and nature of azimuthal modes and can be used as an additional degree of freedom to control unstable modes. In [105] the authors propose to reduce the symmetry order of the configuration using baffles to prevent combustion instabilities in F-1 rocket engines [30]. Stow and Dowling [159] used Helmholtz resonators in order to break the circumferential symmetry on an annular academic test bench. Recently, Moeck et al. [90] and Gelbert et al. [46] performed experiments in a annular Rijke tube with 12 heating grids acting like flames. They introduced azimuthal variations by feeding the heating grids with different power inputs, which

modified the azimuthal modes behavior. Notably, the staging pattern could split nominally degenerate azimuthal modes (doublets) with the same frequency and growth rate, into non-degenerate pairs (singlets). This behavior was already described by Perrin and Charnley [114], who proposed a theoretical approach based on group symmetry theory in order to explain bell structural vibration modes. Introducing a certain degree of asymmetry in the bell structure can suppress the phenomenon of bell warble. In [41], Evesque et al. introduced the spin-ratio, an analytical parameter to discriminate spinning modes from standing ones, but they did not provide prediction of the mode nature. Noiray et al. [100] study the effect of azimuthal staging on the thermoacoustic behavior of annular chambers theoretical and numerically, taking into account nonlinear phenomena such as flame saturation. They identify key parameters of the analytical model that determine the nature of the corresponding azimuthal mode. In [140], Schuermans et al. propose a theoretical model that suggest that standing modes are observed for low amplitudes and a transition to spinning modes occurs for higher amplitudes.

The swirl mean flow can be also important, as shown in [170] by Wolf et al., where full combustor LES is performed. The authors show that the azimuthal mode switches alternately between standing and spinning, and the direction of the spinning mode is promoted by the mean swirl flow. Dawson et al. [174, 171] use clockwise/anti-clockwise swirlers in order to investigate the mean flow effect on combustion instabilities, showing a strong correlation between the bulk swirl direction and the preferential direction of the azimuthal spinning mode.
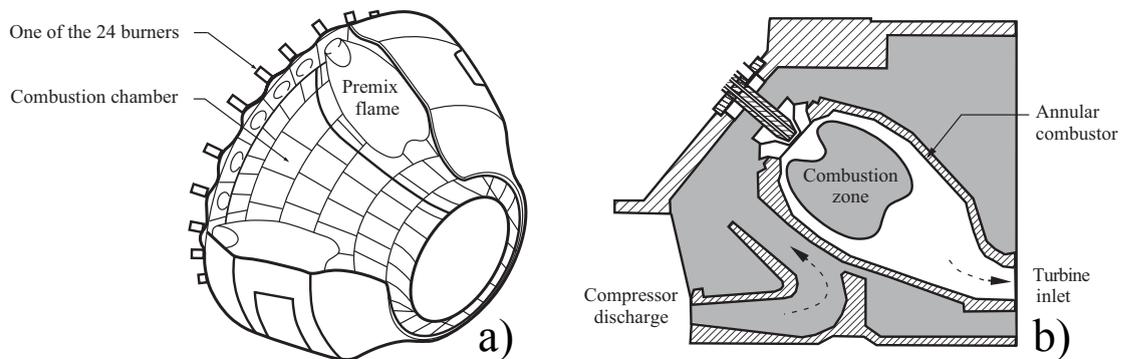
Figure 5.1: a) A sketch of the combustor used in the Vx4.3A series Siemens gas turbines. b) Longitudinal cut along the burner axis, showing the combustion chamber and the casing [30].

The simplified annular configuration used in this chapter corresponds to a schematic version of the 24 burners industrial power generator combustor studied in [30, 12, 71] (Fig. 5.1), where the first, second and fourth standing modes appeared to be unstable. A geometrical modification of the burner, referred to as Cylindrical Burner Outlet (CBO), was used in order to increase the flames time-delay τ_i by approximately a quarter of the acoustic period (Fig. 5.2 a)). Moreover, the azimuthal symmetry of the configuration was broken by misaligning the centerlines of a few of the the burner nozzles, which was found to improve the stability of the system. Berenbrink and Hoffmann [12] and Krueger et al. [71] performed symmetry breaking by mixing burners with and without CBO. As shown in Fig. 5.2 b), increasing the number of burners with CBO always improves the stability of the system (reaching larger power outputs), which, in this particular case, leads to the following
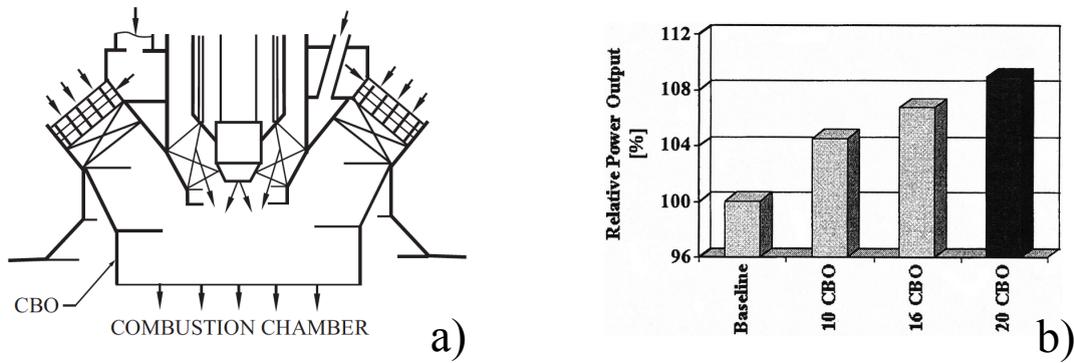
Figure 5.2: a) Siemens Hybrid burner with cylindrical burner outlet (CBO). b) Stability limits for different cylindrical burner outlet (CBO) configurations [12] Longitudinal cut along the burner axis, showing the combustion chamber and the casing [30].

question: is stabilization due to the use of CBO's or is it promoted by the symmetry breaking? The configuration described in the following section is simulated with AVSP in order to try to answer this question. The AVSP results are compared with an extension of the analytical model by Parmentier et al. [111], further developed by M. Bauerheim, currently PhD. student at CERFACS.

5.2 Description of the academic annular configuration with $N = 24$ burners

The geometry of a simplified annular chamber with N=24 burners used for the AVSP simulation is displayed in Fig. 5.3. In order to ensure mesh independency of the results, the geometry is discretized using a very fine mesh (given the simplicity of the geometry and the typical wavelength to capture). It contains 436704 nodes and 2301192 cells. A detail of the mesh of a single sector and the sound speed field is shown in Fig. 5.4. Concerning boundary conditions, impermeable walls ($u_1 = 0$) are used everywhere except at the burners inlet, where null acoustic pressure fluctuation $p_1 = 0$ is imposed, emulating the connection to a large plenum.

With the parameters specified in Tab. 5.1, the frequencies of the first 5 acoustic modes with passive flame appear in Tab. 5.2. The repeated frequencies (93.7 and 182.0 Hz) correspond to the two first degenerate azimuthal modes.

The Crocco's model (see Chapter 2) is used here for the flame model, since it is well adapted for the analytical comparison when the flames are compact [97].

a) Annular chamber with 24 burners
geometry for AVSP

b) Radial cut plane along the
burner axis
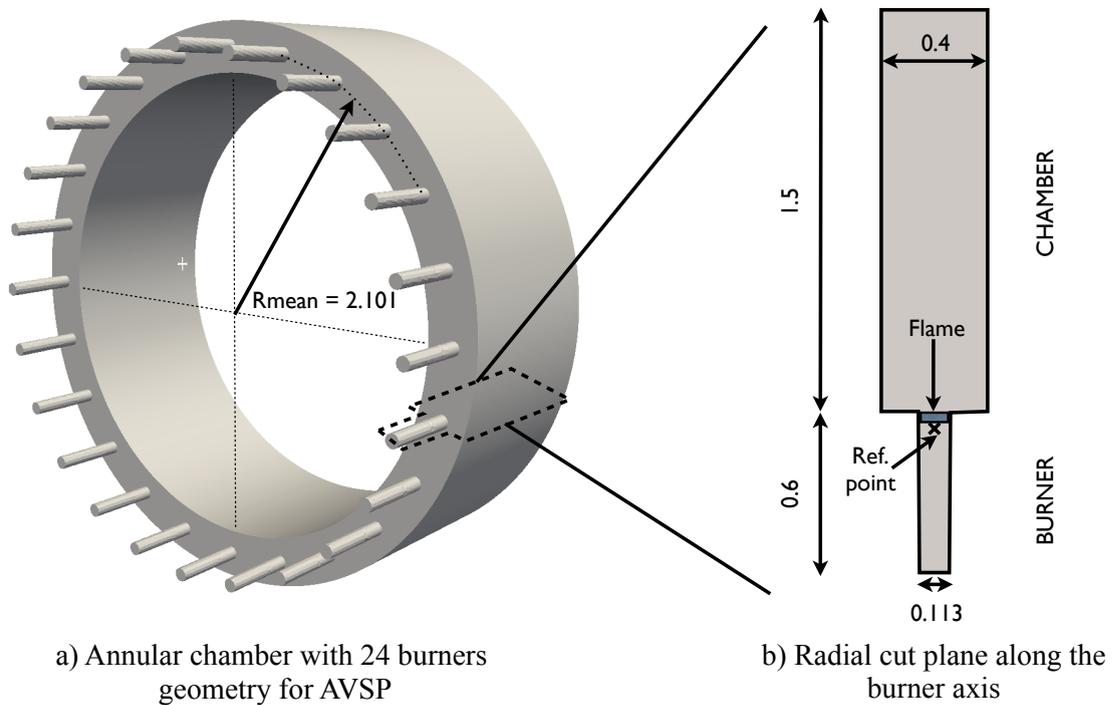
Figure 5.3: Geometry of the simplified annular chamber used for AVSP. The flames are compact and they are placed in the burner/chamber junction (in the burner side). The reference points used in the flame model described in Chapter 2 are placed right upstream the flames.
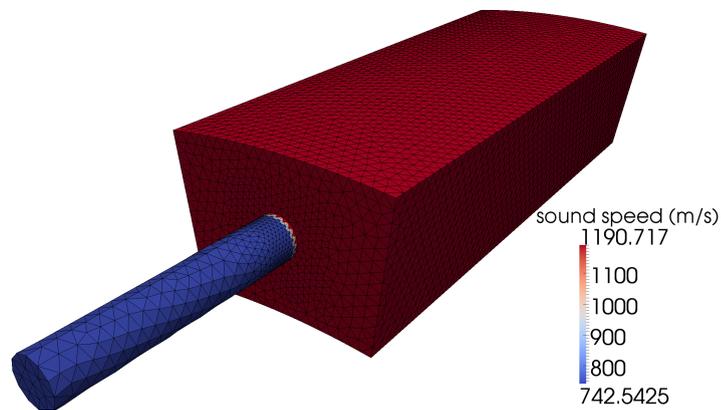
Figure 5.4: Mesh of one of the 24 sectors of the annular chamber. The fresh gases are in the tubes (burners) while the hot gases fill the annular chamber.

5.3 A network model for a BC (Burner + Chamber) non-symmetric configuration

The analytical methodology called ATACAMAC (Analytical Tool to Analyze and Control Azimuthal Modes in Annular Chambers) by Parmentier et al. [111] to study azimuthal modes in BC (Burners + Chamber) configurations, where an annular chamber is fed by N burners (Fig. 5.5), has been generalized by M. Bauerheim, currently PhD student at

Chamber			
Half perimeter	L_c	6.59	m
Section	S_c	0.6	m^2
Burner			
Length	L_i^0	0.6	m
Section	S_i	0.01	m^2
Fresh gases			
Mean temperature	T_u^0	700	K
Mean density	ρ_u^0	9.79	kg/m^3
Mean sound speed	c_u^0	743	m/s
Burnt gases			
Mean temperature	T^0	1800	K
Mean density	ρ^0	3.81	kg/m^3
Mean sound speed	c^0	1191	m/s
Flame parameters			
Interaction index	n_i	1.0	$-$
Time-delay	τ_i	*variable*	s

Table 5.1: Geometrical and physical parameters used in AVSP and for the analytical model. They correspond to a typical large scale industrial gas turbine.

	Freq. (Hz)	Nature
1.	25.8	1st Longitudinal
2.	93.7	1st Azimuthal
3.	93.7	1st Azimuthal
4.	182.0	2nd Azimuthal
5.	182.0	2nd Azimuthal

Table 5.2: First 5 eigenfrequencies of the annular chamber with 24 cylindrical burners with passive flame, corresponding to the first longitudinal mode and the first and second azimuthal modes.

CERFACS. This extension allows to obtain an expression for eigenfrequencies for a general asymmetric case for any mode of order p and any number of burners N. Moreover, it gives the structure and nature of the mode (spinning, standing or mixed). The main aspects of this analytical model are described in Secs. 5.3.1 to 5.3.5. More details can be found in [10, 111].
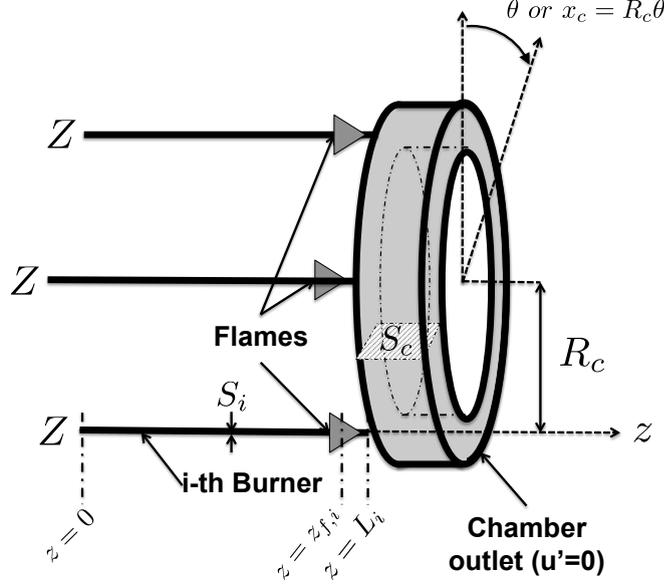
Figure 5.5: BC (Burners + Chamber) configuration to study azimuthal modes in annular chambers

5.3.1 Model description

This model focuses on a BC (Burner + Chamber) configuration where an annular chamber is fed by N burners (Fig. 5.5). An impedance Z is imposed at the entrance of each burner. Mean density and sound speed in the annular chamber are noted ρ^0 and c^0, while the mean density and sound speed of the unburnt gases in the burners are noted ρ_u^0 and c_u^0. The perimeter and the section of the annular chamber are noted $2L_c = 2\pi R_c$ and S_c, respectively. The length and section of the burner i are L_i and S_i, being $\alpha = z_{f,i}/L_i$ the normalized abscissa that defines the flame location in the burner i. The model assumes that the pressure fluctuations in the chamber depends only on the azimuthal coordinate θ, being constant along the direction z. This hypothesis is satisfied in combustors terminating in a choked nozzle, which behaves as a rigid wall ($u' = 0$ under the low Mach number assumption [85]). The pressure in the burners depends only on the abscissa z.

5.3.2 ANR methodology to obtain the analytical dispersion relation of asymmetric annular combustors

To reduce the size of the system, the ANR (Annular Network Reduction) methodology proposed in [10] is applied: the annular chamber is split into N sectors which only differ in the burner/chamber junctions (Fig. 5.6). Between each burner, the free propagation of the azimuthal waves is modeled by a transfer matrix R_i, as proposed in [111]:

$$\left[R_i\right] = \begin{bmatrix} w & 0 \\ 0 & \frac{1}{w} \end{bmatrix}, \tag{5.1}$$
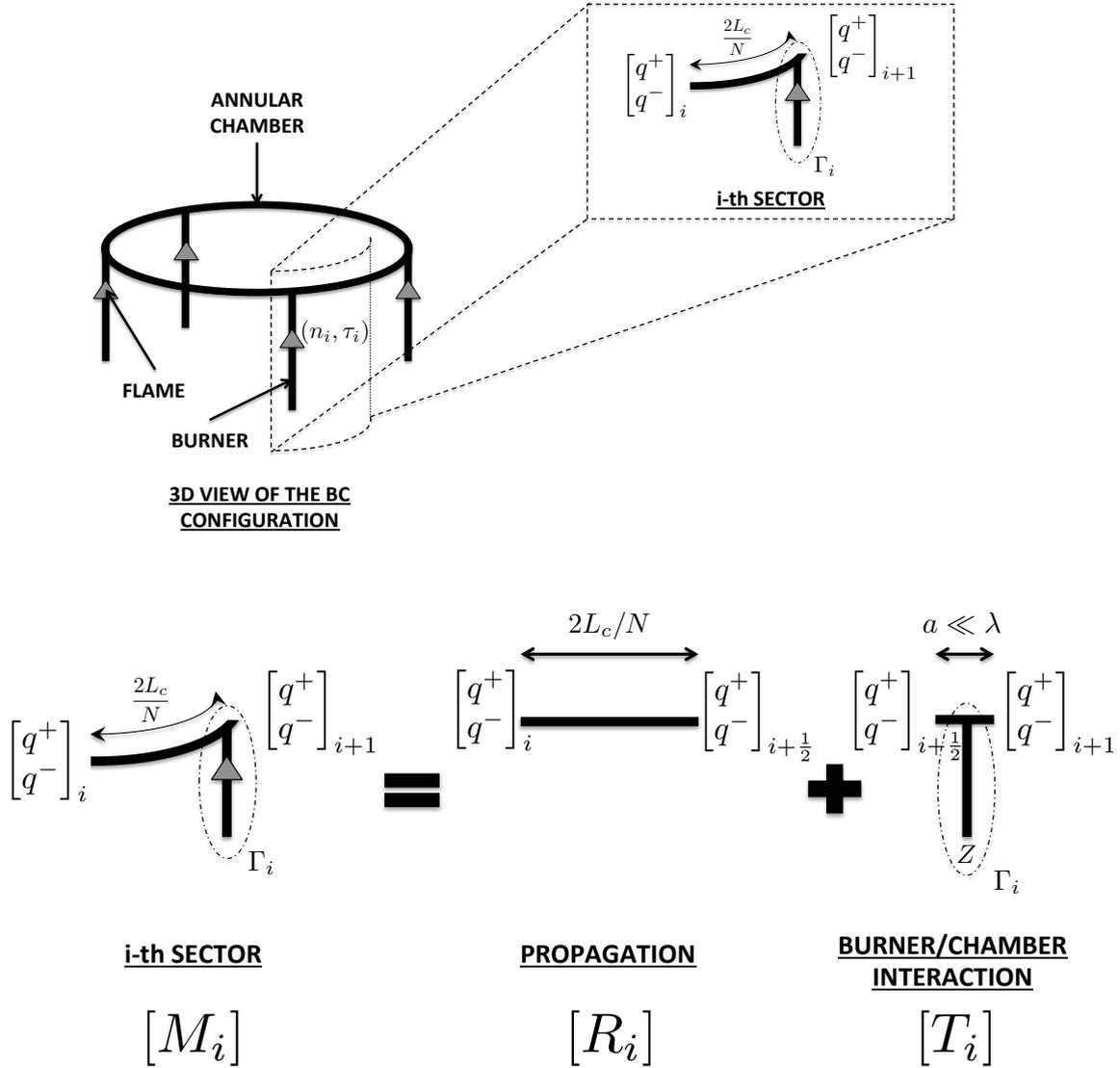
Figure 5.6: Schematic 3D view of a BC configuration with $N = 4$ burners. Zoom on the ith sector, where Γ_i represents the burner/chamber interaction [111] (top). Each sector is decomposed into a free propagation of azimuthal waves q^+ and q^- (characteristic length $2L_c/N$) and a compact burner/chamber interaction (characteristic length $a \ll \lambda$) modeled by the coupling parameter Γ_i (bottom).

where $w = e^{2jkL_c/N}$.

The junction where the interaction between the ith burner and the annular chamber occurs has been investigated by O'Connor et al. [104, 60, 61] and can be assumed compact. A transfer matrix T_i^* for the interaction part of Fig. 5.6 can be deduced:

$$
\begin{bmatrix} p' \\ \rho^0 c^0 u' \end{bmatrix}_{i+1} = \begin{bmatrix} T_i^* \end{bmatrix} \begin{bmatrix} p' \\ \rho^0 c^0 u' \end{bmatrix}_{i+\frac{1}{2}} = \begin{bmatrix} 1 & 0 \\ 2j\Gamma_i & 1 \end{bmatrix} \begin{bmatrix} p' \\ \rho^0 c^0 u' \end{bmatrix}_{i+\frac{1}{2}}, \tag{5.2}
$$

where the coupling parameter Γ_i [111, 10, 108, 143] can be written in terms of the equivalent

admittance Y_{tr} of the whole i^{th} burner as:

$$\Gamma_i = -\frac{j}{2}\frac{S_i}{S_c}Y_{tr}(Z, \alpha, Li, n_i, \tau_i) \qquad (5.3)$$

When a velocity node ($Z = \infty$) or a pressure node ($Z = 0$) is imposed at the upstream end of each burner and the flame are located right in the burner/chamber junction ($\alpha = 1$), an expression for the coupling parameters Γ_i has been deduced in [111]:

$$\Gamma_i = \frac{1}{2}\frac{S_i\rho^0 c^0}{S_c\rho_u^0 c_u^0}tan(k_u L_i)\left(1 + N_{1i}e^{j\omega\tau_i}\right) \quad (Z = \infty) \qquad (5.4)$$

$$\Gamma_i = -\frac{1}{2}\frac{S_i\rho^0 c^0}{S_c\rho_u^0 c_u^0}cotan(k_u L_i)\left(1 + N_{1i}e^{j\omega\tau_i}\right) \quad (Z = 0) \qquad (5.5)$$

where $k_u = \frac{\omega}{c_u}$ and (N_{1i}, τ_i) are the interaction index and the time-delay of the FTF for the ith flame.

The matrix T_i^* of Eq. (5.2) is recast to use characteristic waves $q^{\pm} = p' \pm \rho^0 c^0 u'$ instead of the primitive variables p' and u', which leads to the T_i definition:

$$\left[T_i\right] = \begin{bmatrix} 1 + j\Gamma_i & j\Gamma_i \\ -j\Gamma_i & 1 - j\Gamma_i \end{bmatrix} \qquad (5.6)$$

Finally, from Fig. 5.6 and [111], the transfer matrix M_i of the ith sector reads as:

$$\begin{bmatrix} q^+ \\ q^- \end{bmatrix}_{i+1} = \underbrace{\left[T_i\right]\left[R_i\right]}_{M_i}\begin{bmatrix} q^+ \\ q^- \end{bmatrix}_i \qquad (5.7)$$

Using the periodicity of the system (i.e. $\begin{bmatrix} q^+ \\ q^- \end{bmatrix}_{N+1} = \begin{bmatrix} q^+ \\ q^- \end{bmatrix}_1$) and the equation of one sector (Eq. (5.7)) leads to:

$$\left(\prod_{i=1}^{N} M_i\right)\begin{bmatrix} q^+ \\ q^- \end{bmatrix}_1 = \begin{bmatrix} q^+ \\ q^- \end{bmatrix}_1 \qquad (5.8)$$

The system defined by Eq. (5.8) has non-trivial solutions only if its determinant is null. Therefore, the ANR methodology provides an implicit analytical dispersion relation for the pulsation ω for a general non-symmetric BC configuration:

$$det\left(\prod_{i=1}^{N} M_i - I_d\right) = 0 \qquad (5.9)$$

where I_d is the 2-by-2 identity matrix.

5.3.3 Eigenfrequencies and modes nature of an annular duct (unperturbed case)

If the coupling parameter $\Gamma_i = 0$ for all the burners, then Eq. (5.8) reduces to:

$$\begin{bmatrix} w^N & 0 \\ 0 & \frac{1}{w^N} \end{bmatrix} \begin{bmatrix} q^+ \\ q^- \end{bmatrix}_1 = \begin{bmatrix} q^+ \\ q^- \end{bmatrix}_1, \tag{5.10}$$

with $\omega = e^{2jkL_c/N}$. The dispersion relation becomes then:

$$\omega^N = 1,$$

whose solutions are roots of the unity $\omega_0 = e^{2jp\pi/N}$. Consequently, the eigenfrequencies of the unperturbed annular duct are:

$$f = \frac{pc_0}{2L_c}, \ \ \forall p \in \mathbb{N}. \tag{5.11}$$

In this situation, the generated eigenspace $\{V\}$ from Eq. (5.10) is two-dimensional: it can be either two standing, two spinning or two mixed azimuthal waves. These two azimuthal modes can be then combined to obtain any type of azimuthal mode (standing, spinning or mixed).

5.3.4 Eigenfrequencies and mode nature of a symmetric BC configuration (N identical burners)

When all the sectors are identical ($M_i = M$), the computation of the equation $\det(\prod M_i - I_d) = 0$ reduces to $\det(M^N - I_d) = 0$. Hence, the whole system can be analyzed by considering only one sector:

$$\det\left(M^N - I_d\right) = 0 \Leftrightarrow \det(M - e^{j2p\pi/N}) = 0 \ \ , \forall p \in \mathbb{N}. \tag{5.12}$$

Eq. (5.12) corresponds to the dispersion relation of one sector perturbed by one burner where the phase-lag $\Delta\phi = \frac{2p\pi}{N}$ is imposed to the pth order mode. Parmentier et al. [111] have solved the problem for $N = 1, 2$ and 4 burners, assuming low-coupling parameters:

$$\Gamma_i \ll 1, \ \ \forall i \in [1, N].$$

Under this low-coupling assumption, characteristic waves q^+ and q^- are suppose to be close of those ones of the unperturbed problem (annular cavity alone, Sec. 5.3.3), what allows to obtain an asymptotic solution for the corresponding wave numbers ϵ^+ and ϵ^-:

$$w^{\pm} = (1 + \mathcal{E}^{\pm})w_0 \ \ \text{i.e.} \ \ kL_c = p\pi + \epsilon^{\pm}, \tag{5.13}$$

where $w_0 = e^{2jp\pi/N}$ and $\mathcal{E}^{\pm} = \frac{2j\epsilon^{\pm}}{N}$. The expression for $\epsilon^{\pm}$ is derived in the following section, as a particular case when all the sectors are identical. For instance, Parmentier et al. have proved in [111] that the the eigenspace $\{V\}$ corresponding to the first azimuthal mode ($p = 1$) in an annular chamber with $N = 4$ identical burners is degenerated, i.e. both eigenmodes have associated the same frequency and growth rate:

$$\epsilon^+ = \epsilon^- = -2\Gamma^0 \ \ \text{and hence} \ \ Im(f^{\pm}) = -\frac{c^0}{\pi L_c}Im(\Gamma^0) \propto N_1 sin(\omega^0\tau), \tag{5.14}$$

where Γ^0 is the value of $\Gamma_i^{\pm}$ when $\omega^{\pm} = \omega^0 = \frac{pc^0\pi}{L_c}$ and N_1, τ are the FTF parameters.

5.3.5 Eigenfrequencies and mode nature of a general non-symmetric BC configuration

The system that describes the general BC configuration with Γ_i that can be different for each burner reads:

$$M = \prod_{1=1}^{N} T_i R_i.$$

Assuming low coupling parameters ($\Gamma_i \ll 1, i = [1, \ldots, N]$), a Taylor expansion of the matrix M at the second order can be performed, which leads to the following dispersion relation at second order:

$$\det(M - Id) = -\frac{w^{2N} - 2w^N + 1}{w^N} - \frac{jS(w^{2N} - 1)}{w^N} + \\ + \sum_{i=1}^{N-1} \sum_{j=i+1}^{N} \Gamma_i \Gamma_j [w^{2N} - w^{N-2(j-i)} - w^{2(j-i)} + 1] + o(\Gamma_i^2), \tag{5.15}$$

where $S = \sum_{i=1}^{N} \Gamma_i$. Under low coupling assumption, the solution is supposed to be close to the one of the unperturbed problem [111]: $kL_c = p\pi + \epsilon^{\pm}$ or $w^{\pm} = (1 + \mathcal{E}^{\pm})w_0$ where $\mathcal{E}^{\pm} = 2j\frac{\epsilon^{\pm}}{N}$ and $w_0 = e^{2jp\pi/N}$. The coupling parameters depends on the frequency, and therefore on the wave number $\epsilon^{\pm}$ too. Thay can be approximated by:

$$\Gamma_i^{\pm}(\omega) = \underbrace{\Gamma_i^{\pm}(\omega = \omega^0)}_{\Gamma_i^0} + \frac{2j\epsilon^{\pm}\omega 0}{N} \underbrace{\left(\frac{\partial \Gamma_i^{\pm}}{\partial \omega}\right)_{\omega=\omega^0}}_{\Gamma_i^1} + o(\epsilon), \tag{5.16}$$

where $\omega^0 = \frac{p\pi c^0}{L_c}$ corresponds to the angular frequency of the unperturbed BC configuration (Sec. 5.3.3).

Knowing that $\Gamma_i^0 \simeq \epsilon^{\pm}$ [1], a Taylor expansion at second order of Eq. (5.15), after the convenient simplifications, leads to the following wave numbers expression:

$$\epsilon^{\pm} = -\frac{1}{2}\left(\Sigma_0 \pm \sqrt{\Sigma_0^2 - A}\right) \tag{5.17}$$

where

$$A = 4\sum_{i=1}^{N-1} \sum_{j=i+1}^{N} \Gamma_i^0 \Gamma_j^0 \left[\sin\left(\frac{2p\pi}{N}(j-i)\right)\right]^2$$

is the non-symmetric part and $\Sigma_0 = \sum_{i=1}^{N} \Gamma_i^0$.

When a given symmetry pattern gives $\sqrt{\Sigma_0^2 - A} = 0$ for a mode of order p then $\epsilon^+ = \epsilon^-$ and the associated subspace $\{V\}$ is two-dimensional (i.e. is a degenerate doublet): the

---

[1]The analytical solution of the dispersion relation will lead to the solution $\epsilon^{\pm} \propto \Gamma_i^0$ showing that Γ_i^0 is indeed a first order term and that $\Gamma_i^0\Gamma_j^0$ and $\Gamma_i^0\epsilon^{\pm}$ are second order terms.

resulting mode can be either spinning, standing or mixed. Otherwise, when $\sqrt{\Sigma_0^2 - A} \neq 0$, the two wave numbers $\epsilon^+ \neq \epsilon^-$ and each one is associated to one different eigenmode $V^\pm$ (two singlets).

Consequently, one can define a splitting strength $\mathcal{S}_0 = \sqrt{\Sigma_0^2 - A}$ in Eq. (5.17), which is a measure of how much a given symmetry pattern splits a degenerate doublet (DD) of order p into two singlets with different frequencies and growth rates. The splitting strength can be recast into:

$$\mathcal{S}_0^2 = \Sigma_0^2 - A = \sum_{i,j=1}^{N} \Gamma_i^0 \Gamma_j^0 cos\left(\frac{4p\pi}{N}(j-i)\right) \tag{5.18}$$

Burner coupling parameter	Γ_i $(i = 1, \ldots, N)$	$\Gamma_i = \frac{1}{2}\frac{S_i \rho^0 c^0}{S_c \rho_u^0 c_u^0} tan(k_u L_i)\left(1 + N_{1i}e^{j\omega\tau_i}\right)$ $(Z = \infty)$ $\Gamma_i = -\frac{1}{2}\frac{S_i \rho^0 c^0}{S_c \rho_u^0 c_u^0} cotan(k_u L_i)\left(1 + N_{1i}e^{j\omega\tau_i}\right)$ $(Z = 0)$
Global coupling parameter	Σ_0	$\Sigma_0 = \sum_{i=1}^{N} \Gamma_i^0$
Splitting strength	$\mathcal{S}_0$	$\mathcal{S}_0^2 = \sum_{i,j=1}^{N} \Gamma_i^0 \Gamma_j^0 cos\left(\frac{4p\pi}{N}(j-i)\right)$

Table 5.3: ATACAMAC controlling parameters.

5.4 Symmetry and azimuthal modes

Following the ideas introduced in [114], this sections intends to establish, qualitative and quantitatively, a classification of the different behaviors of azimuthal modes that can take place in annular combustion chambers, as a function of the symmetry of the system and of the order p of the azimuthal mode. Exploring these questions with the 3D solver AVSP would be virtually impossible because of the cost of simulations. The ATACAMAC method provides analytical solutions which are more efficient to understand what controls the growth rates of modes.

The symmetry order (SO) of a given configuration is defined here as the number of basic identical elements it is composed of using a rotation operation. In other words, it is the number of elemental sectors (one burner if they are all identical or several if they are different) that are needed to get the whole annular chamber (Fig. 5.7) by rotation.[2]

Depending on the mode and symmetry orders p and SO, respectively, the subspace formed by the modes associated to an azimuthal eigenfrequency is one-dimensional or two-dimensional. We distinguish between symmetric (N identical burners and SO $= N$) and general non-symmetric configurations.

---

[2]Patterns obtained by reflection symmetries are nor covered by the present qualitative analysis.

Basic repetition element


SO = 8   SO = 4   SO = 2
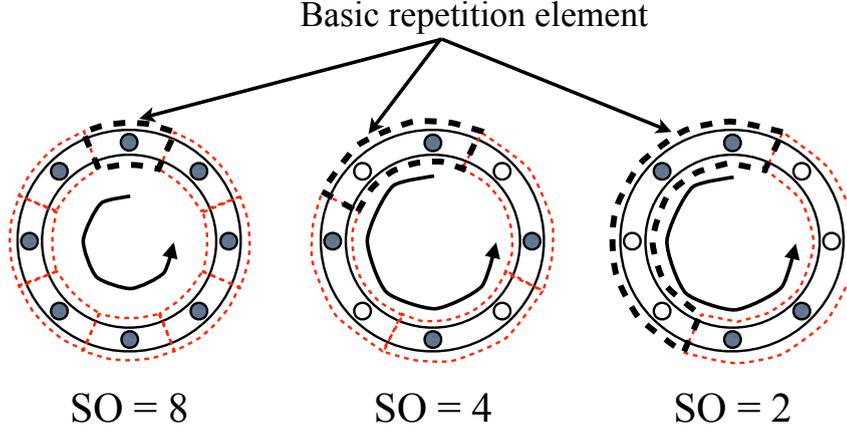
Figure 5.7: Annular chambers with N=8 burners. Using two types of burners, 3 different patterns with decreasing symmetry order.

5.4.1   Symmetric case (N identical burners)

When all burners are identical then SO=N. Two different behaviors are possible:

- **Non-degenerate singlets**: When $p = mN/2$, $\forall m \in \mathbb{N}$ (only $p = mN$ exists in cases with an odd number of burners), the splitting strength $\mathcal{S}_0$ is not null and the corresponding wave numbers given by ATACAMAC are:

$$\begin{cases} \epsilon^- = 0 \\ \epsilon^+ = -N\Gamma^0 \end{cases} \tag{5.19}$$

Associated to each wave number $\epsilon^\pm$ there is one eigenmode $V^\pm$. Qualitatively, the first mode V^- is standing and imposes a pressure node at every burner, so that it is unperturbed by them ($\epsilon^- = 0$) resulting in a neutral mode. The second mode V^+ is also standing but imposing a velocity node (i.e. a pressure anti-node) at every burner ($\epsilon^+ = -N\Gamma^0$), so that it is highly perturbed by burners. The rotation angle between both modes is $\pi/(2p)$ (see Fig. 5.8). Both modes have different frequencies and they are both standing, since they must remain locked with respect to the burner(s) positions (if not, their respective frequencies would change).

- **Degenerate doublets**: All other azimuthal modes with order $p \neq mN/2$, $\forall m \in \mathbb{N}$ ($p \neq mN$ when N is and odd number) are degenerate. They are associated with two eigenmodes $V^\pm$, since the corresponding frequencies are the same because $\mathcal{S}_0 = 0$:

$$\epsilon^- = \epsilon^+ = -\frac{N}{2}\Gamma^0 \tag{5.20}$$

Qualitatively, both waves are equally perturbed by the burners, independently of the rotation angle ϕ (particularly $\pi/(2p)$) that is applied to them (Fig. 5.9). It means that no matter how the mode is oriented with respect to the burners, the associated eigenfrequency does not change. It also means that, a priori, the mode can
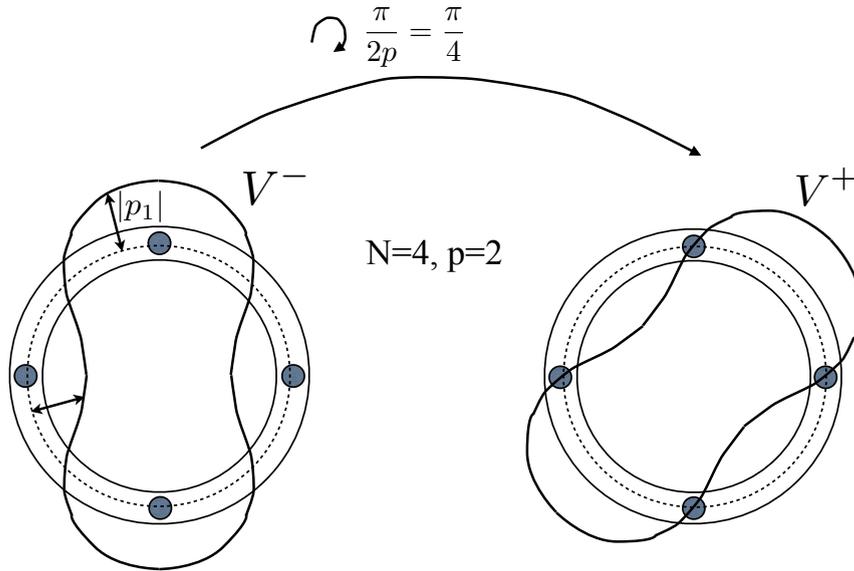
Figure 5.8: Representation of two singlets: an azimuthal mode or order $p = 2$ in a BC configuration with N=4 identical burners. V^- has pressure anti-nodes at the burners, and thus is highly perturbed. V^+ is obtained by rotating V^- an angle $\pi/(2p) = \pi/4$. It has pressure nodes at the burners location, resulting in a neutral mode with a frequency that differs from the one of V^-.

be spinning, standing or mixed, since there is no privileged position for the mode to lock on. Therefore the eigenspace $\{V\}$ associated to the corresponding frequency is two-dimensional: it is formed by two azimuthal waves (both either standing, spinning or mixed) that can be combined to form any type of azimuthal mode (standing, spinning or mixed). Noiray et al. [99] have shown that non-linearities on the FTF can however promote one of these natures, a phenomenon which can not be capture by ATACAMAC with classical FTFs.

5.4.2 General non-symmetric case

When a certain pattern with different kind of burners is used, the SO of the configuration is reduced with respect to the symmetric case (SO=N), i.e., SO<N. Still, two options are possible, depending on the SO and on the order p of the azimuthal mode:

- **Non-degenerate singlets**: Azimuthal modes with order $p = \frac{m\text{SO}}{2}$, $\forall m \in \mathbb{N}$ ($p = m\text{SO}$ when SO is an odd number) are non-degenerate singlets with wavenumber perturbations:

$$\begin{cases} \epsilon^- = 0 \\ \epsilon^+ = -\Sigma_0 = -\sum_{i=1}^{N} \Gamma_i^0 \end{cases} \tag{5.21}$$

As for the symmetric case, these modes impose either a pressure or pressure anti-node at each burner, leading to an unperturbed standing wave ($\epsilon^- = 0$) or a highly
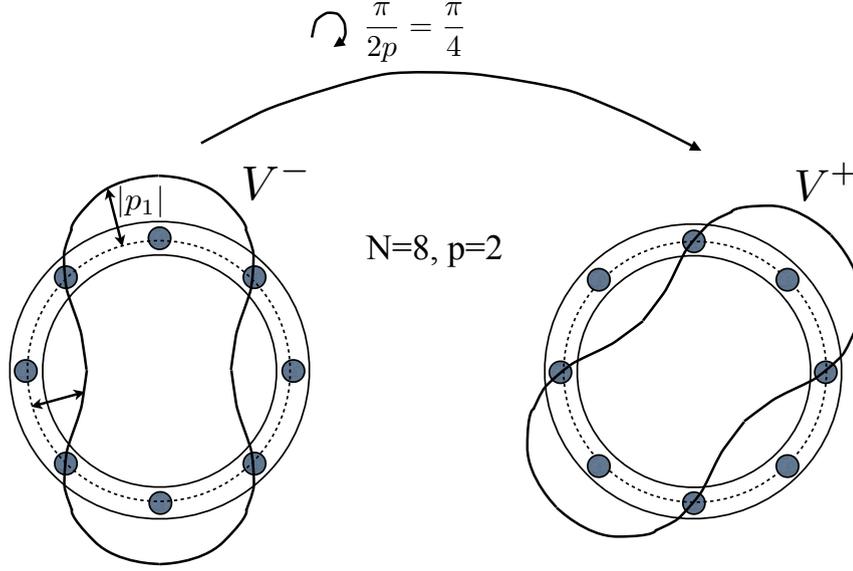
Figure 5.9: Representation of two degenerate doublets: an azimuthal mode or order $p = 2$ in a BC configuration with N=8 identical burners. V^- have pressure anti-nodes at two of the burners. When it is rotated of $\pi/4$ it leads to V^+, which has still anti-nodes pressure on two of the burners, so that it is the equivalent to V^-, having associated the same eigenfrequency.

perturbed standing mode ($\epsilon^+ = -\Sigma_0$), respectively. With respect to the symmetric case, non-degenerate singlets appear for lower order modes, since SO $< N$.

- **Nearly-degenerate singlets**: Azimuthal modes with order $p \neq \frac{m\text{SO}}{2}$ $\forall m \in \mathbb{N}$ ($p \neq m\text{SO}$ when SO is and odd number) are nearly-degenerate singlets [114]: the degenerate doublet of symmetric configurations (denoted DD with $\epsilon_{DD} = -\frac{1}{2}\Sigma_0$) is split depending on the splitting strength $\mathcal{S}_0$. Therefore the wave number perturbations are:

$$\epsilon^{\pm} = \underbrace{-\frac{1}{2}\Sigma_0}_{\epsilon_{DD}} \pm \underbrace{\frac{1}{2}\mathcal{S}_0}_{\text{Splitting}} \tag{5.22}$$

5.4.3 A necessary condition for stability

Breaking the azimuthal symmetry of the system may appear as an additional degree of freedom in order to get stable modes. Nevertheless, independently of the asymmetry pattern, there is a necessary condition for stability that must be satisfied. From Eq. (5.22) it is clear that $\max(Im(\epsilon^+), Im(\epsilon^-)) > \frac{1}{2}Im(\epsilon^+ + \epsilon^-)$. Therefore, the necessary condition to stabilize a mode, which does not depend on the asymmetry pattern is:

$$\frac{1}{2}Im(\epsilon^+ + \epsilon^-) = -\frac{1}{2}Im(\Sigma_0) < 0. \tag{5.23}$$

Otherwise, the imaginary frequency of the mode associated to $\max(Im(\epsilon^+), Im(\epsilon^-))$ would be positive and hence the mode would be unstable.

If the chosen pattern results in a degenerate doublet with $\epsilon^+ = \epsilon^-$, then Eq. (5.23) constitutes a necessary and sufficient condition for stability. On the other hand, when the asymmetry pattern splits the degenerate doublet into two singlets ($\mathcal{S}_0 \neq 0$), Eq. (5.23) is not enough to ensure the stability of the mode (see Fig. 5.10).


Figure 5.10: When the chosen asymmetry pattern is such that $\mathcal{S}_0 \neq 0$, the condition $\frac{1}{2}Im(\Sigma_0) < 0$ (Eq. (5.23)) is not enough to ensure the stability of the mode, since one of the nearly-degenerate singlets may have a positive growth rate and thus be unstable.

5.5 Effect of symmetry breaking on stability and mode nature

The BC configuration with $N = 24$ burners described in sec. 5.2 is used now to study the effect of symmetry breaking on the stability and the modes nature with AVSP. The results obtained with AVSP are compared to those obtained with ATACAMAC (sec. 5.3).

The stability of the first mode of the annular chamber is first analyzed using the same FTF (N_{1i}, τ_i) for all burners (symmetric case) as a function of the time delay τ. The value of the interaction index N_1 is taken equal to 1 (knowing that typical values for N_1 are around $\frac{T_2}{T_1} - 1 = 1.57$ here) while the time delay τ varies between 0 and the period of the first azimuthal mode $T_1^0 = 1/f_1^0 = \frac{2L_c}{c^0} \simeq 11 \; ms$. The frequency and growth rate of the first azimuthal mode (p=1), obtained with ATACAMAC (analytical and numerical solution of the dispersion relation) and AVSP are plotted in Fig. 5.11. The agreement between the analytical (low coupling assumption) and numerical solutions given by ATACAMAC and AVSP is very good.

To perform symmetry breaking two different burners are used, characterized by different time-delays, τ_1 and τ_2 (Fig. 5.11). The time delay $\tau_1 = 3.25 \; ms$ corresponds approximately to the most unstable burner ($Im(f_{AVSP}) = 2.98 \; s^{-1}$), which is assimilated here to the unstable baseline case in [12, 71], a burner without CBO ($\circ$ in Tab. 5.4). As explained in [12, 71], a CBO device can be mounted on some of the burners to stabilize the chamber.

Figure 5.11: Stability map depending on τ of the first azimuthal mode ($p = 1$) of the symmetric BC configuration with $N = 24$ burners. T_1 is the period of the (unperturbed) first azimuthal mode $T_1 = 1/f_1^0 = \frac{2L_c}{pc^0} \simeq 11ms$.

The length of the cylinder is such that the time lag from the injection port to the flame front is increased by approximately a quarter of an acoustic period. In our case it is equivalent to consider $\tau_2 = \tau_1 + \frac{1}{4f_1^0} \simeq 6ms$. Fig. 5.11 shows that the value $\tau_2 = 6\ ms$ corresponds indeed to a stable burner with $Im(f_{AVSP}) = -1.01\ s^{-1}$ (● in Tab. 5.4). Note that using 20 burners with $\tau_2 = 6\ ms$ and 4 burners with $\tau_1 = 3.25\ ms$ respects the necessary condition given by Eq. (5.23) to get stable modes (represented by $-\frac{1}{2}Im(\Sigma_0^{C20})$ in Fig. 5.12). The stability of the four patterns proposed in Tab. 5.4 is studied using ATACAMAC and AVSP. The results are plotted in Figs. 5.12 (growth rates) and 5.13 (frequencies).

The agreement between AVSP and ATACAMAC is very good in all cases:

- **B24_C0:** This configuration corresponds to the unstable baseline case: the necessary condition (Eq. (5.23)) is not satisfied. Some burners have to be changed in order to get a stable combustor.

- **B24_C20_P2:** 20 CBOs devices have been mounted in the hope to stabilize the mode. The necessary condition (Eq. (5.23)) is now satisfied. However this pattern has a large splitting strength $\mathcal{S}_0$. Consequently it splits azimuthal modes into two singlets with different growth rates making one of them unstable. This case is an excellent example of how, for asymmetric circumferential patterns, one can use stable burners that match the condition $-\frac{1}{2}Im(\Sigma_0) < 0$ and yet, due to the asymmetry term $\mathcal{S}_0$, have an unstable mode as shown in Fig. 5.10.

- **B24_C20_P4:** This pattern has a lower splitting strength $\mathcal{S}_0$ than the previous

Name	N	CBO	Asymmetry pattern
B24_C0	24	0	○○○○○○○○○○○○○○○○○○○○○○○○
B24_C20_P1	24	20	●●●●●●●●○○●●●●●○○●●●●●●●
B24_C20_P2	24	20	●●●●●●●●●○○○○●●●●●●●●●●
B24_C20_P3	24	20	●●●●●○●●●●●○●●●●●○●●●●○
B24_C20_P4	24	20	●●●●●○●●●●○●●●●●○●●●●○
B24_C24	24	24	●●●●●●●●●●●●●●●●●●●●●●●●

Table 5.4: BC configurations investigated with both the 3D Helmholtz solver AVSP and the analytical approach ATACAMAC. ○ — Burner without CBO (τ_1 in Fig. 5.11); ● — Burner with CBO (τ_2 in Fig. 5.11)

Figure 5.12: Growth rate of the first azimuthal mode ($p = 1$) for various asymmetric combination of burners with and without CBO: B24_C0 (24 noCBO burner, perfectly symmetric case), B24_C24 (24 CBO burners, perfectly symmetric case) and the four patterns B24_C20 (non-symmetric cases). --- : Values of $-\frac{1}{2}I_m(\Sigma_0)$ (necessary condition, Eq. (5.23)) depending on the configuration (C_0, C_{20} and C_{24}).

one and both singlets remain stable in this case.

- **B24_C20_P1 and B24_C20_P3:** These patterns have a null splitting strength $\mathcal{S}_0$ (analytical solution of ATACAMAC), leading to a stable degenerate doublet. In

Figure 5.13: Frequencies of the first azimuthal mode ($p = 1$) for various asymmetry combination of burners with and without CBO: B24_C0 (24 noCBO burners), B24_C24 (24 CBO burners) and the four patterns B24_C20. **DD**: Degenerate Doublets.

these cases, Eq. (5.23) becomes a necessary and sufficient condition for stability.

- **B24_C24:** Using 24 stable burners obviously respects the necessary condition (Eq. (5.23)) and results in a stable degenerate doublet.

Considering the dashed-lines ($-\frac{1}{2}Im(\Sigma_0)$) in Fig. 5.12, it is interesting to notice that, independently of the asymmetry patterns, combining 20 CBOs and 4 noCBOs burners give potentially less stable modes than using 24 CBOs showing that breaking symmetry has a limited interest here compared to adding CBOs on all burners. Nevertheless, if for any reason (ignition, pollution, construction, etc.) one must keep the two types of burners, the present analytical model offers an easy way to optimize the circumferential distribution of the burners by minimizing the imaginary part of the splitting strength $Im(\mathcal{S}_0)$ to stabilize the pth mode. In the present study, if one must keep 4 unstable burners, patterns B24_C20_P1 and B24_C20_P3 are the best options since they have null splitting strength ($\mathcal{S}_0 = 0$).

The other key point of symmetry breaking is that it can also modify the dynamic nature of the acoustic modes. The modulus (noted *Abs_press*) and phase (noted *Arg_press*) of the acoustic pressure of the first azimuthal mode obtained with AVSP are plotted in Fig. 5.14 for the four studied patterns, showing two distinct behaviors:

- Patterns P1 and P3: as expected, asymmetry patterns leading to degenerate doublets can be either spinning, standing or mixed. In this case, P1 gives mixed waves, while P3 gives purely spinning ones. For these patterns, the two waves $V^{\pm}$ have the same frequency and they can be seen as the waves q^{+} and q^{-} that are combined to obtain either a spinning, a standing or a mixed azimuthal mode.

- Patterns P2 and P4 give two standing modes. The two eigenmodes $V^{\pm}$ oscillate in opposite phase with different (yet very close) frequencies (e.g. 90.3 and 91.3 Hz for the P2 pattern). As shown in Fig. 5.12, for the P2 pattern, one mode is amplified whereas the other one is damped, resulting in an unstable standing mode.
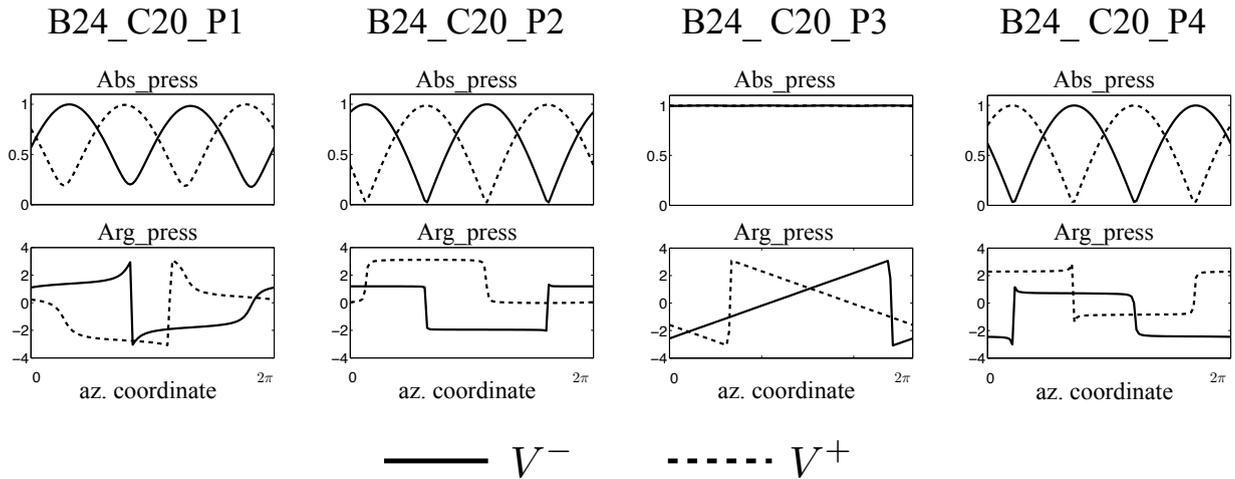

Figure 5.14: Structure of the two eigenmodes $V^{\pm}$ (—— and ---) corresponding to the first azimuthal mode ($p = 1$) for the four patterns of Tab. 5.4, obtained with AVSP.

5.6 Concluding remarks

The effect of symmetry breaking on the stability of azimuthal modes has been investigated using an academic annular chamber with 24 burners. The results obtained with AVSP are compared with analytical results from ATACAMAC, showing a very good agreement for all cases. In [12, 71], the authors suggest that breaking the circumferential annular of the combustor improves the stability of the system, mixing two types of burners (with and without CBO) with different time-delay τ. The results obtained here, suggest that the stabilization of the system is rather due to the use of burners with CBO and that the symmetry breaking obtained by mixing the two burners has a limited effect. In other words, if a burner that gives stable modes is available, it must be used for all sectors of the annular combustor, since any other azimuthal combination resulting of mixing it with another burner will be potentially less stable.

If one must keep a certain number of burners without CBO, then the analytical approach ATACAMAC allows to obtain easily the optimal azimuthal pattern with the lowest splitting strength, closest to the most possible stable doublet given by the condition $-\frac{1}{2}Im(\Sigma_0) < 0$.

Moreover, the nature of the azimuthal modes (standing, spinning or mixed) has been shown to be affected by the employed staging pattern.

The ATACAMAC analytical tool provides interesting results for a simple annular geometry, but it can not be used for the study of real complex industrial configurations where the geometry becomes important and complicated. AVSP is used in Chapter 6 to study the stability of azimuthal modes in an industrial gas turbine combustion chamber. However, ATACAMAC has proved to be an excellent tool to analyze the stability of annular combustors, allowing a cross validation with AVSP in the present simple case of Fig. 5.5 and revealing physical information which would have been impossible to obtain with AVSP only.

Chapter 6

Thermoacoustic analysis of an industrial gas turbine combustion chamber

Contents

In this chapter AVSP is used to study the thermoacoustic modes of an industrial gas turbine combustor taking into account all geometry details. Thanks to the efficiency of the algorithms described and studied in Chapters 3 and 4, respectively, the 360° geometry can be simulated with AVSP without considering any additional hypothesis or geometry simplifications, which allows to take into account all the complexity of the real combustor.

First, the modes with passive flame are computed to establish a classification of the numerous low-frequency modes (between 0 and 200Hz). Longitudinal and azimuthal modes are found, and this allows to establish a first classification. Different zones of the combustion chambers are involved in azimuthal modes, showing an important longitudinal coupling between them.

Flame Transfer Functions (FTF) obtained from LES of a single sector during the PhD of S. Hermeth [53] are used in AVSP (thanks to the ISAAC assumption of Chapter 2) to

obtain the stability of the modes. The acoustic coupling of longitudinal modes in axial combustion chambers has been studied in [143]. Nevertheless the coupling between cavities that exhibit azimuthal modes has not been investigated in the literature to the best of our knowledge. In [10] (see Appendix), two annular cavities linked by N cylindrical burners has been studied analytical and numerically. Here, the coupling between cavities affecting azimuthal modes in a real combustor is further investigated, using an energetic approach based on the acoustic fluxes between cavities.

The influence of the FTF parameters, the interaction index n and the time-delay τ, is investigated using constant fields of n and τ. This allows to know how the modes change (structure, frequency, growth rate) when the interaction index n increases. The stability of azimuthal modes is also investigated as a function of the time-delay τ, showing that this parameter plays an important role in the coupling between cavities.

Finally, the study of symmetry breaking performed in Chapter 5 for an academic annular combustion chamber, is extended to the industrial configuration treated in this chapter, revealing similarities and discrepancies between both configurations.

6.1 Description of the configuration
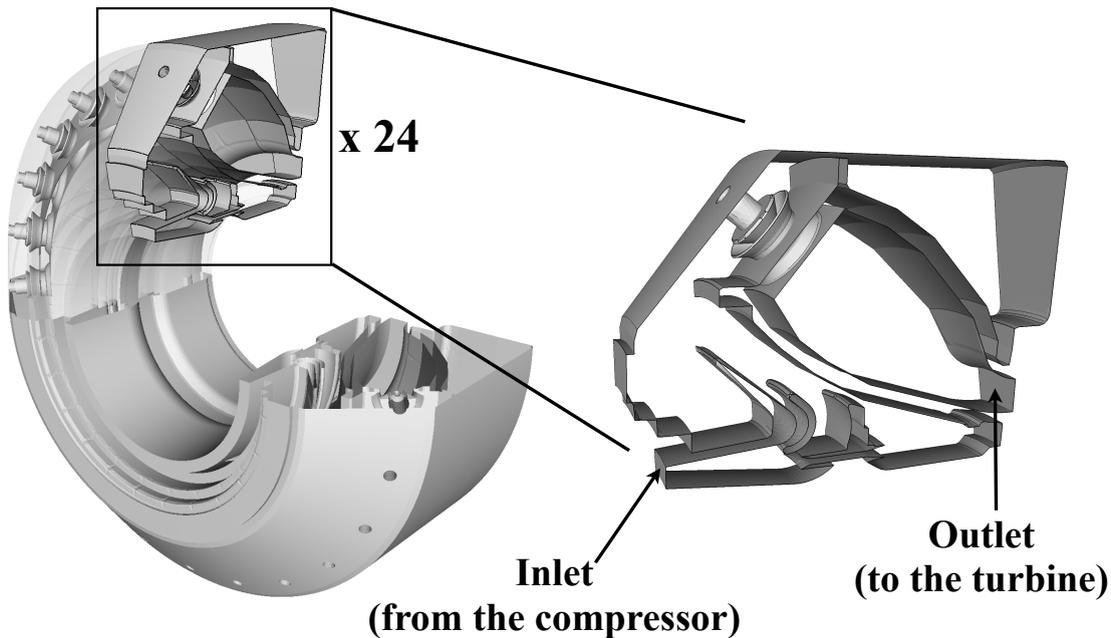
Figure 6.1: 360° view of the power generator combustor with 24 circumferentially-arranged burners (left). Geometry of a single sector, showing the inlet to the casing and the outlet of the combustion chamber.

The configuration studied in this chapter corresponds to a full annular power generator combustor formed by 24 identical sectors (Fig. 6.1). The diameter of the configuration is about 4 meters, which is much bigger than a typical aeronautical combustion chamber. It means that one can expect to find a larger number of modes at very low frequencies than
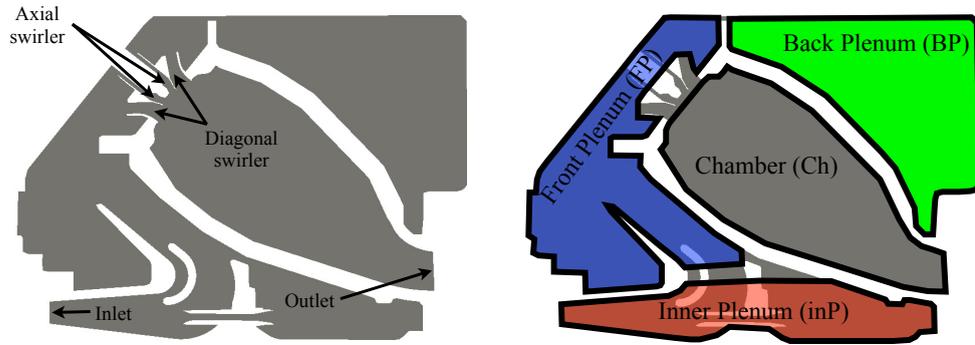
Figure 6.2: Longitudinal cut of one sector, showing the burner geometry (left). Division of the combustor into four zones (right).

in typical aeronautical combustors. Each sector is composed of a casing and a chamber, connected through both a diagonal and an axial swirler (Fig. 6.2). The cold flow coming from the compressor enters the casing, which feeds the combustion chamber through an axial and a diagonal swirler. Burnt gases exhaust the combustion chamber through a choked nozzle.
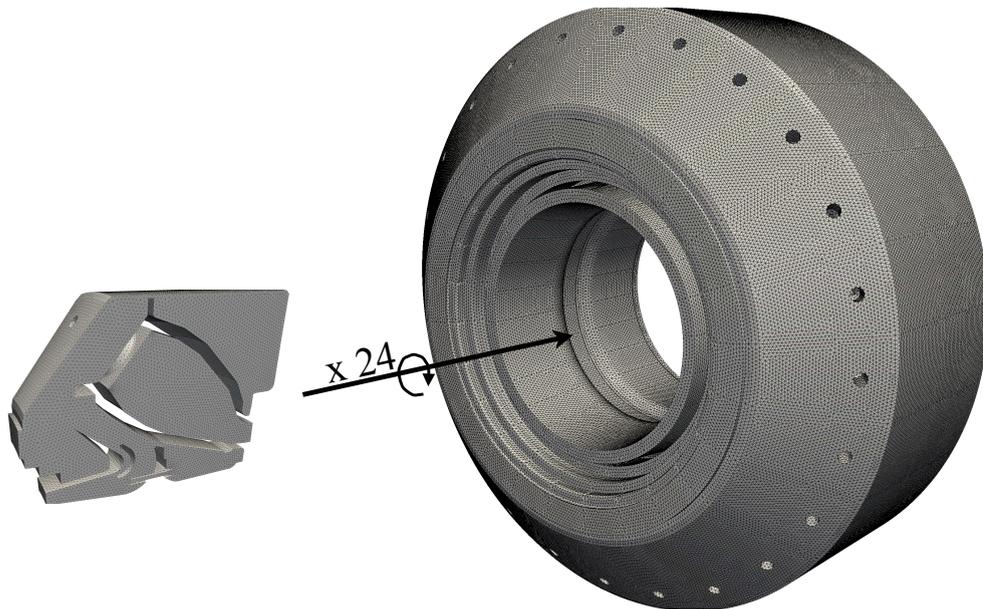

Figure 6.3: 360° mesh obtained from a single sector mesh used for AVSP simulations: 1,782,384 nodes and 9,527,472 cells.

The mesh is composed of 1,782,384 nodes and 9,527,472 cells. It allows to to capture all the geometrical details of the configuration. It is obtained from a single vector mesh, which is rotated and multiplied 23 times to obtain the 360 geometry, along with the sound speed field obtained from a single-sector time-averaged compressible LES[1].

In order to establish a classification of the modes, the sector that generates the annular combustor is divided into four parts (Fig. 6.2): the *Chamber* (Ch), the *Front Plenum* (FP),

---

[1]LES performed by S. Hermeth at CERFACS [53]

the *Back Plenum* (BP) and the *inner Plenum* (inP). This division is intended to give an unequivocal name to each azimuthal mode, depending on which part(s) of the configuration present(s) the highest level of acoustic pressure and on the azimuthal order. Since the combustor is composed of many cavities connected to each other (Fig. 6.2), a longitudinal coupling between them can be expected regardless of the azimuthal nature of the mode. Thus certain azimuthal modes cannot be attributed to a clear zone of the combustor and the name of the concerned zones are used in these cases to identify the mode.

On the other hand, purely longitudinal modes for which there does not exist any azimuthal coordinate dependency can be studied using only one sector. They are designated by a number that indicates their order of appearance (from lower to higher frequencies) followed by the letters GL (*Global Longitudinal*).

6.2 Acoustic modes with passive flame

Given the complexity of the current configuration, a first step consists in computing the acoustic modes without active flame (by setting $n_{local} = 0$ in Eq. (2.34)). The effect of the combustion on the gas temperature is retained however by taking into account a realistic sound speed field (Fig. 6.4) issued from a single sector time-averaged reactive compressible LES, for the operation point specified in Tab. 6.1. Alternatively, a simple description of the sound speed (522 m/s in the fresh gases and 829 m/s in the burnt gases) can also be used, leading to almost identical results.

T	p	Air flow rate	ϕ
690K	17.5 bar	19 Kg/s	0.5–0.7

Table 6.1: Combustor operating point.
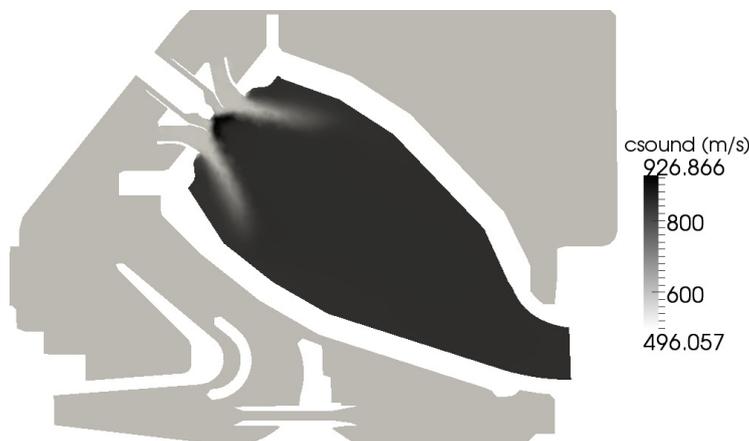
Figure 6.4: Longitudinal cut: sound speed $c_0(\vec{x})$ field obtained from a LES time-average solution used for AVSP simulations.

Boundary conditions are set to rigid walls ($u_1 = 0$) everywhere, including the inlet

and the outlet. The frequencies obtained with these boundary conditions and the sound speed field of Fig. 6.4 are displayed in Fig. 6.5, giving in each case an unequivocal name indicating their nature, order and the zones of the combustor associated with the modes. It is interesting to observe how certain modes are very close in frequency and yet, their structures are completely different (Fig. 6.6).

Passive flame modes
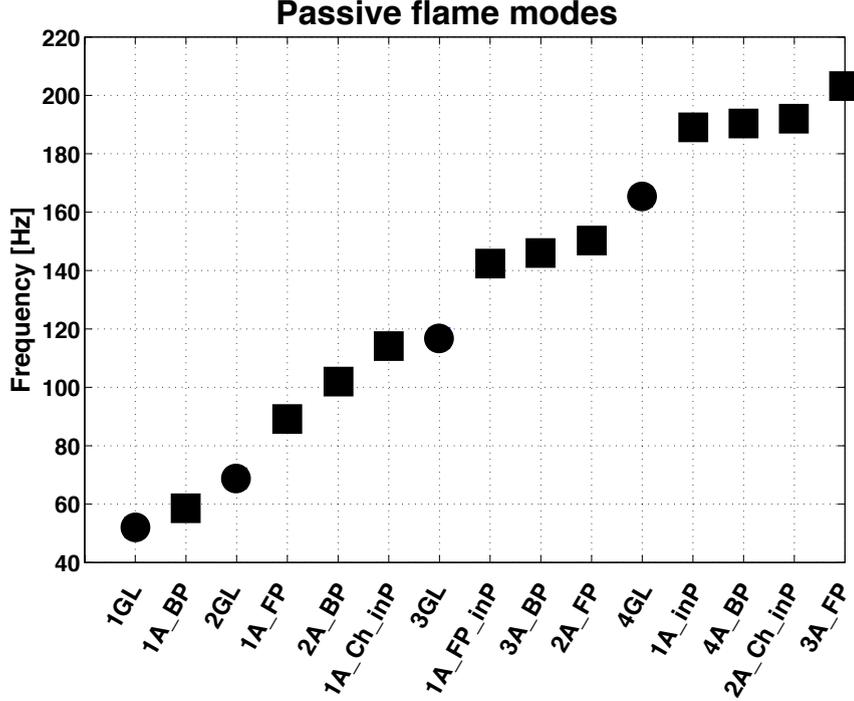
Figure 6.5: Frequencies corresponding to the first 15 modes (lowest frequency) of the annular combustor with passive flame: squares are azimuthal modes and circles are pure longitudinal modes.

The analytical frequency of the pth azimuthal mode of a simple annular cavity with a mean radius R and a mean sound speed c_0 is given by:

$$f_p^0 = \frac{pc_0}{2\pi R}. \tag{6.1}$$

It is possible to choose an equivalent mean radius R and a mean sound speed c_0 for each zone of the combustor. Tab. 6.2 summarizes these values for the four zones of Fig. 6.2. If each zone was decoupled from each other, then the frequencies provided by Eq. 6.1, would be very close to the ones computed by AVSP for azimuthal modes. This is not the case and the mode structures computed with AVSP show that the different cavities are coupled. Nevertheless, if the coupling is weak and only one cavity presents important acoustic activity, the frequency obtained using Eq. 6.1 for that cavity and the frequency computed by AVSP for the corresponding mode must be close.

Among azimuthal modes of Fig. 6.6, it is possible to distinguish the following families:

- **Front Plenum modes**: **1A_FP, 2A_FP and 3A_FP** are modes for which the front plenum zone presents the highest level of acoustic pressure. Nevertheless,

1A_BP — 58.7Hz
1A_FP — 89.1Hz
2A_BP — 101.8Hz
1A_Ch_inP — 114.1Hz
1A_FP_inP — 142.5Hz
3A_BP — 145.9Hz

2A_FP — 150.6Hz
1A_inP — 189.2Hz
4A_BP — 190.4Hz
2A_Ch_inP — 192.2Hz
3A_FP — 203.1Hz

p_1
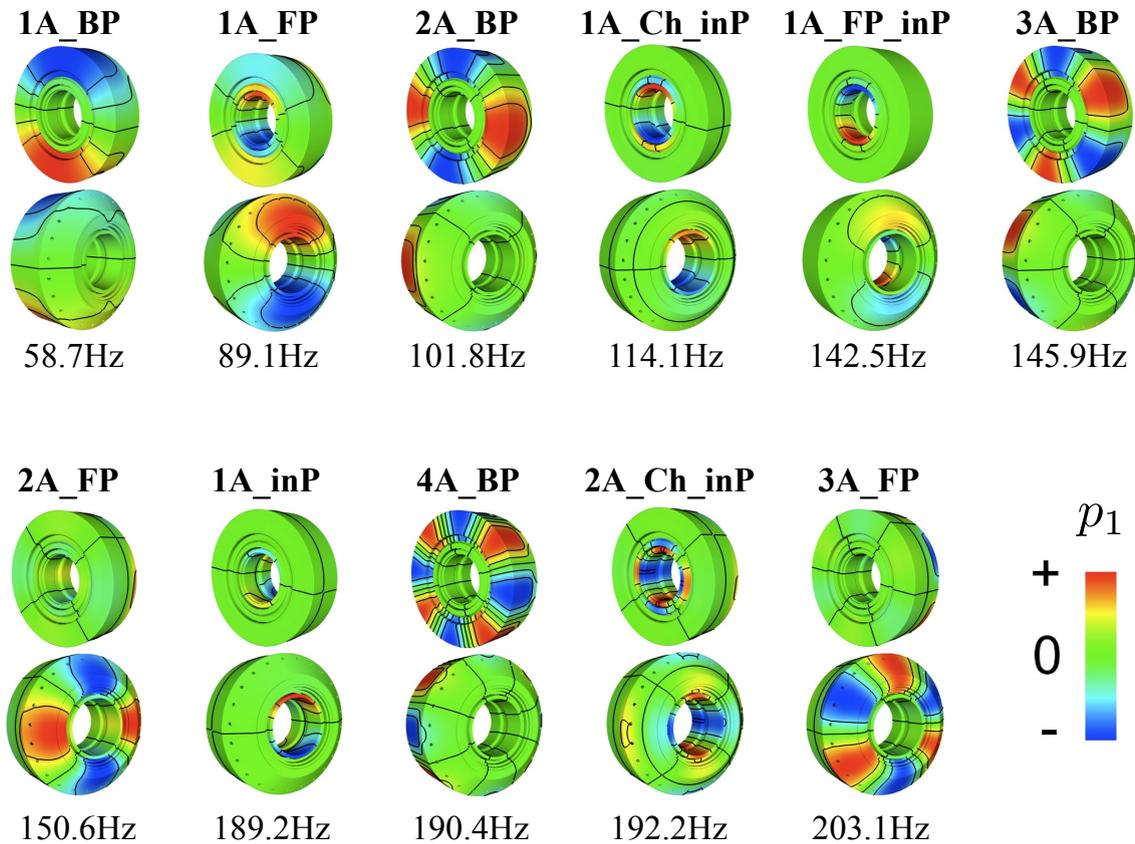
Figure 6.6: Back and front view of the combustor: structure of azimuthal modes $(p_1(\vec{x}))$ of Fig. 6.5.

1GL — 52Hz
2GL — 68Hz
**3GL** — 116Hz
4GL — 165Hz

p_1
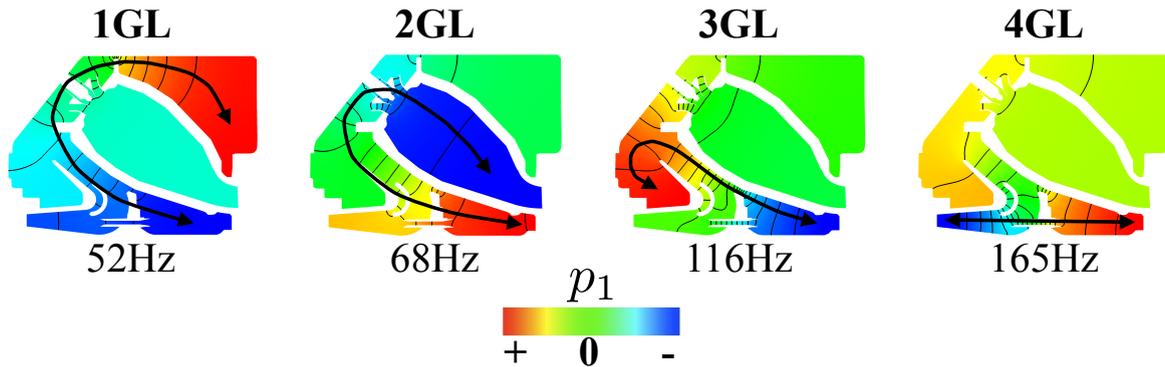
Figure 6.7: Longitudinal modes: the arrow goes through the cavities affected by the longitudinal modes, with the extrema at the maximum/minimum pressure levels.

a certain level of coupling with the back plenum (which can be appreciated e.g. for the mode 1_FP in Fig. 6.6) and with the chamber can be observed. The maximum pressure level in the Chamber and in the Back Plenum normalized by the maximum pressure amplitude in the Front Plenum, are plotted in Fig. 6.8, showing that the coupling between these cavities seems to disappear for high order modes.

Tab. 6.3 displays the frequencies of the Front Plenum modes computed with AVSP

	Back Plenum (BP)	Front Plenum (FP)	Chamber (Ch)	Inner Plenum (inP)
R (m)	1.72	1.2	1.4	0.86
c_0 (m/s)	522	522	829	522

Table 6.2: Approximated equivalent mean radius and sound speed for the four zones of the combustor used to computed analytical frequencies using Eq. (6.1).
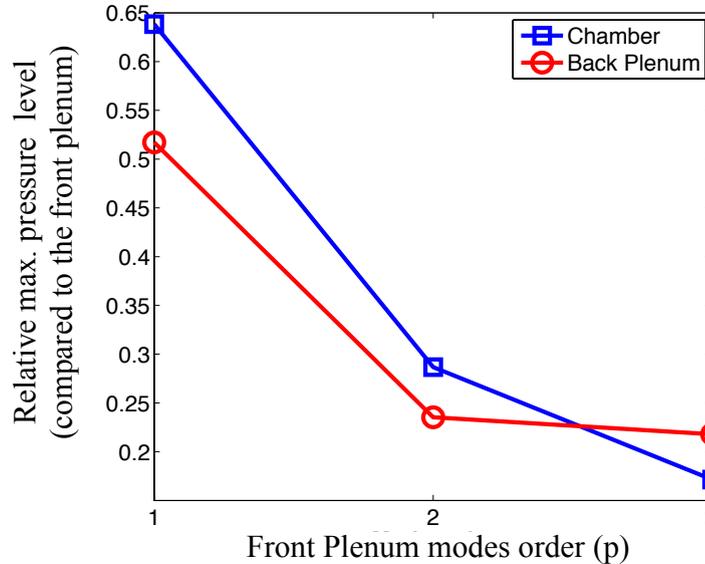

Figure 6.8: Front Plenum modes. The coupling between front plenum, back plenum and chamber diminishes drastically when the mode order p increases.

as well as the frequencies computed with Eq. (6.1) for the Front Plenum cavity (as if it was completely decoupled from the rest). These results show that the frequencies of a simple annular cavity are good approximations of the actual frequencies (AVSP) when the mode order p increases, which confirms the progressive decoupling of the Front Plenum cavity from the other cavities observed in Fig. 6.8.

Mode order	$p = 1$	$p = 2$	$p = 3$
	1A_FP	2A_FP	3A_FP
AVSP freq. (Hz)	89.1	150.6	203.1
FP analytical freq. (Hz)	69.2	138.5	207.7

Table 6.3: Front Plenum mode frequencies computed by AVSP and using Eq. (6.1) (analytical) for the Front Plenum cavity.

Tab. 6.3 shows a very important result: for example for a mode like 3A_FP at 203Hz, the frequency is dictated by the resonant azimuthal mode of the Front Plenum only

($f_3^0 = 207.7Hz$) and although an azimuthal mode is also present in the Chamber (see Fig. 6.9), the geometry (the mean radius) and sound speed field of the Chamber plays almost no role. Actually, for the Chamber, 203Hz would correspond more to the 2nd azimuthal mode (Eq. (6.1) gives $f_2^0 = 188.5Hz$ for the Chamber only), showing that the cavity that imposes the mode is the Front Plenum. It also means that for the 3A_FP mode, the combustion chamber exhibits a strange structure: it has the structure of an azimuthal mode of order $p = 3$ at a frequency matching a $p = 2$ azimuthal mode. This implies that the mode structure in the Chamber is not imposed by azimuthal acoustic waves in the Chamber. Information in the Chamber is controlled by the acoustic field in the Front Plenum which propagates to the Chamber through the burners. this is also an important statement experimentally: in this combustor, azimuthal modes can be observed in the Chamber at frequencies which do not correspond to azimuthal modes of the Chamber alone.
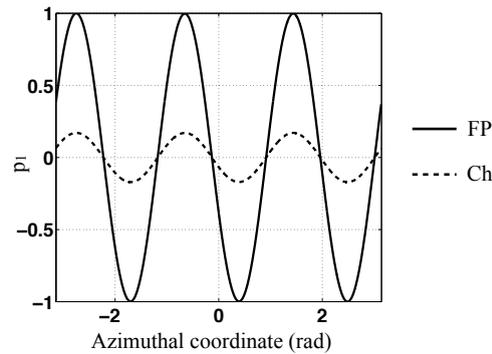

Figure 6.9: 3A_BP mode: acoustic pressure (p_1) in the Front Plenum and Chamber cavities corresponding to an azimuthal mode of order $p = 3$.

- **Back Plenum modes: 1A_BP, 2A_BP, 3A_BP and 4A_BP** are modes that can be mainly associated to the Back Plenum cavity. However, as is the case for the Front Plenum modes, the chamber and the front plenum are coupled with the Back Plenum (as seen e.g. for the mode 1A_BP in Fig. 6.6). Fig. 6.10 plots the maximum pressure level in the Chamber and in the Front Plenum normalized by the maximum pressure amplitude in the Back Plenum, showing again an important reduction of the coupling between cavities for high order modes. In Tab. 6.4 appear the frequencies

Mode order	$p = 1$	$p = 2$	$p = 3$	$p = 4$
	1A_BP	2A_BP	3A_BP	4A_BP
AVSP freq. (Hz)	58.7	101.8	145.9	190.4
BP analytical freq. (Hz)	48.3	96.6	144.9	193.2

Table 6.4: Back Plenum modes frequencies computed by AVSP and using Eq. (6.1) (analytical) for the Back Plenum cavity.

of the Back Plenum modes computed with AVSP as well as the frequencies computed
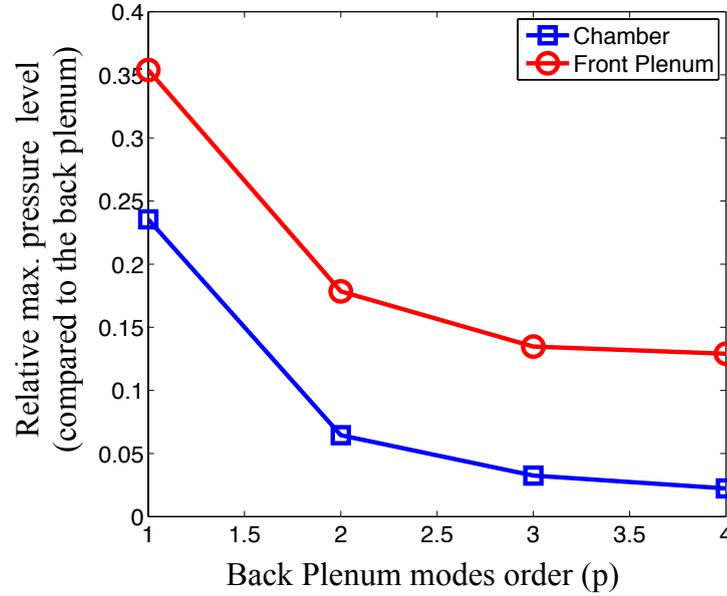
Figure 6.10: Back plenum modes. The coupling between back plenum, front plenum and chamber diminishes drastically when the mode order p increases. For $p = 4$ the back plenum is practically the only cavity with acoustic activity.

with Eq. (6.1) for the Back Plenum cavity (as if it was completely decoupled from the rest). As for the Front Plenum modes, these results show that the frequencies of the Back Plenum alone (Eq. (6.1)) are good approximations of the frequencies computed with AVSP, especially when the mode order p increases, which confirms the decoupling of the Back Plenum cavity from the other ones for high order modes observed in Fig. 6.10.
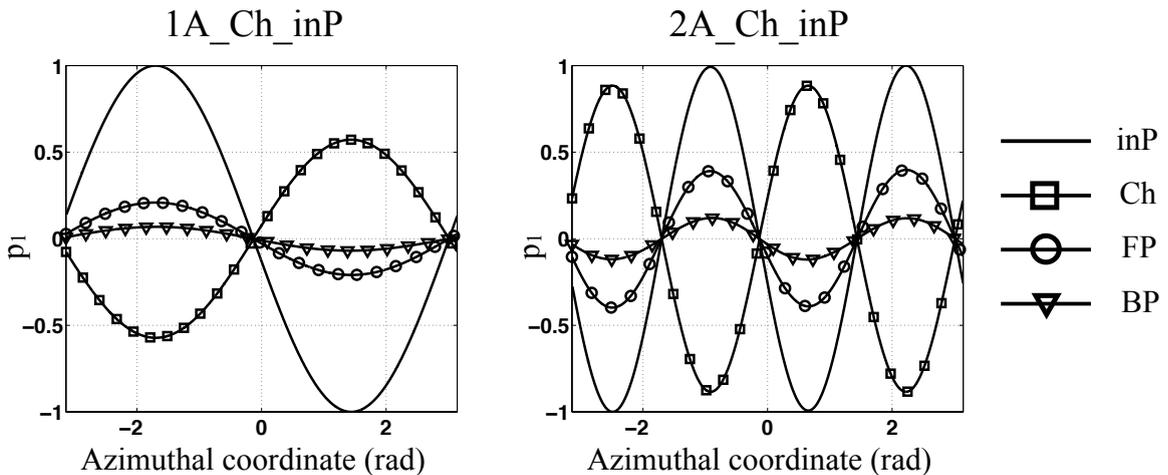

Figure 6.11: Chamber/inner Plenum modes: acoustic pressure (p_1) in the different zones of the combustor corresponding to an azimuthal mode of order $p = 1$ and $p = 2$. Although the highest pressure levels are in the Chamber and in the inner Plenum, the Front Plenum and Back Plenum cavities also exhibit azimuthal modes.

- **Chamber/inner Plenum modes: 1A_Ch_inP and 2A_Ch_inP** modes present important acoustic pressure level in both the inner Plenum and the Chamber cavities (Fig. 6.11). This can be explained by the fact that the differences of mean radius R and sound speed c_0 between both cavities compensate to give similar analytical frequencies (Tab. (6.5)) and thus the resonant modes of both cavities are expected to appear at similar frequencies. The frequencies displayed in Tab. 6.5 show a very good agreement for the 2nd azimuthal mode between the AVSP frequency and the analytical ones. The frequency of the the 2A_Ch_inP mode is imposed by the resonant frequencies of the Chamber and of the inner Plenum cavities. For this mode, the Front Plenum and the Back Plenum cavities exhibit a second azimuthal mode at a frequency (191.7Hz) which is not the frequency that corresponds to a 2nd azimuthal mode in these cavities. Therefore, the mode structure in the Front Plenum and Back Plenum is imposed by the Chamber and the inner Plenum.

Mode order	$p = 1$	$p = 2$
	1A_Ch_inP	2A_Ch_inP
AVSP freq. (Hz)	114.1	192.2
Ch analytical freq. (Hz)	94.2	188.4
inP analytical freq. (Hz)	96.6	193.2

Table 6.5: Chamber/inner Plenum modes frequencies computed by AVSP and using Eq. (6.1) (analytical) for the Chamber and the inner Plenum cavities.

The remaining modes of Fig. 6.6, i.e., 1A_FP_inP and 1A_inP modes, are azimuthal modes with a large longitudinal variation of the acoustic pressure in the Front Plenum and in the inner Plenum. This longitudinal component can explain why their AVSP frequencies are very different from the analytical frequencies provided by Eq. (6.1) (which does not take into account longitudinal variations of the pressure in the equivalent annular cavity) for these cavities.

6.3 Acoustic modes with active flame

In order to compute modes with active flame, according to the flame model described in Chapter 2, the local fields of the Flame Transfer Function (FTF) parameters $n_{local}(\vec{x})$ and $\tau_{local}(\vec{x})$ are required. These quantities can be obtained either numerically [97], analytically [109] or experimentally [38, 56, 82]. In the present case, S. Hermeth performed forced reactive LES of a single sector [53], which has allowed to obtain directly the required local fields of $n_{local}(\vec{x}), \tau_{local}(\vec{x})$, as well as the corresponding adimensional global values N_3, τ (see Tab. 2.2 in Chapter 2), for several frequencies. Since the FTF parameters depend on frequency, ideally, the local fields of n_{local} and τ_{local} should be known for a continuous range of frequencies, choosing the convenient one for each frequency. In practice, the high cost of LES computations makes this impossible, and the present procedure consists in choosing, among the available local n_{local}, τ_{local} fields, the ones closest to the frequency of interest.

Nevertheless, as shown in [53], for the present case, the dependency of the global parameters N_3 and τ_3 is smooth, so that no big differences with respect to the ideal procedure are expected from using this frequency-interpolation technique.

### 6.3.1 Acoustic modes with FTF from LES
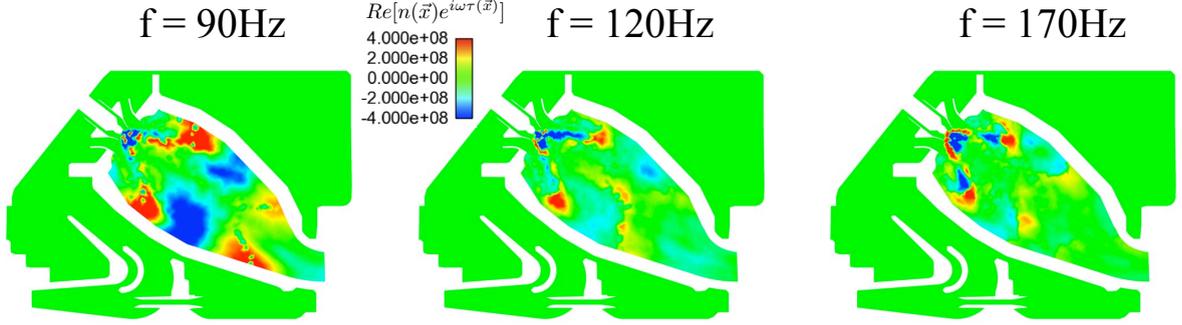
Figure 6.12: Real part of $n_{local}(\vec{x})e^{i\omega\tau_{local}(\vec{x})}$ obtained from LES for three different pulsation frequencies [53].

The n_{local}, τ_{local} fields of Fig. 6.12 are used in AVSP, along with the sound speed field of Fig. 6.4, with rigid boundary condition ($u_1 = 0$) everywhere, in order to solve:

$$\nabla \cdot c_0^2(\vec{x})\nabla\hat{p}(\vec{x}) + \omega^2\hat{p}(\vec{x}) = \frac{(\gamma-1)}{\rho_0(\vec{x})}n_{local}(\vec{x},\omega)e^{i\omega\tau_{local}(\vec{x},\omega)}\nabla\hat{p}(\vec{x}_{ref}) \cdot \vec{n}_{ref}. \quad (6.2)$$

Fig. 6.13 displays the frequencies and corresponding growth rates of the modes obtained with AVSP using the FTFs obtained from LES (red circles), whereas blue crosses correspond to the modes with passive flame (which are neutral). The arrows indicate the correspondence between modes with active flame and those with passive flame, according to a qualitative mode-structure identification, but they do not represent actual trajectories. How the frequencies with passive and with active flame change is not trivial, and some modes can even disappear with active flame (e.g. 1A_Ch_inP and 2GL modes). In Sec. 6.4.2, the evolution of frequencies will be further studied using a continuation method: starting from $n = 0$ (passive flame), the interaction index n value is increased, tracking down the modes for each value of n, which allows to establish the actual frequency trajectories.

It is possible to relate modes with active flame to the ones with passive flame by comparing mode structures, but there are important differences between both families of modes. The structures of the modes with passive and with active flame are compared in Fig. 6.15, using unrolled cylindrical cuts (Fig. 6.14).

The comparison of modes with passive and active flame (Fig. 6.15) shows that, in general, the coupling with the Chamber is increased by the active flame, leading to higher levels of acoustic pressure in this cavity. Indeed, the level of acoustic pressure in the Chamber in higher for all active flame modes displayed in Fig. 6.15, except for the 2A_Ch_inP mode. Another difference between modes with passive and active flame is that, while for passive flame modes the pressure in the cavities is perfectly either in or out-of-phase (i.e. nodes
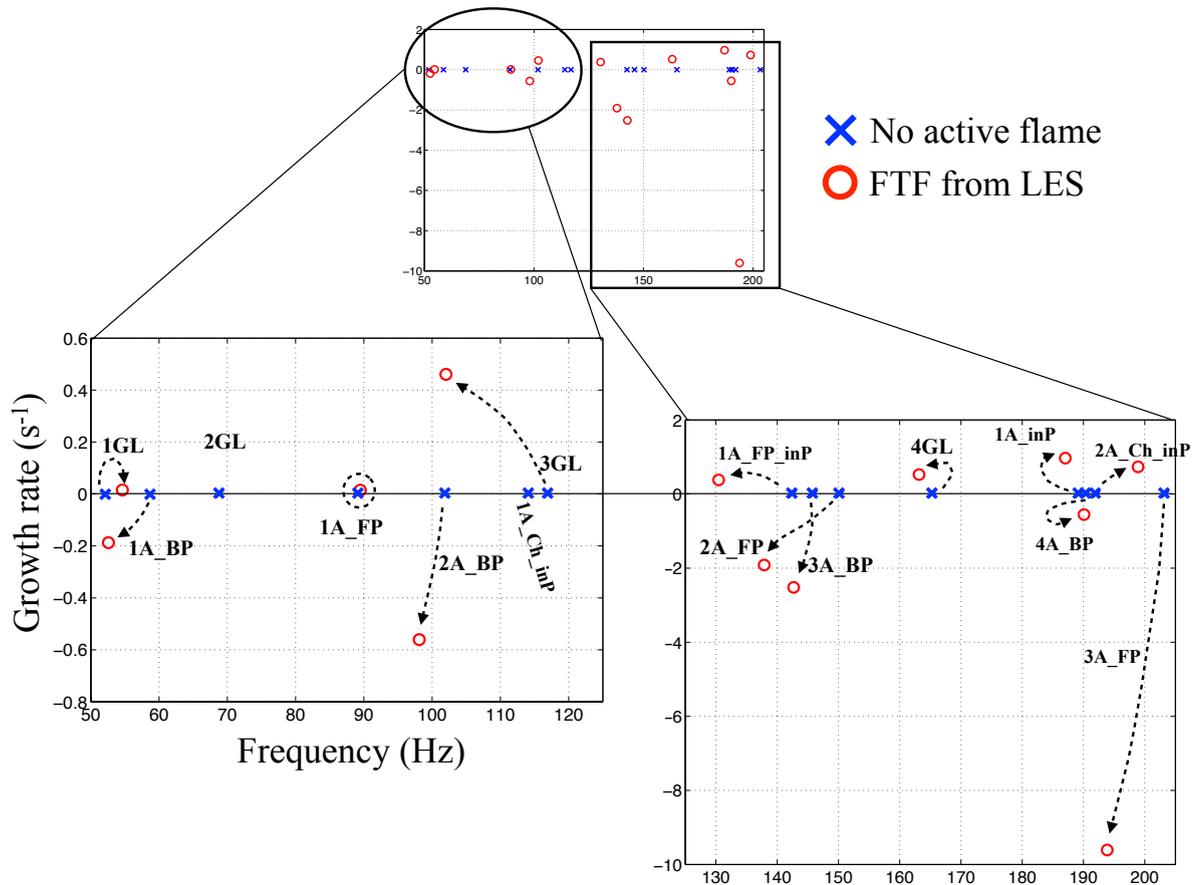
Figure 6.13: Frequencies and growth rates of acoustic modes with active flame (red circles) and modes with passive flame (blue crosses). Arrows indicate the evolution of modes from passive to active flame.
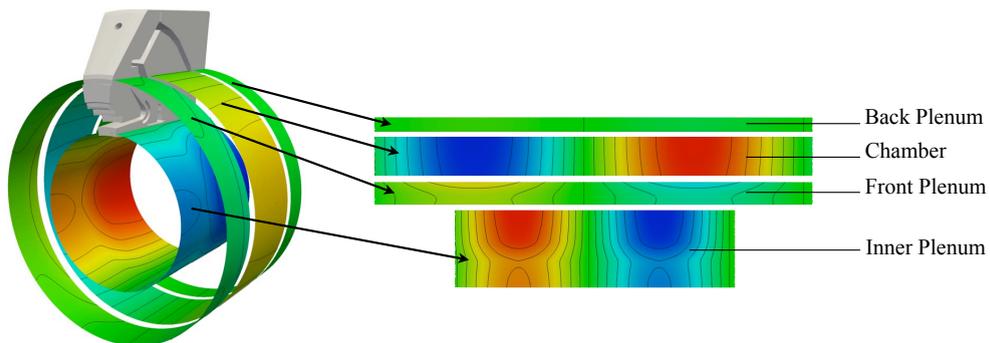

Figure 6.14: Cylindrical cuts performed through the different cavities that allow to see the structures of the acoustic mode at each zone.

and/or anti-nodes occurs at the same azimuthal locations), the active flame introduces a phase-shift between the different cavities.

This can be seen in Fig. 6.16, where the acoustic pressure p_1 in the BP, FP and Ch cavities is plotted for the 3A_BP mode, with and without active flame. It allows to see
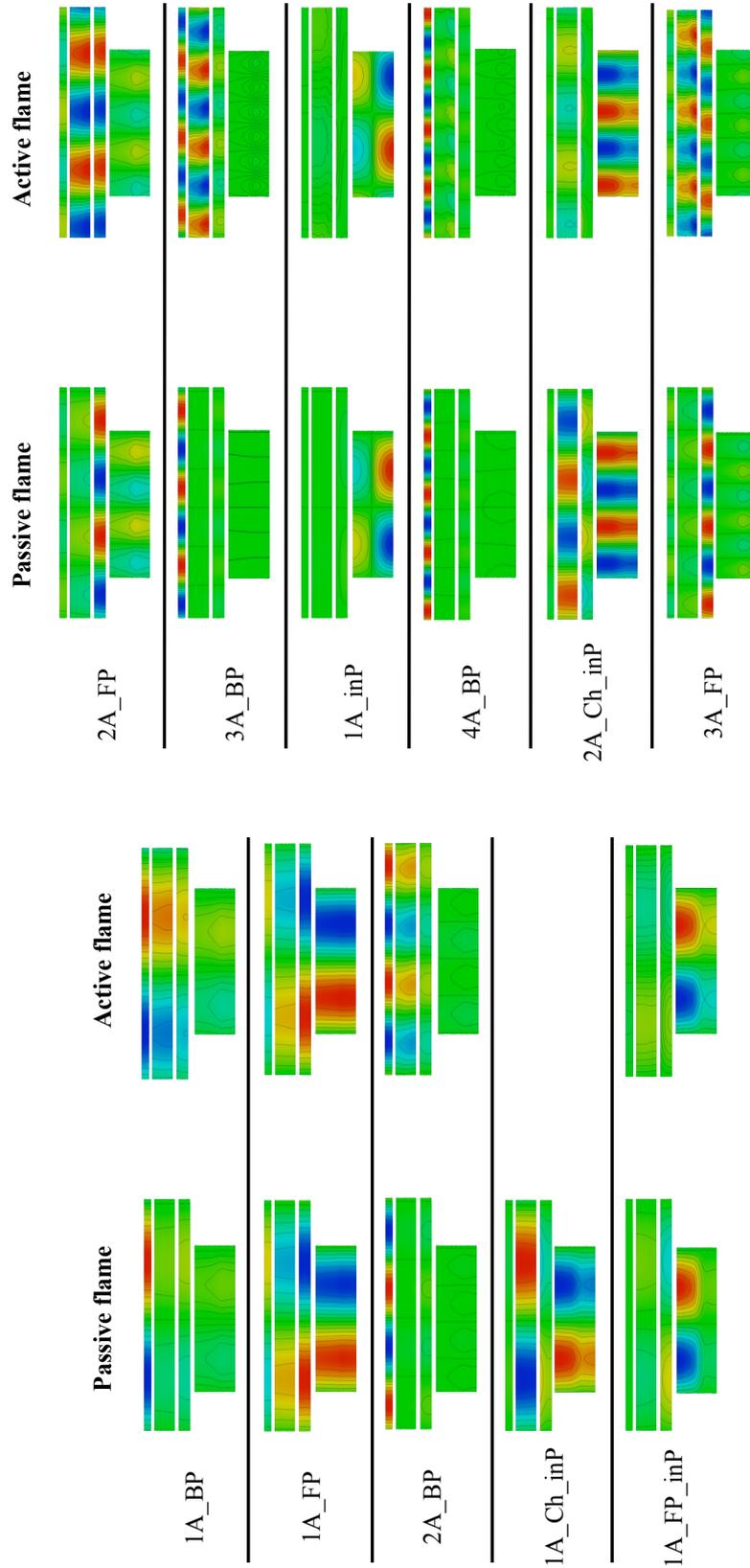
Figure 6.15: Structure of the acoustic modes with passive and with active flame.
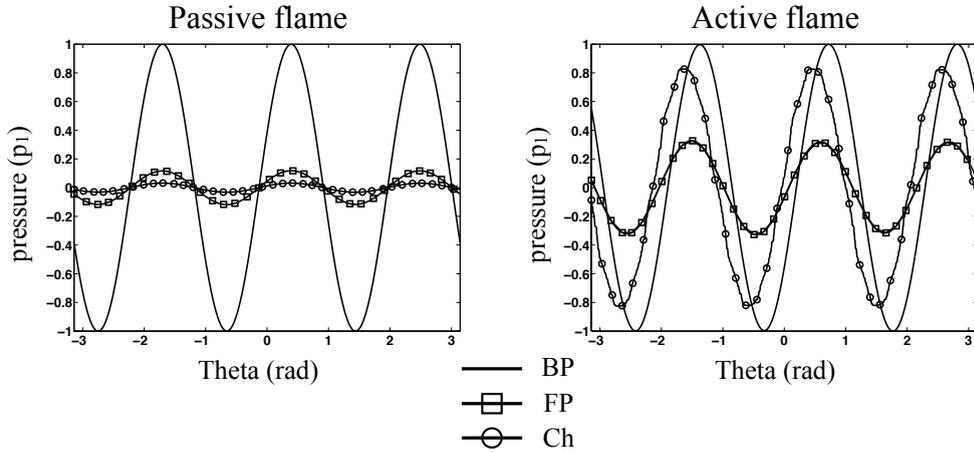
Figure 6.16: Acoustic pressure in the BP, FP and Ch, taken over the unrolled surfaces for the 3A_BP mode with and without active flame.
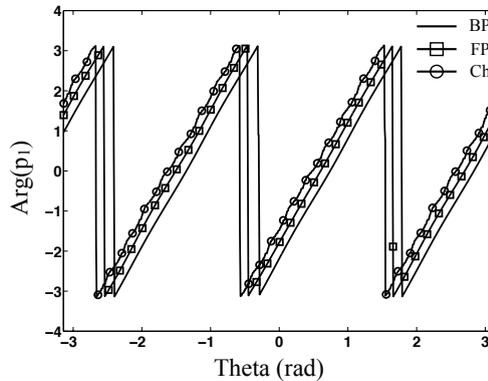

Figure 6.17: Acoustic pressure in the BP, FP and Ch, taken over the unrolled surfaces for the 3A_BP mode with and without active flame.

that the pressure amplitude in the Chamber and in the Front Plenum are much higher with active flame compared to the respective levels with passive flame. The phase-shift between the pressure waves in each cavity can be seen clearly in Fig. 6.17, where the phase of the pressure p_1 is plotted in each cavity. The phase-shift between the cavities is coherent with the fact that they are connected in a certain order: the pressure in the Back Plenum is followed by the pressure in the Front Plenum and the pressure in the Chamber follows the one in the Front Plenum. This behavior becomes clearer for higher order modes. In sec. 6.4 the phase-shift observed between cavities will be analyzed as a function of the time delay τ.

6.3.2 Energetic analysis of azimuthal modes with cavities longitudinally coupled

A name for each mode has been chosen as a function of the level of acoustic pressure in each cavity of the combustor. When the coupling diminishes for high order modes without active flame (see Sec. 6.2), it is easy to identify the cavity that imposes the frequency and
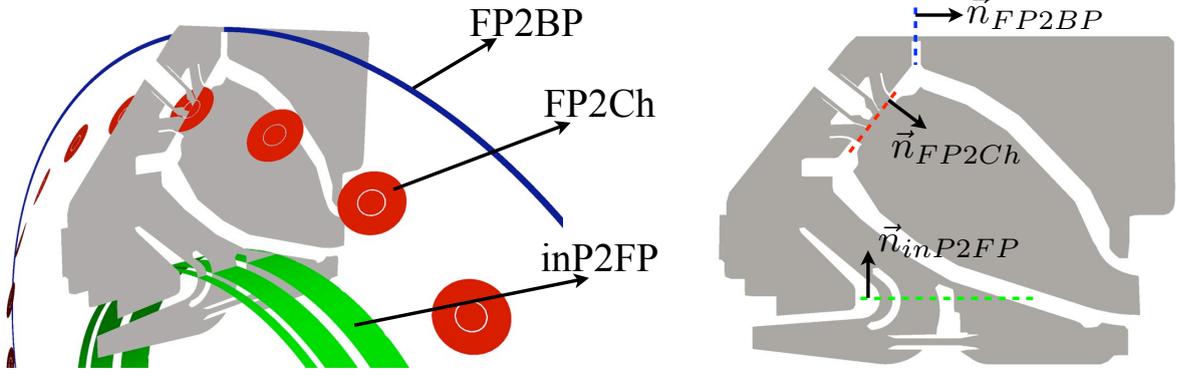
Figure 6.18: Surfaces that separate the different zones of the combustor used for computing the acoustic flux between the cavities, according to their normal directions.

the structure of the mode (and the name of the mode is chosen accordingly). Nevertheless, when the acoustic coupling between cavities is important (which is the case of modes with active flame, even for high order modes) it is difficult to establish which cavity (or cavities) is mainly responsible for the mode.

In the following, a quantitative analysis of the coupling between cavities is proposed, based on acoustic energy fluxes between cavities. The idea is to evaluate the variation of acoustic energy over a period in the whole combustor and then, compute the fraction of this total acoustic energy variation corresponding to each cavity. The cavity with the largest fraction of acoustic energy variation can be assimilated to the cavity driving the mode, since the growth rate of the mode is mainly imposed by it. On the other hand, a cavity whose acoustic energy does not vary in a period (or does little) does not contribute to the growth rate of the mode and thus it does not contribute to the mode.

Three surfaces are chosen at the interface between the zones previously defined (see Fig. 6.2): Back Plenum, Front, Plenum, Chamber and inner Plenum. The acoustic flux through these surfaces is computed over a period, according to their normals (Fig. 6.18). Since non-dissipative boundary conditions have been used ($u' = 0$), no energy gain or losses can exist due to acoustic fluxes through boundaries. The only eventual acoustic energy gain or dissipation in the system is necessarily due to the volumic term R_1 of Eq. (6.3), which is associated to the flame (see Chapter 2):

$$\frac{d}{dt}E_1(t) = R_1 = \int_\Omega \frac{\gamma - 1}{\gamma p_0} p_1(\vec{x}, t) q_1(\vec{x}, t) dV. \tag{6.3}$$

Eq. (6.3) is, in this case, equivalent to the Rayleigh criterion: if the coupling between combustion (q_1) and acoustics (p_1) yields $R_1 > 0$, then the system gains energy in time and so it is unstable; if, at contrary $R_1 < 0$, then the system energy decreases over time and hence it is stable.

In the present case, since $q_1 \neq 0$ only in the Chamber cavity (Ch), and there are no acoustic losses at boundaries, all the acoustic energy is either produced or dissipated in the Chamber. Studying the acoustic fluxes over a period through the surfaces defined in Fig. 6.18 allows to know how the energy produced or dissipated in the Chamber is distributed over (or provided by) the rest of the cavities. In other words, it is possible

to establish the fraction of acoustic energy variation over a period corresponding to each cavity. For resonant modes involving many coupled cavities, the study of their acoustic energy variation over a period allows to establish which cavities impose the mode: cavities with largest fractions of acoustic energy variation drive the mode and viceversa, a cavity that presents a very low fraction of energy variation does not contribute to the mode. It is possible to distinguish two cases (see Fig. 6.21):

- The mode is unstable: acoustic energy is generated in the Chamber, which contributes to the increment of acoustic energy of the different cavities of the combustor. A net acoustic flux exits the Chamber to the Front Plenum (FP2Ch flux), which feeds the Back Plenum (FP2BP flux) and the inner Plenum (inP2FP flux) (see Fig. 6.19). The energy generated in the chamber increases the acoustic energy in the combustor. The cavity (or cavities) that presents the largest positive acoustic energy variation (i.e. the cavity that receives the most part of the energy produced in the Chamber) is the one that contribute the most to the mode.
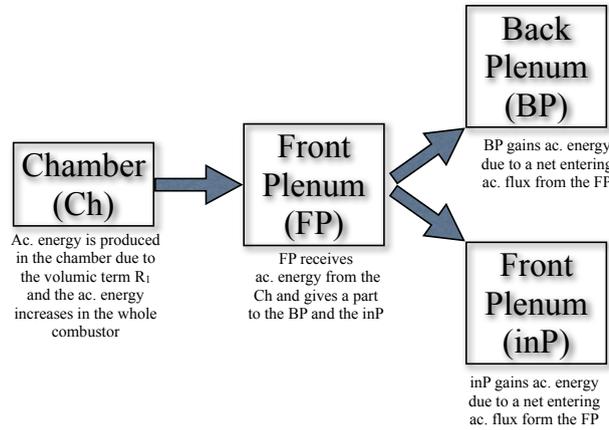

Figure 6.19: Unstable mode: the acoustic energy produced in the Chamber contributes to the increment of acoustic energy in the rest of cavities. Arrows indicate the direction of the acoustic fluxes between cavities.

- The mode is stable: the acoustic energy over a period diminishes in the whole combustor, although it can be dissipated only in the Chamber. Consequently, acoustic fluxes exit the different cavities towards the Chamber, which yields a negative acoustic energy variation in each cavity. Starting from the inner Plenum and the Back Plenum, the exiting acoustic fluxes from these cavities are collected by the Forward Plenum, which feeds the Chamber (see Fig. 6.20). In this case, the cavity (or cavities) that drives the stability of the mode is the one that presents the largest fraction of negative acoustic energy variation.

Integrating Eq. (6.3) over a period T we have:

$$E_1(T) - E_1(0) = E_{1T} = \int_T R_1 dt = \int_T \int_\Omega \frac{\gamma - 1}{\gamma p_0} p_1(\vec{x}, t) q_1(\vec{x}, t) dV dt,$$
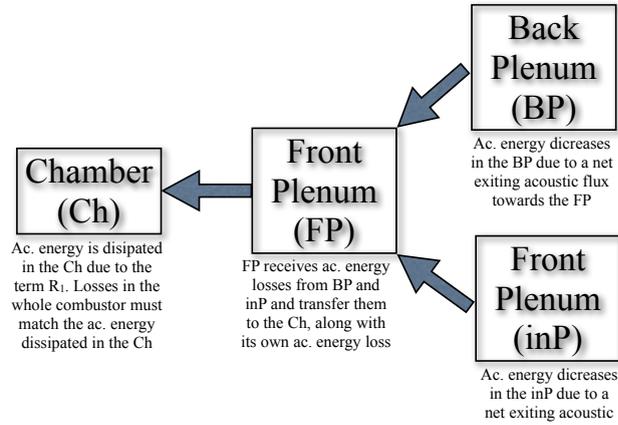
Figure 6.20: Stable mode: the acoustic energy dissipated in the Chamber is provided by the different cavities. Arrows indicate the direction of the acoustic fluxes between cavities.
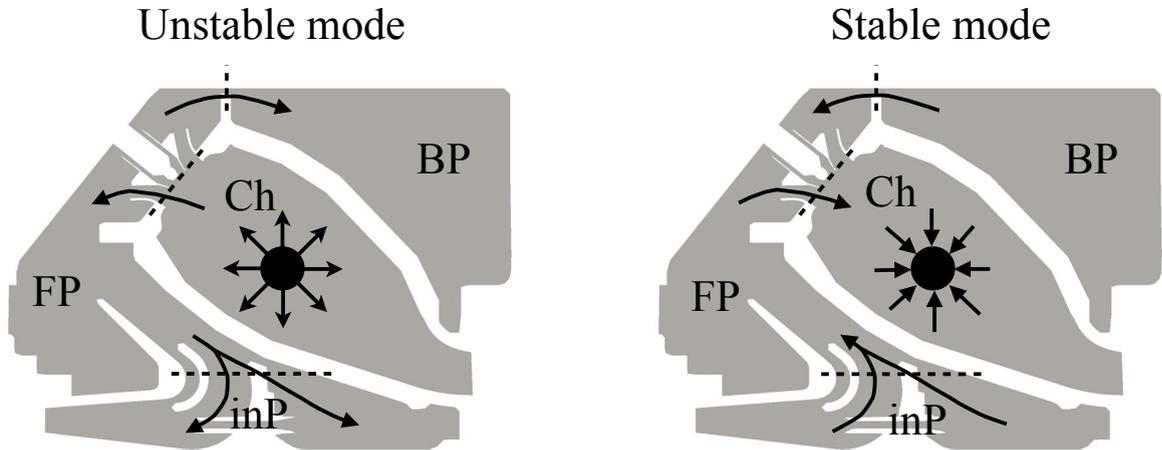
Figure 6.21: Direction of the acoustic fluxes depending on whether the chamber is an energy source (left) or and energy sink (right).

which corresponds to the net variation of acoustic energy in the combustor over a period T ($E_{1T} > 0$ if the mode is unstable and $E_{1T} < 0$ if the mode is stable). On the other hand, the fluxes through the surfaces during a period T are computed as

$$F_1 = \int_T \int_S p_1(\vec{x},t) u_1(\vec{x},t) \cdot \vec{n} \; dS \; dt,$$

where $\vec{n}$ is the surface normal. Then, the fraction (in hundred percent with respect to the total energy variation E_{1T}) of acoustic energy variation during a period T in each cavity, is computed as follows (the fluxes are already considered with the sign imposed by the chosen normal directions):

$$E_{Ch}(\%) = \frac{E_{1T} + F_1^{FP2Ch}}{|E_{1T}|} \times 100 \tag{6.4}$$

$$E_{FP}(\%) = \frac{-F_1^{FP2Ch} - F_1^{FP2BP} + F_1^{inP2FP}}{|E_{1T}|} \times 100 \tag{6.5}$$

$$E_{BP}(\%) = \frac{F_1^{FP2BP}}{|E_{1T}|} \times 100 \tag{6.6}$$

$$E_{inP}(\%) = \frac{-F_1^{inP2FP}}{|E_{1T}|} \times 100 \tag{6.7}$$

Obviously, the sum of these terms is one (100% of the total acoustic energy variation E_{1T}). Each of them measures the fraction by which each cavity contributes to the growth rate of the mode (positive or negative). Note that this analysis can be used only when the growth rate of the mode is not zero. The acoustic energy for neutral modes does not change with time, so that $E_{1T} = 0$ and the present procedure can not be applied.

Fig. 6.22 displays azimuthal modes (with a non zero associated growth rate), showing in each case the fraction of the total acoustic energy variation E_{1T} associated to each cavity (Eqs. (6.4-6.7)). The '+' sign preceding the fraction of acoustic energy variation in the case of unstable modes indicates that the cavity gains acoustic energy. On the contrary the '−' sign precedes the fraction of energy variation for stable modes, indicating that the acoustic energy in the cavity decreases with time. Results displayed in Fig. 6.22 are a quantitative measure of the longitudinal coupling between cavities for azimuthal modes: if all cavities present similar fractions of acoustic energy variation then they all contribute to the mode; whereas if one cavity has a very large fraction of the acoustic energy variation compared to the rest, then this cavity drives the mode and can be considered decoupled from the rest. For the Back Plenum and Front Plenum modes, the Chamber presents, in general, large values of $|E_{Ch}|$, which confirms the increase of coupling with the Chamber for active flame modes compared with passive flame modes.

For example, the 1A_BP mode presents similar fractions of acoustic energy variation in the Back Plenum ($E_{BP} = -36.11\%$), Front Plenum ($E_{FP} = -22.70\%$) and Chamber ($E_{Ch} = -37.9\%$), while acoustic energy in the inner Plenum varies very little ($E_{inP} = -3.29\%$). It means that the three cavities (BP, FB and Ch) are strongly coupled in this mode, and the three cavities contribute to the growth rate of the mode. Of course, only the Chamber feeds energy into the mode but the resonance also involves the Back and Front plenums mainly and not the inner Plenum. This is coherent with the high level of acoustic pressure in these cavities (see e.g. Fig. 6.15). However, this is not necessarily true for the final value of the frequency, which is mainly imposed by the Back Plenum cavity. Indeed, the frequency of the mode computed by AVSP is about 52Hz, while for a $p = 1$ mode Eq. (6.1) gives 48.3Hz for the Back Plenum, 69.2Hz for the Front Plenum and 94.2Hz for the Chamber. This means that the structure of the pressure in the Front Plenum and the Chamber is imposed by the Back Plenum due to the coupling between these cavities.

The 4A_BP mode is a good example of a mode for which the growth rate is imposed mainly by one cavity: the fraction of acoustic energy variation in the Back plenum ($E_{BP} = -84.63\%$) corresponds almost entirely to the total variation of acoustic energy in the whole
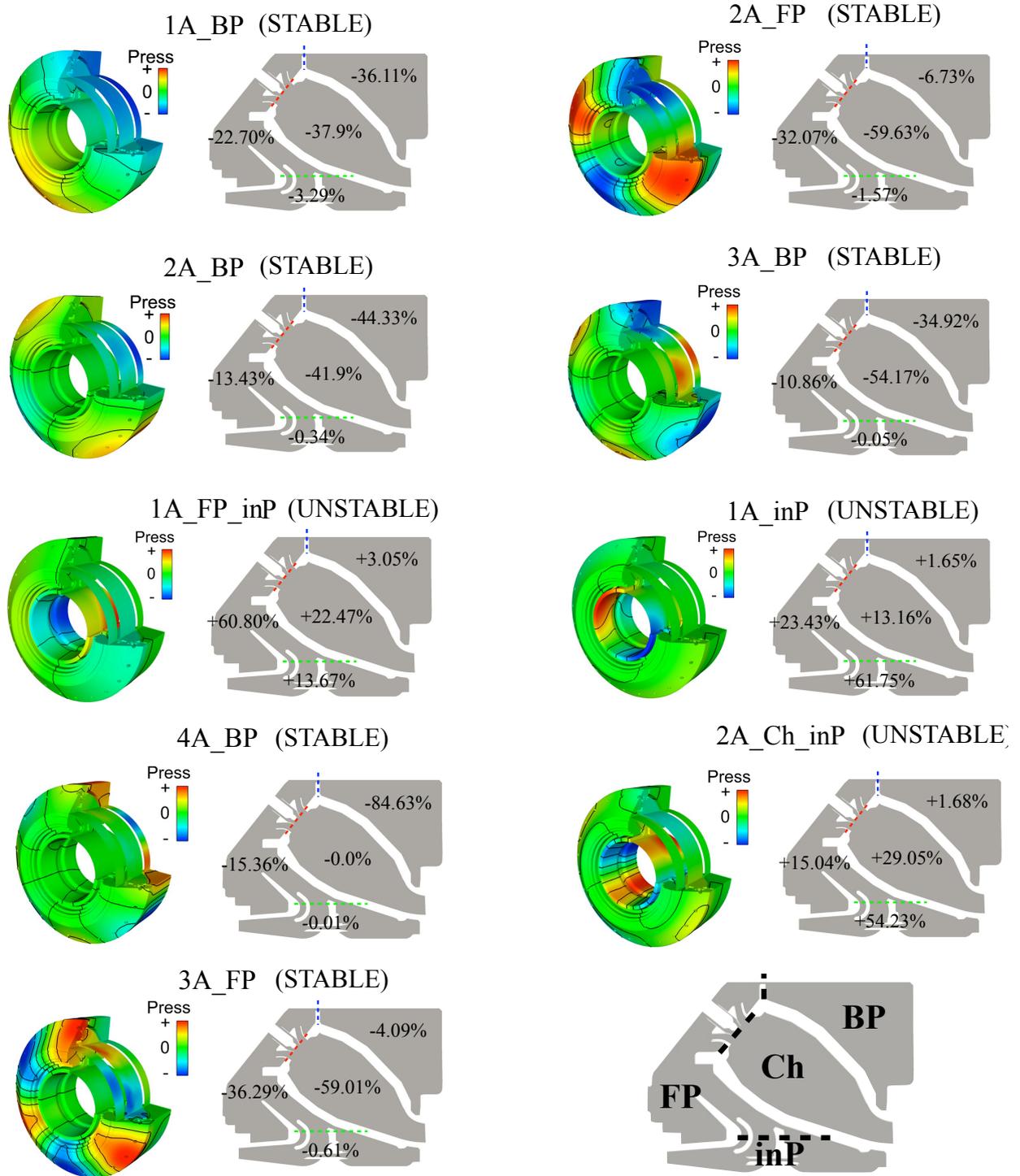
Figure 6.22: Percentage of acoustic energy produced or dissipated over a period in each one of the four cavities for azimuthal modes.

combustor. In this case, the Back Plenum cavity is decoupled from the rest (which is also coherent with the very low level of acoustic pressure in the other cavities) and the structure and frequency of the mode is imposed by this cavity: the mode computed by AVSP has a frequency about 190Hz and the frequency provided by Eq. (6.1) for the Back Plenum for

$p = 4$ is 193.2Hz, which is a very good approximation.

This methodology provides interesting information about the cavities responsible for the growth rate of the mode. From the point of view of control of combustion instabilities, this is an useful information since it tells us which cavity plays the most important role in the mode stability.

6.4 Stability study with constant $n - \tau$ fields

6.4.1 Local and global FTF

It is useful to investigate the combustor stability by supposing scenarios where the flame delay τ would be modified to change stability. This is the procedure used in practice: engineers modify fuel staging or swirl in injectors to obtain stable regimes. In companies like Siemens or Ansaldo, they mix burners with different characteristics to have different τ. All these strategies can be investigated in AVSP. In Sec. 6.3, this has not been done because there is not a single time delay τ which can be varied but a field of time delay $\tau(\vec{x})$. One possible scenario is to assume that the flame is compact and thus use a single global delay τ for the whole flame, which allows to study stability as a function of τ. To do this we drop the local fields $(n_{local}(\vec{x}), \tau_{local}(\vec{x}))$ obtained from LES and constant fields of these parameters are used instead. Constant values of the interaction index $n_{local}(\vec{x}) = n_{local}$ and time-delay $\tau_{local}(\vec{x}) = \tau_{local}$ are imposed over a volume which is representative of the actual flame (from a time-average LES solution). The flame volume is chosen here according to the heat release field provided by the time-average LES solution: points with a heat release value greater than a given threshold, are considered to be in the flame, which allows to define a certain flame zone with a volume V_f. The constant values of n_{local} and τ_{local} are then chosen in such way that when they are integrated over the flame volume V_f, the global values N_2 and τ obtained from the volumic integration of the LES fields $(n_{local}(\vec{x}), \tau_{local}(\vec{x}))$, are retrieved. The computation of the constant values $(n_{local}, \tau_{local})$ is performed as follows:

1. Integrate the FTF from LES in order to obtain the global FTF parameters (N_2, τ):

$$\int_V n_{local}(\vec{x})e^{i\omega\tau_{local}(\vec{x})}dV = N_2 e^{i\omega\tau}. \tag{6.8}$$

2. Distribute the global FTF parameters (N_2, τ) over the flame volume V_f defined from the heat release, so that the the constant local values are $n_{local} = N_2/V_f$ and $\tau_{local} = \tau$.

In the case of compact flames, local and global descriptions of the flame are equivalent: using a realistic distribution $(n_{local}(\vec{x}), \tau_{local}(\vec{x}))$ or constant values $(n_{local}, \tau_{local})$ in AVPS leads to the same results, provided that the global values (N_2, τ) obtained by integrating both fields are the same. In the present case, the FTF obtained from LES occupies practically all the Chamber (see Fig. 6.12) and it can not be considered as compact. Using constant FTF parameters $(n_{local}, \tau_{local})$ or realistic distributions $(n_{local}(\vec{x}), \tau_{local}(\vec{x}))$ does not yield exactly the same results, even if the integration of both fields leads to the same

global values. To illustrate this, the longitudinal mode around 100Hz (3GL) is computed using constant FTF parameters for different flame volumes V_f (see Fig. 6.23), which are defined by the points where the mean volumic heat release (HR) is greater than a chosen threshold. In all cases, the integration of the constant values n_{local}, τ_{local} over the flame volume V_f, leads to the same global values (N_2, τ), which have been obtained from the integration of the $n_{local}(\vec{x})$, $\tau_{local}(\vec{x})$ values corresponding to the FTF obtained from LES for 90Hz[2].

$$V_f = 1.39e\text{-}2 \text{ m}^3$$
(HR > 1e9 W/m³)

$$V_f = 4.08e\text{-}2 \text{ m}^3$$
(HR > 1e7 W/m³)

$$V_f = 0.11 \text{ m}^3$$
(HR > 1e3 W/m³)

$$V_f = 0.16 \text{ m}^3$$
(HR > 10 W/m³)
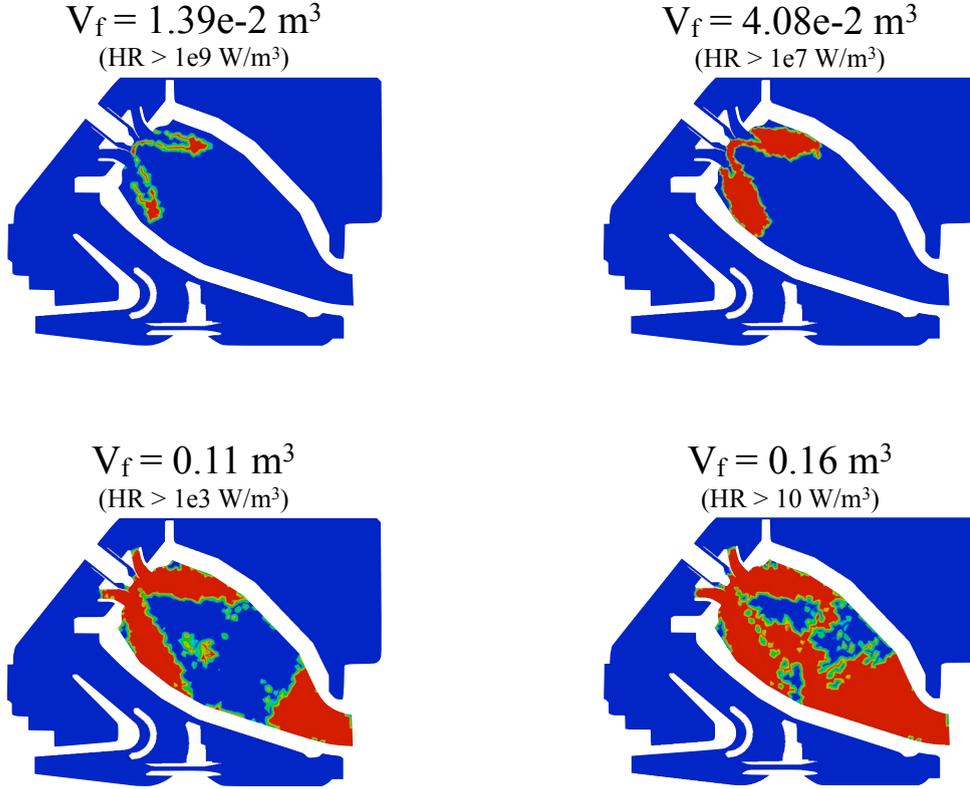
Figure 6.23: Different flame zones where $n_{local} \neq 0$ and $\tau_{local} \neq 0$ defined from the volumic heat release (HR) distribution of a time-average LES solution. The value of the constant time delay τ_{local} is the same for all flames, while the constant interaction index $n_{local} = N_2/V_f$ changes for each flame volume.

The frequencies and growth rates obtained for each flame volume V_f are displayed in Fig. 6.24. The reference case ($--$) corresponds to the frequency and growth rate computed with the FTF obtained from LES. The results obtained with constant $n - \tau$ fields are not very different from the reference case, so that using a single constant interaction index n_{local} and a constant single single delay τ_{local} does not constitute a major simplification: it can be used now in this section, where we want to perform a parametric study as a function of the parameters N_2, τ. The flame volume V_f obtained considering that points with a volumic heat release greater than $10^7 W/m^3$ are in the flame zone (Fig. 6.23) is retained for the computations presented in the rest of the chapter.

---

[2]The integration of the local FTF at 90Hz as in Eq. (6.8) leads to the values $N_2 = 32073483 \; J/m$ and $\tau = 2.36 \; ms$.
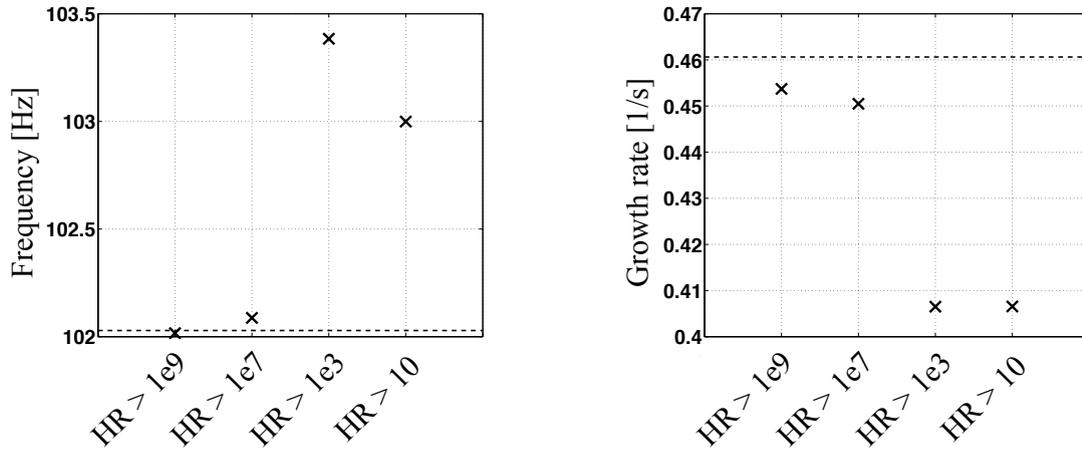
Figure 6.24: Frequencies and growth rates corresponding to the mode 3GL obtained using the FTFs of Fig. 6.23. (− −) correspond to the results obtained using the FTF issued from LES for 90Hz (Fig. 6.12).

6.4.2   From passive to active flame: modes trajectories

In sec. 6.3 the modes computed with active flame are related to those with passive flame, according to a mode structure identification. In many cases, the frequencies of corresponding modes are however quite different with and without active flame. This sections shows how a continuation method can be used to study how the modes (frequency, growth rate and structure) change when the interaction index N_1 increases from zero (passive flame) to a certain value, following the frequencies trajectories. For this study, the time-delay τ is fixed to 3ms, while the interaction index N_1 varies. The Crocco's coefficient N_1 (see Chapter 2) is used in what follows in order to express the value of the FTF interaction index in a more convenient fashion[3].

Longitudinal and azimuthal modes are studied separately. Fig. 6.25 plots the frequency and growth rate of the longitudinal modes for different values of N_1 going from 0 (passive flame) to 6. Although the 1GL and 4GL modes are not very dependent from N_1, when N_1 starts to grow they become unstable and then, for higher values of N_1 they become nearly neutral again, while their frequencies change. On the other hand, the frequencies of the 2GL and 3GL modes change rapidly with N_1: the 3GL mode gets unstable at first ($N_1 = 0 - -0.2$) and when N_1 keeps growing, its growth rate decreases again while its frequency gets smaller. Finally the 2GL mode becomes very unstable when N_1 begins to grow and then disappears for values of N_1 greater than 0.2.

The structure of the longitudinal modes is displayed in Fig. 6.26 for several values of N_1. Although their shape does not change significantly for different values of N_1, one can see small changes of the pressure amplitude in the Chamber.

The evolution of the first 5 azimuthal modes is also investigated when the interaction index N_1 grows from zero. Fig. 6.27 shows the trajectories of the modes, in a frequency-growth rate diagram. The behavior of the 1A_BP, 2A_BP and 1A_FP_inP modes is quite

---

[3]Integrating the FTF issued from LES corresponding to 120Hz, the equivalent global value $N_1 = 1.83$ is retrieved, using $S_{ref} = 1m^2$, $\gamma = 1.27$ and $p_0 = 17bar$ in the Crocco's flame model.
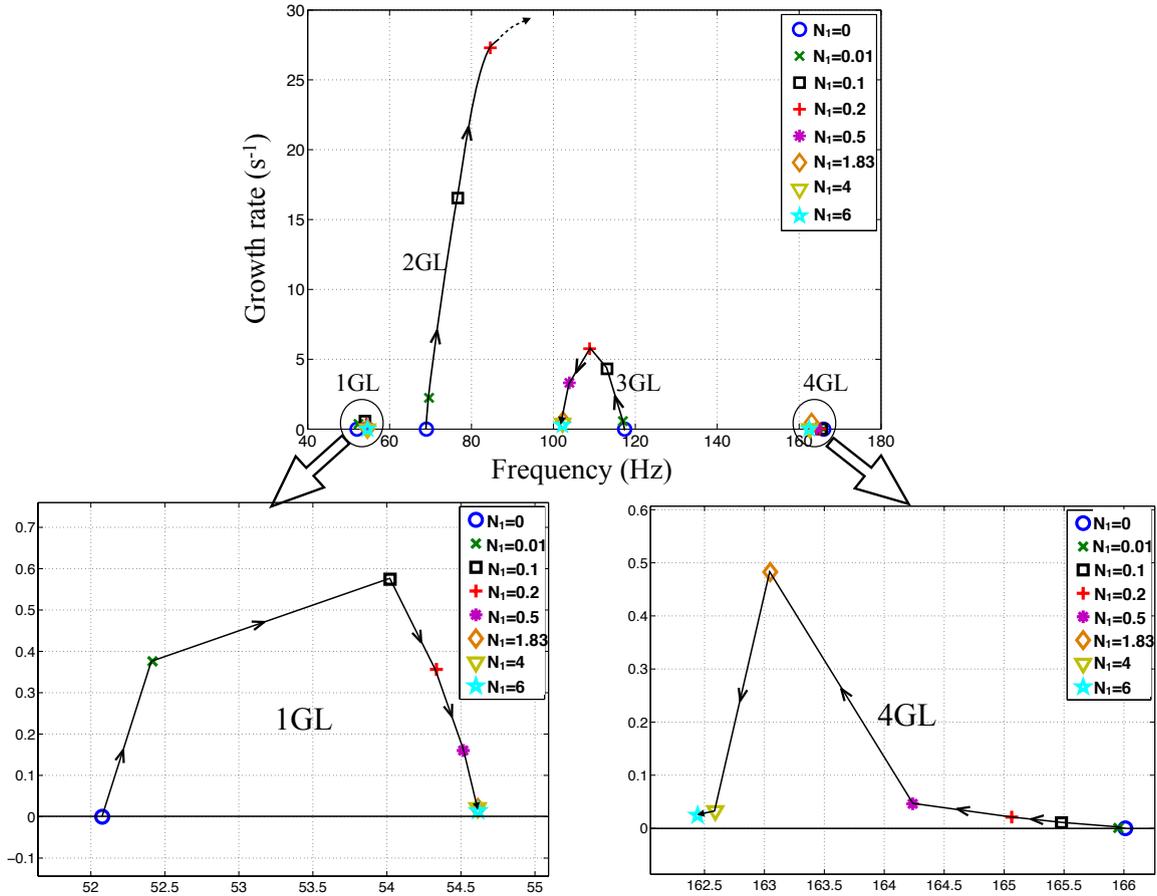
Figure 6.25: Trajectories of the globally longitudinal modes for increasing values of the interaction index N_1 ($\tau = 3ms$ is fixed).

similar to the one of longitudinal modes, describing a canon-bullet trajectory: initially neutral for $N_1 = 0$, the absolute value of their growth rate increases at first and then, for larger N_1 values, the absolute value of the growth rates decreases again, while their frequencies decrease monotonically with significant variations. The 1A_FP mode does not change with N_1. The 1A_Ch_inP mode becomes very unstable and then it disappears for values of N_1 larger than 0.2, as the longitudinal 2GL mode does.

The structure of the azimuthal modes is displayed in Fig. 6.28 for different values of N_1. The 1A_FP mode does not change with N_1, which is in agreement with the fact that its frequency do not change either. The structure of the 1A_Ch_inP mode, on the other hand, strongly depends on the value of N_1, getting very perturbed for $N_1 = 0.2$ before disappearing. For the 1A_BP and 2A_BP modes one can see how the pressure level in the Chamber becomes higher for larger values of N_1, which explains also their frequency variation. The structure of the 1A_FP_inP mode does not change much. It is possible to see though that the pressure in the Front Plenum decreases while the pressure level in the front part of the inner Plenum and the Chamber increases.

Although the FTF used in this section are different from those coming from LES, the results (frequency trajectories and mode structures) for longitudinal and azimuthal modes
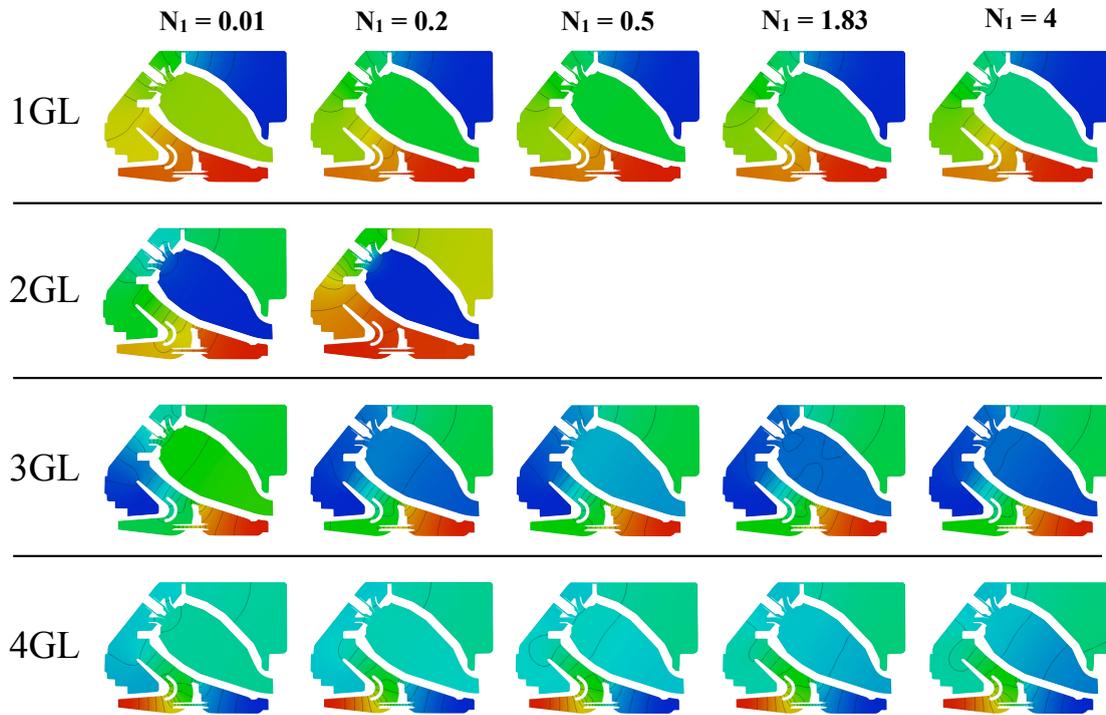
**Figure 6.26:** Structure of the longitudinal modes for increasing values of N_1
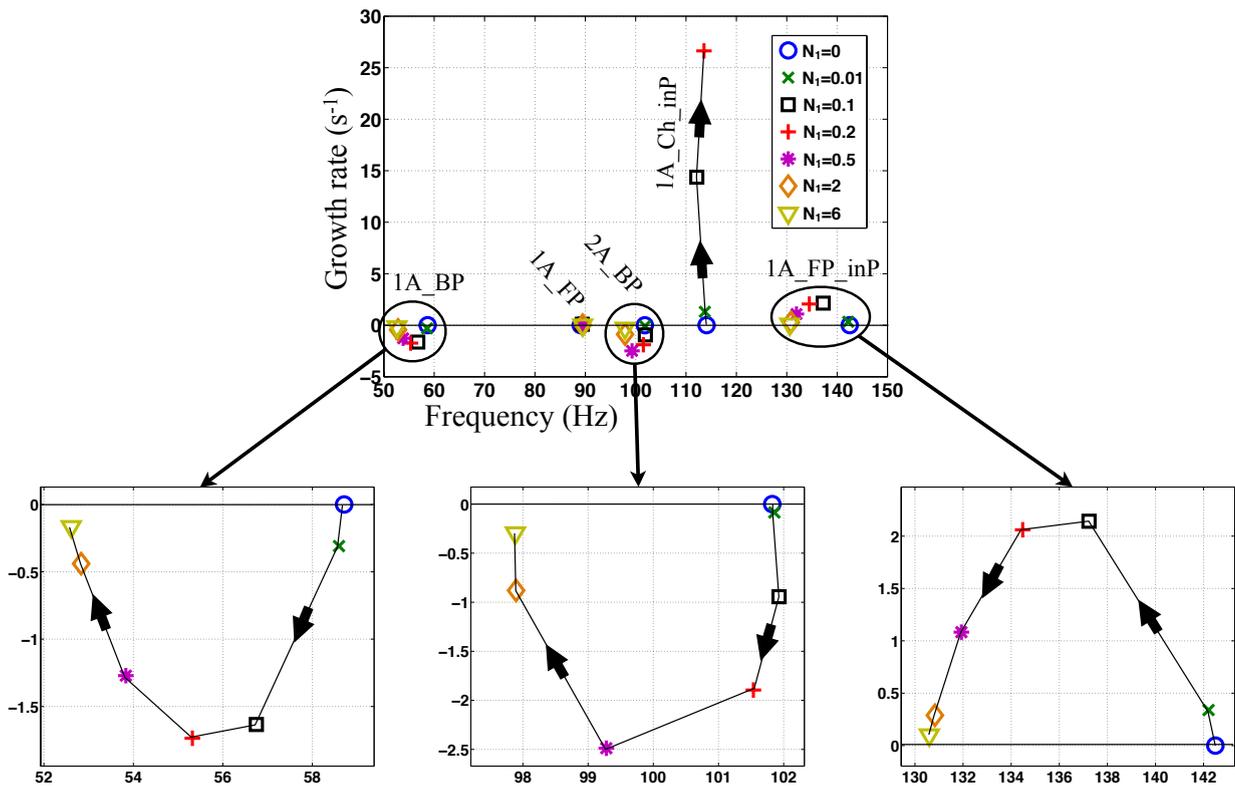
Figure 6.27: Frequency trajectories of the first 5 azimuthal modes for different values of N_1 ($\tau = 3ms$).
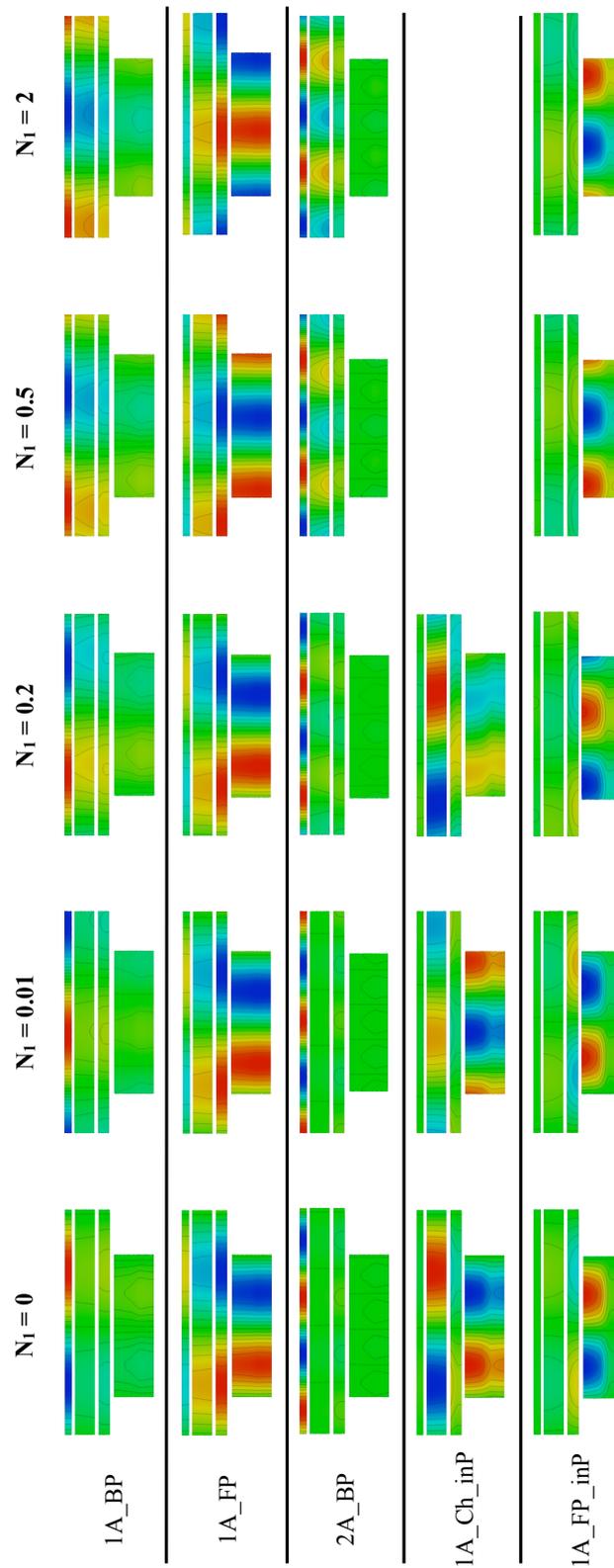
Figure 6.28: Structure of the azimuthal modes for increasing values of N_1.

are in agreement with the modes identification established in Fig. 6.13 between modes with

passive flame and modes with active flame. The active flame can modify the frequency, stability and structure of modes significantly, showing that a good acoustic solver must take it into account.

6.4.3 Stability maps and symmetry breaking

6.4.3.1 Global stability map

Keeping a value for the interaction index $N_1 = 1.83$, the stability of the azimuthal modes studied in Sec. 6.4.2 is investigated now as a function of the time-delay τ, which varies from zero to the period T of the corresponding mode. The results are plotted in Fig. 6.29[4].
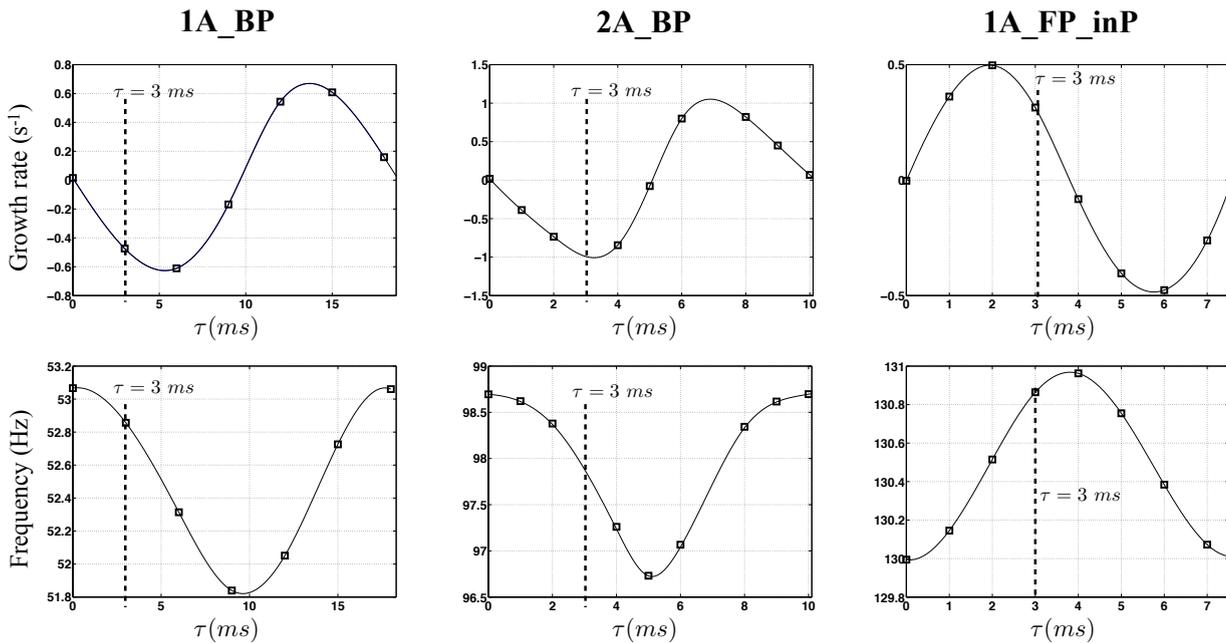
Figure 6.29: Frequency and growth rate of azimuthal modes as function of the time delay τ. ($\square$): AVSP (—): interpolating spline

Despite the complexity of the present case, with several coupled cavities, the stability curves of Fig. 6.29 are classic and not very different from those of a simple annular cavity with N burners (see e.g. [111]): the growth rate roughly looks like a sinus while the frequency curve is similar to a cosinus. For $\tau = 0$ all modes are neutral, which is in agreement with the Rayleigh criterion and the need for a certain delay between between the pressure p_1 and the heat release q_1 to instabilities to arise, and their stability changes at $\tau \approx T/2$.

When τ starts to grow from zero, the 1A_BP and 2A_BP modes are stable until $\tau \approx T/2$ (being T the period of the corresponding mode) and then they switch to unstable for larger

---

[4]In Sec. 6.4.2 the first 5 azimuthal modes are studied: 1A_BP, 1A_FP, 2A_BP, 1A_Ch_inP and 1A_FP_inP modes. However, the 1A_FP mode is neutral for any value of *tau* and the 1A_Ch_inP mode disappears for $N_1 > 0.2$. Consequently, only the stability of the three remaining modes is studied here as a function of τ.

values of τ, before becoming neutral again for values of $\tau \approx T$. On the contrary, the 1A_FP_inP mode is unstable at first (for $\tau < T/2$) and then stable (for $T/2 < \tau < T$). This behavior is controlled by the phase between the acoustic pressure and the acoustic velocity, which depends on the boundary impedances. In the present case, since $u_1 = 0$ for all boundaries, it is the impedance at the entry of the chamber which controls whether the mode is stable or unstable for low values of τ. This can be a problem if one decides to control, for example, an instability associated to the 1A_BP or 2A_BP modes, by reducing the time-delay τ. A small value of τ, will indeed damp the instability associated to these modes, according to the stability curves of Fig. 6.29. Nevertheless a value of τ which is too low could trigger a new instability associated to the 1A_FP_inP mode, which is unstable for small values of τ. In Fig. 6.30 the stability of the three modes as a function of τ is displayed, showing the range of time delay τ for which the three modes are stable simultaneously. This range is quite small: from 4 to 5 ms. For all other values of τ, an unstable mode will be triggered.
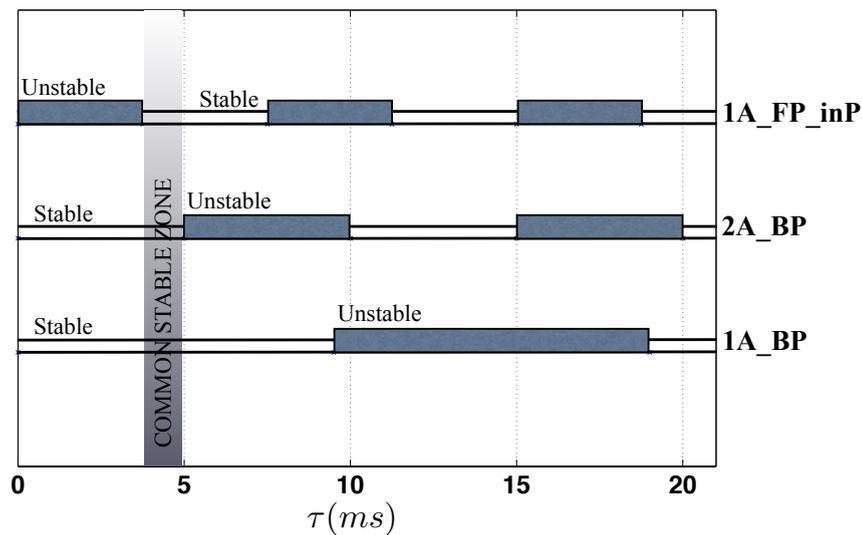
Figure 6.30: Stability map of the 1A_BP, 2A_BP and 1A_FP_inP modes as a function of τ. The only values of τ that ensures the simultaneous stability of the three modes are between 4 and 5 ms approximately.

6.4.3.2 Coupling and time-delay τ

The coupling between the Chamber and the Back Plenum for the 2A_BP mode is investigated for different values of the time delay τ, keeping constant the interaction index N_1. The azimuthal pressure p_1 (acoustic pressure along the azimuthal coordinate θ taken over the unrolled surfaces) in the Chamber and in the Back Plenum is plotted in Fig. 6.31 for increasing values of the time-delay τ. The acoustic pressure p_1 levels are normalized by $\max(p_1)$ in the Back plenum, so that the relative level between both cavities the Chamber and the Back Plenum are conserved.

As discussed in Sec. 6.2, it is interesting to see that, due to the coupling, an azimuthal mode of the same order ($p = 2$) takes place in two cavities (the Back Plenum and the

Chamber) with very different values of the sound speed ($c_0 = 522 \ m/s$ in the BP and $c_0 = 829 \ m/s$ in the Ch). The frequency computed by AVSP for this mode is about 98Hz. Using Eq. 6.1 for $p = 2$, we obtain a frequency of 96.6Hz for the Back Plenum cavity and 188.4Hz for the Chamber. Therefore, the frequency and structure of the mode is clearly imposed by the Back Plenum cavity and the geometry and sound speed in the Chamber do not play any role. The information in the Back Plenum travels to the Chamber through the burners and results in an azimuthal mode of order $p = 2$ in it at a frequency which corresponds rather to a mode or order $p = 1$ in the Chamber.
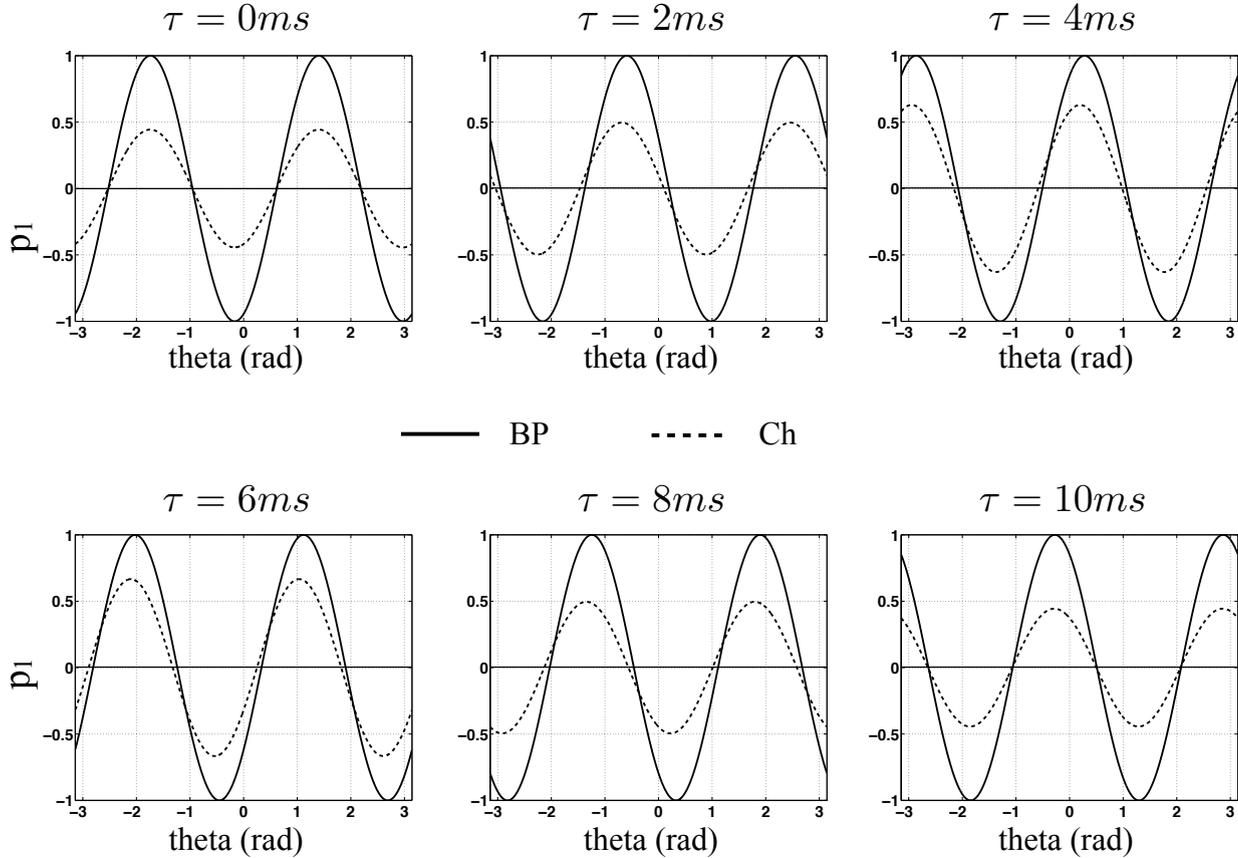
Figure 6.31: 2A_BP mode: acoustic pressure (p_1) in the Back Plenum (—) and in the Chamber ($--$) along the azimuthal coordinate, showing a strong coupling both cavities.

Two facts arise from the results displayed in Fig. 6.31:

- The coupling between the Back Plenum and the Chamber depends on the FTF time-delay τ: while the amplitude of p_1 remains the same in the Back Plenum ($\max(p_1) = 1$), in the Chamber it gets larger for values of $0 < \tau < T/2$ and then it decreases again for $T/2 < \tau < T$. This is shown quantitatively in Fig. 6.32, where the amplitude of the acoustic pressure $\max(p_1)$ in the Chamber is plotted as a function of τ. It is worth noticing how the amplitude of p_1 grows from ≈ 0.45 for $\tau = 0ms$ to ≈ 0.7 for $\tau = 5ms$ and then decreases again, describing a curve similar to a cosinus, as does the frequency of the mode (see Fig. 6.29).
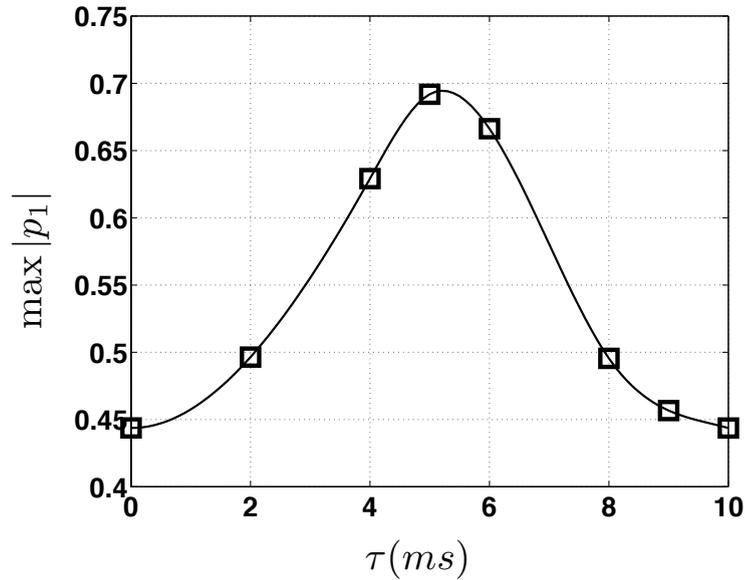
Figure 6.32: Amplitude of the acoustic pressure p_1 in the Chamber normalized by the amplitude in the back Plenum as a function of the time delay τ for the 2A_BP mode. ($\square$): AVSP (—): interpolating spline

- The phase-shift of the azimuthal pressure p_1 between the Chamber and the Back Plenum changes with τ. In Fig. 6.33 the difference between the phase of p_1 in the Chamber and the in the Back Plenum (noted as $\Delta\theta$) is plotted as a function of τ. According to Fig. 6.33, the phase-lag between the cavities seems to be proportional
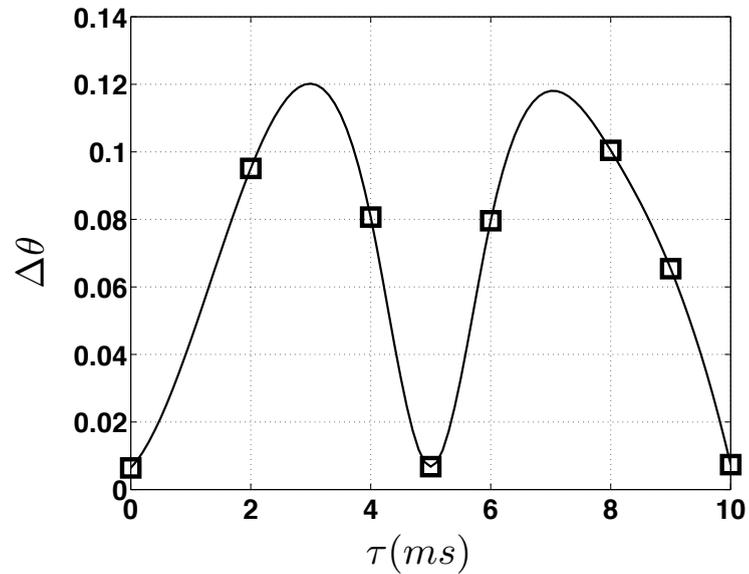
Figure 6.33: Difference of pressure phase ($\Delta\theta$ (rad)) between the Chamber and the Back Plenum for the 2A_BP mode as a function of the FTF time-delay τ. ($\square$): AVSP (—): interpolating spline

to the growth rate of the mode (see Fig. 6.29 for the mode 2A_BP). This phase-shift between cavities has been already observed in an helicopter annular combustion

195

chamber in [144], and it has been capture as well by a compressible reactive LES as well in [153]. Whether the phase-lag between cavities is important or not from the point of view of stability is not clear, but it is worth noticing that there is a link between the time delay τ and the pressure phase-shift between the cavities.

6.4.3.3   Symmetry breaking and stability

The effect of using azimuthal staging patterns on stability and modes nature was studied in Chapter 5 for a simple annular cavity connected to 24 cylindrical burners. The azimuthal patterns used in Chapter 5 (which are recalled in Tab. 6.6) have stable (noted with $\bullet$) and unstable burners (noted with $\circ$). Their effect on the azimuthal modes stability is investigated now in the present industrial configuration. For a given azimuthal mode, a burner is considered stable if it has associated a time-delay τ such that when it is used for the 24 flames the mode is stable, and viceversa. The notation is the same as in Chapter 5.

Name	N	Stable burners	Asymmetry pattern
B24_C0	24	0	∘ ∘
B24_C20_P1	24	20	● ● ● ● ● ● ● ∘ ∘ ● ● ● ● ∘ ∘ ● ● ● ● ● ● ● ● ●
B24_C20_P2	24	20	● ● ● ● ● ● ● ● ● ∘ ∘ ∘ ∘ ● ● ● ● ● ● ● ● ● ● ●
B24_C20_P3	24	20	● ● ● ● ● ∘ ● ● ● ● ● ∘ ● ● ● ● ● ● ∘ ● ● ● ● ∘
B24_C20_P4	24	20	● ● ● ● ● ∘ ● ● ● ● ∘ ● ● ● ● ● ● ∘ ● ● ● ● ● ∘
B24_C24	24	24	● ●

Table 6.6: Staging patterns configurations investigated AVSP. $\circ$ — Unstable burner (τ_1 in Fig. 5.11); $\bullet$ — Stable burner (τ_2 in Fig. 5.11)


Figure 6.34: Stability of the 1A_FP_inP mode and time-delays τ_1 ($\circ$) and τ_2 ($\bullet$) used for the patterns of Tab. 6.6.

The stability and modes nature of the azimuthal 1A_FP_inP mode of order $p = 1$, are studied for the four patterns of Tab. 6.6. The obtained results are compared with the results obtained for the simple annular cavity in Chapter 5. The two values of τ_1 and τ_2 that characterize the unstable ($\circ$) and the stable ($\bullet$) burners appear over the stability curve of the 1A_FP_inP mode in Fig. 6.34.
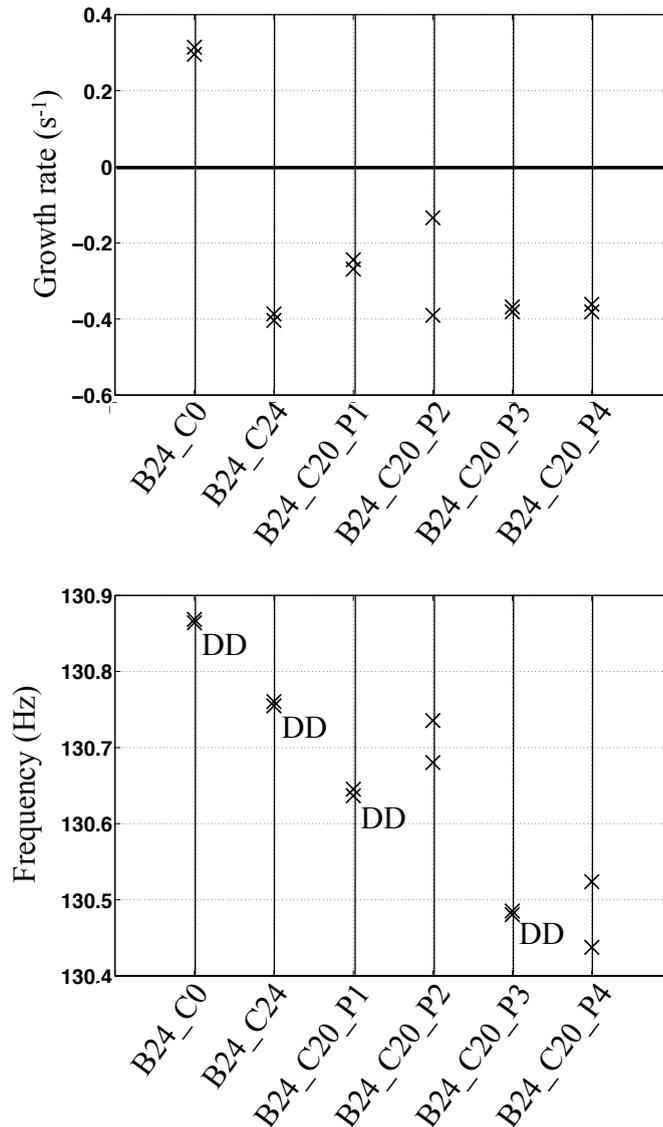
Figure 6.35: Growth rate (top) and frequencies (bottom) of the 1A_FP_inP mode for the patterns of Tab. 6.6. 'DD' indicates the patterns that result in degenerate doublets.

Results (growth rates and frequencies) for the different patterns are displayed in Fig. 6.35. The degenerate doublets (DD) present small differences between the growth rates of their two waves q^+ and q^-, especially for the pattern P1. This is probably due to the fact that the FTF are not azimuthally symmetric. The frequencies of both waves (q^+ and q^-) are though practically identical. There are similarities and discrepancies with respect to the results obtained in Chapter 5. On one hand, the split of the imaginary frequency due to the patterns is very similar to the behavior found for a simple annular cavity: the pattern

P2 is the one that splits the more, while patterns P1 and P3 give degenerate doublets and P4 splits slightly. Nevertheless, regarding the real part of the frequency, the pattern P4 splits more than the pattern P2, which does not happen for the academic configuration. On the other hand, for the academic annular chamber of Chapter 5, the analytical model ATACAMAC as well as AVSP have shown that the sum of the frequencies and the sum of the growth rates associated to the waves q^+ and q^- are constant for the four patterns, i.e. all the patterns split around the same frequency and growth rate values (see Sec. 5.5). This is not so for the present case: as shown in Fig. 6.35, the sum of the frequencies and the sum of the growth rates are different for each pattern. Moreover, the frequencies of the modes obtained for the four patterns are not included between the frequencies of the B24_C0 and B24_C24 modes.
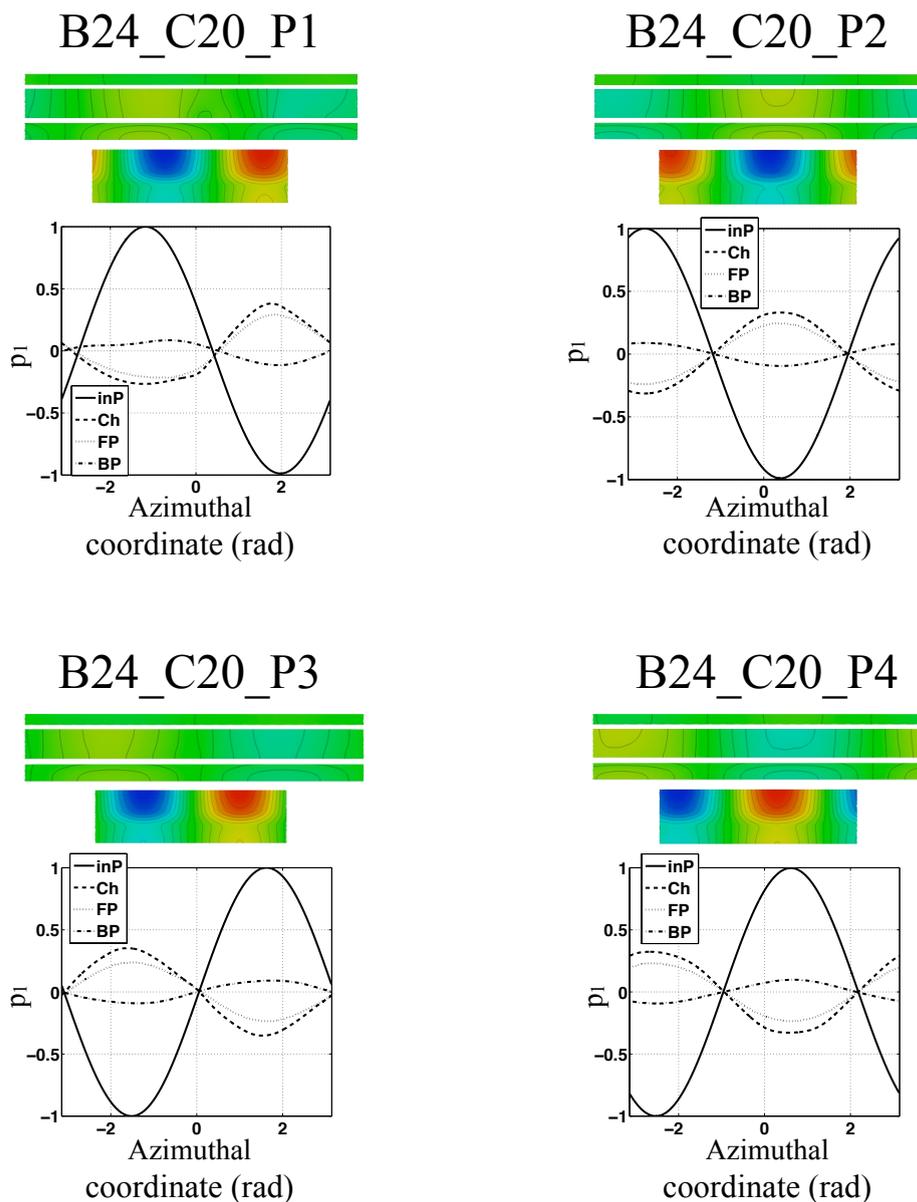

Figure 6.36: Structure of the 1A_FP_inP mode for the four patterns of Tab. 6.6.

The discrepancies observed between the industrial and the academic configurations can be due to the fact that many hypothesis considered for the academic case may not be respected here: 3D effects, compact flames, many coupled cavities, low coupling assumption, etc. The low-coupling assumption seems to be respected since the stability curve (Fig. 6.34) does not show nonlinear behavior. The coupling between cavities is strong though, and it appear as the most likely explanation for the discrepancies found between the academic and the industrial configurations: while for the academic chamber using 24 stable burners is clearly the best option in terms of stability, in the present case, the patterns P3 and P4 give modes which are practically as stable as the one obtained using 24 stable burners (B24_C24). This result suggests that, for the present case, using staging patterns can be an interesting passive control technique [12, 71].
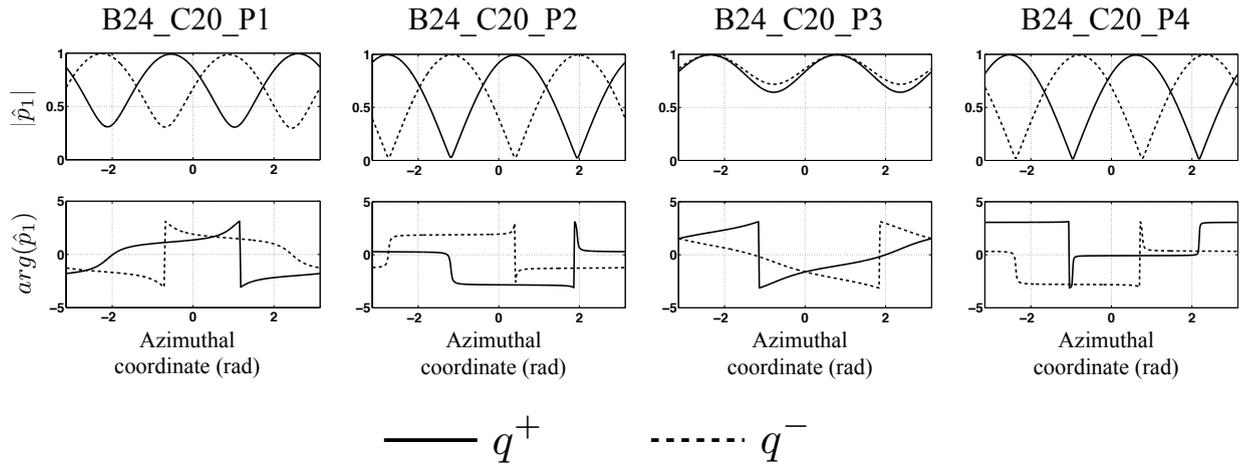

Figure 6.37: Nature of the 1A_FP_inP mode obtained for the four patterns (Tab. 6.6). Both waves q^+ and q^- are displayed.

The structure and the nature of the modes obtained for the different patterns appear in Fig. 6.36 and Fig. 6.37, respectively. There are no big differences in terms of mode structure between the four patterns, although it can be seen that, for the pattern P1, the azimuthal pressure p_1 in certain cavities has not exactly a sinus shape. The nature (standing, spinning or mixed) depends on the patterns:

- Patterns P1 and P3: the two patterns exhibit an azimuthal mode which is formed by two mixed waves q^+ and q^-. They can be combined to give either a standing, spinning or mixed azimuthal mode, since the azimuthal symmetry of these patterns do not impose any particular kind of mode of order $p = 1$.

- Patterns P2 and P4: these patterns split the degenerate doublet into two standing modes with different frequencies and growth rates associated. Each wave q^+ and q^- must be seen as two different standing modes since they are associated to different frequencies. Therefore, these two patterns lead to two standing modes with different frequencies and with different growth rates.

Concerning the nature of the modes, the results of Fig. 6.37 are very similar to the ones obtained for a simple annular chamber in Chapter 5, showing that using staging patterns in

annular combustion chambers, has a well determined effect on the modes nature: when the symmetry breaking leads to the split of a degenerate doublet into two singlets, the resulting modes are expected to be standing.

Conclusions and perspectives

Modern pollutant emission regulation has led to the use of lean premixed combustion in gas turbine combustors, which are prone to develop thermoacoustic instabilities. In this work, combustion instabilities are studied using a Helmholtz equation with a reactive term, which is obtained from the linearized Euler equations within the context of linear acoustics. The discretization of the Helmholtz equation on unstructured meshes leads to a large sparse non-symmetric complex nonlinear eigenvalue problem, whose solution provides the frequencies and growth rates (complex eigenvalues) and the structure (eigenvectors) of the resonant modes of the system (Chapter 2).

One of the objectives of this work is to study and implement algorithms for the solution of the nonlinear eigenproblem. Thermoacoustic instabilities arise at low frequencies, which means that the eigenproblem must be solved to obtain a few smallest magnitude eigenvalues. The nonlinear eigenproblem is linearized using a Fixed Point method: nonlinear eigenvalues and eigenvectors corresponding to the acoustic modes of the system are computed by solving a sequence of linear eigenproblems. The following algorithms (see Chapter 3) for the solution of linear eigenproblems have been investigated during this work:

- Implicitly Restarted Arnoldi algorithm: the ARPACK parallel library that implements this method was already available in AVSP. Its study has allowed an optimal use within the numerical frame of AVSP.

- Krylov-Schur algorithm: a parallel version of this algorithm has been developed for AVSP, showing very good numerical performances and offering a solid alternative to ARPACK.

- Harmonic Krylov-Schur algorithm: the harmonic version of the Krylov-Schur algorithm has also been implemented in AVSP.

- Block Krylov-Schur algorithm: a block version of th Krylov-Schur algorithm has been developed during this work. To the best of our knowledge, a block version of this block algorithm for general complex non-symmetric matrices was not available. This work has contributed with the description of a block Krylov-Schur algorithm.

- Jacobi-Davidson algorithm: a parallel implementation of the Jacobi-Davidson style QR algorithm has been developed for AVSP as well, improving the performance of the previous Jacobi-Davidson solver present in AVSP.

- Subspace Iteration algorithm with Chebyshev acceleration: the pertinence of this algorithm to recycle solutions previously computed has been investigated, showing that it might be an interesting alternative within a numerical context different from the one of AVSP.

Moreover, several strategies aiming at accelerating each fixed point iteration have been proposed (Chapter 4). Among them, the strategies which has been shown to be well adapted for AVSP have been included in the code, leading to important computational resources savings.

Thanks to the achieved numerical improvements, the study of industrial configurations has become possible in short scales of time. Today, most modern gas turbine combustors are annular, and the combustion instabilities take the form of azimuthal modes. These modes are characterized by a variation of the pressure with the azimuthal coordinate, and they can be either spinning, standing or mixed. Azimuthal modes have been studied in this work, contributing to the publication of [111] in the international journal *Combustion and Flame*. In the Appendix are included two other papers to which the present work has contributed: the first of them [10] is under revision for its publication in *Combustion and Flame* and the second one ("Analytical and numerical study of symmetry breaking in annular combustors to control azimuthal thermo-acoustic oscillations") will be shortly submitted. In these works, analytical models are developed and used to predict azimuthal modes in academic annular configurations. AVSP has been used to perform a cross validation of these models, showing a very good agreement in all cases.

An industrial power generator gas turbine combustor has been studied with AVSP (Chapter 6), revealing important acoustic coupling between the different cavities forming the combustor, making the analysis of the resonant modes difficult. Flame Transfer Functions (FTF) obtained from single sector Large Eddy Simulations (from the PhD. of S. Hermeth [53]) have been used to compute the modes of the complete annular combustor. The influence of the FTF parameters (the interaction index n and the time delay τ) on the system stability and on the coupling between cavities has been investigated as well. The study of symmetry breaking performed with the analytical tool ATACAMAC [10, 111] for an academic annular combustion chamber (Chapter 5), is extended to the industrial combustor using AVSP. The nature of the azimuthal modes (spinning, standing or mixed) can be predicted by AVSP, depending on the symmetry of the configuration. Discrepancies between the results obtained for the academic annular chamber and for the industrial annular combustor are found, which are probably due to the acoustic coupling in the last case.

Perspectives and future work

Concerning the numerical aspects treated in this work, potential improvements might include:

- The modification of the numerical routines that compute the operator associated to the eigenproblem in AVSP. Today, the matrix is not known explicitly, and only the result of applying it to an input vector is available. Building the matrix explicitly

would allow to perform matrix-matrix products, which are numerically more efficient than matrix-vector products and would improve the use of block methods. Moreover, knowing the operator explicitly, would allow to consider explicit preconditioning techniques, e.g., within the context of shift-and-invert transformations or for accelerating the solution of the correction equation when using the Jacobi.Davidson algorithm. The use of implicit preconditioning techniques (such as FGMRES) are though possible and their study would be of interest.

- The development of efficient nonlinear eigensolvers could lead to new algorithms for a faster and robust solution of the nonlinear eigenproblem in AVSP.

The considered hypotheses to obtain the Helmholtz equation include a strong assumption: the Mach number is assumed null. Inclusion of the Mach number effect in the modelization of thermoacoustic-instabilitis constitutes an important improvement in the physical model of AVSP. Currently, analytical models including Mach number effects are being developed at CERFACS.

The computations of the industrial annular combustor acoustic modes (Chapter 6) have been performed considering simple boundary conditions (perfectly reflecting acoustic walls). More realistic boundaries conditions, including complex impedances, multi-perforated plates, etc. should be considered in future works.

Bibliography

[1] S Akamatsu and AP Dowling. Three-dimensional thermoacoustic oscillation in a premix combustor. *Proceedings of the ASME Turbo expo 2001*, 2001. 26

[2] Kevin Anderson and Alice Bows. Reframing the climate change challenge in light of post-2000 emission trends. *Philosophical Transactions of the Royal Society A: Mathematical, Physical and Engineering Sciences*, 366(1882):3863–3882, 2008. 17

[3] C. A. Armitage, R. Balachandran, E. Mastorakos, and R. Cant. Investigation of the non-linear response of turbulent premixed flames to imposed inlet velocity oscillations. *Combust. Flame*, 146:419–436, 2006. 38

[4] W.E. Arnoldi. The principle of minimized iterations in the solution of the matrix eigenvalue problem. *Quart. Appl. Math*, 9(1):17–29, 1951. 29, 64

[5] J. Baglama, D. Calvetti, and L. Reichel. Algorithm 827: irbleigs: A MATLAB program for computing a few eigenpairs of a large sparse Hermitian matrix. *ACM Transactions on Mathematical Software (TOMS)*, 29(3):337–348, 2003. 80

[6] J. Baglama, D. Calvetti, and L. Reichel. IRBL: An implicitly restarted block-Lanczos method for large-scale Hermitian eigenproblems. *SIAM Journal on Scientific Computing*, 24(5):1650–1677, 2003. 80, 81

[7] Z. Bai, D. Day, and Q. Ye. ABLE: an adaptive block lanczos method for non-Hermitian eigenvalue problems. *SIAM Journal on Matrix Analysis and Applications*, 20(4):1060–1082, 1999. 81

[8] R Balachandran, AP Dowling, and E Mastorakos. Non-linear response of turbulent premixed flames to imposed inlet velocity oscillations of two frequencies. *Flow, Turbulence and Combustion*, 80(4):455–487, 2008. 39

[9] Friedrich L Bauer. Das verfahren der treppeniteration und verwandte verfahren zur lösung algebraischer eigenwertprobleme. *Zeitschrift für angewandte Mathematik und Physik ZAMP*, 8(3):214–235, 1957. 86

[10] M. Bauerheim, J.F. Parmentier, P. Salas, F. Nicoud, and T. Poinsot. A simple analytical model to study combustion instabilities in annular combustors. *Combustion*

and Flame, pages CNF–D–13–00088, 2013 - under review. 26, 146, 150, 151, 152, 168, 202

[11] Benjamin D Bellows, Mohan K Bobba, Jerry M Seitzman, and Tim Lieuwen. Nonlinear flame transfer function characteristics in a swirl-stabilized combustor. *TRANSACTIONS-ASME JOURNAL OF ENGINEERING FOR GAS TURBINES AND POWER*, 129(4):954, 2007. 24, 39

[12] P. Berenbrink and S. Hoffmann. Suppression of dynamic combustion instabilities by passive and active means. In *ASME Turbo Expo 2001. Paper 2001-GT-42*, 2001. 25, 147, 148, 160, 164, 199

[13] D. T. Blackstock. *Fundamentals of Physical Acoustics*. John Wiley & Sons, 2000. 44

[14] J. Blimbaum, M. Zanchetta, T. Akin, V. Acharya, J. O'Connor, Noble D.R., and T. Lieuwen. Transverse to longitudinal acoustic coupling processes in annular chambers. Spring Technical Meeting of the Central States Section of the Combustion Institute, April 2012. 42

[15] GJ Bloxsidge, AP Dowling, and PJ Langhorne. Reheat buzz: an acoustically coupled combustion instability. part 2. theory. *Journal of Fluid Mechanics*, 193(1):445–473, 1988. 26

[16] F. Boudy, D. Durox, T. Schuller, and S. Candel. Nonlinear mode triggering in a multiple flame combustor. *Proc. Combust. Inst.* , 33:1121–1128, 2011. 39

[17] J.F. Bourgouin, D. Durox, J. P. Moeck, T. Schuller, and S. Candel. Self-sustained instabilities in an annular combustor coupled by azimuthal and longitudinal acoustic modes. In *ASME Turbo Expo 2013 GT2013-95010*, June 2013. 26, 27

[18] T. Braconnier. *Sur le calcul des valeurs propres en précision finie*. PhD thesis, 1994. 102

[19] S. Candel. Combustion instabilities coupled by pressure waves and their active control. In *24th Symp. (Int.) on Combustion*, pages 1277–1296. The Combustion Institute, Pittsburgh, 1992. 23, 27

[20] S. Candel, D. Durox, and T. Schuller. Flame interactions as a source of noise and combustion instabilities. In *10th AIAA/CEAS Aeroacoustics Conference - AIAA 2004-2928*, 2004. 26

[21] S. M. Candel, E. Maistret, N. Darabiha, T. Poinsot, D. Veynante, and F. Lacas. Experimental and numerical studies of turbulent ducted flames. In *Marble Symposium*, pages 209–236, Caltech, 1988. 26

[22] Sébastien Candel. Combustion dynamics and control: progress and challenges. *Proceedings of the combustion institute*, 29(1):1–28, 2002. 25

[23] CLEAN AIR TECHNOLOGY CENTER. Nitrogen oxides (nox), why and how are they controlled. Technical report, Office of Air Quality Planning and Standard Report, 1999. 16

[24] Elliott Ward Cheney and Elliott Ward Cheney. *Introduction to approximation theory*, volume 3. McGraw-Hill New York, 1966. 87

[25] L.T.W. Chong, T. Komarek, R. Kaess, S. Foller, and W. Polifke. Identification of flame transfer functions from les of a premixed swirl burner. In ASME Paper GT2010-22769, editor, *ASME Turbo expo*, Glasgow, UK, June 2010. 39

[26] PAUL Clavin, PIERRE Pelce, and Longting He. One-dimensional vibratory instability of planar flames propagating in tubes. *J. Fluid Mech*, 216:299–322, 1990. 26

[27] D. G. Crighton, A. P. Dowling, J. E. Ffowcs Williams, M. Heckl, and F. Leppington. *Modern methods in analytical acoustics*. Lecture Notes. Springer Verlag, New-York, 1992. 27

[28] L. Crocco. Aspects of combustion instability in liquid propellant rocket motors. Part I. *J. American Rocket Society* , 21:163–178, 1951. 30, 37, 40

[29] L. Crocco. Aspects of combustion instability in liquid propellant rocket motors. part II. *J. American Rocket Society* , 22:7–16, 1952. 30, 37, 40

[30] F. E. C. Culick and P. Kuentzmann. *Unsteady Motions in Combustion Chambers for Propulsion Systems*. NATO Research and Technology Organization, 2006. 23, 25, 146, 147, 148

[31] J. Daniel, WB Gragg, L. Kaufman, and GW Stewart. Reorthogonalization and stable algorithms for updating the Gram-Schmidt QR factorization. *Math. Comp*, 30(136):772–795, 1976. 83

[32] James Demmel, Laura Grigori, Mark Hoemmen, and Julien Langou. Communication-optimal parallel and sequential qr and lu factorizations. *SIAM Journal on Scientific Computing*, 34(1):A206–A239, 2012. 139

[33] A. P. Dowling. The calculation of thermoacoustic oscillations. *J. Sound Vib.* , 180(4):557–581, 1995. 23, 26, 44

[34] A. P. Dowling. Nonlinear self-excited oscillations of a ducted flame. *J. Fluid Mech.* , 346:271–290, 1997. 24, 39

[35] A. P. Dowling and S. R. Stow. Acoustic analysis of gas turbine combustors. *Journal of Propulsion and Power*, 19, 2003. 23, 26, 34

[36] Ann P Dowling. The challenges of lean premixed combustion. In *Proceedings of the International Gas Turbine Congress, Tokyo*, 2003. 25

[37] Sebastian Ducruix, Thierry Schuller, Daniel Durox, and Sebastien Candel. Combustion instability mechanisms in premixed combustors. *PROGRESS IN ASTRONAUTICS AND AERONAUTICS*, 210:179, 2005. 26

[38] Sébastien Ducruix, Daniel Durox, and Sébastien Candel. Theoretical and experimental determinations of the transfer function of a laminar premixed flame. *Proceedings of the Combustion Institute*, 28(1):765–773, 2000. 30, 39, 176

[39] Daniel Durox, Thierry Schuller, and Sébastien Candel. Combustion dynamics of inverted conical flames. *Proceedings of the combustion Institute*, 30(2):1717–1724, 2005. 38

[40] S. Evesque and W. Polifke. Low-order acoustic modelling for annular combustors: Validation and inclusion of modal coupling. In *International Gas Turbine and Aero-engine Congress & Exposition, ASME Paper*, volume GT-2002-30064, 2002. 25, 26, 146

[41] S. Evesque, W. Polifke, and C. Pankiewitz. Spinning and azimuthally standing acoustic modes in annular combustors. In *9th AIAA/CEAS Aeroacoustics Conference*, volume AIAA paper 2003-3182, 2003. 27, 147

[42] M. Fleifil, A. M. Annaswamy, Z. A. Ghoneim, and A. F. Ghoniem. Response of a laminar premixed flame to flow oscillations: A kinematic model and thermoacoustic instability results. *Combust. Flame*, 106(4):487–510, 1996. 39

[43] D. R. Fokkema. *Subspace methods for linear, non-linear and eigen problems*. PhD thesis, Utrecht University, Utrecht, The Netherlands, 1996. 73

[44] D.R. Fokkema, G.L.G. Sleijpen, and H.A. Van der Vorst. Jacobi-Davidson style QR and QZ algorithms for the reduction of matrix pencils. *SIAM Journal on Scientific Computing*, 20:94, 1998. 73, 89, 99, 113, 116, 120

[45] R.W. Freund. Band Lanczos method (Section 4.6). *Templates for the Solution of Algebraic Eigenvalue Problems: A Practical Guide, Z. Bai, J. Demmel, J. Dongarra, A. Ruhe, and H. van der Vorst, eds., Philadelphi, PA*, 2000. 81

[46] Gregor Gelbert, Jonas P Moeck, Christian O Paschereit, and Rudibert King. Feedback control of unstable thermoacoustic modes in an annular Rijke tube. *Control Engineering Practice*, 20(8):770–782, August 2012. 26, 27, 146

[47] A Gentemann, Andreas Fischer, Stéphanie Evesque, and Wolfgang Polifke. Acoustic transfer matrix reconstruction and analysis for ducts with sudden change of area. In *9th AIAA/CEAS Aeroacoustics Conference and Exhibit, Hilton Head*, 2003. 44

[48] Gene H Golub and Henk A Van der Vorst. Eigenvalue computation in the 20th century. *Journal of Computational and Applied Mathematics*, 123(1):35–65, 2000. 29

[49] G.H. Golub, F.T. Luk, and M.L. Overton. A block Lanczos method for computing the singular values and corresponding singular vectors of a matrix. *ACM Transactions on Mathematical Software (TOMS)*, 7(2):149–169, 1981. 81

[50] E. Gullaud, S. Mendez, C. Sensiau, F. Nicoud, and T. Poinsot. Effect of multiperforated plates on the acoustic modes in combustors. *C. R. Acad. Sci. Mécanique*, 337(6-7):406–414, 2009. 30

[51] C-C Hantschk and D Vortmeyer. Numerical simulation of self-excited thermoacoustic instabilities in a rijke tube. *Journal of Sound and Vibration*, 227(3):511–522, 1999. 26

[52] M. Hauser, M. Lorenz, and T. Sattelmayer. Influence of transversal acoustic excitation of the burner approach flow on the flame structure. *Journal of engineering for gas turbines and power*, 133(4), 2011. 42

[53] Sebastian Hermeth. *Mechanisms affecting the dynamic response of swirled flames in gas turbines.* PhD thesis, 2012. 39, 167, 169, 176, 177, 202

[54] M.E. Hochstenbach and Y. Notay. Controlling inner iterations in the Jacobi-Davidson method. *SIAM Journal on Matrix Analysis and Applications*, 31(2):460–477, 2009. 116, 117

[55] T.M. Huang, F.N. Hwang, S.H. Lai, W. Wang, and Z.H. Wei. A parallel polynomial Jacobi–Davidson approach for dissipative acoustic eigenvalue problems. *Computers & Fluids*, 45(1):207–214, 2011. 116, 120

[56] Ying Huang and Vigor Yang. Dynamics and stability of lean-premixed swirl-stabilized combustion. *Prog. Energy Comb. Sci.* , 35(4):293–364, 2009. 39, 176

[57] Estelle Iacona, Jean Taine, and Bernard Tamain. *Les enjeux de l'énergie: après Fukushima.* Dunod, 2012. 16

[58] ICAO. Environmental report 2010, 2010. 17, 18, 19

[59] C.G.J. Jacobi. Über ein leichtes verfahren die in der Theorie der Säculärstörungen vorkommenden Gleichungen numerisch aufzulösen. *J. reine angew. Math*, 30:51–94, 1846. 89, 93

[60] J.O'Connor and T.Lieuwen. Influence of transverse acoustic modal structure on the forced response of a swirling nozzle flow. *ASME TURBOEXPO 2012*, 2012. 152

[61] J.O'Connor and T.Lieuwen. Recirculation zone dynamics of a transversely excited swirl flow and flame. *Physics of fluids*, 24(075107), 2012. 152

[62] K Joseph George and RI Sujith. On chu's disturbance energy. *Journal of Sound and Vibration*, 330(22):5280–5291, 2011. 26, 42

[63] Matthew P Juniper. Triggering in the horizontal rijke tube: non-normality, transient growth and bypass transition. *Journal of Fluid Mechanics*, 667(1):272–308, 2011. 39

[64] R. Kaess, W. Polifke, T. Poinsot, N. Noiray, D. Durox, T. Schuller, and S. Candel. Cfd-based mapping of the thermo-acoustic stability of a laminar premix burner. In *Proc. of the Summer Program* , pages 289–302, Center for Turbulence Research, NASA AMES, Stanford University, USA, 2008. 39

[65] N. Karimi, M.J. Brear, S.-H. Jin, and J.P. Monty. Linear and non-linear forced response of a conical, ducted, laminar premixed flame. *Combust. Flame*, pages 2201–2212, 2009. 38

[66] Daesik Kim, Jong Guen Lee, Bryan D Quay, Domenic A Santavicca, Kwanwoo Kim, and Shiva Srinivasan. Effect of flame structure on the flame transfer function in a premixed gas turbine combustor. *Journal of Engineering for Gas Turbines and Power*, 132:021502, 2010. 37

[67] A. N. Kolmogorov. The local structure of turbulence in incompressible viscous fluid for very large reynolds numbers. *C. R. Acad. Sci. , USSR*, 30:301, 1941. 26

[68] V. Kornilov, R. Rook, J. ten Thije Boonkkamp, and L. de Goey. Experimental and numerical investigation of the acoustic response of multi-slit bunsen burners. *Combust. Flame*, pages 1957–1970, 2009. 37, 38

[69] W. Krebs, G. Walz, and S. Hoffmann. Thermoacoustic analysis of annular combustor. In AIAA Paper 99-1971, editor, *5th AIAA Aeroacoustics Conference*, 1999. 42

[70] Werner Krebs, PATRICK FLOHR, BERND PRADE, and Stefan Hoffmann. Thermoacoustic stability chart for high-intensity gas turbine combustion systems. *Combustion Science and Technology*, 174(7):99–128, 2002. 146

[71] U. Krueger, J. Hueren, S. Hoffmann, W. Krebs, P. Flohr, and D. Bohn. Prediction and measurement of thermoacoustic improvements in gas turbines with annular combustion systems. In ASME Paper, editor, *ASME TURBO EXPO*, Munich, Germany, 2000. 146, 147, 160, 164, 199

[72] C. Lanczos. *An iteration method for the solution of the eigenvalue problem of linear differential and integral operators.* United States Governm. Pr. Office, 1950. 28, 64

[73] John LeConte. On the influence of musical sounds on the flame of a jet of coal-gas. 1858. 22

[74] A. H. Lefebvre. *Gas Turbines Combustion.* Taylor & Francis, 1999. 21

[75] R. Lehoucq and D. Sorensen. Arpack: Solution of large scale eigenvalue problems with implicitly restarted arnoldi methods. www.caam.rice.edu/software/arpack. User's guide, 1997. 29, 69, 102

[76] RB Lehoucq and KJ Maschhoff. Implementation of an implicitly restarted block Arnoldi method. *Preprint MCS-P649-0297, Argonne National Lab*, 1997. 80, 125

[77] RB Lehoucq and JA Scott. An evaluation of software for computing eigenvalues of sparse nonsymmetric matrices. *Preprint MCS-P547*, 1195, 1996. 102

[78] R.B. Lehoucq and D. C. Sorensen. Deflation techniques for an implicitly re-started Arnoldi iteration. *SIAM J. Matrix Anal. Appl*, 17:789–821, 1996. 29, 64, 66

[79] Nathan S Lewis. Powering the planet. *MRS bulletin*, 32(10):808–820, 2007. 16

[80] T. Lieuwen. Modeling premixed combustion-acoustic wave interactions: A review. *J. Prop. Power* , 19(5):765–781, 2003. 37

[81] T. Lieuwen and Y. Neumeier. Nonlinear pressure-heat release transfer function measurements in a premixed combustor. In *Proc. Combust. Inst.* , volume 29, pages 99–105, 2002. 24

[82] T. Lieuwen and V. Yang. Combustion instabilities in gas turbine engines. operational experience, fundamental mechanisms and modeling. In *AIAA Prog. in Astronautics and Aeronautics* , volume 210, 2005. 23, 25, 27, 39, 176

[83] Tim C Lieuwen. Experimental investigation of limit-cycle oscillations in an unstable gas turbine combustor. *Journal of Propulsion and Power*, 18(1):61–67, 2002. 25

[84] Edward D Lynch, Brian Lariviere, Douglas G Talley, and Suresh Menon. Alrest high fidelity modeling program approach. Technical report, DTIC Document, 2011. 22

[85] F. E. Marble and S. Candel. Acoustic disturbances from gas nonuniformities convected through a nozzle. *J. Sound Vib.* , 55:225–243, 1977. 151

[86] GH Markstein. Flames as amplifiers of fluid mechanical disturbances. In *Proceedings of the Sixth National Congress on Applied Mechanics*, pages 11–33, 1970. 26

[87] L.R.S. Matrices. Note the iterative calculation of a few of the lowest eigenvalues and corresponding eigenvectors of large real-symmetric matrices. *Journal of Computational Physics*, 17:87–94, 1975. 89

[88] K. McManus, T. Poinsot, and S. Candel. A review of active control of combustion instabilities. *Prog. Energy Comb. Sci.* , 19:1–29, 1993. 25

[89] V. Mehrmann and C. Schröder. Nonlinear eigenvalue and frequency response problems in industrial practice. *Journal of Mathematics in Industry*, 1(1):1–18, 2011. 120

[90] J.P. Moeck, M. Paul, and C. Paschereit. Thermoacoustic instabilities in an annular flat rijke tube. In *ASME Turbo Expo 2010 GT2010-23577*, 2010. 26, 27, 146

[91] R.B. Morgan. Computing interior eigenvalues of large matrices. *Linear Algebra and its Applications*, 154:289–309, 1991. 77, 117

[92] R.B. Morgan and M. Zeng. Harmonic projection methods for large non-symmetric eigenvalue problems. *Numerical linear algebra with applications*, 5(1):33–55, 1998. 117

[93] A. S. Morgans and S. R. Stow. Model-based control of combustion instabilities in annular combustors. *Combust. Flame*, 150(4):380–399, 2007. 42

[94] CL Muntz. Solution direct de l'equation seculaire et de quelques problems analogues. *Comptus Rendus de l'Academie des Sciences*, 156:43–46, 1913. 59

[95] Richard M Murray, Clas A Jacobson, R Casas, AI Khibnik, CR Johnson Jr, R Bitmead, AA Peracchio, and WM Proscia. System identification for limit cycling systems: a case study for combustion instabilities. In *American Control Conference, 1998. Proceedings of the 1998*, volume 4, pages 2004–2008. IEEE, 1998. 25

[96] Peter Newton, C Holsclaw, M Ko, and M Ralph. Long-term technology goals for caep. In *Seventh Meeting of CAEP*, 2007. 18

[97] F. Nicoud, L. Benoit, C. Sensiau, and T. Poinsot. Acoustic modes in combustors with complex impedances and multidimensional active flames. *AIAA J.* , 45:426–441, 2007. 27, 28, 30, 34, 35, 38, 148, 176

[98] F. Nicoud and T. Poinsot. Thermoacoustic instabilities: should the rayleigh criterion be extended to include entropy changes ? *Combust. Flame*, 142:153–159, 2005. 23, 26

[99] N. Noiray, M. Bothien, and B. Schuermans. Analytical and numerical analysis of staging concepts in annular gas turbines. In *n3l - Int'l Summer School and Workshop on Non-normal and non linear effects in aero and thermoacoustics*, 2010. 158

[100] N. Noiray, M. Bothien, and B. Schuermans. Investigation of azimuthal staging concepts in annular gas turbines. *Combust. Theory Model.* , pages 585–606, 2011. 27, 147

[101] N. Noiray, D. Durox, T. Schuller, and S. Candel. Self-induced instabilities of premixed flames in a multiple injection configuration. *Combust. Flame*, 145(3):435–446, 2006. 26

[102] N. Noiray, D. Durox, T. Schuller, and S. Candel. Passive control of combustion instabilities involving premixed flames anchored on perforated plates. *Proc. Combust. Inst.* , 31:1283–1290, 2007. 26

[103] N Noiray and B Schuermans. On the dynamic nature of azimuthal thermoacoustic modes in annular gas turbine combustion chambers. *Proceedings of the Royal Society A: Mathematical, Physical and Engineering Sciences*, 469(2151):20120535–20120535, December 2012. 27

[104] J. O'Connor and T.Lieuwen. Further characterization of the distrbance field in a transversely excited swirl-stabilized flame. *Journal of Engineering for Gas Turbines and Power*, 134(011501-9), 2012. 152

[105] Joseph C Oefelin and Vigor Yang. Comprehensive review of liquid-propellant combustion instabilities in f-1 engines. *Journal of Propulsion and Power*, 9(5):657–677, 1993. 146

[106] J. Olsen, P. Jørgensen, and J. Simons. Passing the one-billion limit in full configuration-interaction (FCI) calculations. *Chemical Physics Letters*, 169(6):463–472, 1990. 89, 90

[107] C.C. Paige, B.N. Parlett, and H.A. Van der Vorst. Approximate solutions and eigenvalue bounds from Krylov subspaces. *Numerical linear algebra with applications*, 2(2):115–133, 1995. 117

[108] P. Palies. *Dynamique et instabilités de combustion de flammes swirlées*. Phd thesis, Ecole Centrale Paris, 2010. 152

[109] P Palies, T Schuller, D Durox, and S Candel. Modeling of premixed swirling flames transfer functions. *Proceedings of the Combustion Institute*, 33(2):2967–2974, 2011. 39, 176

[110] Beresford N. Parlett. *The symmetric eigenvalue problem*. Prentice-Hall, Inc., Upper Saddle River, NJ, USA, 1998. 102

[111] J.F. Parmentier, P. Salas, P. Wolf, G. Staffelbach, F. Nicoud, and T. Poinsot. A simple analytical model to study and control azimuthal instabilities in annular combustion chambers. *Combustion and Flame*, 159(7):2374 – 2387, 2012. 25, 26, 27, 44, 146, 148, 149, 150, 151, 152, 153, 154, 155, 192, 202

[112] ML Parry, OF Canziani, JP Palutikof, PJ Van Der Linden, and CE Hanson. Intergovernmental panel on climate change. climate change 2007. impacts, adaptation, and vulnerability, contribution of working group ii to the fourth assessment report of the intergovernmental panel on climate change, 2007. 18

[113] C. O. Paschereit and E. Gutmark. Control of thermoacoustic instabilities in a premixed combustor by fuel modulation. In AIAA Paper 99-0711, editor, *37th AIAA Aerospace Sciences Meeting and Exhibit*, Reno, NV, 1999. 26

[114] R. Perrin and T. Charnley. Group theory and the bell. *Journal of Sound and Vibration*, 31(4):411–418, 1973. 147, 156, 159

[115] T. Poinsot. Controle actif indirect des instabilites de combustion. *Centralien*, 1991. 25

[116] T. Poinsot. Contrôle actif des instabilités de combustion. In *Conférence invitée au Colloque ÔControl of fluids and structures O*, Institut Henri Poincare, Paris, 1998. 25

[117] T. Poinsot and D. Veynante. *Theoretical and Numerical Combustion*. R.T. Edwards, 2nd edition, 2005. 24

[118] T. Poinsot and D. Veynante. *Theoretical and Numerical Combustion*. Third Edition (www.cerfacs.fr/elearning), 2011. 21, 26, 27, 34, 36, 40, 42

[119] W. Polifke, C. Paschereit, and K. Doebbeling. Constructive and destructive interference of acoustic and entropy waves in a premixed combustor with a choked exit. *Int. J. Acoust. Vib.* , 6:135–146, 2001. 26

[120] W. Polifke and C. O. Paschereit. Determination of thermo-acoustic transfer matrices by experiment and computational fluid dynamics. page 38. ERCOFTAC bulletin, 1998. 26

[121] W. Polifke, A. Poncet, C. O. Paschereit, and K. Doebbeling. Reconstruction of acoustic transfer matrices by instationnary computational fluid dynamics. *J. Sound Vib.* , 245(3):483–510, 2001. 44

[122] RL Raun, MW Beckstead, JC Finlinson, and KP Brooks. A review of rijke tubes, rijke burners and related devices. *Progress in Energy and Combustion Science*, 19(4):313–364, 1993. 22

[123] L. Rayleigh. The explanation of certain acoustic phenomena. *Nature*, July 18:319–321, 1878. 22, 23, 43

[124] P. L. Rijke. Notice of a new method of causing a vibration of the air contained in a tube open at both ends. *Phil. Mag.*, 17:419–422, 1859. 22

[125] J.E. Roman, M. Kammerer, F. Merz, and F. Jenko. Fast eigenvalue calculations in a massively parallel plasma turbulence code. *Parallel Computing*, 36(5):339–358, 2010. 118

[126] M. Rudgyard, T. Schoenfeld, R. Struijs, G. Audemar, and P. Leyland. A modular approach for computational fluid dynamics. Technical Report TR/CFD/95/07, CERFACS, 1995. 46, 139

[127] A. Ruhe. Implementation aspects of band Lanczos algorithms for computation of eigenvalues of large sparse symmetric matrices. *Math. Comp*, 33(146):680–687, 1979. 82

[128] Y. Saad. On the rates of convergence of the Lanczos and the block-Lanczos methods. *SIAM Journal on Numerical Analysis*, 17(5):687–706, 1980. 81

[129] Y. Saad. *Numerical methods for large eigenvalue problems*, volume 158. SIAM, 1992. 29, 59, 86, 87, 88, 102, 132, 134

[130] Y. Saad. *Iterative methods for sparse linear systems*. Society for Industrial and Applied Mathematics, 2003. 75, 81

[131] Y. Saad and M.H. Schultz. GMRES: A generalized minimal residual algorithm for solving nonsymmetric linear systems. *SIAM Journal on scientific and statistical computing*, 7(3):856–869, 1986. 116

[132] M. Sadkane. Block-Arnoldi and Davidson methods for unsymmetric large eigenvalue problems. *Numerische Mathematik*, 64(1):195–211, 1993. 81

[133] M. Sadkane. A block Arnoldi-Chebyshev method for computing the leading eigenpairs of large sparse unsymmetric matrices. *Numerische mathematik*, 64(1):181–193, 1993. 81

[134] M. Sadkane and R.B. Sidje. Implementation of a variable block Davidson method with deflation for solving large sparse eigenproblems. *Numerical Algorithms*, 20(2):217–240, 1999. 81

[135] T. Sattelmayer. Influence of the combustor aerodynamics un combustion instabilities from equivalence ratio fluctuations. In *International Gas Turbine and Aeroengine Congress and Exhibition*, Munich, 2000. ASME Paper. 23

[136] R. F. Sawyer. Science based policy for adressing energy and environmental problems. *Proc. Combust. Inst.* , 32:45–56, 2009. 16

[137] P. Schmitt, T. Poinsot, B. Schuermans, and K. P. Geigle. Large-eddy simulation and experimental study of heat transfer, nitric oxide emissions and combustion instability in a swirled turbulent high-pressure burner. *J. Fluid Mech.* , 570:17–46, 2007. 25

[138] T. Schønfeld and M. Rudgyard. Steady and unsteady flows simulations using the hybrid flow solver avbp. *AIAA J.* , 37(11):1378–1385, 1999. 46, 139

[139] B. Schuermans, V. Bellucci, and C. Paschereit. Thermoacoustic modeling and control of multiburner combustion systems. In *International Gas Turbine and Aeroengine Congress & Exposition, ASME Paper*, volume 2003-GT-38688, 2003. 44

[140] B. Schuermans, C. Paschereit, and P. Monkewitz. Non-linear combustion instabilities in annular gas-turbine combustors. In *44th AIAA Aerospace Sciences Meeeting and Exhibit*, volume AIAA paper 2006-0549, 2006. 27, 42, 147

[141] B. Schuermans, W. Polifke, and C. O. Paschereit. Modeling transfer matrices of premixed flames and comparison with experimental results. In *Int'I Gas Turbine & Aeroengine Congress & Exposition*, Indianapolis/Indiana, 1999. ASME Paper. 26, 44

[142] T. Schuller, D. Durox, and S. Candel. A unified model for the prediction of laminar flame transfer functions: comparisons between conical and v-flames dynamics. *Combust. Flame*, 134:21–34, 2003. 30, 38, 39

[143] T. Schuller, D. Durox, P. Palies, and S. Candel. Acoustic decoupling of longitudinal modes in generic combustion systems. *Combustion and Flame*, 159:1921–1931, 2012. 152, 168

[144] C. Sensiau. *Simulations numériques des instabilités thermoacoustiques dans les chambres de combustion aéronautiques - TH/CFD/08/127*. PhD thesis, Université de Montpellier II, - Institut de Mathématiques et de Modélisation de Montpellier, France, 2008. 27, 30, 46, 196

[145] C. Sensiau, F. Nicoud, and T. Poinsot. A tool to study azimuthal and spinning modes in annular combustors. *Int. Journal Aeroacoustics*, 8(1):57–68, 2009. 27, 30, 41

[146] Claude Sensiau, Franck Nicoud, Martin Van Gijzen, and JW Van Leeuwen. A comparison of solvers for quadratic eigenvalue problems from combustion. *International journal for numerical methods in fluids*, 56(8):1481–1487, 2008. 29

[147] J.R. Seume, N. Vortmeyer, W. Krause, J. Hermann, C. Hantschk, P. Zangle, S. Gleis, D. Vortmeyer, and A. Orthmann. Application of active combustion instability control to a heavy gas turbine. *J. Engineering for Gas Turbines and Power*, 120:721–726, 1998. 25

[148] Camilo Fernando Silva, Franck Nicoud, Thierry Schuller, Daniel Durox, and Sebastien Candel. Combining a helmholtz solver with the flame describing function to assess combustion instability in a premixed swirled combustor. *Combustion and Flame*, 2013. 30, 38

[149] G.L.G. Sleijpen, A.G.L. Booten, D.R. Fokkema, and H.A. Van der Vorst. Jacobi-Davidson type methods for generalized eigenproblems and polynomial eigenproblems. *BIT Numerical Mathematics*, 36(3):595–633, 1996. 29, 89

[150] G.L.G. Sleijpen and H.A. Van der Vorst. A Jacobi-Davidson iteration method for linear eigenvalue problems. *SIAM Review*, pages 267–293, 2000. 29, 89, 116

[151] G.L.G. Sleijpen, H.A. van der Vorst, and E. Meijerink. Efficient expansion of subspaces in the Jacobi-Davidson method for standard and generalized eigenproblems. *Electron. Trans. Numer. Anal*, 7:75–89, 1998. 29, 89, 116

[152] J. Smagorinsky. General circulation experiments with the primitive equations: 1. the basic experiment. *Mon. Weather Rev.* , 91:99–164, 1963. 26

[153] G. Staffelbach, L.Y.M. Gicquel, G. Boudier, and T. Poinsot. Large eddy simulation of self-excited azimuthal modes in annular combustors. *Proc. Combust. Inst.* , 32:2909–2916, 2009. 26, 42, 196

[154] AM Steinberg, I Boxx, M Stöhr, CD Carter, and W Meier. Flow–flame interactions causing acoustically coupled heat release fluctuations in a thermo-acoustically unstable gas turbine model combustor. *Combustion and Flame*, 157(12):2250–2266, 2010. 39

[155] G. W. Stewart. A Krylov–Schur Algorithm for Large Eigenproblems. *SIAM J. Matrix Anal. Appl.*, 23(3):601–614, March 2001. 70, 72

[156] G.W. Stewart. *Matrix Algorithms: Eigensystems*, volume 2. Society for Industrial Mathematics, 2001. 28, 29, 58, 59, 61, 62, 65, 69, 70, 72, 73, 76, 77, 89, 92, 94, 95, 98, 102, 120

[157] G.W. Stewart. Addendum to "A Krylov–Schur Algorithm for Large Eigenproblems". *SIAM journal on matrix analysis and applications*, 24(2):599–601, 2002. 78

[158] S. R. Stow and A. P. Dowling. Thermoacoustic oscillations in an annular combustor. In *ASME Paper*, New Orleans, Louisiana, 2001. 26, 42, 146

[159] S. R. Stow and A. P. Dowling. Modelling of circumferential modal coupling due to helmholtz resonators. In *ASME Paper 2003-GT-38168*, Atlanta, Georgia, USA, 2003. 146

[160] Solomon Susan. *Climate change 2007-the physical science basis: Working group I contribution to the fourth assessment report of the IPCC*, volume 4. Cambridge University Press, 2007. 17

[161] Nedunchezhian Swaminathan and Kenneth Noel Corbett Bray. *Turbulent premixed flames*. Cambridge University Press, 2011. 23

[162] Luis Tay-Wo-Chong and Wolfgang Polifke. Large eddy simulation-based study of the influence of thermal boundary condition and combustor confinement on premix flame transfer functions. *Journal of Engineering for Gas Turbines and Power*, 135:021502, 2013. 38, 39

[163] F. Tisseur and K. Meerbergen. The quadratic eigenvalue problem. *Siam Review*, 43(2):235–286, 2001. 121

[164] K. Truffin and T. Poinsot. Comparison and extension of methods for acoustic identification of burners. *Combust. Flame*, 142(4):388–400, 2005. 39, 44

[165] Department of Economic United Nations and Social affairs, editors. *World Population Prospects: The 2012 Revision, Key Findings an Advance Tables*. ESA/P/WP.227. 2013. 16

[166] K. Ward, Hongkong, and Shanghai Banking Corporation. *Energy in 2050: Will Fuel Constraints Thwart Our Growth in Projections?* HSBC, 2011. 16

[167] D.S. Watkins. *The matrix eigenvalue problem: GR and Krylov subspace methods*. Society for Industrial and Applied Mathematics, 2007. 29, 59

[168] F. A. Williams. *Combustion Theory*. Benjamin Cummings, Menlo Park, CA, 1985. 26

[169] Pierre Wolf, Gabriel Staffelbach, Laurent Y M Gicquel, Jens-Dominik Müller, and Thierry POINSOT. Acoustic and Large Eddy Simulation studies of azimuthal modes in annular combustion chambers. *COMBUSTION AND FLAME*, 159(11):3398–3413, November 2012. 26, 27

[170] Pierre Wolf, Gabriel Staffelbach, Laurent Y M Gicquel, Jens-Dominik Müller, and Thierry POINSOT. Acoustic and Large Eddy Simulation studies of azimuthal modes in annular combustion chambers. *COMBUSTION AND FLAME*, 159(11):3398–3413, November 2012. 27, 42, 44, 147

[171] Nicholas A Worth and James R Dawson. Self-excited circumferential instabilities in a model annular gas turbine combustor: Global flame dynamics. *Proc. Combust. Inst. *, pages 1–8, June 2012. 27, 39, 42, 146, 147

[172] Nicholas A Worth and James R Dawson. Modal dynamics of self-excited azimuthal instabilities in an annular combustion chamber. *Combustion and Flame*, 2013. 26

[173] Nicholas A Worth and James R Dawson. Self-excited circumferential instabilities in a model annular gas turbine combustor: Global flame dynamics. *Proceedings of the Combustion Institute*, 34(2):3127–3134, 2013. 26

[174] Nicholas A. Worth and James R. Dawson. Modal dynamics of self-excited azimuthal instabilities in an annular combustion chamber. *Combustion and flame*, 2013, submitted. 27, 42, 146, 147

[175] Q. Yin and L. Lu. An Implicitly Restarted Block Arnoldi Method in a Vector-Wise Fashion. *NUMERICAL MATHEMATICS-ENGLISH SERIES-*, 15(3):268, 2006. 80

[176] D. You and P. Moin. A dynamic global-coefficient subgrid-scale eddy-viscosity model for large-eddy simulation in complex geometries. *Phys. Fluids *, 19(6):065110, June 2007. 26

[177] Ya. B. Zeldovitch, G. I. Barenblatt, V. B. Librovitch, and G. M. Makhviladze. *Mathematical Theory of Combustion and Explosion*. Nauka, Moscow, 1980. 16

[178] Y. Zhou and Y. Saad. Block Krylov–Schur method for large symmetric eigenvalue problems. *Numerical Algorithms*, 47(4):341–359, 2008. 81, 84, 125, 126

Part IV

APPENDIX

A simple analytical model to study combustion instabilities in annular combustors

M. Bauerheim[a], J.-F. Parmentier[a], P. Salas[b], F. Nicoud[c], T. Poinsot[d]

[a]CERFACS, CFD team, 42 Av Coriolis, 31057 Toulouse, France
[b]INRIA Bordeaux - Sud Ouest, HiePACS Project, joint INRIA-CERFACS lab. on High
Performance Computing
[c]Université Montpellier 2. I3M.UMR CNRS 5149
[d]IMF Toulouse, INP de Toulouse and CNRS, 31400 Toulouse , France

Abstract

This study describes an analytical method to compute azimuthal modes due to flame/acoustics coupling in annular combustors. It is based on a one-dimensional zero-Mach number formulation where N burners are connected to an upstream annular plenum and a downstream chamber. Flames are supposed to be compact and are modeled using identical Flame Transfer Function for all burners, characterized by an amplitude and a phase shift. Manipulation of the corresponding acoustic equations leads to a simple methodology called ANR (Annular Network Reduction). It allows to retain only the useful information related to the azimuthal modes of the annular cavities. It yields a simple dispersion relation which can be solved numerically and allows to construct coupling factors between the different cavities of the combustor. A fully analytical resolution can be performed in specific situations where coupling factors are small (weak coupling). A bifurcation appears at high coupling factors leading to a frequency lock-in of the two annular cavities (strong coupling). This tool is applied to an academic case where four burners connect an annular plenum to a chamber. For this configuration, analytical results are compared to a full three-dimensional Helmholtz solver to validate the analytical model in both weak and strong coupling regimes. Results show that this simple analytical tool allows to predict modes in annular combustors and investigate strategies to control them.

Keywords: azimuthal modes, analytical, combustion instabilities, coupling

1. Introduction

Describing the unstable acoustic modes which appear in annular gas turbine combustion chambers and finding methods to control them is the topic of multiple present research activities [1, 2, 3, 4, 5]. The complexity of these phenomena and the difficulty of performing simple laboratory-scale experiments explain why progress in this field has been slow for a long time. Recently, the development of smaller annular chambers in laboratories has opened the path to new descriptions of azimuthal instability modes in annular chambers and new investigation methods [4, 6]. At the same time, theoretical and numerical approaches have progressed in three directions: (1) full 3D LES of annular chambers have been developed [7, 8], (2) 3D acoustic tools have been adapted to annular chambers [9, 10] and (3) analytical approaches have been proposed to avoid the costs of 3D formulations and allow to investigate the stability and control of modes at low cost [5, 11]. This last class of approach is especially interesting to elucidate mechanisms because they can provide explicit solutions for the frequency and the growth rate of all modes. The difficulty in these methods is to be able to construct a model which can be handled by simple analytical approaches while retaining most of the important physical phenomena and geometrical specificities of annular chambers.

One interesting issue in studies of instabilities in annular chambers is to classify them. For example, standing and turning modes are both observed [1, 5, 8, 12] but predicting which mode type will appear in practice and whether they can be studied and controlled with the same method remains difficult. Similarly, most large scale annular chambers exhibit multiple acoustic modes in the frequency range of interest (typically 10 to 30 acoustic modes can be identified in a large scale industrial chamber between 0 and 300 Hz) and classifying them into categories is the first step to control them. These categories are typically 'longitudinal vs azimuthal modes' or 'modes involving only a part of the chamber (decoupled modes) vs modes involving the whole system (coupled modes)'. Knowing that a given unstable mode is controlled only by a certain part of the combustor is an obvious asset for any control strategy. In the case of combustors including an annular plenum, burners and an annular chamber, such a classification is useful for example to understand how azimuthal modes in the plenum and in the chamber (which have a different radius and sound speed and therefore different frequencies) can interact or live independently. Unfortunately determining whether cer-

tain parts of a chamber can be 'decoupled' from the rest of the chamber is a task for which there is no clear strategy. 'Decoupling' factors have been derived for longitudinal modes in academic burners where all modes are longitudinal [13]. Extending these approaches to annular systems requires first to derive analytical solutions allowing to isolate the effect of parameters on the modes structure. This is one of the objectives of this paper.

Parmentier et al [11] have derived an analytical method called ATACA-MAC (for Analytical Tool to Analyze and Control Azimuthal Modes in Annular Chambers) for a configuration called BC (N Burners + Chamber) (Fig.1 left). By describing acoustic wave propagation and flame action in a network of ducts representing the BC configuration and introducing a reduction method for the overall system corresponding to wave propagation in this network, they were able to predict the frequencies and growth rate of azimuthal and longitudinal modes, to identify their nature and predict their response to passive control methods such as symmetry breaking. This study in BC geometries did not correspond exactly to real annular chambers where the N burners are connected not only downstream (to the combustion chamber) but also upstream to the plenum which feeds them. The present paper extends the methodology of Parmentier et al [11] to a PBC (Plenum + N Burner + Chamber) (Fig.1 right) configuration. In most network approaches for combustion instabilities, a very large matrix is built to describe the acoustics of the system [13, 14, 15]. Here, we introduce a significantly simpler methodology called ANR (Annular Network Reduction) which allows to reduce the size of the acoustic problem in an annular system to a simple 4-by-4 matrix containing all information of the combustor resonant modes. This method allows to obtain explicit dispersion relations for PBC configurations and to exhibit the exact forms of the coupling parameters for azimuthal modes between the plenum and the burners on one hand and between the burners and the chamber on the other hand.

The paper is organized as follows: Section 2 describes the principle of the ANR (Annular Network Reduction) methodology and the submodels to account for active flames. The decomposition of the network into H-shaped connectors and azimuthal propagators allows to build an explicit dispersion relation giving the frequency, growth rate and structure of all modes. In Section 3, thermoacoustic regimes (from fully decoupled to strongly coupled) are defined depending on the analytical coupling parameters conducted in Section 2. Finally, this analytical model is validated using the model annular chamber described in Section 4 with simplistic shapes to construct coupling

3
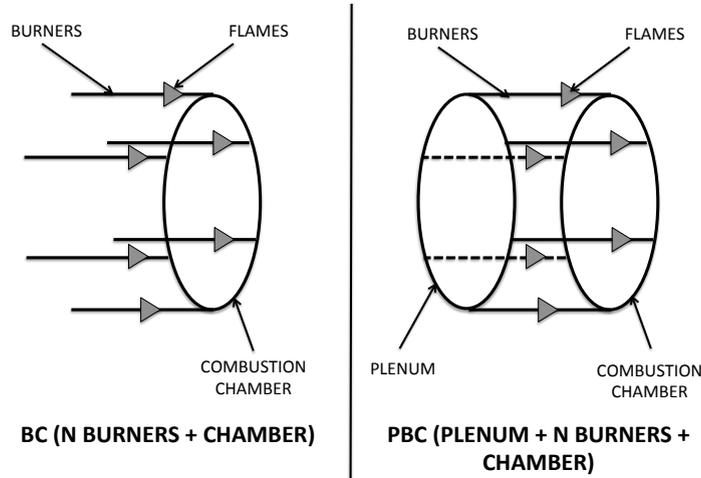
Figure 1: Configurations to study unstable modes in annular chambers

factors and study azimuthal modes for a case where a plenum is connected to a chamber by four similar burners ($N = 4$). First the weakly coupled regime (Section 5) and then the strongly coupled regime (Section 6) are investigated. The bifurcation [16] from weakly to strongly coupled situations is triggered by increasing the flame interaction index controlling the flame response to the acoustic flow. Results show that ATACAMAC allows to predict azimuthal turning and standing modes in a PBC configuration and performs as well as a 3D Helmholtz solver for all three regimes while a simple BC model is not able to capture the bifurcation from weakly to strongly coupled regimes.

2. A network model for PCB (Plenum+Burners+Chamber) configurations

2.1. Model description

The model is based on a network view of the annular chamber fed by burners connected to an annular plenum (Fig. 2). This model is limited to situations where pressure fluctuations depend on the angle θ (or x) but not on z in the chamber and the plenum (they depend on the coordinate z only in the N burners). This case can be observed in combustors terminating in choked nozzles which behave almost like a rigid wall (i.e. $u' = 0$ under the low upstream Mach number assumption [17]). Note however that this

restriction prevents the present model to represent academical combustors where the combustion chamber is opened to the atmosphere [4, 6].

Since the chamber inlet is also close to a velocity node, modes which have no variation along z can develop in the chamber, as shown by recent LES [18]. Radial modes (where p' depends on r) are neglected because often occurring at high frequency. Gas dynamics are described using standard linearized acoustics for perfect gases in the low Mach number approximation. The mean flow induced by swirlers remains slow [18] and azimuthal waves propagate at the sound speed which is different in the plenum (fresh gas at sound speed c_u^0) and the chamber (burnt gas at sound speed c^0).
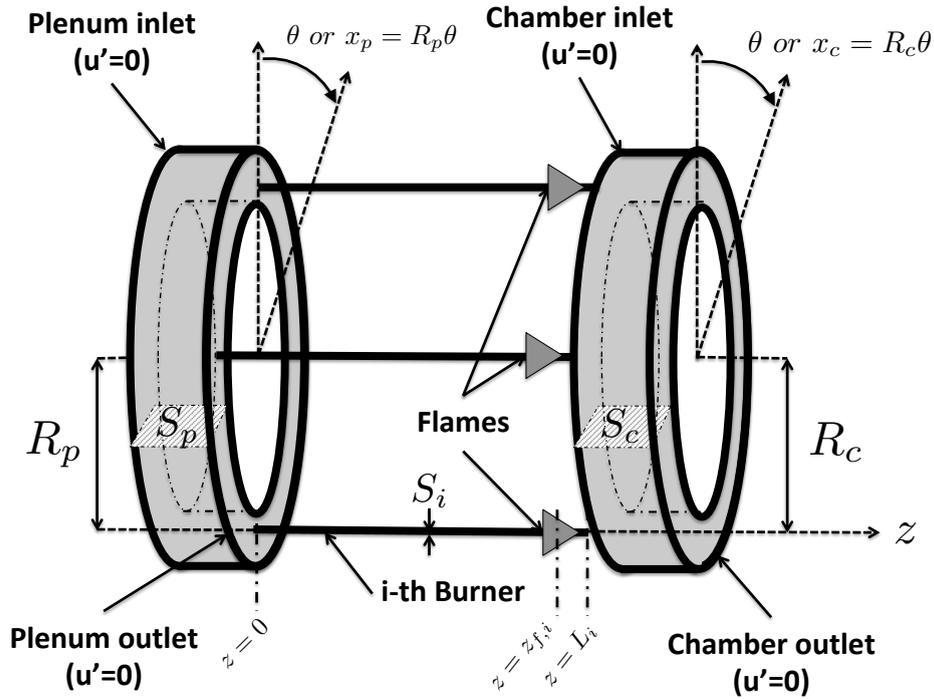
Figure 2: Network representation of the plenum, burners and chamber (PBC configuration)

In the initial ATACAMAC study of Parmentier et al. [11], a BC (Burners+Chamber) configuration was considered: an annular chamber is fed by N burners without taking into account the existence of a plenum ; the impedance imposed at the inlet of the N burners corresponded to a closed end ($u' = 0$) and flames were located at the burners extremity ($z_{f,i} \simeq L_i$

5

where L_i is the length of the ith burner). This section describes how this BC case is extended to PBC (Plenum+Burners+Chamber) configurations where an annular plenum feeds N ducts ("burners") which are all connected to an annular chamber. Most annular gas turbine chambers can be modeled using this scheme (Fig. 2).

Mean density in the annular chamber is noted ρ^0 (ρ_u^0 in the plenum). The subscript u stands for unburnt gases. The perimeter and the section of the annular plenum are noted $2L_p = 2\pi R_p$ and S_p respectively while L_i and S_i stand for the length and cross section area of the ith burner. The perimeter and the section of the annular chamber are noted $2L_c = 2\pi R_c$ and S_c respectively. The position along the annular plenum and chamber is given by the angle θ defining abscissa $x_p = R_p\theta$ for the plenum and $x_c = R_c\theta$ for the chamber. The location of the flames in the burners is given by the normalized abscissa $\alpha = z_{f,i}/L_i$ (Fig. 2).

2.2. Acoustic waves description and ANR methodology

To reduce the size of the system, a new methodology called ANR (Annular Network Reduction) is proposed to extract only useful information of azimuthal modes of the resonant combustor. First, the combustor is decomposed into N sectors (Fig. 3) by assuming that every sector can be studied separately and that no flame-to-flame interaction occurs between neighboring sectors, a question which is still open today [19, 20]. Staffelbach et al. [18] have shown that this was the case in LES of azimuthal modes. Worth and Dawson [4, 21] have also demonstrated experimentally that this assumption in annular combustor is valid when the distance between burners is large enough to avoid flames merging.

For each individual sector, the acoustic problem may be split into two parts: propagation (Section 2.2.1) and H-shaped connector (Section 2.2.2) (Fig. 4). The angle θ and the coordinates of the plenum x_p and chamber x_c take their origin at the burner i. The end of the sector i is located at $x_p = \frac{2L_p}{N}$ and $x_c = \frac{2L_c}{N}$ (thus assuming that burners are evenly located around the annular combustor).

2.2.1. Propagation

Assuming linear acoustics, the pressure and velocity perturbations inside the ith sector of the annular chamber (denoted via the subscript c, i) can be written as:

6
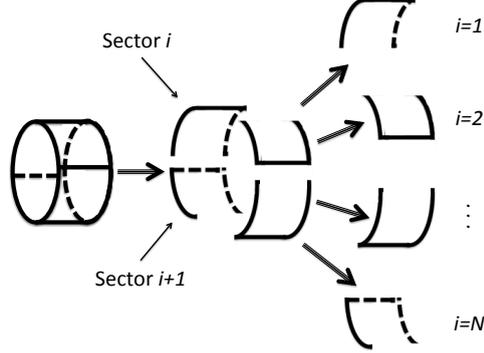
Figure 3: Decomposition of an annular combustor in N sectors
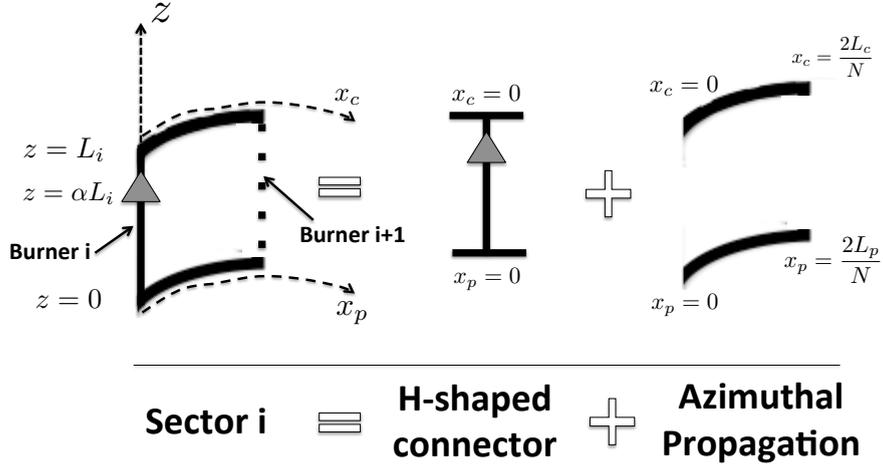
Figure 4: ANR methodology: splitting of one sector into propagation and H-shaped section parts for a PBC configuration

$$p'_{c,i}(x_c, t) = (A_i cos(kx_c) + B_i sin(kx_c))e^{-j\omega t} \qquad (1)$$

$$\rho^0 c^0 u'_{c,i}(x_c, t) = j(A_i sin(kx_c) - B_i cos(kx_c))e^{-j\omega t} \qquad (2)$$

where $j^2 = -1$, $k = \omega/c^0$ is the wavenumber, A_i and B_i are complex constants.

From Eqs. (1) and (2), pressure and velocity perturbations at two posi-

7

tions in the chamber x_{c0} and $x_{c0} + \Delta x_c$ are linked by:

$$
\begin{bmatrix} p'_{c,i} \\ \frac{1}{j}\rho^0 c^0 u'_{c,i} \end{bmatrix}_{(x_{c0}+\Delta x_c, t)} = \underbrace{\begin{bmatrix} cos(k\Delta x_c) & -sin(k\Delta x_c) \\ sin(k\Delta x_c) & cos(k\Delta x_c) \end{bmatrix}}_{R(k\Delta x_c)} \begin{bmatrix} p'_{c,i} \\ \frac{1}{j}\rho^0 c^0 u'_{c,i} \end{bmatrix}_{(x_{c0}, t)} \tag{3}
$$

The matrix $R(k\Delta x_c)$ is a 2D rotation matrix of angle $k\Delta x_c$. In the case where N burners are equally distributed over the annular chamber, the propagation in the chamber between each burner is fully described by the transfer matrix $R(k\frac{2L_c}{N})$ where $2L_c$ is the chamber perimeter.

Wave propagation in the ith sector of the plenum satisfies the same equation than in the chamber Eq. (3) if the sound speed in fresh gases c_u^0 is used:

$$
\begin{bmatrix} p'_{p,i} \\ \frac{1}{j}\rho_u^0 c_u^0 u'_{p,i} \end{bmatrix}_{(x_0+\Delta x_p, t)} = \underbrace{\begin{bmatrix} cos(k_u\Delta x_p) & -sin(k_u\Delta x_p) \\ sin(k_u\Delta x_p) & cos(k_u\Delta x_p) \end{bmatrix}}_{R(k_u\Delta x_p)} \begin{bmatrix} p'_{p,i} \\ \frac{1}{j}\rho_u^0 c_u^0 u'_{p,i} \end{bmatrix}_{(x_0, t)} \tag{4}
$$

where $k_u = \omega/c_u^0$.

Propagation in the ith burner from the plenum ($z = 0$) to the flame ($z = \alpha L_i$) and from $z = \alpha L_i$ to $z = L_i$ (Fig. 5) can be described in the same way considering propagation in fresh gases for the first part ($0 < z < \alpha L_i$) and hot gases in the second part ($\alpha L_i < z < L_i$):

Therefore, equations for the wave propagation in the ith burner are:

$$
\begin{bmatrix} p'_i \\ \frac{1}{j}\rho_u^0 c_u^0 w'_i \end{bmatrix}_{(\alpha L_i, t)} = R(k_u\alpha L_i) \begin{bmatrix} p'_i \\ \frac{1}{j}\rho_u^0 c_u^0 w'_i \end{bmatrix}_{(0, t)} \tag{5}
$$

and

$$
\begin{bmatrix} p'_i \\ \frac{1}{j}\rho^0 c^0 w'_i \end{bmatrix}_{(L_i, t)} = R(k(1-\alpha)L_i) \begin{bmatrix} p'_i \\ \frac{1}{j}\rho^0 c^0 w'_i \end{bmatrix}_{(\alpha L_i, t)} \tag{6}
$$

2.2.2. H-shaped connector

The physical parameters at the entrance (located at the end of the $i - 1^{th}$ sector corresponding to $\theta = \frac{2\pi}{N}$ and consequently $x_p = \frac{2L_p}{N}$ and $x_c = \frac{2L_c}{N}$) must be linked to the output parameters (corresponding to the beginning of the ith sector located at $\theta = 0$ and consequently $x_p = x_c = 0$) as shown in Fig. 6.
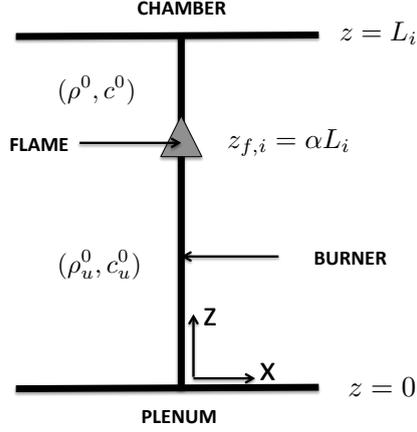
Figure 5: Propagation in the ith burner for a PBC configuration in the ANR method
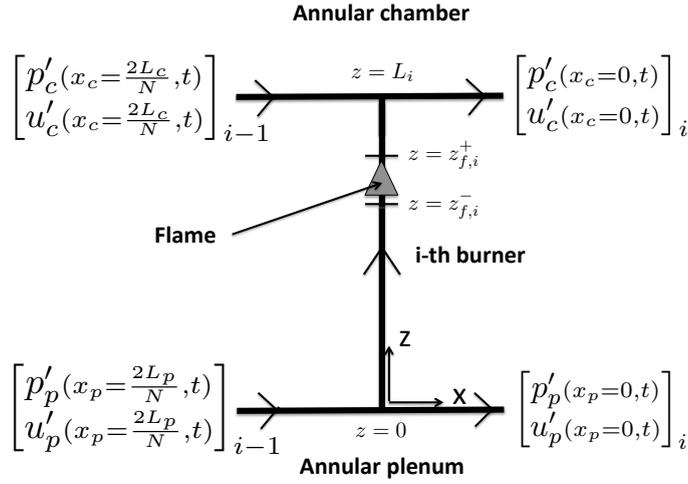
Figure 6: H-shaped overview in the ANR method

Jump conditions are first written along the x direction at $z = 0$ and $z = L_i$: at low Mach number [2], they correspond to the continuity of pressure and volume rate through the interface. At $z = L_i$:

$$p'_{c,i-1}(x_c = \frac{2L_c}{N}, t) = p'_{c,i}(x_c = 0, t) = p'_i(z = L_i) \tag{7}$$

$$S_c u'_{c,i-1}(x_c = \frac{2L_c}{N}, t) + S_i w'_i(z = L_i) = S_c u'_{c,i}(x_c = 0, t) \tag{8}$$

and at $z = 0$:

$$p'_{p,i-1}(x_p = \frac{2L_p}{N}, t) = p'_{p,i}(x_p = 0, t) = p'_i(z = 0) \tag{9}$$

$$S_p u'_{p,i-1}(x_p = \frac{2L_p}{N}, t) = S_i w'_i(z = 0) + S_p u'_{p,i}(x_p = 0, t) \tag{10}$$

Jump conditions are also required in the burners through the flames located at $z = z_{f,i}$. They are assumed to be planar and compact: their thickness is negligible compared to the acoustic wavelength. Flames are located at $z = z_{f,i}^+ = z_{f,i}^- \simeq \alpha L_i$ where superscripts $+$ and $-$ denote the downstream and upstream positions of the ith flame. At low Mach number, jump conditions through the flame imply equality of pressure and flow rate discontinuity due to an extra volume source term related to unsteady combustion [2]:

$$p'_i(z_{f,i}^+) = p'_i(z_{f,i}^-) \tag{11}$$

$$S_i w'_i(z_{f,i}^+) = S_i w'_i(z_{f,i}^-) + \frac{\gamma_u - 1}{\gamma_u P^0} \dot{\Omega}'_{T,i} \tag{12}$$

where P^0 is the mean pressure and γ_u is the heat capacity ratio of fresh gases. The unsteady heat release $\dot{\Omega}'_{T,i}$ is expressed using the FTF model (Flame Transfer Function) [22]:

$$\frac{\gamma_u - 1}{\gamma_u P^0} \dot{\Omega}'_{T,i} = S_i n_i e^{j\omega\tau_i} w'_i(z_{f,i}^-) \tag{13}$$

where the interaction index n_i[1] and the time-delay τ_i are input data (depending on frequency) describing the interaction of the ith flame with acoustics. Therefore, the jump condition in Eq. (12) is recast using Eq. (13):

$$S_i w'_i(z_{f,i}^+) = S_i(1 + n_i e^{j\omega\tau_i}) w'_i(z_{f,i}^-) \tag{14}$$

---

[1]Typical values of the interaction index n_i can reach $T_b/T_u - 1$ at low frequency.

Thanks to Eqs. (7 - 14), a transfer matrix T_i of the H-shaped connector of Fig. 6 is defined as:

$$
\begin{bmatrix}
p'_{p(x_p=0,t)} \\
\frac{1}{j}\rho_u^0 c_u^0 u'_{p(x_p=0,t)} \\
p'_{c(x_c=0,t)} \\
\frac{1}{j}\rho^0 c^0 u'_{c(x_c=0,t)}
\end{bmatrix}_i
= T_i
\begin{bmatrix}
p'_{p(x_p=\frac{2L_p}{N},t)} \\
\frac{1}{j}\rho_u^0 c_u^0 u'_{p(x_p=\frac{2L_p}{N},t)} \\
p'_{c(x_c=\frac{2L_c}{N},t)} \\
\frac{1}{j}\rho^0 c^0 u'_{c(x_c=\frac{2L_c}{N},t)}
\end{bmatrix}_{i-1}
\tag{15}
$$

where the transfer matrix T_i is:

$$
T_i = I_d + 2
\begin{bmatrix}
0 & 0 & 0 & 0 \\
-\Gamma_{i,1} & 0 & \Gamma_{i,2} & 0 \\
0 & 0 & 0 & 0 \\
\Gamma_{i,3} & 0 & -\Gamma_{i,4} & 0
\end{bmatrix}
\tag{16}
$$

and the coefficients $\Gamma_{i,k}$, $k = 1$ to 4 are:

$$
\Gamma_{i,1} = \frac{1}{2}\frac{S_i}{S_p}\frac{\cos(k(1-\alpha)L_i)\cos(k_u\alpha L_i) - \mathbb{F}\sin(k(1-\alpha)L_i)\sin(k_u\alpha L_i)}{\cos(k(1-\alpha)L_i)\sin(k_u\alpha L_i) + \mathbb{F}\sin(k(1-\alpha)L_i)\cos(k_u\alpha L_i)}
\tag{17}
$$

$$
\Gamma_{i,2} = \frac{1}{2}\frac{S_i}{S_p}\frac{1}{\cos(k(1-\alpha)L_i)\sin(k_u\alpha L_i) + \mathbb{F}\sin(k(1-\alpha)L_i)\cos(k_u\alpha L_i)}
\tag{18}
$$

$$
\Gamma_{i,3} = \frac{1}{2}\frac{S_i}{S_c}\frac{\mathbb{F}}{\cos(k(1-\alpha)L_i)\sin(k_u\alpha L_i) + \mathbb{F}\sin(k(1-\alpha)L_i)\cos(k_u\alpha L_i)}
\tag{19}
$$

$$
\Gamma_{i,4} = \frac{1}{2}\frac{S_i}{S_c}\frac{\mathbb{F}\cos(k(1-\alpha)L_i)\cos(k_u\alpha L_i) - \sin(k(1-\alpha)L_i)\sin(k_u\alpha L_i)}{\cos(k(1-\alpha)L_i)\sin(k_u\alpha L_i) + \mathbb{F}\sin(k(1-\alpha)L_i)\cos(k_u\alpha L_i)}
\tag{20}
$$

with the flame parameter $\mathbb{F}$:

$$
\mathbb{F} = \frac{\rho^0 c^0}{\rho_u^0 c_u^0}(1 + ne^{j\omega\tau})
\tag{21}
$$

These coefficients are the coupling parameters for PBC configurations. $\Gamma_{i,1}$ and $\Gamma_{i,2}$ are linked to the plenum/burner junction (depending on S_i/S_p which measures the ratio between the burner section S_i and the plenum section S_p) while $\Gamma_{i,3}$ and $\Gamma_{i,4}$ are linked to the chamber/burner junction (depending on S_i/S_c which measures the ratio of the burner section to the chamber section (Fig. 2)).

2.3. Dispersion relation calculation given by the ANR method

In previous sections, the overall problem has been split into smaller parts and now has to be reconstructed in order to obtain the dispersion relation for the whole system. First, the pressure and velocity fluctuations at the end of the $i - 1^{th}$ sector are linked to those at the end of the ith sector using Eqs. (3), (4) and (15).

$$
\begin{bmatrix}
p'_p(x_p=\frac{2L_p}{N},t) \\
\frac{1}{j}\rho_u^0 c_u^0 u'_p(x_p=\frac{2L_p}{N},t) \\
p'_c(x_c=\frac{2L_c}{N},t) \\
\frac{1}{j}\rho^0 c^0 u'_c(x_c=\frac{2L_c}{N},t)
\end{bmatrix}_i
= R_i
\begin{bmatrix}
p'_p(x_p=0,t) \\
\frac{1}{j}\rho_u^0 c_u^0 u'_p(x_p=0,t) \\
p'_c(x_c=0,t) \\
\frac{1}{j}\rho^0 c^0 u'_c(x_c=0,t)
\end{bmatrix}_i
= R_i T_i
\begin{bmatrix}
p'_p(x_p=\frac{2L_p}{N},t) \\
\frac{1}{j}\rho_u^0 c_u^0 u'_p(x_p=\frac{2L_p}{N},t) \\
p'_c(x_c=\frac{2L_c}{N},t) \\
\frac{1}{j}\rho^0 c^0 u'_c(x_c=\frac{2L_c}{N},t)
\end{bmatrix}_{i-1}
\tag{22}
$$

where T_i is the matrix defined in Eq. (16) and R_i is the propagation matrix inside the plenum and chamber in the ith sector defined by:

$$
R_i =
\begin{bmatrix}
R(k_u \frac{2L_p}{N}) & & 0 & 0 \\
 & & 0 & 0 \\
0 & 0 & & \\
0 & 0 & & R(k\frac{2L_c}{N})
\end{bmatrix}
\tag{23}
$$

where $R(k_u\frac{2L_p}{N})$ and $R(k\frac{2L_c}{N})$ are 2-by-2 matrices defined in Eqs. (3) and (4)

Then, Eq. (22) can be repeated through the N sectors and periodicity imposes that:

$$
\begin{bmatrix}
p'_p(x_p=\frac{2L_p}{N},t) \\
\frac{1}{j}\rho_u^0 c_u^0 u'_p(x_p=\frac{2L_p}{N},t) \\
p'_c(x_c=\frac{2L_c}{N},t) \\
\frac{1}{j}\rho^0 c^0 u'_c(x_c=\frac{2L_c}{N},t)
\end{bmatrix}_{i=1}
= \left(\prod_{i=N}^{1} R_i T_i\right)
\begin{bmatrix}
p'_p(x_p=\frac{2L_p}{N},t) \\
\frac{1}{j}\rho_u^0 c_u^0 u'_p(x_p=\frac{2L_p}{N},t) \\
p'_c(x_c=\frac{2L_c}{N},t) \\
\frac{1}{j}\rho^0 c^0 u'_c(x_c=\frac{2L_c}{N},t)
\end{bmatrix}_{i=1}
\tag{24}
$$

System Eq. (24) leads to non-null solutions if and only if its determinant is null:

$$
det\left(\prod_{i=N}^{1} R_i T_i - I_d\right) = 0
\tag{25}
$$

where I_d is the 4-by-4 identity matrix and the matrix $M = \prod_{i=N}^{1} R_i T_i$ is the transfer matrix of the overall system. Eq. (25) provides an implicit equation for the pulsation ω and gives the stability limits and the frequency of unstable

modes. Note that Eq. (25) given by the ANR methodology only involves a 4-by-4 determinant[2] irrespective of the number of burners N.

3. Analytical procedure and coupling limits

Due to significant non linearities, Eq. (25) cannot be solved analytically in the general case. However different situations (Fig. 7) can be exhibited where Eq. (25) can be solved depending on values taken by the coupling parameters $\wp_{p,i}$ and $\wp_{c,i}$:

$$\wp_{p,i} = max(|\Gamma_{i,1}|, |\Gamma_{i,2}|) \tag{26}$$

and

$$\wp_{c,i} = max(|\Gamma_{i,3}|, |\Gamma_{i,4}|) \tag{27}$$

The parameters $\wp_{p,i}$ and $\wp_{c,i}$ measure the coupling effect of the plenum/burner junction and the chamber/burner junction respectively for the ith sector. They depend only on the geometry (section ratios S_i/S_p and S_i/S_c as well as the burners length L_i) and the flame (the flame interaction factor $\mathbb{F}$ and the flame position α). Longitudinal modes in the burners can be obtained with this model but only purely azimuthal modes will be studied in this paper (Fig. 7).

3.1. Fully decoupled situations (FDPp and FDCp)

If the coupling parameters have vanishing small values ($\wp_{p,i} = 0$ and $\wp_{c,i} = 0$), the coupling matrices of each sector (T_i in Eq. (25)) are the identity matrix. As a consequence, the dispersion relation (Eq. (25)) reduces to:

$$det\left(\prod_{i=N}^{1} R_i - I_d\right) = 0 \tag{28}$$

---

[2]The ANR methodology retains only useful information related to azimuthal modes of the annular cavities. Knowing that these modes are a combination of two characteristic waves, the minimum size of the matrix system is $2\mathcal{C}$-by-$2\mathcal{C}$ where $\mathcal{C}$ is the number of annular cavities (here $\mathcal{C} = 2$: plenum + chamber)
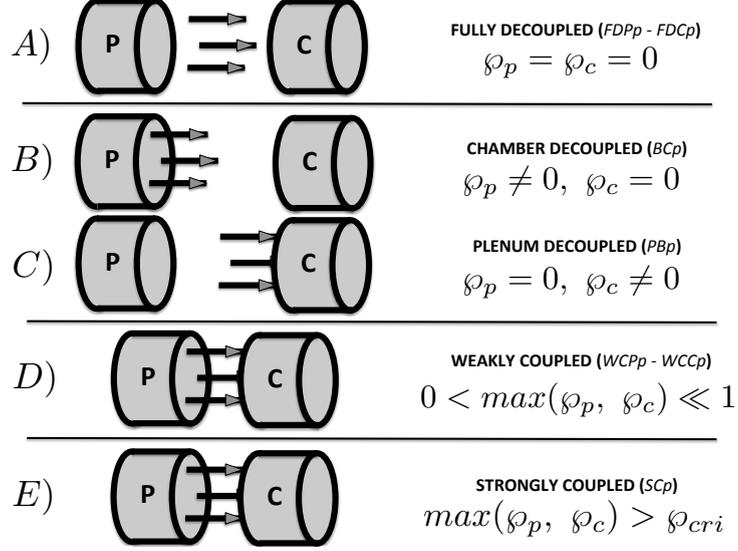
Figure 7: The four coupling situations depending on the parameters $\wp_p$ and $\wp_c$

The matrices R_i being block matrices of 2-by-2 rotation matrices which satisfy $R(\theta_1)R(\theta_2) = R(\theta_1 + \theta_2)$, Eq. (28) becomes:

$$
\begin{aligned}
det\left(\prod_{i=N}^{1} R_i - I_d\right) &= det\left(\begin{bmatrix} R(2k_uL_p) - I_d & \begin{matrix} 0 & 0 \\ 0 & 0 \end{matrix} \\ \begin{matrix} 0 & 0 \\ 0 & 0 \end{matrix} & R(2kL_c - I_d) \end{bmatrix}\right) \\
&= det\left(R(2k_uL_p) - I_d\right) det(R(2kL_c) - I_d) = 0 \quad (29)
\end{aligned}
$$

Solutions of Eq. (29) are $k_uL_p = p\pi$ and $kL_c = p\pi$ where p is an integer. They correspond to two families of modes which live separately (case A in Fig. 7):

- **FDPp - Fully Decoupled Plenum mode of order p:** they satisfy the relation $k_uL_p = p\pi$ and correspond to the azimuthal modes of the annular plenum alone (Fig. 7).

- **FDCp - Fully Decoupled Chamber mode of order p:** they satisfy the relation $kL_c = p\pi$ and correspond to the azimuthal modes of the annular chamber alone (Fig. 7).

14

3.2. Chamber or plenum decoupled situations (PBp and BCp)

These situations correspond to cases where either the plenum or the chamber are fully decoupled from the burners, i.e. respectively $\wp_p = 0$ or $\wp_c = 0$ (cases B and C in Fig. 7). The transfer matrices of each sector are block-triangular leading to a simple relation for the determinant and consequently for the dispersion relation (Eq. 25) without assumption on the non-null parameter $\wp_p$ or $\wp_c$. As for the fully decoupled situations, two families of modes can be exhibited (cases B and C in Fig. 7):

- **PBp - Plenum/Burners mode of order p:** in this situation, $\wp_c = 0$. The annular chamber is fully decoupled from the system (burners+plenum) and the dispersion relation Eq. (25) reduces to two equations:

$$det(R(2kL_c) - 1) = 0 \qquad (30)$$

$$det\left(\prod_{i=N}^{1} R\left(\frac{2k_u L_p}{N}\right)\begin{bmatrix} 1 & 0 \\ -\Gamma_{i,1} & 1 \end{bmatrix} - I_d\right) = 0 \qquad (31)$$

  Eq. (30) corresponds to the dispersion relation of a FDCp mode while Eq. (31) is the dispersion relation of a PB (Plenum + Burners) configuration where an impedance $Z = 0$ is imposed at the downstream end of the burner simulating the large chamber decoupled from the system (case B in Fig. 7). This latter mode is referred to as "PBp" standing for Plenum/Burners mode of order p. These situations are, however, unrealistic because they neglect all interactions between the annular plenum and chamber: the only solution to obtain $\wp_c \to 0$ in a PBC configuration is an infinite cross section of the chamber ($S_c \to \infty$ in Eqs. (19 - 20)). Therefore, this paper will focus on other situations (e.g. cases D and E in Fig. 7) which are more representative of real engines by including the interaction between annular cavities.

- **BCp - Burners/Chamber mode of order p:** in this situation, $\wp_p = 0$ so that the annular plenum is fully decoupled from the rest of the system and the dispersion relation Eq. (25) reduces to two equations:

$$det(R(2k_u L_p) - 1) = 0 \qquad (32)$$

15

$$det\left(\prod_{i=N}^{1} R\left(\frac{2kL_c}{N}\right)\begin{bmatrix} 1 & 0 \\ -\Gamma_{i,4} & 1 \end{bmatrix} - I_d\right) = 0 \qquad (33)$$

The first equation (Eq. (32)) is the dispersion relation of a FDPp mode while Eq. (33) is the dispersion relation of a BC (Burners + Chamber) configuration where a pressure node ($Z = 0$) is imposed at the upstream end of the burner modeling the large plenum decoupled from the burners and the annular chamber (case C in Fig. 7). This latter mode is called "BCp" for Burners/Chamber mode of order p and was already studied by Parmentier et al. [11].

3.3. Weakly coupled situations (WCPp and WCCp)

When $\wp_p$ and $\wp_c$ are both non zero, both azimuthal modes of the plenum and the chamber can exist and interact through the burners. If $\wp_p$ and $\wp_c$ remain small (Eq. (34)), an asymptotic solution can be constructed.

$$\forall i, \ 0 < \wp_{p,i} << 1 \text{ and } 0 < \wp_{c,i} << 1 \qquad (34)$$

The parameters $\wp_{p,i}$ (Eq. 26) and $\wp_{c,i}$ (Eq. 27) measure the strength of the coupling effect of the plenum/burner junction and the chamber/burner junction respectively for the ith sector. If they are small, the transfer matrices of each sector ($T_i R_i$ in Eq. (25)) are close to the rotation matrix R_i defined in Eq. (4) so that the eigenfrequencies of the system will be close to a FDPp or a FDCp mode. Consequently, as for fully decoupled modes, two families of modes can be exhibited (case D in Fig. 7):

- **WCPp - Weakly Coupled Plenum mode of order p:** this mode is close to a FDPp mode and the solution for the wavenumber k_u can be searched as an expansion around this case:

$$k_u L_p = p\pi + \epsilon_p \qquad (35)$$

where $\epsilon_p \ll p\pi$

- **WCCp - Weakly Coupled Chamber mode of order p:** this mode is close to a FDCp mode and the solution for the wavenumber k can be searched as an expansion around this case:

$$k L_c = p\pi + \epsilon_c \qquad (36)$$

16

where $\epsilon_c \ll p\pi$

For both WCPp and WCCp modes, this low coupling assumption allows a Taylor expansion of the dispersion relation (Eq. 25) which can be truncated and solved providing analytical solutions for ϵ_c and ϵ_p. This expansion is case-dependent: the $N = 4$ case will be detailed in Section. 5. Basically, results show that azimuthal modes will be either Chamber or Plenum modes slightly modified by their interaction with the rest of the combustor.

Note that the low coupling assumption ($\wp_{p,i} \ll 1$ and $\wp_{c,i} \ll 1$) does not imply low thermo-acoustic coupling ($n_i \ll 1$) because surface ratios between burner and plenum or chamber are usually small ($S_i/S_c \ll 1$ and $S_i/S_p \ll 1$).

In the specific configuration where the flames are located at the end of the burner ($\alpha = z_{f,i}/L_i = 1$ in Fig. 2), however, the coupling parameters simplify as:

$$\Gamma_{i,1} = \frac{1}{2}\frac{S_i}{S_p}\ cotan(k_u L_i) \tag{37}$$

$$\Gamma_{i,2} = \frac{1}{2}\frac{S_i}{S_p}\frac{1}{\sin(k_u L_i)} \tag{38}$$

$$\Gamma_{i,3} = \frac{1}{2}\frac{S_i}{S_c}\frac{\mathbb{F}}{\sin(k_u L_i)} \tag{39}$$

$$\Gamma_{i,4} = \frac{1}{2}\frac{S_i}{S_c}\mathbb{F}\ cotan(k_u L_i) \tag{40}$$

where $\mathbb{F}$ is the flame parameter defined in Eq. (21). Eq. (37) to (40) correspond to an extension of the coupling parameters proposed by Palies and Schuller [13] for longitudinal instabilities and Parmentier et al. [11] for azimuthal instabilities in a BC configuration. They show that decoupling ($\wp_{p,i} \ll 1$ and $\wp_{c,i} \ll 1$) can be expected in this case for small sections ratios $S_i/S_p << 1$ and $S_i/S_c << 1$, when the flame parameter $\mathbb{F}$ (Eq. (21)) is small too.

3.4. Strongly coupled situations (SCp)

The low coupling assumption ($\wp_{p,i} \ll 1$ and $\wp_{c,i} \ll 1$) is not valid at high flame interaction factor ($\mathbb{F} = \frac{\rho^0 c^0}{\rho_u^0 c_u^0}(1 + ne^{j\omega\tau})$) or high surface ratios (S_i/S_p or S_i/S_c). In these situations (case E in Fig. 7), a numerical resolution of the analytical dispersion relation (Eq. (25)) is required. It can be achieved by a non-linear solver based on the Newton-Raphson algorithm.

No rule already exists to distinguish a weakly or strongly coupled situation for real engines (characterized by an unknown critical parameter $\wp_{crit}$, Fig. 7). Moreover, classifying modes in two families as it is the case for fully decoupled situations (FDPp and FDCp modes), plenum or chamber decoupled situations (PBp and BCp modes) and weakly decoupled situations (WCPp and WCCp modes) is not possible anymore due to the interaction between all parts of the system. A first attempt to identify key parameters and rules to differentiate weakly and strongly coupled situations is described in Section 6.

In the remaining of the paper, the weakly and strongly coupled situations (Fig.7) will be studied on the PBC configuration with four burners ($N = 4$) described in Section 4. The transition from weakly (Section 5) to strongly coupled (Section 6) regimes is controlled by a critical coupling limit factor $\wp_{crit}$. The transition occurs when $max(\wp_p, \ \wp_c) > \wp_{crit}$. The geometry being fixed (Table 1) and the coupling parameters ($\wp_p$ and $\wp_c$) depending only on the geometry and the flame, the transition will be triggered by increasing the flame interaction index n_i of the flames from $n_i = 1.57$ (weak coupling) to $n_i = 8.0$ (strong coupling).

4. Validation in a simplified model chamber

Eigenfrequencies and mode structures of the analytical resolution of the dispersion relation under the low coupling factors assumption (Fig. 7, all modes except SCp) are first compared to a full 3D acoustic code and to the direct resolution of Eq. (25) in the case of a simplified 3D PBC configuration which is used as a toy-model for ATACAMAC and corresponds to a typical industrial gas turbine.

4.1. Description of the simplified PBC configuration

The 3D geometry (Fig. 8) corresponds to a PBC setup with $N = 4$ burners similar to Fig. 2 (characteristics defined in Tab. 1). The mean radii R_p and R_c of the cylindrical chamber and plenum are derived from the half perimeter L_p and L_c of the analytical model. Boundary conditions correspond to impermeable walls everywhere.

4.2. Description of the 3D acoustic code

To validate the assumptions used in ATACAMAC formulation, it is interesting to compare its results to the output of a full 3D acoustic solver.

Chamber			
Half perimeter	L_c	6.59	m
Section	S_c	0.6	m^2
Plenum			
Half perimeter	L_p	6.59	m
Section	S_p	0.6	m^2
Burner			
Length	L_i^0	0.6	m
Section	S_i	0.03	m^2
Fresh gases			
Mean pressure	p^0	$2 \cdot 10^6$	Pa
Mean temperature	T_u^0	700	K
Mean density	ρ_u^0	9.79	kg/m^3
Mean sound speed	c_u^0	743	m/s
Burnt gases			
Mean pressure	p^0	$2 \cdot 10^6$	Pa
Mean temperature	T^0	1800	K
Mean density	ρ^0	3.81	kg/m^3
Mean sound speed	c^0	1191	m/s
Flame parameters			
Interaction index	n_i	$variable$	$-$
Time-delay	τ_i	$variable$	s
Thickness	e_{fl}	0.03	m

Table 1: Parameters used for numerical applications. They correspond to a typical large scale industrial gas turbine.

Here, AVSP was used: AVSP is a parallel 3D code devoted to the resolution of acoustic modes of industrial combustion chambers [23]. It solves the eigenvalues problem issued from a discretization on unstructured meshes of the Helmholtz equation with a source term due to the flames. The mesh used here (Fig. 8, left) is composed of 230,000 cells which ensures grid independence. The flame-acoustic interaction is taken into account via the FTF model [22] similar to the expression used in Eq. (13). The local reaction term is expressed in burner i as:

$$\dot{\omega}_i = n_{u,i}\, e^{j\omega\tau_i}\, w'(\mathbf{x}_{ref,i}) \tag{41}$$

19
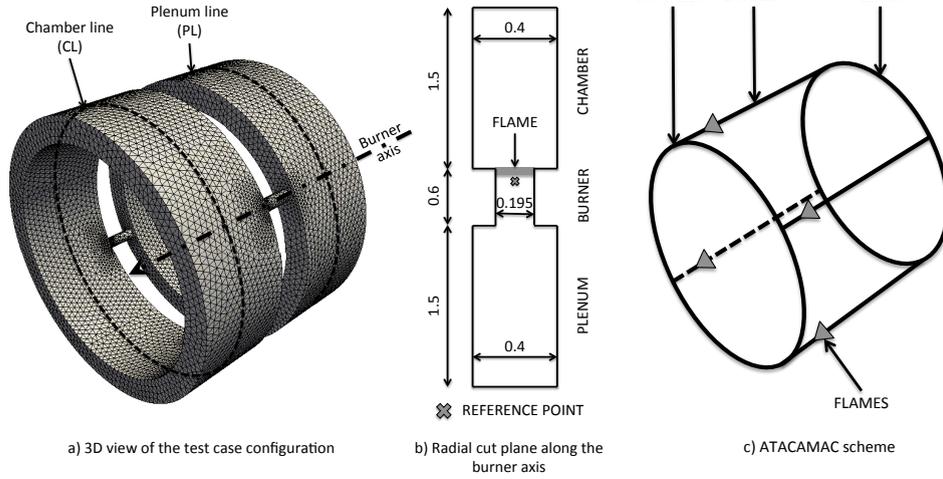
Figure 8: 3D toy-model to validate the ATACAMAC methodology. Perfect annular chamber and plenum connected by four burners ($N = 4$). --- : line in the plenum (PL) and in the chamber (CL) along which absolute pressure and phase will be plotted

The local interaction index $n_{u,i}$ describes the local flame-acoustic interactions. The values of $n_{u,i}$ are assumed to be constant in the flame zone i (Fig. 8) and are chosen to recover the global value of interaction index n_i of the infinitely thin flame when integrated over the flame zone i [23]. They are also assumed to be independent on frequency for simplicity. Heat release fluctuations in each flame zone are driven by the velocity fluctuations at the reference points $\mathbf{x_{ref,i}}$ located in the corresponding burner. In the infinitely thin flame model these reference points are the same as the flame locations z_f. In AVSP, the reference points were placed a few millimeters upstream of the flames (Fig. 8) in order to avoid numerical issues. This was proved to have only a marginal effect on the computed frequency [23, 24].

4.3. Modeling procedure for ATACAMAC

A one-dimensional model of a simplified PBC configuration described in Section 4.1 is obtained using characteristics defined in Tab. 1. Even though the present model is one-dimensional, simple corrections can be incorporated to capture 3D effects.

First, the burners considered in Fig. 8 are long narrow tubes for which end effects modify acoustic modes. In the low frequency range, this can be

accounted for [25] and a standard length correction for a flanged tube [26] is applied at the two burner's ends. The corrected length L_i for the burners is:

$$L_i = L_i^0 + 2 \times 0.4\sqrt{4S_i/\pi} \qquad (42)$$

where L_i^0 is the ith burner length without correction and S_i is the surface of the ith burner.

Second, the position of the compact flames is defined via the parameter $\alpha = z_{f,i}/L_i$ where L_i is the corrected burner length and $z_{f,i}$ is the position of the center of the flame. In Sections 5 and 6, the flame position parameter is set to $\alpha = 0.88$, a location chosen because it is far away from all pressure nodes.

5. Mode analysis of a weakly coupled PBC configuration with four burners ($N = 4$)

Under the weak coupling factors assumption ($0 < \wp_{p,i} \ll 1$ and $0 < \wp_{c,i} \ll 1$) frequencies of the whole system can be analyzed considering small perturbations around the chamber alone (FDCp mode at $k^0 L_c = p\pi$) or plenum alone (FDPp mode at $k_u^0 L_p = p\pi$) wave numbers leading to two families of modes which appear separately (Section 3.3):

$$kL_c = p\pi + \epsilon_c \text{ (WCCp)} \qquad (43)$$
$$\text{or}$$
$$k_u L_p = p\pi + \epsilon_p \text{ (WCPp)} \qquad (44)$$

where p is the mode order, $\epsilon_c << p\pi$ and $\epsilon_p << p\pi$. Since the two families of modes behave in the same manner (only radius, density and sound speed are changed), only WCCp modes will be detailed in this Section.

Due to symmetry considerations of the case $N = 4$, odd-order modes ($p = 2q + 1$, $q \in \mathbb{N}$) and even-order modes ($p = 2q$, $q \in \mathbb{N}$) will not behave in the same manner and are analyzed in Section 5.1 and 5.2 respectively.

5.1. Odd-order weakly coupled modes of the PBC configuration with four burners ($N = 4$)

Considering odd order modes ($p = 2q + 1$, $q \in \mathbb{N}$) with the low coupling limit assumption ($0 < \wp_{p,i} \ll 1$ and $0 < \wp_{c,i} \ll 1$) leads to the expansion $kL_c = p\pi + \epsilon_c$ (for a WCCp mode). A Taylor expansion can therefore be used to obtained a simplified analytical expression of the transfer matrix of

21

the ith sector and consequently of the dispersion relation (Eq. (25)). This approach is fully detailed in Appendix A for the WCC1 mode on a single burner case ($N = 1$) for simplicity. The same approach for WCCp modes and four burners ($N = 4$) leads to (see Tab. A.2):

$$sin(p\pi\beta)^2[\epsilon_c^2 - 4\epsilon_c\Gamma_4^0 + 4\Gamma_4^0] + o(\epsilon_c^2) = 0 \qquad (45)$$

where $\beta = \frac{c^0 L_p}{c_u^0 L_c}$ and Γ_4^0 is the value of Γ_4 when $kL_c = p\pi$. Note that all the burners share the same length and cross section in this configuration so that the index i of Eq. (20) was removed for simplicity.

The β parameter can be viewed as a tuning parameter between cavities: it compares the period of the azimuthal modes in the plenum alone ($\tau_p^0 = \frac{2L_p}{pc_u^0}$) and in the chamber alone ($\tau_c^0 = \frac{2L_c}{pc^0}$). In general, the two annular volumes are not tuned and the periods τ_p^0 and τ_c^0 of the azimuthal modes of the plenum and the chamber do not match, i.e. $\beta = \tau_p^0/\tau_c^0 \neq l$, $l \in \mathbb{N}$ (for example for the first chamber and plenum modes ($p = 1$) of Table 1 where $\beta \simeq 1.60$) so that the only solution to satisfy Eq. (45) is:

$$\epsilon_c^2 - 4\epsilon_c\Gamma_4^0 + 4\Gamma_4^0 + o(\epsilon_c^2) = 0 \qquad (46)$$

This quadratic equation has a double root [3] :

$$\epsilon_c = 2\Gamma_4^0 \qquad (47)$$

where Γ_4^0 is the value of Γ_4 (Eq. (20)) at $\omega = \omega^0 = p\pi c^0/L_c$

Real and imaginary parts of the frequency obtained in Eq. (47) are compared to the exact numerical resolution of the dispersion relation Eq. (25) and to AVSP results in Fig. 9. A very good agreement is found showing that the asymptotic expression of Eq. (47) is correct.

From Eq. (47), a simple analytical stability criterion can be derived as

---

[3]This approach can be extended at higher orders to unveil plenum/chamber interactions. From a third-order truncation of the dispersion relation (Eq. 25), a second-order correction on eigenfrequencies found in Eq. (47) is obtained for WCCp modes:

$$\epsilon_c = 2\Gamma_4^0 - H(\beta)\Gamma_2^0\Gamma_3^0 \quad \text{(WCCp modes)}$$

where $H(\beta) = 4\tan(p\pi\beta/2)$.
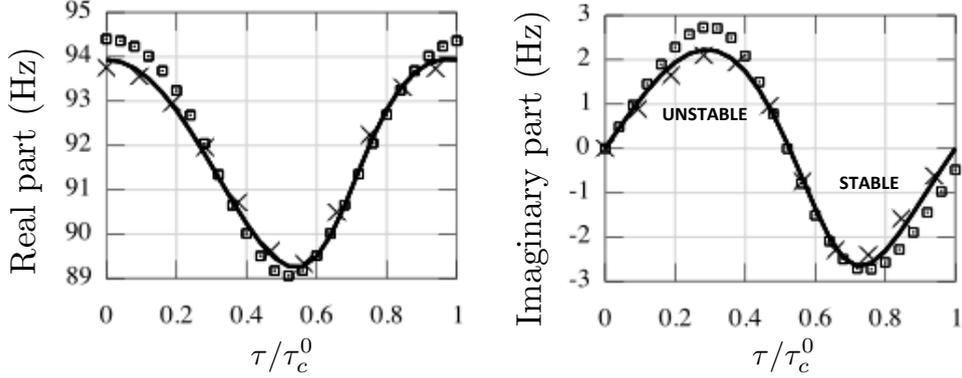
Figure 9: Eigenfrequency of the WCC1 mode for four burners ($N = 4$) with $n_i = 1.57$ as a function of τ/τ_c^0. —— : Numerical resolution of the dispersion relation Eq. (25), $\square$: Analytical model prediction Eq. (47), $\times$: AVSP results

explained in Appendix B for WCCp modes (Eq. (B.3)):

$$\underbrace{sin\left(2\pi\frac{\tau}{\tau_c^0}\right)}_{\text{effect of }\tau} \underbrace{sin\left(2p\pi\frac{\alpha L_i c^0}{L_c c_u^0}\right)}_{\text{effect of }\alpha} < 0 \quad \text{(WCCp modes)} \tag{48}$$

where $\tau_c^0 = \frac{2c^0}{pL_c}$

Time-delay τ of the FTF and flame position α have an effect on the stability and can be studied separately:

- **Time-delay -** From Eq. (48), a critical time-delay controlling the transition from stable to unstable regimes can be obtained: $\tau_{crit} = \tau_c^0/2 = \frac{L_c}{pc^0}$ for WCCp modes. This result being also valid for WCPp modes (see Eq. (B.4) leading to the critical time-delay $\tau_p^0/2 = \frac{L_p}{pc_u^0}$), stability ranges of the two first azimuthal modes WCC1 and WCP1 can be displayed simultaneously (Fig. 10). It shows that the region where both the WCC1 and WCP1 modes are stable is smaller than the stability ranges of modes taken separately: stabilizing one mode of the system cannot ensure the stability of the whole system. Of course, this result does not include any dissipation or acoustic fluxes through the boundaries [27] which would increase stability regions.

23
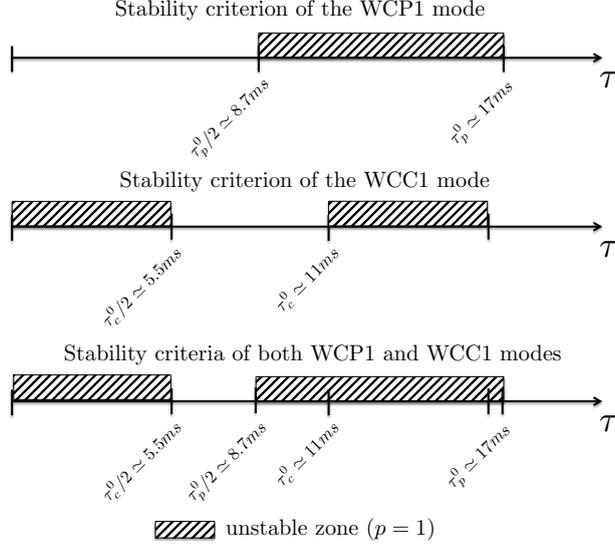
Figure 10: Stability maps (Eq. (48)) of the two first azimuthal modes ($p = 1$) for a flame located at $\alpha \simeq 0.88$: WCP1 (top), WCC1 (middle) and both WCP1 and WCC1 (bottom)

- **Flame position -** Similarly to longitudinal modes in the Rijke tube [13, 2, 28], the flame position (defined by α) also controls the stability (Eq. (48)). Appendix C demonstrates an analytical expression of the critical flame position for weakly couple modes (Eq. (C.2)) at which the stability change occurs. These expressions are close to the solution found in Rijke tubes (Eq. (C.1)) and have been validated for several weakly coupled modes (Tab. C.4 and Fig. C.20).

5.2. Even-order modes of the PBC configuration with four burners ($N = 4$)

Considering even-order WCCp modes ($p = 2q,\ q \in \mathbb{N}$) and using Eq. (25) with the low coupling limit assumption ($0 < \wp_{p,i} \ll 1$ and $0 < \wp_{c,i} \ll 1$), the dispersion relation (Eq. (25)) becomes (Tab. A.2):

$$sin(p\pi\beta/2)^2[\epsilon_c^2 - 4\epsilon_c\Gamma_4^0] + o(\epsilon_c^2) = 0 \tag{49}$$

where $\beta = \frac{k_u L_p}{k L_c}$ and Γ_4^0 is the value of Γ_4 when $kL_c = p\pi$.

When chamber and plenum frequencies do not match, i.e. $\beta \neq 1$ (for example for the WCC2 mode of Table 1 where $\beta \simeq 1.60$), the only solution to satisfy Eq. (49) is to have:

$$\epsilon_c^2 - 4\epsilon_c\Gamma_4^0 + o(\epsilon_c^2) = 0 \tag{50}$$

24

This quadratic equation has two distinct roots:

$$\epsilon_c = 0 \text{ and } \epsilon_c = 4\Gamma_4^0 \tag{51}$$

The first solution ($\epsilon_c = 0$) of Eq. (51) corresponds to modes which are not affected by the flames: the symmetry of the four burners case ($N = 4$) allows even-order modes to impose a pressure node at each burner location suppressing the flame effect on these modes which become neutral.

The second solution of Eq. (51) ($\epsilon_c = 4\Gamma_4^0$) correspond to modes which are modes strongly affected by the flame because it imposes a pressure anti-node (maximum pressure) downstream of each burner.

Real and imaginary parts of the frequency obtained from Eq. (51) are compared to the numerical solutions of the dispersion relation Eq. (25) and to AVSP results in Fig. 11. A very good agreement is found and the non-perturbed mode ($\epsilon_c = 0$) is correctly captured (straight lines).
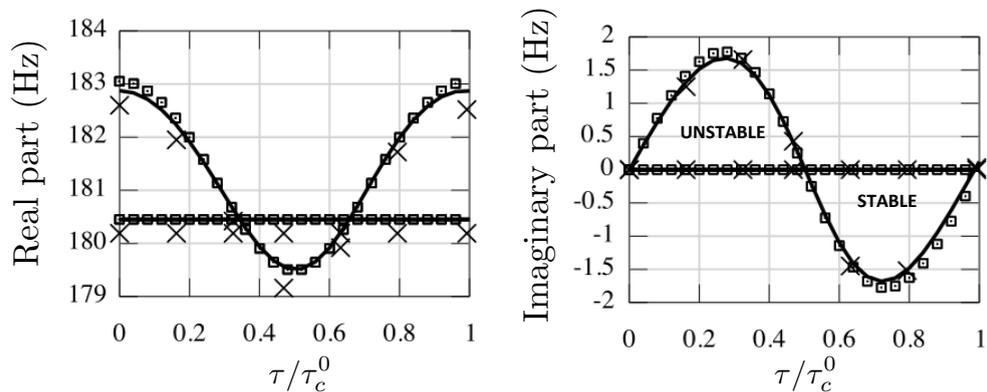
Figure 11: Eigenfrequency of the WCC2 mode for four burners ($N = 4$) with $n_i = 1.57$ as a function of τ/τ_c^0. ——— : Numerical resolution of the dispersion relation Eq. (25), □: Analytical model prediction Eq. (51), ×: AVSP results

From Eq. (51) and using Appendix B, a simple stability criterion can also be derived for WCCp even-order modes (Eq. (B.3)):

$$sin(2\pi\tau/\tau_c^0)\sin\left(2p\pi\frac{\alpha L_i c^0}{L_c c_u^0}\right) < 0 \quad \text{(WCCp modes)} \tag{52}$$

This result being also valid for WCPp modes (Eq. (B.4)) and using the results from Section 5.1, stability maps of the WCC1, WCC2, WCP1 and

25

WCP2 modes can be plotted together (Fig. 12) highlighting the difficulty to get a stable system in the absence of dissipation as supposed here: considering only these four modes, no stable region is found for time-delays lower than $19.1ms$ in the case described in Tab. 1 (Fig. 12).
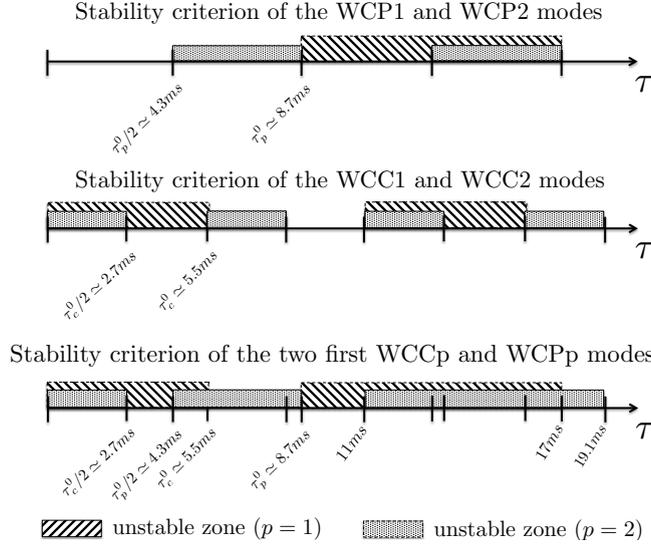
Figure 12: Stability maps of the WCC1, WCC2, WCP1 and WCP2 modes

5.3. Mode structure of weakly coupled modes

In weakly coupled situations, acoustic activity is present only in one annular cavity and in the burners as shown in Fig. 13 for the WCC1 mode (the same mode with the opposite rotation direction is also captured by AVSP but not shown here). Fig. 14 shows that this mode is purely rotating in the chamber while it is mixed in the plenum. Therefore, the combination of the two WCC1 modes with the clockwise rotation (show in Fig. 14) and the anti-clockwise rotation (not shown) enable to have purely rotating or purely standing modes but not necessarily in the two annular cavities at the same time.

5.4. Stability map of weakly coupled situations

Sections 5.1 and 5.2 focused on weakly coupled situations where the low coupling factor assumption ($\wp_p \ll 1$ and $\wp_c \ll 1$) is valid. Stability maps
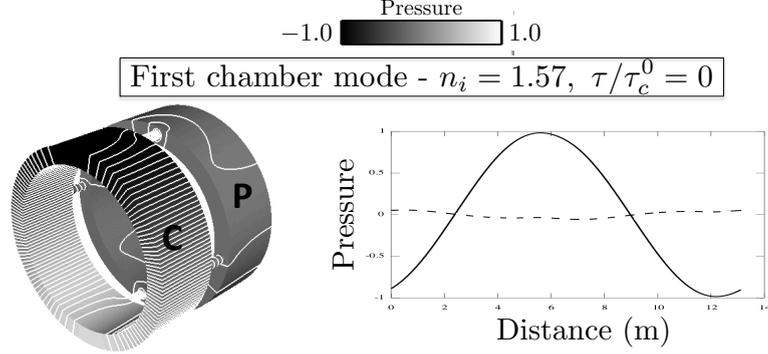
Figure 13: Pressure mode structures ($p' = |p'|cos(arg(p'))$) obtained with AVSP with pressure isolines (left) and pressure along the azimuthal direction in the annular chamber (——) and annular plenum (- - -) for the WCC1 mode of a PBC configuration with four burners ($N = 4$) and $n_i = 1.57$ at the time-delay: $\tau/\tau_c^0 = 0$
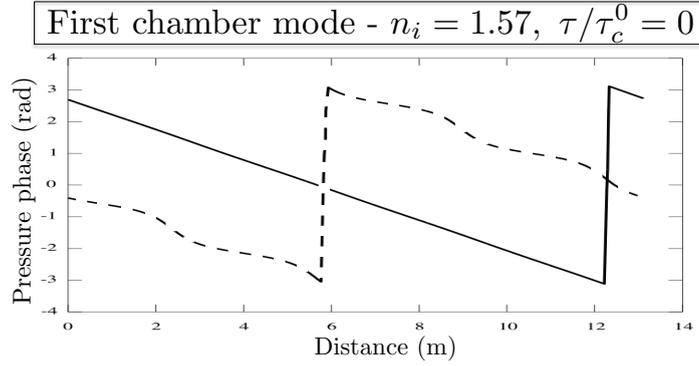
Figure 14: Pressure phase of the WCC1 mode obtained with AVSP at $n_i = 1.57$ along the azimuthal direction in the annular chamber (——) and the annular plenum (- - -) for time-delay: $\tau/\tau_c^0 = 0$

of perturbed modes (i.e. $\epsilon \neq 0$) in the complex plane $[R_e(f), I_m(f)]$ are well suited to show differences between the several regimes - weakly coupled and strongly coupled situations. These maps are oriented circles (- - - (WCP1) and —— (WCC1) in Fig.15) centered at the frequency $f(n_i = 0) \simeq f_0$ which corresponds to a passive flame mode ($n_i = 0$: $\times$ in Fig.15) and is approximately the frequency of the cavity alone ($f_0 = \frac{pc^0}{2L}$). The radius is proportional to the coupling factor which can be increased via the surface

ratios (S_i/S_p and S_i/S_c) or the flame interaction index n_i. In the weakly coupled regime, WCCp and WCPp modes do not strongly interact as shown in Fig. 15: WCP1 and WCC1 live separately.
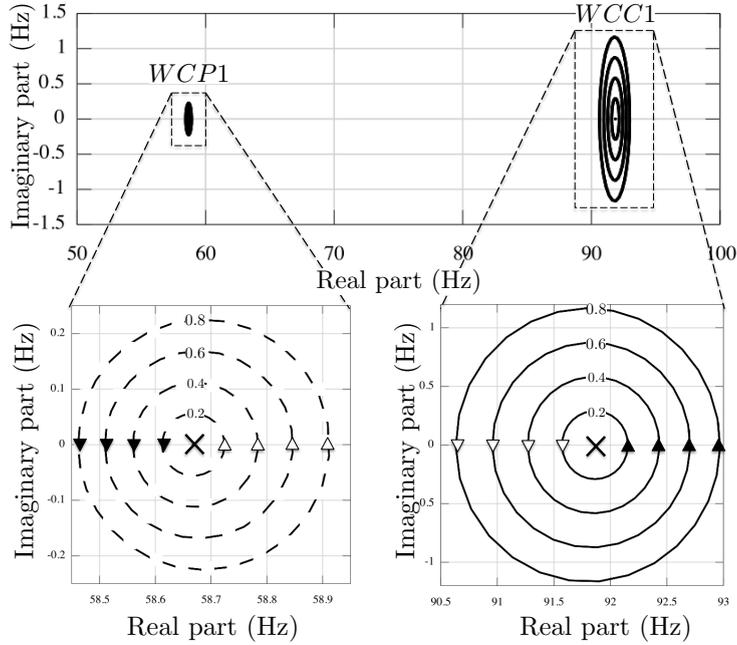
Figure 15: Eigenfrequencies of both WCP1 and WCC1 modes (top) and zoom on WCP1 (bottom left) and WCC1 (bottom right) when the flame delay changes for PBC configuration with four burners ($N = 4$) with $n_i = 0.2$, 0.4, 0.6 and 0.8, ×: Passive flame ($n_i = 0$), - - - : WCP1 mode, —— : WCC1 mode, ▶: $\tau/\tau_p^0 = 0$ or $\tau/\tau_c^0 = 0$ oriented in the increasing τ direction, ▷: $\tau/\tau_p^0 = 1/2$ or $\tau/\tau_c^0 = 1/2$

6. Mode analysis of a strongly coupled PBC configuration with four burners ($N = 4$)

For weakly coupled cases (Section 5), the frequencies of the azimuthal modes in the plenum and in the chamber are only marginally affected by the flame (Figs. 9 and 11) so that they can never match (Fig. 15). However, if the flame interaction index (n_i) is larger, the frequencies of the azimuthal modes of the annular plenum and the annular chamber change more and the possibility of having there two frequencies match opens an interesting

situation where the whole system can resonate. This corresponds to the strongly coupled modes of order p (referred as "SCp" modes) studied in this section.

Figure 16 shows the stability maps of the WCC1 (——) and WCP1 (---) modes obtained with low flame interaction index ($n_i = 5.0$ and 6.0) as well as the SC1 (○) and SC2 modes (●) obtained for higher flame interaction index ($n_i = 7.0$ and 8.0[4] at the zero frequency limit). Three points in the SC2 trajectory with $n_i = 8.0$ corresponding to several time-delays ($\tau/\tau_c^0 = 0$ (A), $\tau/\tau_c^0 = 0.54$ (B) and $\tau/\tau_c^0 = 0.9$ (C)) are displayed in Fig. 16 and will be used as typical cases to show pressure structures in the annular plenum and chamber.
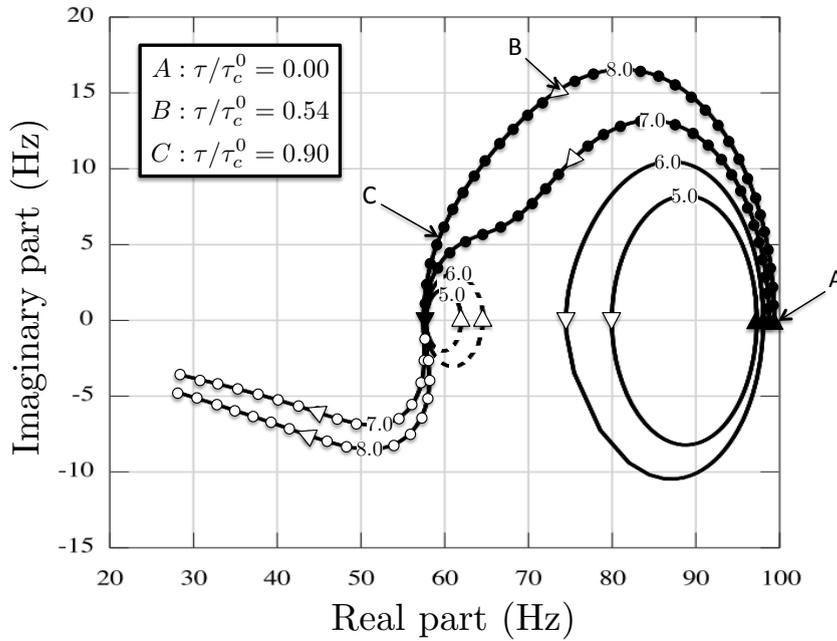
Figure 16: Eigenfrequencies on the complex plane for a PBC configuration with four burners ($N = 4$), ---: WCP1 mode ($n_i = 5.0$ and 6.0), ——: WCC1 mode ($n_i = 5.0$ and 6.0), ○: SC1 mode ($n_i = 7.0$ and 8.0), ●: SC2 mode ($n_i = 7.0$ and 8.0), ▶: $\tau/\tau_p^0 = 0$ or $\tau/\tau_c^0 = 0$ oriented in the increasing τ direction and ▷: $\tau/\tau_p^0 = 1/2$ or $\tau/\tau_c^0 = 1/2$

---

[4]Note that the typical order of magnitude of the interaction index n_i is $T_b/T_u - 1$

29

For low flame interaction index ($n_i = 5.0$ and 6.0), the first two modes always have different frequencies and can be identified as plenum (WCPp: ---) or chamber modes (WCCp: ——) as studied in Section 5.

However, for higher flame interaction indices ($n_i = 7.0$ and 8.0) a bifurcation occurs: frequencies of the annular plenum, burners and annular chamber can match leading to strongly coupled modes where the whole system resonates. The trajectory of the first strongly coupled mode (SC1: ∘) goes from the WCP1 mode (for small time-delays $\tau < \tau_p^0/2$) to a longitudinal mode (not presented here around 40Hz, for large time-delays $\tau > \tau_p^0/2$). A second strongly coupled mode (SC2: •) has a trajectory in the complex plane coming from the WCC1 mode (for small time-delays $\tau < \tau_c^0/2$) and going to the WCP1 mode (for large time-delays $\tau > \tau_c^0/2$).

The stability map of the SC2 mode (•) at $n_i = 8.0$ has been validated against the 3D finite element solver AVSP (Fig. 17). A good agreement between AVSP (×) and the numerical resolution of Eq. (25) (——) is found. The growth rate is slightly underestimated but the global trend is well captured: the mode is fully unstable for all time-delays which corresponds to a new behavior compared to the weakly coupled modes (WCPp and WCCp). The analytical approach developed in Section 5 for the weakly coupled regime (□ in Fig. 17) is not able to capture this new highly non-linear behavior.
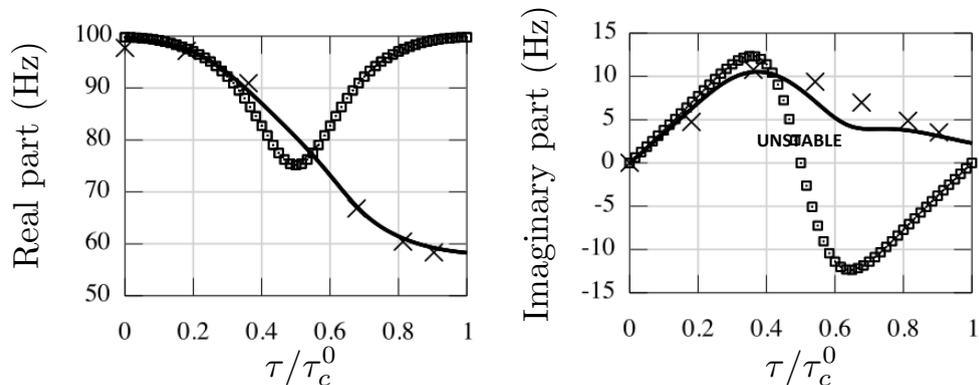
Figure 17: Eigenfrequency of the first order chamber mode ($p = 1$) for four burners ($N = 4$) as a function of τ/τ_c^0 with $n_i = 8.0$. —— : Numerical resolution of Eq. (25), □: Analytical model prediction for weakly coupled situations (Eq. (47)), ×: AVSP results

When the flame interaction index is sufficiently large ($n_i > 7.0$), i.e. when the flame is sufficiently intense, the modes of plenum and chamber lock-in

30

and become unstable for all time delays.

Pressure structures ($p' = |p'|cos(arg(p'))$) along the azimuthal direction in the plenum (PL line in Fig. 8) and in the chamber (CL line in Fig. 8) obtained with AVSP for the SC2 mode are displayed in Fig. 18 for a high flame interaction index ($n_i = 8.0$) and several time-delays (A: $\tau/\tau_c^0 = 0$, B: $\tau/\tau_c^0 = 0.54$ and C: $\tau/\tau_c^0 = 0.9$ from Fig. 16). For null time-delays (A in Fig. 16), acoustic activity is only present in the chamber (——) and the frequency is close to the WCC1 mode. The acoustic activity in the second annular cavity (i.e. the plenum: ---) grows with the time-delay τ. For $\tau/\tau_c^0 = 0.54ms$ (B in Fig. 16) a strong interaction with the burners appears leading to higher growth rates. Surprisingly, this case corresponds only to a moderate acoustic activity in the second annular cavity (i.e. the annular plenum: ---). For $\tau/\tau_c^0 = 0.9$ (C in Fig. 16) a first order mode is present in both annular cavities highlighting a strongly coupled situation. This strong interaction between plenum and chamber revealed by the presence of acoustic activity in both annular cavities leads, however, to a marginally unstable mode.

Fig. 19 shows the pressure phase in the annular plenum (---) and in the annular chamber (——) for several time-delays. The same mode with opposite direction is also found with AVSP but not shown here. For small time-delay ($\tau/\tau_c^0 = 0$ for case A and $\tau/\tau_c^0 = 0.54$ for case B of Fig. 16), pressures in the plenum and in the chamber have different natures: purely spinning mode in the chamber (linear phase) and a mixed mode in the plenum (wave shape of the phase). The combination of clockwise and anti-clockwise mode can generate purely spinning or purely standing mode but not necessarily in both annular cavities at the same time. However, higher time-delays cases (as for case C where $\tau/\tau_c^0 = 0.9$) correspond to strongly coupled situations where both annular cavities lock-in (Fig. 18 C). In such a case, pressure in the chamber and plenum exhibit the same nature: purely spinning in both cavities in Fig. 19 C (the same mode with the opposite rotating direction is also found by AVSP but not shown here). The combination of the purely spinning modes (clockwise and anti-clockise) can also lead to standing modes in both annular cavities at the same time: this is a specific behavior only encountered in locked-in modes as case C.

Finally, it demonstrates that a highly unstable mode does not necessarily exhibit strong acoustic activity in both annular cavities (as for case B) and that a mode where acoustic activity appears in the whole system can be only marginally unstable (as for case C). Moreover, the phase-lag between pressure
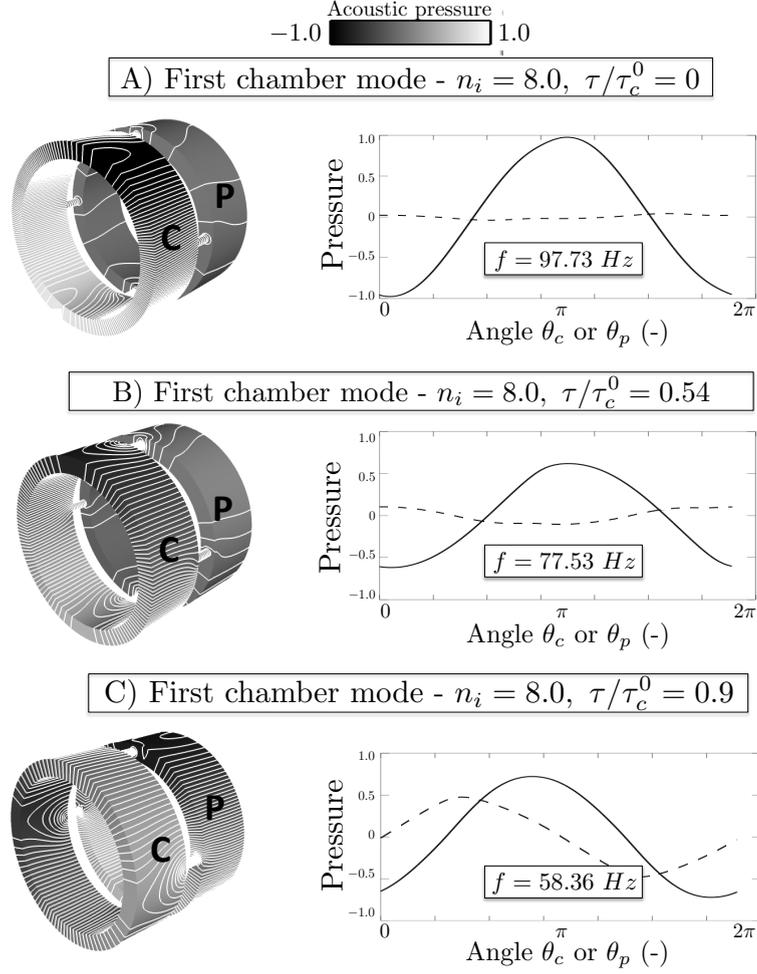
Figure 18: Pressure structures and isolines ($p' = |p'|cos(arg(p'))$) obtained with AVSP (left) and pressure along the azimuthal direction in the annular chamber (——) and annular plenum (- - -) for the SC2 mode of a PBC configuration with four burners ($N = 4$) and $n_i = 8.0$ at several time-delay: $\tau/\tau_c^0 = 0$ (top), 0.54 (middle) and 0.9 (bottom). The configuration corresponds to $f_{FDP1} = 56$ Hz and $f_{FDC1} = 90$ Hz

in the annular cavity and the annular chamber as well as the nature of the mode (spinning, standing or mixed) changes when acoustic activity is present in both annular cavities, a property which could be checked experimentally.
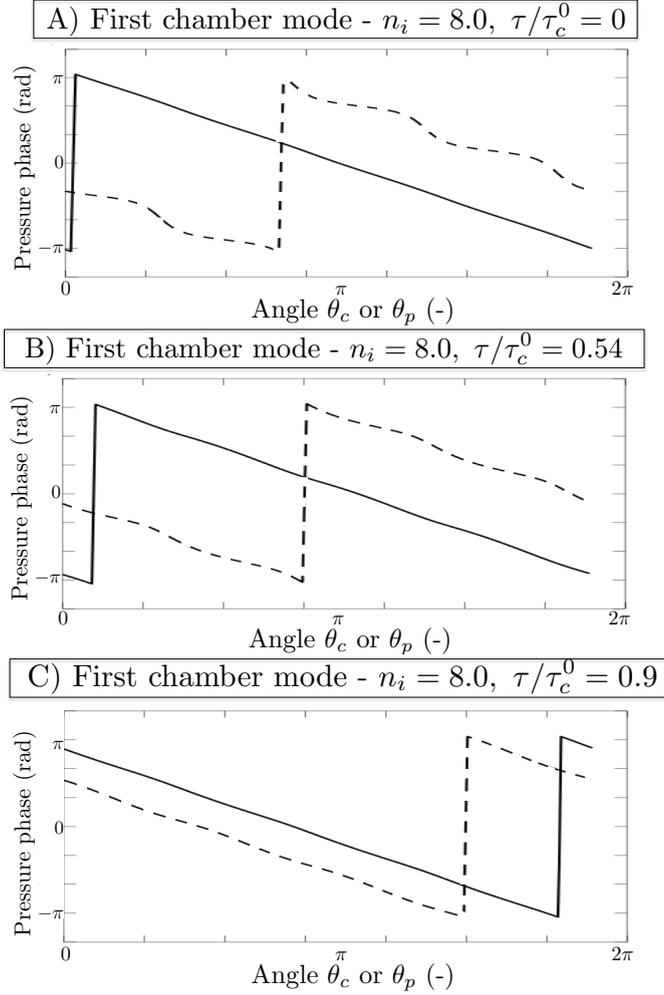
Figure 19: Pressure phase obtained with AVSP for the SC2 mode at $n_i = 8.0$ along the azimuthal direction in the annular chamber (——) and the annular plenum (- - -) for several time-delays: $\tau/\tau_c^0 = 0$ (top), 0.54 (middle) and 0.9 (bottom).

7. Conclusion

To complement expensive Large Eddy Simulation [29] and Helmholtz [23] 3D codes used to study azimuthal modes in annular combustors, simple tools are required to understand the physics of these modes and create pre-designs of industrial combustors. This paper describes a simple analytical theory to

33

compute the azimuthal modes appearing in these combustors. It is based on a one-dimensional acoustic network where N burners are connected to an annular plenum and chamber. A manipulation of the corresponding acoustic equations in this configuration leads to a simple analytical dispersion relation which can be solved numerically. This method allows to exhibit coupling factors between plenum, burners and chamber which depend on area ratios and flame transfer function (FTF). For $N = 4$, a fully analytical resolution can be performed in specific situations where coupling factors of the FTF [11, 13] are small and simple stability criteria can be proposed. For higher coupling factors, a bifurcation occurs yielding a strongly coupled regime where acoustic activity is present in both annular cavities. The nature of such a mode (standing, spinning or mixed) changes with the time-delay. Purely spinning or purely standing modes in the annular plenum and in the chamber were found simultaneously only when a strongly coupled situation occurs (Fig. 19 C). For strongly coupled cases, a PBC configuration where two annular cavities are connected to N burners is required to predict correctly eigenmodes and stability maps. This analytical tool has been compared systematically to the predictions of a full three-dimensional Helmholtz solver. A very good agreement is found showing that the present asymptotic resolution is correct. These results show that a simple analytical formulation to study azimuthal modes in annular combustors is an interesting tool which can be used as a pre-design tool or as an help to post-process acoustic or LES simulations.

Appendix A. Analytical dispersion relation of a PBC configuration with a single burner ($N = 1$)

The analytical dispersion relation (Eq. (25)) is obtained for a general PBC configuration with N burners. To explain the ATACAMAC approach leading to the analytical eigenfrequencies of the system, the case of a single burner ($N = 1$) will be detailed.

Considering only one burner, the transfer matrix $M = R_1 T_1 - Id$ of the

whole system is:

$$M = \begin{bmatrix} cos(2k_uL_p) - 1 & -sin(2k_uL_p) \\ sin(2k_uL_p) - 2cos(2k_uL_p)\Gamma_1 & 2sin(2k_uL_p)\Gamma_1 + cos(2k_uL_p) - 1 \\ 0 & 0 \\ 2cos(k_uL_p)\Gamma_3 & -2sin(2k_uL_p)\Gamma_3 \end{bmatrix} \cdots$$

$$\cdots \begin{bmatrix} 0 & 0 \\ 2cos(2kL_c)\Gamma_2 & -2sin(2kL_c)\Gamma_2 \\ cos(2kL_c) - 1 & -sin(2kL_c) \\ sin(2kL_c) - 2cos(2kL_c)\Gamma_4 & 2sin(2kL_c)\Gamma_4 + cos(2kL_c) - 1 \end{bmatrix} \quad (A.1)$$

In the general case with N burners, a Taylor expansion of this matrix has to be performed as a first simplification. Here, the matrix is simple enough to compute analytically the determinant leading to the exact dispersion relation:

$$\begin{aligned} & + & (\Gamma_1\Gamma_4 - \Gamma_2\Gamma_3)sin(2kL_c)sin(2k_uL_p) \\ & - & 2\Gamma_1[1 - cos(2kL_c)]sin(2k_uL_p) \\ & - & 2\Gamma_4[1 - cos(2k_uL_p)]sin(2kL_c) \\ & + & 4[1 - cos(2kL_c)][1 - cos(2k_uL_p)] = 0 \end{aligned} \quad (A.2)$$

The dispersion relation Eq. (A.2) is non-linear. The idea is to use a Taylor expansion at the second (or third) order and to solve it analytically. The expansion has to be done around a FDCp (i.e. $kL_c = p\pi + \epsilon_c$) or FDPp (i.e. $k_uL_p = p\pi + \epsilon_p$) mode (see Section 3.3 for details). For instance, in the case of the WCC1 mode ($kL_c = \pi + \epsilon$ which implies $k_uL_p = \beta(\pi + \epsilon_c)$ where $\beta = \frac{c^0 L_p}{c_u^0 L_c}$), the dispersion relation Eq. (A.2) becomes:

$$[cos(2\pi\beta) - 1][\epsilon_c\Gamma_4^0 - \epsilon_c^2 + o(\epsilon_c^2)] = 0 \quad (A.3)$$

where Γ_4^0 is the value of Γ_4 evaluated at $kL_c = p\pi$

Note that solutions of Eq. (A.3) being $\epsilon_c = \Gamma_4^0$, it justifies that the term $\epsilon_c\Gamma_4^0$ is of the same order of magnitude than ϵ_c^2 and therefore has to be kept in the analytical dispersion relation Eq. A.2.

Analytical dispersion relations for $N > 1$ are more complex to derive but follow a similar procedure. When $N = 4$, the dispersion relation of Tab. (A.2) are obtained:

35

Type	Odd/Even	Second-order dispersion relation $(o(\epsilon^2))$
WCC	Odd	$sin(p\pi\beta)[\epsilon^2 - 4\epsilon\Gamma_4^0 + 4\Gamma_4^0] = 0$
	Even	$sin(p\pi\beta/2)[\epsilon^2 - 4\epsilon\Gamma_4^0] = 0$
WCP	Odd	$sin(p\pi/\beta)[\epsilon^2 - 4\epsilon\Gamma_1^0 + 4\Gamma_1^0] = 0$
	Even	$sin(p\pi/(2\beta))[\epsilon^2 - 4\epsilon\Gamma_1^0] = 0$

Table A.2: Analytical expressions of wave number perturbation for WCCp and WCPp azimuthal modes

Appendix B. Stability criterion of weakly coupled modes for a four burners configuration ($N = 4$)

A mode is stable if the imaginary part of the wave number is negative. Table B.3 shows analytical expressions of the wave number perturbation ϵ for WCPp and WCCp modes:

Type	Odd/Even	Wave number perturbation (ϵ)
WCC	Odd	$2\Gamma_4^0 - H(\beta)\Gamma_2^0\Gamma_3^0$
	Even	$2\Gamma_4^0 - G(\beta)\Gamma_2^0\Gamma_3^0$
WCP	Odd	$2\Gamma_1^0 - H(1/\beta)\Gamma_2^0\Gamma_3^0$
	Even	$2\Gamma_1^0 - G(1/\beta)\Gamma_2^0\Gamma_3^0$

Table B.3: Analytical expressions of wave number perturbation ϵ for WCCp and WCPp modes where $H(x) = 4tan(p\pi x/2)$ and $G(x) = 4\frac{sin(p\pi x/2)}{cos(p\pi x/2) - (-1)^{p/2}}$ have real values.

Analytical stability criteria can be derived by calculating the sign of $Im(\Gamma_1^0)$, $Im(\Gamma_4^0)$ and $Im(\Gamma_2^0\Gamma_3^0)$ using the following definitions: $\mathbb{F}^*$ is the complex conjugate of the flame parameter $\mathbb{F} = \frac{\rho^0 c^0}{\rho_u^0 c_u^0}\left(1 + n.e^{j\omega^0\tau}\right)$, $\theta^0 = \omega^0(1 - \alpha)L_i/c^0 \in \mathbb{R}$ and $\theta_u^0 = \omega^0\alpha L_i/c_u^0 \in \mathbb{R}$. The notation $\mathfrak{D}$ refers to $\mathfrak{D} = |\cos(\theta^0)\sin(\theta_u^0) + \mathbb{F}\sin(\theta^0)\cos(\theta_u^0)|^2$

With these notations, the sign of the imaginary part of these coupling parameters are:

$$Im(\Gamma_1^0) = -\frac{S_i}{4S_p\mathfrak{D}}\sin(2\theta^0)Im(\mathbb{F}) \qquad (B.1)$$

$$Im(\Gamma_4^0) = \frac{S_i}{4S_c\mathfrak{D}} \sin(2\theta_u^0) Im(\mathbb{F}) \qquad (B.2)$$

Eqs. (B.1 - B.2) lead to simple analytical stability criteria for WCCp and WCPp modes:

$$sin(2\pi\tau/\tau_c^0) \sin\left(2p\pi\frac{\alpha L_i c^0}{L_c c_u^0}\right) < 0 \quad \text{for WCCp modes} \qquad (B.3)$$

$$sin(2\pi\tau/\tau_p^0) \sin\left(2p\pi\frac{(1-\alpha)L_i c_u^0}{L_p c^0}\right) > 0 \quad \text{for WCPp modes} \qquad (B.4)$$

Appendix C. Flame position effect on annular combustors stability

Similarly to longitudinal modes in the Rijke tube [13, 2, 28], the flame position (defined by α) also controls the stability (Eq. (48)). In a quasi-isothermal Rijke tube, for common (small) values of the FTF time-delay τ, stability of the first longitudinal mode is obtained only when the flame is located in the upper half of the tubes [30, 31], i.e. $\alpha > 1/2$, which can be extended for the p-th longitudinal mode:

$$\frac{2m+1}{2p} < \alpha < \frac{2(m+1)}{2p}, \quad \forall m \in \mathbb{N} \quad \text{(Rijke tube)} \qquad (C.1)$$

Eq. (48) highlights a similar behavior for azimuthal modes in a PBC configuration: for a WCCp mode with small values of the time-delay $\tau < \tau_c^0/2$, $\sin(2\pi\frac{\tau}{\tau_c^0})$ is positive and Eq. (48) leads to:

$$\frac{2m+1}{2p}\frac{L_c c_u^0}{L_i c^0} < \alpha < \frac{2(m+1)}{2p}\frac{L_c c_u^0}{L_i c^0}, \quad \forall m \in \mathbb{N} \quad \text{(WCCp modes)} \qquad (C.2)$$

Usually, the critical flame position $\alpha_{crit} = \frac{L_c c_u^0}{2pL_i c^0}$ is larger than unity because the half-perimeter of the annular cavity is much longer than the burner length ($L_c \gg L_i$). Since the range of the normalized flame position α is $[0-1]$, the flame position may affect the stability only for high-order modes (i.e. p large enough to get $\alpha_{crit} < 1$). For instance, in the case described in Table 1 with the corrected burner length $L_i \simeq 0.76 \ m$, the critical flame positions α_{crit} and the stability ranges (Eq. (C.2)) are shown in Tab. C.4.

The change of stability with the flame position α for small time-delays predicted in Tab. C.4 has been validated using the numerical resolution of

37

Mode order (p)	$p = 1$	$p = 3$	$p = 5$	$p = 7$
$\alpha_{crit} = \frac{L_c c_u^0}{2pL_i c^0}$	2.70	0.9	0.54	0.39
α satisfying Eq. (C.2)	none	[0.9 - 1]	[0.54 − 1]	[0.39 − 0.78]

Table C.4: Critical flame positions α_{crit} and flame positions satisfying Eq. (C.2) for WCCp odd-order modes of the case described in Table 1

the dispersion relation (Eq. (25)) in Fig. C.20. The critical flame positions obtained in Tab. C.4 are well captured for all modes. A situation where the plenum/chamber interaction is not negligible is shown for the WCC1 mode with $\alpha = 0.3$ (i.e. the flame is close the pressure node imposed by the large annular plenum).
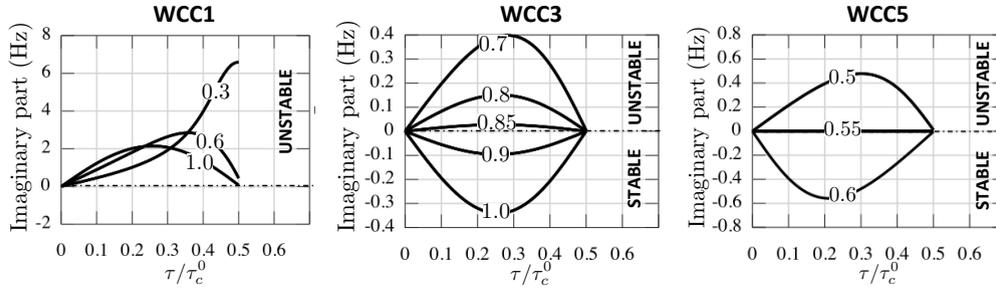
Figure C.20: Growth rate for several flame positions α of the WCC1 ($\alpha = 0.3$, 0.6, 1.0 - left), WCC3 ($\alpha = 0.5$, 0.8, 0.85, 0.9, 1.0 - middle) and WCC5 ($\alpha = 0.5$, 0.55, 0.6 - right) modes for small time delays ($\tau/\tau_c^0 < 1/2$) using the numerical resolution of the dispersion relation (Eq. (25)) with $n_i = 1.57$

References

[1] W. Krebs, P. Flohr, B. Prade, S. Hoffmann, Combust. Sci. Tech. 174 (2002) 99–128.

[2] T. Poinsot, D. Veynante, Theoretical and Numerical Combustion, Third Edition (www.cerfacs.fr/elearning), 2011.

[3] T. Lieuwen, V. Yang, Combustion Instabilities in Gas Turbine Engines. Operational Experience, Fundamental Mechanisms and Modeling, 2005.

[4] N. Worth, J. Dawson, Proceedings of the Combustion Institute 34 (2013, in press) 3127–3134.

[5] N. Noiray, M. Bothien, B. Schuermans, Combust. Theory and Modelling (2011) 585–606.

[6] J. Moeck, M. Paul, C. Paschereit, in: ASME Turbo Expo 2010 GT2010-23577.

[7] C. Fureby, Flow, Turb. and Combustion 84 (2010) 543–564.

[8] P. Wolf, G. Staffelbach, L. Gicquel, J. Muller, P. T., Combustion and Flame 159 (2012) 3398–3413.

[9] M. Leyko, F. Nicoud, S. Moreau, T. Poinsot, C. R. Acad. Sci. Mécanique 337 (2009) 415–425.

[10] C. Sensiau, F. Nicoud, T. Poinsot, Int. Journal Aeroacoustics 8 (2009) 57–68.

[11] J. Parmentier, P. Salas, P. Wolf, G. Staffelbach, F. Nicoud, T. Poinsot, Combustion and Flame 159 (2012) 2374–2387.

[12] B. Schuermans, C. Paschereit, P. Monkewitz, in: 44th AIAA Aerospace Sciences Meeeting and Exhibit, 0549.

[13] T. Schuller, D. Durox, P. Palies, S. Candel, Combustion and Flame 159 (2012) 1921–1931.

[14] P. Palies, D. Durox, T. Schuller, S. Candel, Combustion Science and Technology 183 (2011) 704–717.

[15] G. Gelbert, J. Moeck, C. Paschereit, R. King, Control Engineering Practice 20 (2012) 770–782.

[16] P. Huerre, P. Monkevitz, Annual review of fluid mechanics 22 (1990) 473–537.

[17] F. E. Marble, S. Candel, J. Sound Vib. 55 (1977) 225–243.

[18] G. Staffelbach, L. Gicquel, G. Boudier, T. Poinsot, Proc. Combust. Inst. 32 (2009) 2909–2916.

[19] J.O'Connor, T.Lieuwen, Physics of fluids 24 - 075107 (2012).

[20] J. O'Connor, T.Lieuwen, Journal of Engineering for Gas Turbines and Power 134 - 011501 (2012).

[21] N. Worth, J. Dawson, Combustion and Flame (2013, submitted).

[22] L. Crocco, J. American Rocket Society 21 (1951) 163–178.

[23] F. Nicoud, L. Benoit, C. Sensiau, T. Poinsot, AIAA Journal 45 (2007) 426–441.

[24] L. Benoit, F. Nicoud, Int. J. Numer. Meth. Fluids 47 (2005) 849–855.

[25] A. D. Pierce, Acoustics: an introduction to its physical principles and applications, McGraw Hill, New York, 1981.

[26] F. Silva, P. Guillemain, J. Kergomard, B. Mallaroni, A. Norris, Journal of Sound and Vibration 322 (2009) 255–263.

[27] F. Nicoud, T. Poinsot, Combust. Flame 142 (2005) 153–159.

[28] R. Kaess, W. Polifke, T. Poinsot, N. Noiray, D. Durox, T. Schuller, S. Candel, in: Proc. of the Summer Program , Center for Turbulence Research, NASA AMES, Stanford University, USA, pp. 289–302.

[29] P. Wolf, G. Staffelbach, A. Roux, L. Gicquel, T. Poinsot, V. Moureau, C. R. Acad. Sci. Mécanique 337 (2009) 385–394.

[30] M. Helck, M. Howe, Journal of Sound and Vibration 305 (2007) 672–688.

[31] D. Zhao, Combustion and Flame 159 (2012) 2126–2137.

Analytical and numerical study of symmetry breaking in annular combustors to control azimuthal thermo-acoustic oscillations

M. Bauerheim[a], P. Salas[b], J.-F. Parmentier[a], F. Nicoud[c], T. Poinsot[d]

[a]*CERFACS, CFD team, 42 Av Coriolis, 31057 Toulouse, France*
[b]*INRIA Bordeaux - Sud Ouest, HiePACS Project, joint INRIA-CERFACS lab. on High Performance Computing*
[c]*Université Montpellier 2. I3M UMR CNRS 5149*
[d]*IMF Toulouse, INP de Toulouse and CNRS, 31400 Toulouse , France*

Abstract

This study presents an analytical method to study azimuthal modes in annular combustors where N burners are connected to an annular chamber. Flames in each burner are supposed to be compact and are modeled using a Flame Transfer Function (FTF) characterized by a coupling factor and a phase-lag which can differ from burner to burner to analyze the effect of asymmetry on combustion instabilities. When coupling factors are small (weak coupling) a fully analytical resolution is presented, allowing to include non-symmetric situations with an arbitrary number of burners N. First, a symmetric configuration with $N = 3$ identical burners is studied. Only two mode behaviors are observed: 1) The two components of the azimuthal mode have the same frequency and are spinning (degenerate doublets) 2) They are standing and have different frequencies (non-degenerate singlets), the latter being rarely encountered in real engines. For non-symmetric cases, results show that azimuthal modes (doublets) can degenerate into non-degenerate pairs (singlets) if the system's symmetry is changed in a particular way, as mentioned in the literature and recent Helmholtz simulations. A splitting strength measuring the effects of asymmetry is shown to control the degeneracy of the modes. Finally, the effect of symmetry breaking is investigated in a $N = 24$ burners case, representative of industrial gas turbines. Results are compared to experimental observations using CBO (Cylindrical Burner Outlet) which are added to the burners to control combustion instabilities in certain gas turbines by changing the coupling factor and the phase-lag of cer-

tain burners. A simple criterion is derived to provide a necessary condition to stabilize an annular combustor. Results show that symmetry breaking can change the mode behavior but has no real impact on the control of combustion instabilities in the weakly coupled regime.

1. Introduction

Combustion instabilities remain a severe problem in the development of modern gas turbines. Lean premixed combustors, designed to reduce significantly nitric oxides emissions are especially prone to these oscillations which can lead to vibrations and structural damage [1, 2, 3].

These unsteady phenomena come from the interaction between acoustics and heat release fluctuations which act as a volume acoustic source [4]. In annular combustion chambers, these instabilities often take the form of azimuthal modes in the annular cavity perturbed by burners and flames [2, 3, 5, 6, 7, 8].

Industrial engines often have identical burners. Therefore, perfectly axisymmetric configurations have been intensively investigated using theoretical, acoustic and LES tools and more rarely experiments [5, 6, 7, 8, 9, 10, 11, 12]. Annular chambers exhibit specific azimuthal modes. These modes can by standing or spinning in the azimuthal direction [13, 14]. Azimuthal modes are often "degenerate": two modes are found at the same frequency (two counter-rotating spinning modes for example). This property can be affected strongly by symmetry modification and it has a direct effect on the unsteady activity as shown by studies of sound produce by bells [15] where non-degenerate but very close azimuthal modes (also called "non-degenerate singlets") lead to "warble", an undesired modulation due to the coupling of two modes with different but very close frequencies.

The effect of asymmetry on the eigenfrequencies and nature of azimuthal modes in annular chambers is still an open question. Earlier work of Oefelein and Yang [16] focused on symmetry breaking using baffles to prevent combustion instabilities in the F-1 rocket engines. They suggested that asymmetry could add degrees of freedom in the system in order to control unstable modes using passive techniques. Stow and Dowling [17] applied azimuthal variations using Helmholtz resonators on an annular academical test bench.

Similarly, Berenbrink and Hoffmann [18] and Krueger et al. [19] (reviewed by Culick et al. in [20]) broke the symmetry of an annular engine by using CBOs (Cylindrical Burner Outlet, Fig. 1-a) to modify the time-delay τ_i of some of the 24 flames and limit instabilities in a $N = 24$ burners industrial combustor. They varied the number of CBOs installed among the 24 burners showing that adding CBOs always improves stability (Fig. 1-b). However, it was not clear if the stabilization was due to the CBO devices rather than, as argued by the authors to, symmetry breaking in this particular case. Lately, Moeck et al. [21] and Gelbert et al. [22] carried out an annular Rijke experiment with heating grids acting like flames. They introduced circumferential variations through asymmetric power distributions of the grids to modify the azimuthal modes behavior. They noticed that the staging pattern can split degenerate azimuthal modes (doublets) into non-degenerate pairs (singlets) as suggested in [15] for bells if the system's symmetry is changed.
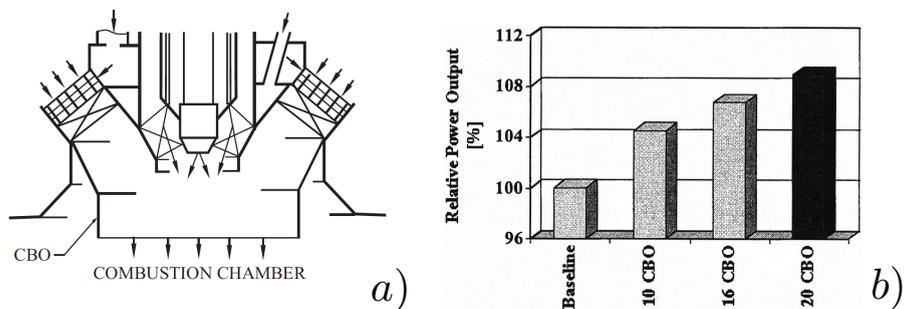
Figure 1: a) Addition of the cylindrical burner outlet (CBO) to the Siemens Hybrid Burner. b) Stability limits for different CBO configurations on a $N = 24$ burners annular gas turbine (Berenbrink and Hoffmann [18])

Recently, theories have been proposed to study the effect of asymmetry on the existence and nature of azimuthal modes (standing, spinning or mixed). In [23], Schuermans et al. suggest that standing modes are observed for low amplitudes but that, at higher amplitudes, one of the two rotating modes eventually dominates. However, Sensiau et al. [14] have shown that even in the linear regime, any change in symmetry can lead to the appearance of one rotating mode dominating the other one: when the rotational symmetry of the configuration is broken, the standing azimuthal mode is changed into two counter-rotating azimuthal modes with different growth rates so that one of them dominates the other. Finally, Noiray et al. [24] have proved that

3

the $2p^{th}$ Fourier coefficient of the heat release, temperature or even acoustic losses azimuthal distribution (where p is the order of the azimuthal mode considered) strongly impacts the frequency as well as the mode nature on an annular rig. Dawson et al. [7, 8] have also shown that the modes nature can result from the interaction with the mean flow by breaking symmetry thanks to clockwise/anti-clockwise swirlers: they observed a strong correlation between the bulk swirl direction and the direction of spin.

Noiray et al. [24] studied analytically asymmetry on a annular rig with a circumferential distribution of heat release, temperature and acoustic losses. However for the sake of simplicity, this annular rig was simplified and contained no burner at all: no study has been conducted on annular chambers connected to burners, a configuration which is more realistic of real gas turbine but more difficult to formulate analytically.

The present paper describes an analytical approach to investigate the effects of symmetry breaking on azimuthal modes in an annular chamber fed by N identical or non-identical burners called BC (Burner+Chamber, Fig. 2). This configuration allows the investigation of asymmetry's effect on eigenfrequencies and nature of circumferential modes. The model is based on a network view of the combustion chamber [5].

This paper is organized as follows: Section 2 briefly describes the principle of the acoustic network model called ATACAMAC ("Analytical Tool to Analyze and Control Azimuthal Modes in Annular Combustors") and how an analytical dispersion relation can be obtained in such a configuration (more details can be found in [5]). In Section 3, analytical calculations of eigenfrequencies are presented for both an unperturbed case (annular cavity alone) and for a general non-symmetric BC configuration (Fig. 2). Section 4 describes the test cases as well as the 3D Helmholtz solver used to validate the ATACAMAC results. Two validation cases are presented : a chamber with $N = 3$ burners and a second one with $N = 24$ burners. In Section 5, ATACAMAC is applied to the BC configuration with $N = 3$ identical burners (Section 5.1) and then $N = 3$ different burners (Section 5.2), highlighting the effect of circumferential patterns on eigenfrequencies and modes nature. The ATACAMAC results are systematically compared to those provided by the 3D acoustic code. Finally, in Section 6, the effects of asymmetry on instabilities are investigated in a $N = 24$ burners configuration typical of real engines. Results are compared to observations made in real gas turbine engines [18, 19].

4
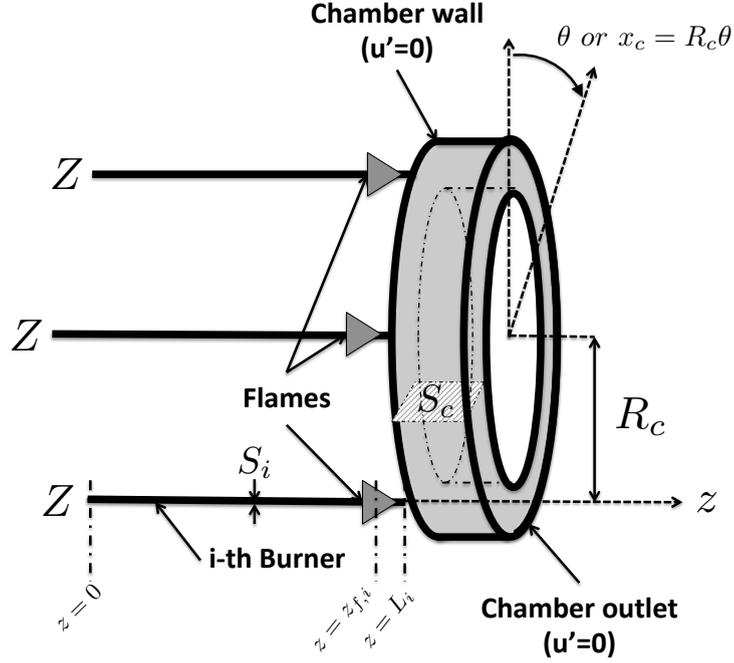
Figure 2: BC configuration to study unstable modes in annular chambers

2. A network model for a BC (Burner+Chamber) non-symmetric configuration

2.1. Model description

This study focuses on a BC (Burners+Chamber) configuration where an annular chamber is fed by N burners (Fig. 2). An impedance Z is imposed at the upstream end of each burner. Mean density and sound speed in the annular chamber are noted ρ^0 and c^0. Mean density and sound speed of the unburnt mixture in the burners are noted ρ_u^0 and c_u^0. The perimeter and the section of the annular chamber are noted $2L_c = 2\pi R_c$ and S_c respectively. The length and section of the ith burner are L_i and S_i. The position along the annular cavity is given by the angle θ defining an abscissa $x_c = R_c\theta$. The location of the flames is similar in all burners and is given by the normalized abscissa $\alpha = z_{f,i}/L_i$ (Fig. 2)

This model is limited to situations where pressure fluctuations depend on the angle θ (or x) but not on the axial direction z in the chamber (they depend on the coordinate z only in the burners). This case can be observed in

5

combustors terminating in choked nozzles which behave almost like a rigid wall (i.e. $u' = 0$ under the low upstream Mach number assumption [25]). Since the chamber inlet is also close to a velocity node, modes which have no variation along z can develop in the chamber, as shown by recent LES in real engines [26].

Parmentier et al. [5] have introduced a simple analytical methodology called ATACAMAC (for Analytical Tool to Analyze and Control Azimuthal Modes in Annular Combustors) to predict the frequency and the structure of modes in such a configuration for a specific mode (i.e. for a given mode order p, asymmetry and number of burners N). No general background on stability for asymmetric BC configuration can be found in the literature. This paper proposes to demonstrate the analytical expression of eigenfrequencies for a general asymmetric case for any mode order p and any number of burners N in order to obtain general rules on stability for annular combustors. Results on structure and nature of azimuthal modes (spinning, standing or mixed) will be derived using this analytical study to show how asymmetry can promote specific modes and modify instabilities as described in the literature [7, 8, 21, 22, 24].

2.2. ANR methodology to obtain the analytical dispersion relation of asymmetric annular combustors

To reduce the size of the system, the ANR (Annular Network Reduction) methodology proposed in [6] is applied: the full annular combustor is split into N sectors which differ only via the burner/chamber junction (Figs. 3 and 4). Between each sector, a free propagation of azimuthal waves occurs and can be modeled by a transfer matrix R_i as proposed in [5] (Fig. 4, propagation):

$$\begin{bmatrix} R_i \end{bmatrix} = \begin{bmatrix} w & 0 \\ 0 & \frac{1}{w} \end{bmatrix} \tag{1}$$

where $w = e^{2jkL_c/N}$.

The area where acoustic interaction between the ith burner and the annular chamber occurs (--- in Fig. 3, top right) was investigated by O'Connor et al. [27, 28, 29] and can be assumed compact. As shown in Fig. 5, using the equations of acoustic propagation in the cold ($0 < z < \alpha L_i$) and hot ($\alpha L_i < z < L_i$) parts of the burner as well as the jump conditions through the ith flame ($z = \alpha L_i$), the effect of the whole i^{th} burner on the annular chamber

6
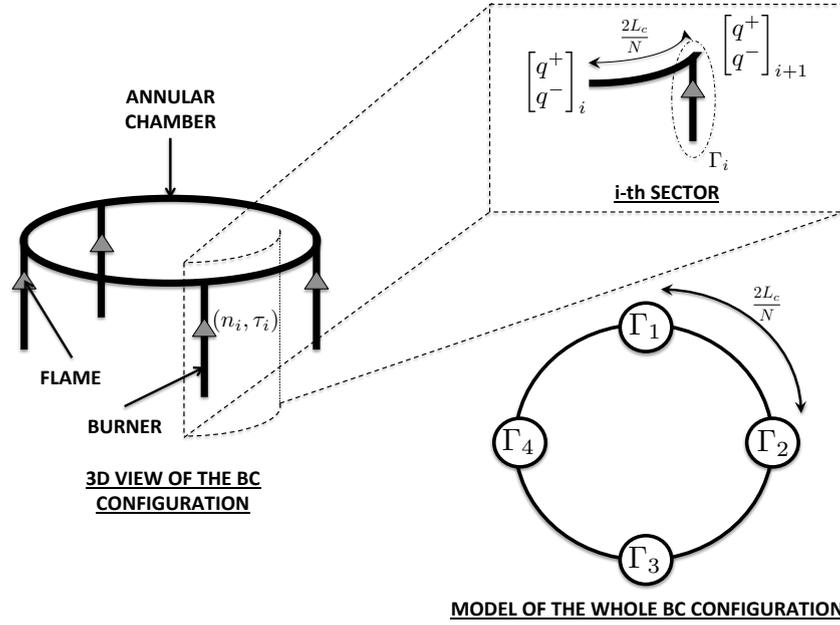
Figure 3: 3D view of a BC configuration with $N = 4$ burners (left), zoom on the ith sector (top right) and model of the whole BC configuration (bottom right) where Γ_i represents the burner/chamber interaction [5]
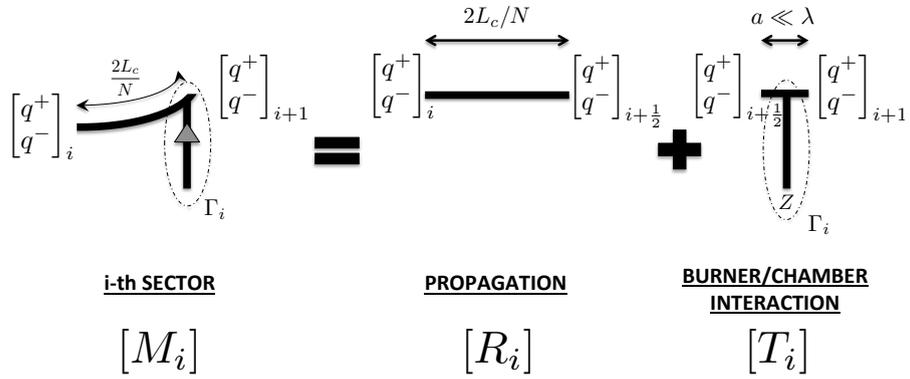
Figure 4: ANR methodology: each sector is decomposed into a free propagation of azimuthal waves (characteristic length $2L_c/N$) and a compact burner/chamber interaction (characteristic length $a \ll \lambda$) modeled by the coupling parameter Γ_i

7

can be reduced to a translated impedance $Z_{tr}(Z, \alpha, Li, n_i, \tau_i) = \frac{p'_{b,i}(z=L_i)}{\rho^0 c^0 u'_{b,i}(z=L_i)}$ [6, 30]:

$$Z_{tr} = \frac{\mathbb{F}S_{1-\alpha}^k[jC_\alpha^{k_u} - S_\alpha^{k_u}Z] + C_{1-\alpha}^k[C_\alpha^{k_u}Z + jS_\alpha^{k_u}]}{\mathbb{F}C_{1-\alpha}^k[jS_\alpha^{k_u}Z + C_\alpha^{k_u}] + S_{1-\alpha}^k[jC_\alpha^{k_u}Z - S_\alpha^{k_u}]} \tag{2}$$

where $\mathbb{F} = \frac{c^0\rho^0}{c_u^0\rho_u^0}(1 + n_i e^{j\omega\tau_i})$, $C_x^y = cos(xyL_i)$, $S_x^y = sin(xyL_i)$, $k = \omega/c^0$ and $k_u = \omega/c_u^0$.

Equivalent impedance of the whole i-th burner
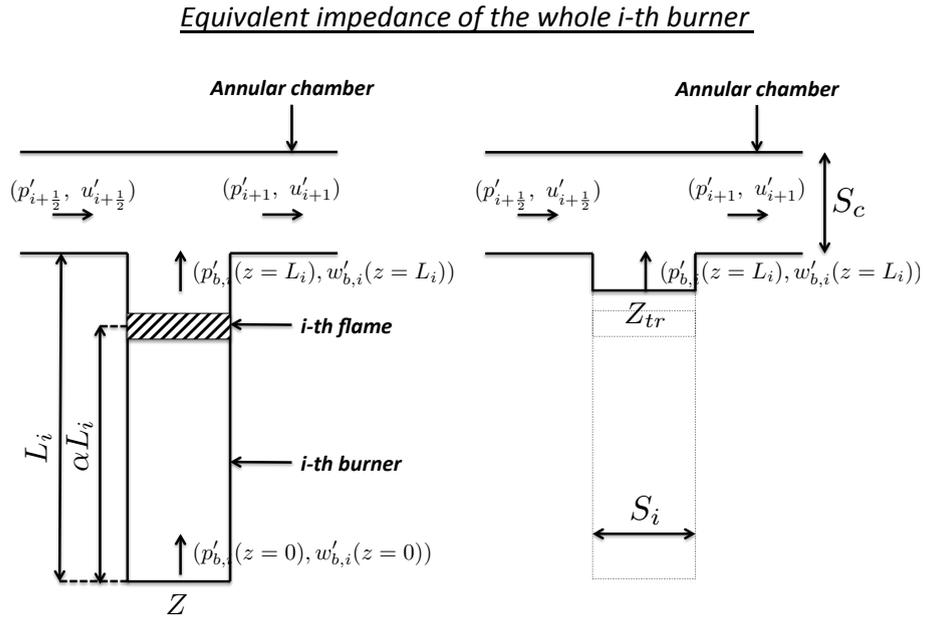
Figure 5: Equivalent impedance of the whole i-th burner (which includes the ith active flame) near the burner/chamber interaction zone (Fig. 4). The translated impedance Z_{tr} takes into account the upstream impedance Z, the propagation in the cold ($0 < z < \alpha L_i$) and hot ($\alpha L_i < z < L_i$) part of the burner as well as the active flame via the Flame Transfer Function (n_i, τ_i)

The jump conditions at the burner/chamber junction at null Mach number read [31, 32]:

$$p'_{i+\frac{1}{2}} = p'_{i+1} = p'_{b,i}(z = L_i) \tag{3}$$

8

$$u'_{i+\frac{1}{2}}S_c + \underbrace{u'_{b,i}(z = L_i)}_{=\frac{p'_{i+\frac{1}{2}}}{\rho^0 c^0 Z_{tr}}} S_i = u'_{i+1}S_c \qquad (4)$$

Consequently, a transfer matrix T_i^* for the interaction part of Fig. 4 can be deduced:

$$\begin{bmatrix} p' \\ \rho^0 c^0 u' \end{bmatrix}_{i+1} = \begin{bmatrix} T_i^* \end{bmatrix} \begin{bmatrix} p' \\ \rho^0 c^0 u' \end{bmatrix}_{i+\frac{1}{2}} = \begin{bmatrix} 1 & 0 \\ 2j\Gamma_i & 1 \end{bmatrix} \begin{bmatrix} p' \\ \rho^0 c^0 u' \end{bmatrix}_{i+\frac{1}{2}} \qquad (5)$$

where the coupling parameter Γ_i [5, 6, 33, 34] (Fig. 4, burner/chamber interaction) is directly linked to the equivalent admittance of the whole i^{th} burner ($Y_{tr} = 1/Z_{tr}$):

$$\Gamma_i = -\frac{j}{2}\frac{S_i}{S_c}Y_{tr}(Z, \alpha, Li, n_i, \tau_i) \qquad (6)$$

When a velocity node ($Z = \infty$) or a pressure node ($Z = 0$) is imposed at the upstream end of each burner and flames are located at the burner/chamber junction ($\alpha = 1$), these coupling parameters reduce to (from [5] or using Eqs. (2) and (6)):

$$\Gamma_i = \frac{1}{2}\frac{S_i\rho^0 c^0}{S_c\rho_u^0 c_u^0}tan(k_u L_i)\left(1 + n_i e^{j\omega\tau_i}\right) \quad (Z = \infty) \qquad (7)$$

$$\Gamma_i = -\frac{1}{2}\frac{S_i\rho^0 c^0}{S_c\rho_u^0 c_u^0}cotan(k_u L_i)\left(1 + n_i e^{j\omega\tau_i}\right) \quad (Z = 0) \qquad (8)$$

where $k_u = \frac{\omega}{c_u}$ and (n_i, τ_i) are the interaction index and the time-delay of the FTF for the ith flame [35].

Finally, in Eq. (5) the transfer matrix T_i^* is recast to use characteristic waves $q^{\pm} = p' \pm \rho^0 c^0 u'$ instead of the primitive variables p' and u' and leads to the definition of the matrix T_i:

$$\begin{bmatrix} T_i \end{bmatrix} = \begin{bmatrix} 1 + j\Gamma_i & j\Gamma_i \\ -j\Gamma_i & 1 - j\Gamma_i \end{bmatrix} \qquad (9)$$

From Fig. 4 and [5], the transfer matrix of the ith sector M_i is:

$$\begin{bmatrix} q^+ \\ q^- \end{bmatrix}_{i+1} = \underbrace{\begin{bmatrix} T_i \end{bmatrix} \begin{bmatrix} R_i \end{bmatrix}}_{M_i} \begin{bmatrix} q^+ \\ q^- \end{bmatrix}_i \qquad (10)$$

9

Using the periodicity of the system (i.e. $\begin{bmatrix} q^+ \\ q^- \end{bmatrix}_{N+1} = \begin{bmatrix} q^+ \\ q^- \end{bmatrix}_1$) and the equation of one sector (Eq. (10)) leads to:

$$\left(\prod_{i=N}^{1} M_i \right) \begin{bmatrix} q^+ \\ q^- \end{bmatrix}_1 = \begin{bmatrix} q^+ \\ q^- \end{bmatrix}_1 \tag{11}$$

The system defined by Eq. (11) has non-trivial solutions only if its determinant is null. Therefore, the ANR methodology provides an implicit analytical dispersion relation for the pulsation ω for a general non-symmetric BC configuration:

$$det \left(\prod_{i=N}^{1} M_i - I_d \right) = 0 \tag{12}$$

where I_d is the 2-by-2 identity matrix.

3. Analytical calculation of eigenfrequencies and mode structures in several annular configurations

The analytical dispersion relation (Eq. 12) allows to study symmetry breaking by investigating the effects of the burners responses (measured by the N parameters Γ_i, $i \in [1, N]$) on the growth rate and the nature of azimuthal modes. Several configurations are investigated (Fig. 6) to understand the effect of symmetry breaking on combustion instabilities.

3.1. Analytical calculation of eigenfrequencies and modes nature in an unperturbed annular cavity (without burners and flames)

First, an annular chamber with no burner (i.e. $\Gamma_i = 0$, $\forall i \in [1, N]$) is studied (Fig. 6, top left). The transfer matrix of each sector (Eq. (10)) reduces to $M_i = R_i$ ($T_i = I_d$): only azimuthal propagation occurs. Consequently Eq. (11) reduces to:

$$\begin{bmatrix} w^N & 0 \\ 0 & \frac{1}{w^N} \end{bmatrix} \begin{bmatrix} q^+ \\ q^- \end{bmatrix}_1 = \begin{bmatrix} q^+ \\ q^- \end{bmatrix}_1 \tag{13}$$

The dispersion relation is therefore $w^N = 1$ where $w = e^{2jkL_c/N}$. Solutions of Eq. (13) are roots of unity $w_0 = e^{2jp\pi/N}$ and leads to real eigenfrequencies of the unperturbed problem:

$$kL_c = p\pi \text{ so that } f = \frac{pc_0}{2L_c}, \ \forall p \in \mathbb{N} \tag{14}$$

10
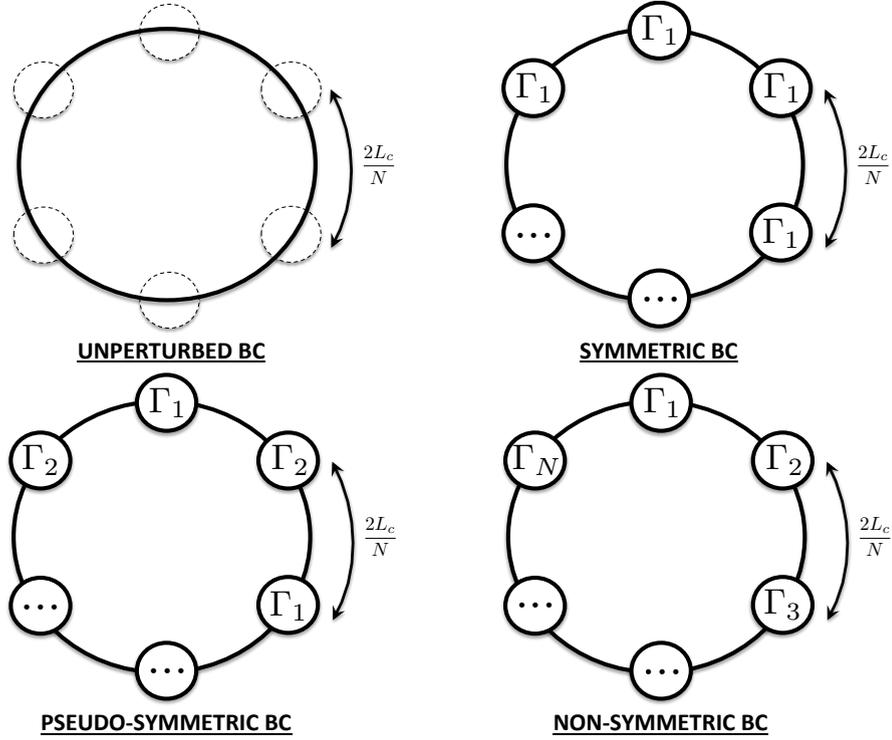
Figure 6: Typical configurations: Unperturbed (top left), symmetric with identical burners (top right), pseudo-symmetric configuration (bottom left) and the general non-symmetric configuration (bottom right)

The equation of the system (Eq. (13)) also provides analytical eigenvectors V associated to the eigenfrequencies f (Eq. (14)). In this situation, the generated eigenspace $\{V\}$ is two-dimensional: all azimuthal modes are degenerated and can be either standing, spinning or mixed. All modes are neutral (zero growth rate: Im(f)=0).

3.2. Analytical calculation of eigenfrequencies in a symmetric BC configuration with actives flames in the low-coupling limit

Real engines often have identical sectors with the same burners and flame dynamics (i.e. the same FTF parameters $(n_i,\ \tau_i)$) and therefore the coupling parameters Γ_i and the transfer matrices M_i are the same.

In such a configuration, Parmentier et al. [5] have solved the problem for

11

$N = 1$, $N = 2$ and $N = 4$ burners assuming low coupling parameters:

$$\Gamma_i \ll 1, \ \forall i \in [1, N] \qquad (15)$$

Under this low coupling assumption, the system is supposed to be close to the unperturbed problem (Section 3.1) and an asymptotic solution can be obtained for the wavenumber perturbations ϵ^+ and ϵ^-:[1]

$$w^\pm = (1 + \mathcal{E}^\pm)w_0 + o(\mathcal{E}^\pm) \ \text{ i.e. } \ kL_c = p\pi + \epsilon^\pm \qquad (16)$$

where $w^\pm = e^{2j(p\pi + \epsilon^\pm)/N}$ and $w_0 = e^{2jp\pi/N}$ is the solution of the unperturbed problem and corresponds to $kL_c = p\pi$ where p is the mode order, $\mathcal{E}^\pm = 2j\frac{\epsilon^\pm}{N}$ and $j^2 = -1$.

For instance, Parmentier et al. [5] proved that the two eigenwaves V^+ and V^- of the first order azimuthal mode ($p = 1$) in the annular chamber with $N = 4$ identical burners share the same frequency and growth rate (i.e. the mode is degenerated ($f^+ = f^-$) and the growth rate corresponds to the imaginary part of the complex frequency $f^\pm$):

$$\epsilon^\pm = -2\Gamma^0 \text{ so that } Im(f^\pm) = -\frac{c^0}{\pi L_c}Im(\Gamma^0) \propto n\sin(\omega^0\tau) \qquad (17)$$

where Γ^0 is the value of $\Gamma_i^\pm$ when $\omega^\pm = \omega^0 = \frac{pc^0\pi}{L_c}$ and $(n, \ \tau)$ are the FTF parameters, identical for all burners.

3.3. Analytical calculation of eigenfrequencies in a non-symmetric BC configuration with active flames in the low-coupling limit

Using a symmetric combustor with non-identical burners is a promising approach for controlling azimuthal modes. This study proposes the full analytical resolution of all eigenfrequencies of a non-symmetric configuration (Fig. 6, bottom right) using the implicit analytical dispersion relation (Eq. (12)). Since all burners can be different, all coupling parameters Γ_i (Eq. (6)) can be different.

---

[1]The two components V^+ and V^- of the azimuthal mode have not necessarily the same wavenumber perturbation $\epsilon^\pm$. Therefore the notation $w^\pm$ is used since the azimuthal propagation of waves w depends on the wavenumber perturbation $\epsilon^\pm$.

Assuming small coupling parameters (Eq. (15)), a Taylor expansion of the transfer matrix of the whole system $(M = \prod_{i=N}^{1} T_i R_i)$ at the second order is performed[2]:

$$M = \begin{bmatrix} w^N[1 + jS - Q(1)] + Q(w) + o(\Gamma_i^2) & j\sum_{i=1}^{N} \Gamma_i \left(\frac{1}{w}\right)^{N-2i+2} + o(\Gamma_i) \\ -j\sum_{i=1}^{N} \Gamma_i w^{N-2i+2} + o(\Gamma_i) & \frac{1}{w^N}[1 - jS - Q(1)] + Q(\frac{1}{w}) + o(\Gamma_i^2) \end{bmatrix}$$

(18)

where

$$\begin{cases} S = \sum_{i=1}^{N} \Gamma_i \\ Q(x) = \sum_{i=1}^{N-1} \sum_{j=i+1}^{N} \Gamma_i \Gamma_j x^{N-2(j-i)} \end{cases}$$

(19)

From Eq. (18), the dispersion relation at second order is:

$$det\,(M - Id) = -\frac{w^{2N} - 2w^N + 1}{w^N} - \frac{jS(w^{2N} - 1)}{w^N}$$

$$+ \sum_{i=1}^{N-1} \sum_{j=i+1}^{N} \Gamma_i \Gamma_j [w^{2N} - w^{N-2(j-i)} - w^{2(j-i)} + 1] + o(\Gamma_i^2)$$ (20)

Under the low coupling assumption (Eq. (15): $\Gamma_i \ll 1, \forall i \in [1, N]$), the system is supposed to be close to the unperturbed problem [5]: $kL_c = p\pi + \epsilon^{\pm}$ or $w^{\pm} = (1 + \mathcal{E}^{\pm})w_0$ where $\mathcal{E}^{\pm} = 2j\frac{\epsilon^{\pm}}{N}$ and $w_0 = e^{2jp\pi/N}$ (Eq. (16)). The coupling parameters $\Gamma_i^{\pm}$ also depend on the frequency and therefore on $\epsilon^{\pm}$ and can be approximated by:

$$\Gamma_i^{\pm}(\omega) = \underbrace{\Gamma_i^{\pm}(\omega = \omega^0)}_{\Gamma_i^0} + \frac{2j\epsilon^{\pm}\omega^0}{N} \underbrace{\left(\frac{\partial \Gamma_i^{\pm}}{\partial \omega}\right)_{\omega = \omega^0}}_{\Gamma_i^1} + o(\epsilon)$$

(21)

where $\omega^0 = \frac{p\pi c^0}{L_c}$ corresponds to the angular frequency of the unperturbed BC configuration (Section 3.1).

Consequently, a Taylor expansion at second order ($o(\epsilon^2)$ knowing that $\Gamma_i^0 \simeq \epsilon^{\pm}$)[3] of Eq. (20) is performed:

---

[2]A first-order Taylor expansion of extra-diagonal terms which have no zero order term is sufficient to compute a second-order dispersion relation $det(M - Id)$. The Landau notation $o(x)$ called "little-o" is used to designate any quantity negligible compared to x.

[3]The analytical resolution of the dispersion relation will lead to the solution $\epsilon^{\pm} \propto \Gamma_i^0$ which proves that Γ_i^0 is a first order term and $\Gamma_i^0 \Gamma_j^0$ or $\Gamma_i^0 \epsilon^{\pm}$ are second order terms.

$$A - 4B\epsilon^{\pm} + 4C\epsilon^{\pm 2} = 0 \tag{22}$$

where

$$
\begin{cases}
A = - \left[w_0^{2N} - 2w_0^N + 1 \right] - j\Sigma_0 \left[w_0^{2N} - 1 \right] \\
\qquad + \sum_{i=1}^{N-1} \sum_{j=i+1}^{N} \Gamma_i^0 \Gamma_j^0 \left[w_0^{2N} - w_0^{N-2(j-i)} - w_0^{2(j-i)} + 1 \right] \\
B = \frac{j}{2} [w_0^{2N} - 1] \left[1 + \frac{\Sigma_1}{N} \right] - \frac{\Sigma_0}{2} [w_0^{2N} + 1] \\
C = \frac{1}{N^2} \left[\binom{N}{N-2} w_0^{2N} + \binom{N+1}{N-1} \right]
\end{cases}
\tag{23}
$$

where $\Sigma_0 = \sum_{i=1}^{N} \Gamma_i^0$ and $\Sigma_1 = \sum_{i=1}^{N} \Gamma_i^1$, knowing that $\Gamma_i^{\pm}(\omega) \simeq \Gamma_i^0 + \frac{2j\epsilon^{\pm}}{N}\Gamma_i^1$ (see Eq. (21)).

Eigenfrequencies are deduced from the quadratic equation Eq. (22):

$$\epsilon^{\pm} = \frac{B \pm \sqrt{B^2 - AC}}{2C} \tag{24}$$

From Section 3.1, $w_0^N = 1$ which leads to simplifications of coefficients A, B and C:

$$
\begin{cases}
A = 4 \sum_{i=1}^{N-1} \sum_{j=i+1}^{N} \Gamma_i^0 \Gamma_j^0 \left[\sin\left(\frac{2p\pi}{N}(j-i) \right) \right]^2 \\
B = -\Sigma_0 \\
C = 1
\end{cases}
\tag{25}
$$

Finally, a simple expression of the wavenumber perturbations is obtained for a general non-symmetric BC configuration from Eq. (24):

$$\epsilon^{\pm} = -\frac{1}{2}\left(\Sigma_0 \pm \sqrt{\Sigma_0^2 - A} \right) \tag{26}$$

where $\Sigma_0 = \sum_{i=1}^{N} \Gamma_i^0$ and A is the non-symmetric part defined in Eq. (25) depending on the number of burners N and the mode order p.

A splitting strength $\mathcal{S}_0 = \sqrt{\Sigma_0^2 - A}$ appears in Eq. (26) which can be recast for simplification:

$$\mathcal{S}_0^2 = \Sigma_0^2 - A = \sum_{i,j=1}^{N} \Gamma_i^0 \Gamma_j^0 cos\left(\frac{4p\pi}{N}(j-i) \right) \tag{27}$$

14

Eq. (26) is a generalization of Parmentier et al. [5] results (Tab. 1). It shows that the splitting strength $\mathcal{S}_0$ controls the nature of the modes: if $\mathcal{S}_0 = 0$ modes are degenerate (i.e. $\epsilon^+ = \epsilon^-$ leading to $\epsilon^\pm = -\frac{1}{2}\Sigma_0$ as obtained for a symmetric combustor ($\Gamma_i = \Gamma$, Section 3.2)) and if $\mathcal{S}_0 \neq 0$, they are not.

Sym/Asym	Order p	Pattern	Solution
$N = 1$ **burner**			
Symmetric	$1, 2$	(Γ_1)	$\epsilon^- = 0$ and $\epsilon^+ = -\Gamma_1^0$
$N = 2$ **burners**			
Symmetric	$1, 2$	(Γ_1, Γ_1)	$\epsilon^- = 0$ and $\epsilon^+ = -2\Gamma_1^0$
Asymmetric	$1, 2$	(Γ_1, Γ_2)	$\epsilon^- = 0$ and $\epsilon^+ = -\Gamma_1^0 - \Gamma_2^0$
$N = 4$ **burners**			
Symmetric	1	$(\Gamma_1, \Gamma_1, \Gamma_1, \Gamma_1)$	$\epsilon^\pm = -2\Gamma_1^0$ **(DD)**
Asymmetric A	1	$(\Gamma_1, \Gamma_2, \Gamma_1, \Gamma_2)$	$\epsilon^- = -2\Gamma_1^0$ and $\epsilon^+ = -2\Gamma_2^0$
Asymmetric B	1	$(\Gamma_1, \Gamma_1, \Gamma_2, \Gamma_2)$	$\epsilon^\pm = -\Gamma_1^0 - \Gamma_2^0$ **(DD)**

Table 1: Results from Parmentier et al. [5] on frequencies of a symmetric and non-symmetric BC configurations with several numbers of burners N. **(DD)** refers as Degenerate Doublet (i.e. eigenwaves $V^\pm$ have the same wavenumber perturbation ϵ).

A summary of this analytical method providing the stability map of the pth azimuthal mode in a chamber with N burners is given in Appendix A.

4. Validation in a simplified multi-burner annular chamber

Analytical expressions of eigenfrequencies (Eq. (26)) of azimuthal modes are compared here to results obtained with AVSP [36], a full 3D Helmholtz solver for the case of a simplified 3D BC configuration with $N = 3$ burners (Section 5). A $N = 24$ burners configuration (Section 6), more representative of real engines, is also considered to investigate the effect of symmetry breaking on instabilities.

4.1. Description of the academic BC configurations

The 3D geometries correspond to a BC setup with $N = 3$ or $N = 24$ burners (Fig. 7) similar to Fig. 2 (physical and geometrical parameters are defined in Tab. 2). The burner/chamber interfaces are placed at $z = 0$ and the flames are on the burner side. The flame width is equal to $2\ mm$
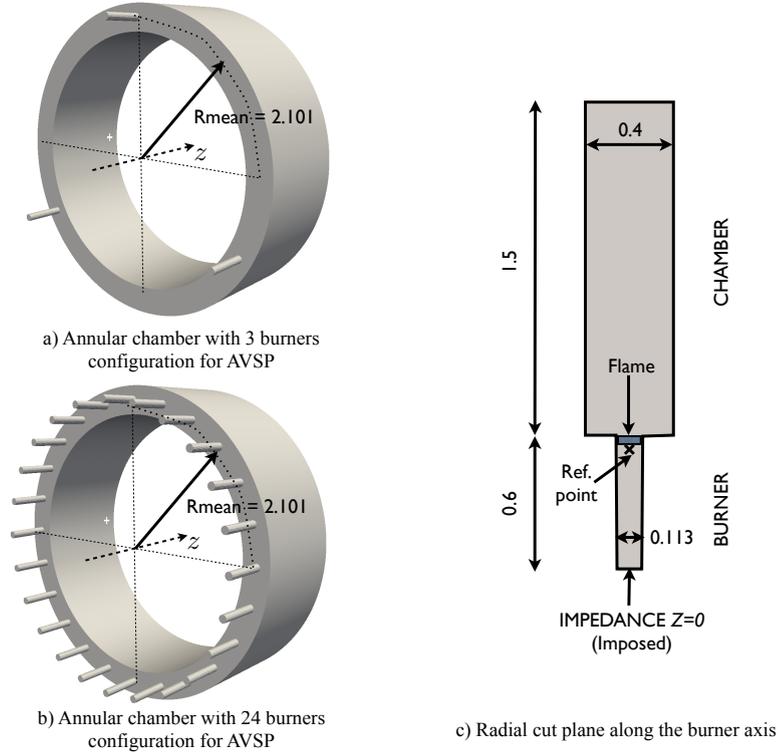
Figure 7: Toy-model to validate the ATACAMAC methodology. (a) Perfect annular chamber with $N = 3$, (b) $N = 24$ cylindrical burners, (c) burner/chamber configuration

which guarantees its compacity with respect to the acoustic waves length. Boundary conditions correspond to impermeable walls everywhere except at the upstream end of burners where an impedance $Z = 0$ (i.e. $p' = 0$) is imposed to mimic a connection to a large plenum. For the $N = 3$ burners configuration, two cases are investigated (Tab. 3): first with identical burners and then with two types of burners with different time-delays τ_1 and τ_2. The interaction index of flames is set to the same value $n = 1.0$ (knowing that typical values for n are around $\frac{T^0}{T^0_u} - 1 \simeq 1.57$ here) in every burner.

For the $N = 24$ configuration (Fig. 7), two types of burners with different time-delays are mixed to mimic the CBO/noCBO burners (Cylindrical Burner Outlet) [18, 19]. Tab. 3 displays the circumferential patterns ($\bullet$ for CBO buners and $\circ$ for burners without CBO) which are considered.

16

Chamber			
Half perimeter	L_c	6.59	m
Section	S_c	0.6	m^2
Burner			
Number	N	3 or 24	$-$
Length	L_i^0	0.6	m
Section	S_i	0.01	m^2
Fresh gases			
Mean temperature	T_u^0	700	K
Mean density	ρ_u^0	9.79	kg/m^3
Mean sound speed	c_u^0	743	m/s
Burnt gases			
Mean temperature	T^0	1800	K
Mean density	ρ^0	3.81	kg/m^3
Mean sound speed	c^0	1191	m/s
Flame parameters			
Interaction index	n_i	1.0	$-$
Time-delay	τ_i	$variable$	s

Table 2: Parameters used for numerical applications. They correspond to a typical large scale industrial gas turbine.

4.2. Description of the 3D acoustic code

Assumptions and results made in ATACAMAC formulation can be validated using a full 3D acoustic solver called AVSP which solves the Helmholtz equation in a reactive flow without the assumptions used in ATACAMAC [36]. AVSP takes into account the interaction between combustion and acoustics in an active way. It solves the eigenvalue problem issued from the discretization on unstructured meshes of the Helmholtz equation. Meshes are composed of approximately 2 millions cells for both the $N = 3$ and $N = 24$ configurations which is sufficient considering the simplicity of the geometry and the wavelength of the modes considered her. Source terms due to the flames are added and modeled here using Flame Transfer Functions (FTF) [35]. The local heat release fluctuations are expressed in the burner i as:

$$q_i' = n_{u,i}\, e^{j\omega\tau_i}\, \vec{u}'(\mathbf{x}_{ref,i}) \cdot \vec{n}_{ref,i}. \tag{28}$$

The local interaction index $n_{u,i}$ describes the local flame-acoustic inter-

Name	N	CBO	Asymmetry pattern
B3_C0	3	0	○ ○ ○
B3_C1	3	1	○ ● ○
B24_C0	24	0	○○○○○○○○○○○○○○○○○○○○○○○○
B24_C20_P1	24	20	●●●●●●●○○●●●●○○●●●●●●●●
B24_C20_P2	24	20	●●●●●●●●●○○○○●●●●●●●●●
B24_C20_P3	24	20	●●●●●○●●●●●○●●●●●○●●●●●○
B24_C20_P4	24	20	●●●●●○●●●●●○●●●●●●○●●●●●○
B24_C24	24	24	●●●●●●●●●●●●●●●●●●●●●●●●

Table 3: BC configurations investigated with both the 3D Helmholtz solver AVSP and the analytical approach ATACAMAC. ○: Burner without CBO ●: Burner with CBO

actions. The values of $n_{u,i}$ are assumed to be constant in the flame zone i (Fig. 7) and are chosen to recover the global value of the interaction index n_i corresponding to the infinitely thin flame when integrated over the flame zone i [36]. For the sake of simplicity, they are assumed to be independent of frequency.

In annular configurations with multiple burners, heat release fluctuations in the burner i are supposed to be driven by the velocity fluctuations at the reference point $\mathbf{x_{ref,i}}$. This assumption, called ISAAC (Independence Sector Assumption in Annular Combustor) in [14] was validated by an LES of a full annular combustor [11] and is used in the present study. In the infinitely thin flame model used in ATACAMAC the reference points are chosen at the flame locations $z_{f,i}$. The normalized abscissa of the flame is set to $\alpha \simeq 0.91$ to take into account corrections on burner's length. Indeed, in the low frequency range, 3D effects near the burner/chamber junctions can be accounted for [37] with a standard length correction for a flanged tube [38] which is applied at the downstream burner's end ($\Delta L_i = 0.4\sqrt{4S_i/\pi}$). In AVSP, the reference points are placed a few millimeters upstream of the flames (Fig. 7).

5. Comparison of symmetric and non-symmetric BC configurations with $N = 3$ burners

Analytical expressions of frequency of azimuthal modes (Eq. (26)) have been obtained for a general annular BC configuration with N burners. First, the symmetric case (Fig. 8, left) with $N = 3$ identical burners will be studied

(Section 5.1). Then, the effect of circumferential variations on combustion instabilities will be investigated (Section 5.2) and validated on an asymmetric BC configuration with $N = 3$ different burners (Fig. 8, right).


Figure 8: Schematic view of the BC configuration with $N = 3$ burners for the validation of numerical and analytical resolutions of Eq. (12): symmetric case (left, all interactions terms Γ_i (Eq. (6)) are equal) and asymmetric case (right, two identical burners with the same Γ_1 and one burner with Γ_2)

5.1. Analysis of the symmetric case and application to a combustor with $N = 3$ identical burners

In an axisymmetric configuration where burners are the same for all sectors (i.e. $\Gamma_i = \Gamma, \forall i \in [1, N]$), only two different behaviors exist. Indeed, the splitting strength $\mathcal{S}_0$ in Eq. (27) simplifies depending on the mode order p and the number of burners N:

$$\begin{cases} \text{If } p = \frac{mN}{2} = \frac{3m}{2}, \ \forall m \in \mathbb{N} : \ \mathcal{S}_0 = N\Gamma^0 = 3\Gamma^0 \\ \text{For any other mode of order } p : \ \mathcal{S}_0 = 0 \end{cases} \tag{29}$$

Consequently, only two different classes of modes can develop in annular BC configurations with $N = 3$ identical burners:

- **Non-degenerate singlets:** If $p = \frac{mN}{2} = \frac{3m}{2}$, $\forall m \in \mathbb{N}$ (only $p = mN$ exists in BC cases with odd number of burners N like this case with $N = 3$) the splitting strength is not null ($\mathcal{S}_0 = \Sigma_0 = 3\Gamma^0$, Eq. (27)) and the azimuthal mode is split into two components V^- and V^+ with different wavenumber perturbations and frequencies:

$$\begin{cases} \epsilon^- = 0 \\ \epsilon^+ = -N\Gamma^0 = -3\Gamma^0 \end{cases} \tag{30}$$

19

Consequently, due to symmetry considerations, these modes (e.g. p=3) can lock on burners ($N = 3$). The first wave V^- is standing and imposes a pressure node at every burner: therefore it is unperturbed by them ($\epsilon^- = 0$); the wave is neutral. The second wave V^+ is also standing but imposing a velocity node (i.e. a pressure anti-node) at every burner ($\epsilon^+ = -3\Gamma^0$): the mode is highly perturbed by burners.

- **Degenerate doublets:** All other azimuthal modes ($p \neq \frac{mN}{2} = \frac{3m}{2}$, $\forall m \in \mathbb{N}$) are composed of two eigenwaves $V^{\pm}$ which have the same frequencies (degenerate modes) because $\mathcal{S}_0 = 0$:

$$\begin{cases} \epsilon^- = -\frac{N}{2}\Gamma^0 = -\frac{3}{2}\Gamma^0 \\ \epsilon^+ = -\frac{N}{2}\Gamma^0 = -\frac{3}{2}\Gamma^0 \end{cases} \tag{31}$$

In this configuration, the transfer matrix of the whole system (M defined in Eq. (18)) is equivalent to the null matrix. The mode nature is undetermined as pointed out in [24]: a standing, spinning or mixed mode can develop. Noiray et al. [24] have shown that non-linearities on the FTF can however promote one of these natures, a phenomenon which cannot be described by ATACAMAC with classical FTFs.

A validation of this symmetric case is displayed in Fig. 9 (waves denoted $A^{\pm}$ where $\tau_1 = \tau_2 = 2.5\ ms$) and Fig. 10 (waves denoted $E^{\pm}$ where $\tau_1 = \tau_2 = 7.5\ ms$). A good agreement of the frequencies f^+ and f^- of the first azimuthal mode ($p = 1$) is obtained between the acoustic code (AVSP) and ATACAMAC. Note that this symmetric case always corresponds to maximum absolute values of the growth rate: $Im(f) \simeq +0.40\ s^{-1}$ (waves $A^{\pm}$, Fig. 9) and $Im(f) \simeq -0.39\ s^{-1}$ (waves $E^{\pm}$, Fig. 10)

5.2. Analysis of the asymmetric case and application to a combustor with N = 3 different burners

This section discusses the behavior of azimuthal modes when one of the three burners has a different FTF (different value of Γ_i^0, see Fig. 8 right). Especially, the observation made in [15, 14] will be investigated: circumferential variations with specific patterns could split nominally degenerate doublets into non-degenerate singlets. For instance, a standing azimuthal mode can be changed into two counter rotating spinning modes with different growth rates [14]. If two burners have a coupling factor Γ_1^0 and the third one Γ_2^0, Eq. (26) can be solved with $N = 3$ and gives the following solution:

20

- **Non-degenerate singlets:** Azimuthal modes with $p = \frac{mN}{2} = \frac{3m}{2}$, $\forall m \in \mathbb{N}$ are non-degenerate singlets characterized by $\mathcal{S}_0 = \Sigma_0 = 2\Gamma_1^0 + \Gamma_2^0$ (Eq. (27)) with wavenumber perturbations:

$$\begin{cases} \epsilon^- = 0 \\ \epsilon^+ = -\Sigma_0 = -2\Gamma_1^0 - \Gamma_2^0 \end{cases} \tag{32}$$

where $\Sigma_0 = \sum_{i=1}^{N} \Gamma_i^0$.

These modes, as in the symmetric cases, impose a pressure node or pressure anti-node at each burner location leading to an unperturbed standing wave ($\epsilon^- = 0$) or a highly perturbed standing wave ($\epsilon^+ = -\Sigma_0 = -2\Gamma_1^0 - \Gamma_2^0$).

- **Nearly degenerate singlets:** For other azimuthal modes ($p \neq \frac{mN}{2} = \frac{3m}{2}$, $\forall m \in \mathbb{N}$), Eq. (26) leads to nearly degenerate singlets [15]: the degenerate doublet encountered in symmetric configurations (denoted DD with $\epsilon_{DD} = -\frac{1}{2}\Sigma_0 = -\Gamma_1^0 - \frac{1}{2}\Gamma_2^0$, Eq. (31)) is split depending on the splitting strength $\mathcal{S}_0 = \Gamma_1^0 - \Gamma_2^0$ (Eq. (27) for the $N = 3$ case with the pattern 121 ($\circ \bullet \circ$, Tab. 3)):

$$\epsilon^{\pm} = \underbrace{-\frac{1}{2}\Sigma_0}_{\epsilon_{DD}} \pm \underbrace{\frac{1}{2}\mathcal{S}_0}_{\text{Splitting}} \tag{33}$$

$$\epsilon^- = -\frac{1}{2}\left(\Gamma_1^0 + 2\Gamma_2^0\right) \text{ and } \epsilon^+ = -\frac{3}{2}\Gamma_1^0 \tag{34}$$

The non-symmetric case is validated (Figs. 9 and 10) on the first azimuthal mode ($p = 1$) of the configuration $B3\_C1$ with the pattern 121 ($\circ \bullet \circ$, Tab. 3) where coupling parameters are defined by Eq. (8)[4].

When $\mathcal{S}_0 \neq 0$, the nominally doublet (here $\epsilon_{DD} = -\frac{1}{2}(2\Gamma_1 + \Gamma_2)$ represented by --- in Figs. 9 and 10) is split into two dissimilar azimuthal waves (e.g. waves denoted B^+ and B^- in Fig. 9 where $\tau_1 = 6\ ms$ and $\tau_2 = 2.5\ ms$) with close frequencies and different growth rates as mentioned in [15, 14]. The term $\mathcal{S}_0 = \Gamma_1^0 - \Gamma_2^0$ for the pattern 121 ($\bullet \circ \bullet$) measures the degree of

---

[4]Analytical expressions of coupling parameters are known for α other than one but have been used here for simplicity: $\Gamma_i^0 = -\frac{1}{2}\frac{S_i \rho^0 c^0}{S_c \rho_u^0 c_u^0}\left(1 + n_i e^{j\omega^0 \tau_i}\right) cotan(k_u^0 L_i)$

degeneracy of the azimuthal mode[5] which is controlled by the difference of coupling factors $\Gamma_1^0 - \Gamma_2^0$ introduced by changing one burner out of three.
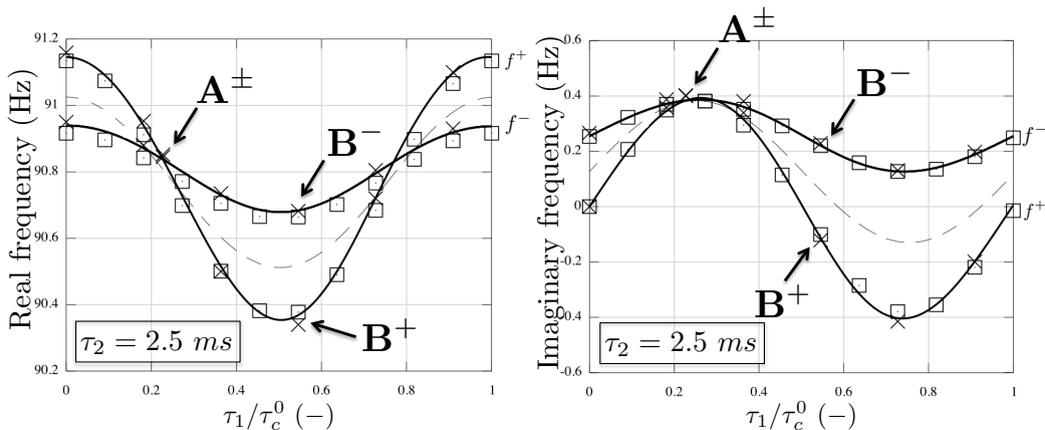

Figure 9: Real and imaginary part of the frequency f^+ and f^- of the two components of the first mode ($p = 1$) in the B3_C1 configuration with the pattern 121 ($\circ \bullet \circ$) and a fixed $\tau_2 = 2.5 \ ms$. ——— : Atacamac (numerical resolution of Eq. (12)), $\square$: Atacamac (analytical formula Eq. (34)), $\times$: AVSP, - - - : The necessary condition for stability Eq. (35). τ_c^0 corresponds to $\frac{1}{f_0} \simeq 11 \ ms$.

Fig. 11 displays the associated mode structure of the symmetric mode ($A^\pm$) composed of two counter-rotating spinning waves (- - - and $\circ$ in Fig. 11) and the splitted mode of the non-symmetric case (waves B^+ and B^-) composed of two standing waves ($\bullet$ and ——— in Fig. 11): the asymmetry has a clear impact on the azimuthal modes nature.

5.3. Conclusion on symmetry breaking in the $N = 3$ case

Results of Sections 5.1 and 5.2 show that a necessary condition for stability independent from the symmetry pattern has to be satisfied: knowing that $max(Im(\epsilon^+), Im(\epsilon^-)) > \frac{1}{2}Im(\epsilon^+ + \epsilon^-)$, the necessary condition to stabilize a mode, which does not depend on the asymmetry pattern, becomes:

$$\frac{1}{2}I_m(\epsilon^+ + \epsilon^-) = -\frac{1}{2}I_m(\Sigma_0) < 0 \tag{35}$$

---

[5]Note that some asymmetry could still give degenerate doublets (i.e. $\mathcal{S}_0 = 0$): for instance, the first order mode ($p = 1$) of a $N = 6$ burners BC configuration with the pattern ($\bullet \circ \bullet \circ \bullet \circ$) or ($\bullet \bullet \bullet \circ \circ \circ$) is a doublet with $\epsilon = -\frac{3}{2}(\Gamma_1^0 + \Gamma_2^0)$.
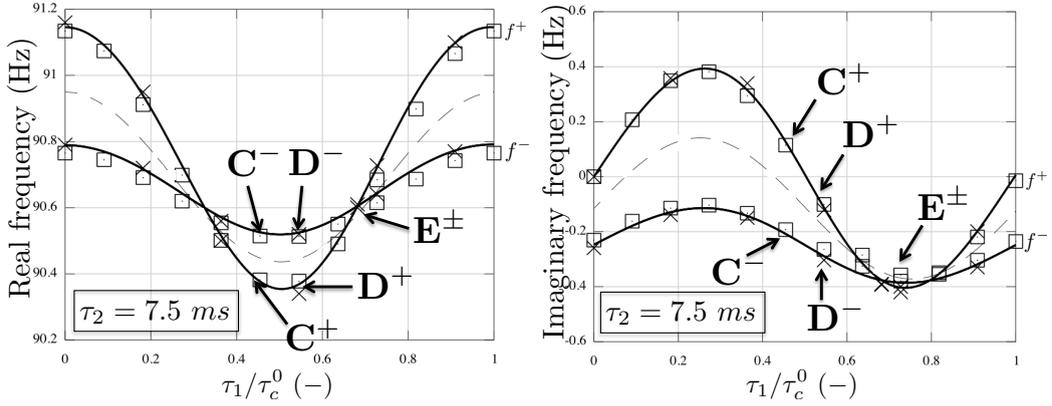
Figure 10: Real and imaginary part of the frequency f^+ and f^- of the two components of the first mode ($p = 1$) in the B3_C1 configuration with the pattern 121 ($\circ \bullet \circ$) and a fixed $\tau_2 = 7.5\ ms$. —— : Atacamac (numerical resolution of Eq. (12)), $\square$: Atacamac (analytical formula Eq. (34)), $\times$: AVSP, - - - : The necessary condition for stability Eq. (35). τ_c^0 corresponds to $\frac{1}{f_0} \simeq 11\ ms$.

If this condition is not fulfilled (Fig. 12, left), there is no hope of stabilizing the mode since at least one wave (V^+ or V^-) will remain unstable (e.g. $A^\pm$ and B^+ in Fig. 9). A remedy is to use a different type of burners, for instance using CBO devices, to change the time-delay τ of the burners and to satisfy the necessary condition (Eq. (35)).

For a symmetric case, Eq. (35) is a necessary and sufficient condition to have a stable mode. However, when symmetry is broken, satisfying condition (35) cannot guarantee stability (Fig. 12, middle and right). In this case, the necessary and sufficient condition becomes:

$$max(Im(\epsilon^+), Im(\epsilon^-)) < 0 \tag{36}$$

Indeed, the splitting introduced by symmetry breaking measured by the splitting strength $\mathcal{S}_0$ (which is equal to $\Gamma_1^0 - \Gamma_2^0$ for the case $N = 3$ with the pattern $\bullet \circ \bullet$) has to be taken into account. For weak splitting (Fig. 12, middle) the two waves V^+ and V^- remain stable (e.g. eigenwaves $D^\pm$ in Fig. 10) but for higher splitting (Fig. 12, right) one wave can become unstable (e.g. wave C^+ in Fig. 10).

23
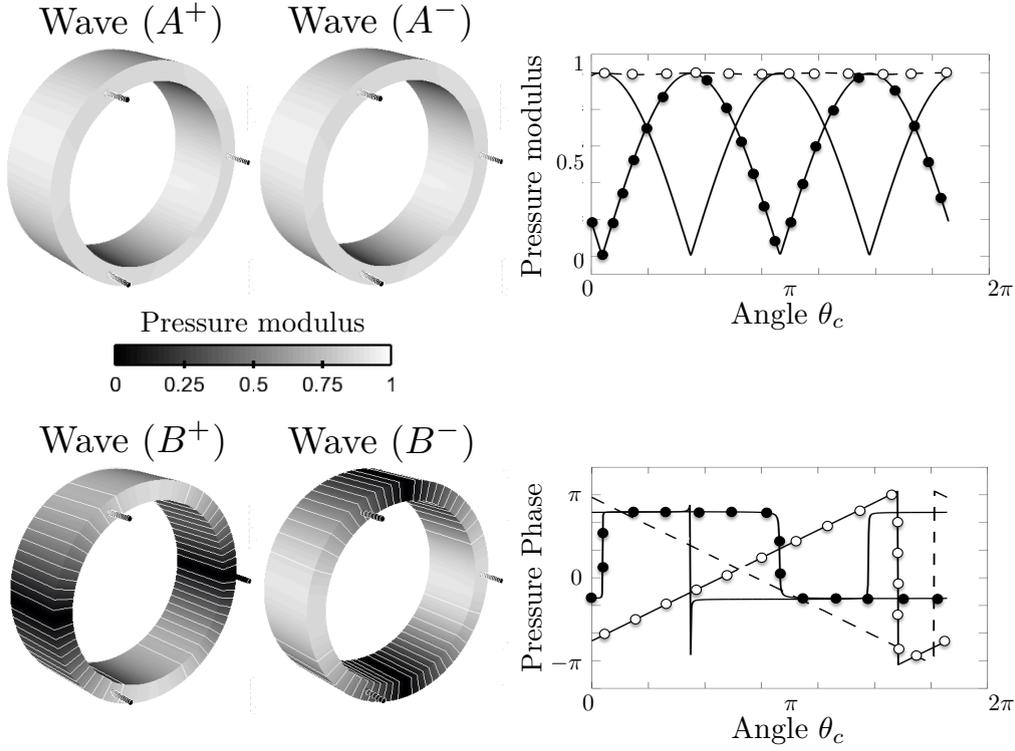
Figure 11: 3D and isolines of pressure modulus (left) and modulus and phase of acoustic pressure (right) of the first azimuthal modes ($p = 1$) of the asymmetric case B3_C1 with the pattern 121 ($\circ \bullet \circ$, Tab. 3) in two situations: mode A ($\tau_1 = \tau_2 = 2.5\ ms$) and mode B ($\tau_1 = 2.5\ ms$ and $\tau_2 = 6.0\ ms$). --- : A^+, $\circ$: A^-, $\bullet$: B^+, —— : B^-

6. Effect of asymmetry on the control of azimuthal combustion instabilities in a $N = 24$ burners BC configuration

Conclusions of Section 5.3 obtained with $N = 3$ burners suggest a strategy to stabilize the pth mode which is described in Fig. 13 for a general N burners configuration.

According to Fig. 13, axisymmetric configurations have only one degree of freedom to stabilize the pth mode which is the time-delay τ_1: if τ_1 satisfies condition Eq. (35), then the configuration is stable.

However, for non-symmetric configurations, satisfying Eq. (35) does not guarantee the stabilization of the configuration. In this case, the asymmetry pattern becomes an additional degree of freedom and one has two options to

24
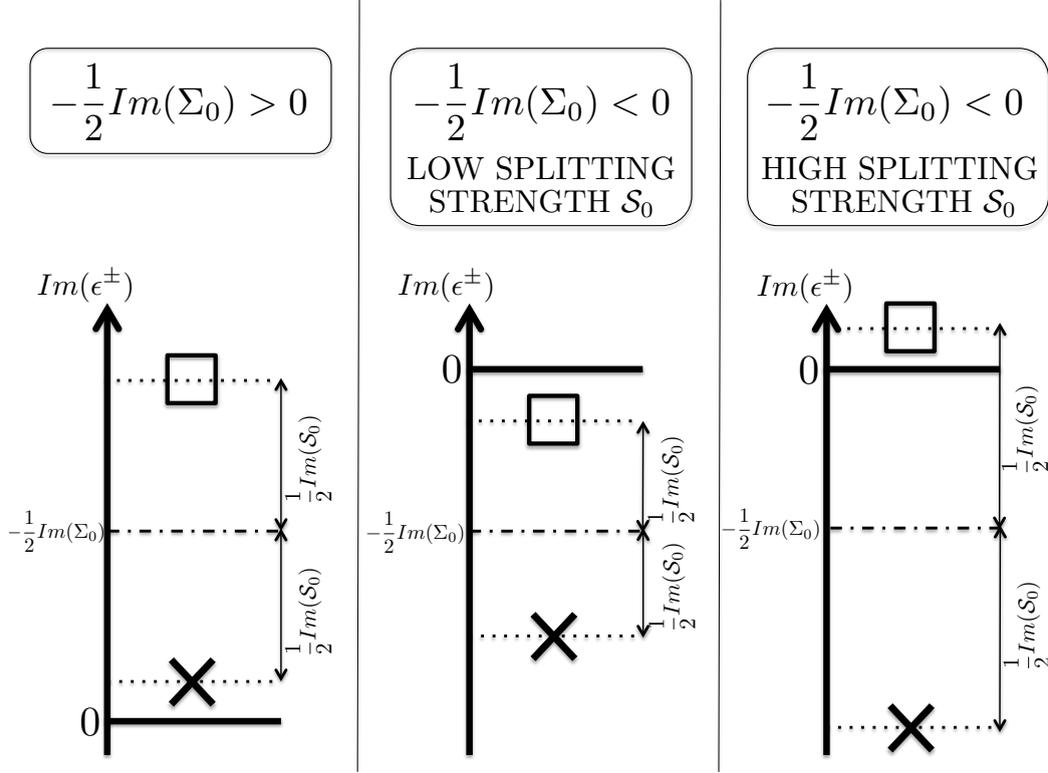
Figure 12: Several situations depending on the condition Eq. (35) and the splitting strength $\frac{1}{2}Im(\mathcal{S}_0)$. $\times$: ϵ^- and $\square$: ϵ^+

ensure the stability of the pth azimuthal mode:

- **Symmetrize the configuration (Option 1)**: if condition (35) is satisfied, at least one kind of injector satisfies $-Im(\Gamma_i^0) < 0$: this kind of burner can be used for all sectors which leads to the mode's stabilization. This option is the most efficient method to stabilize an azimuthal mode since no splitting occurs in a symmetrized annular combustor.

- **Reduce the asymmetry effect (Option 2)**: An other solution is to keep the same kind of burners $(\Gamma_1^0, ..., \Gamma_N^0)$ but rearrange them to reduce the splitting of the azimuthal mode and stabilize it. Optimization can be performed to find the best pattern, which leads to the smallest value of the splitting strength $\mathcal{S}_0$.

25
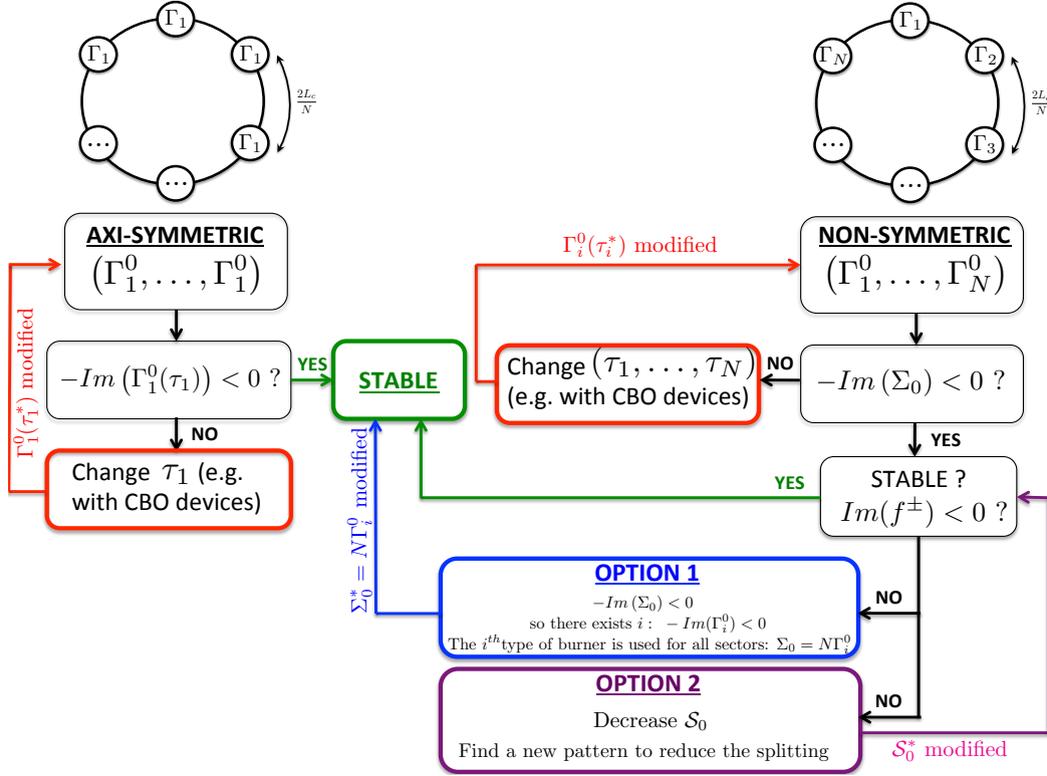
Figure 13: Strategy to stabilize an axisymmetric or non-symmetric annular combustor. Two solutions are highlighted for non-symmetric combustors

In order to further develop the ideas of Section 5.3 and the strategy presented in Fig. 13, symmetry breaking is studied on a $N = 24$ burners configuration [18, 19] representative of real industrial gas turbines. First, the stability of the first azimuthal mode ($p = 1$) of the symmetric configuration is studied as a function of the time-delay τ, with the interaction index $n = 1.0$. Results (Fig. 14), show a very good agreement between the numerical and analytical solutions given by ATACAMAC and the 3D Helmholtz solver AVSP.

To break symmetry two different burners are mixed, characterized by different time-delays, τ_1 and τ_2 (Fig. 14). A time delay $\tau_1 = 3.25\ ms$ corresponds approximately to the most unstable burner ($Im(f_{AVSP}) = 2.98\ s^{-1}$, in Fig. 14 right), which is assimilated here to the baseline case, a burner without CBO ($\circ$ in Tab. 3). As explained in [18, 19], a CBO (Cylindrical

26
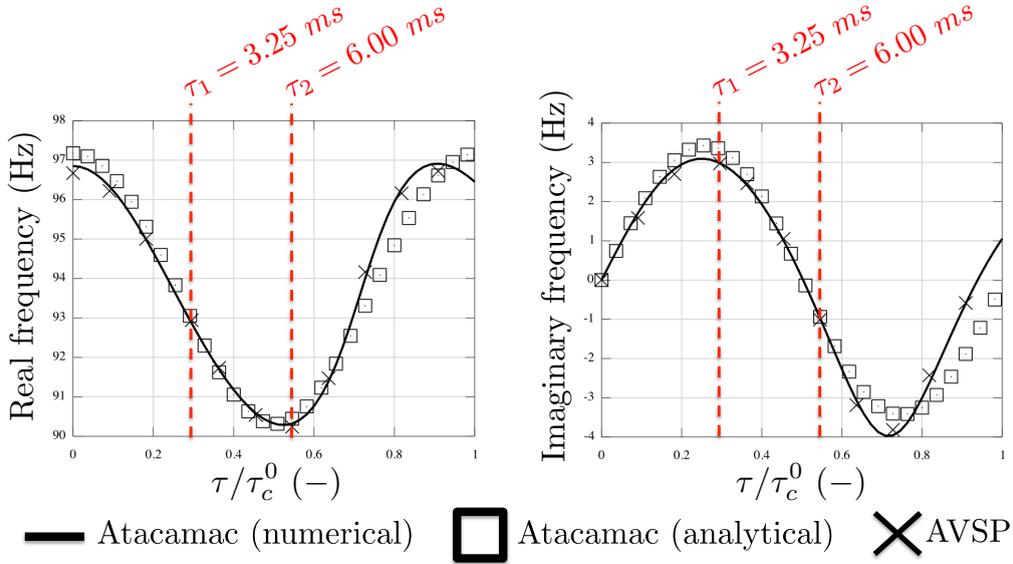
Figure 14: Stability map depending on τ of the first azimuthal mode ($p = 1$) of the symmetric BC configuration with 24 burners. τ_c^0 is the period of the first azimuthal mode $\tau_c^0 = 1/f^0 = \frac{2L_c}{pc^0} \simeq 11ms$

Burner Outlet) device can be mounted on some of the burners to stabilize the chamber. The length of the cylinder is such that the time lag τ_2 from the injection port to the flame front is increased by approximately a quarter of an acoustic period: $\tau_2 = \tau_1 + \frac{1}{4f^0} \simeq 6ms$ (since the first azimuthal mode has a frequency $f^0 \simeq 90Hz$): it corresponds indeed to a stable burner where $Im(f_{AVSP}) = -1.01\ s^{-1}$ in Fig. 14 ($\bullet$ in Tab. 3). Note that using 20 burners with $\tau_2 = 6\ ms$ and 4 burners with $\tau_1 = 3.25\ ms$ respects the necessary condition given by Eq. (35) to get stable modes (--- for the configuration C_{20} in Fig. 15). The stability of the four patterns proposed in Tab. 3 is studied using ATACAMAC and AVSP. Results are plotted in Figs. 15 (growth rates) and 16 (frequencies).

- **B24_C0:** This configuration corresponds to the unstable baseline case: the necessary condition (Eq. (35)) is not satisfied. Some burners have to be changed in order to get a stable combustor.

- **B24_C20_P2:** 20 CBOs devices have been mounted in the hope to stabilize the mode. The necessary condition (Eq. (35)) is satisfied.

27
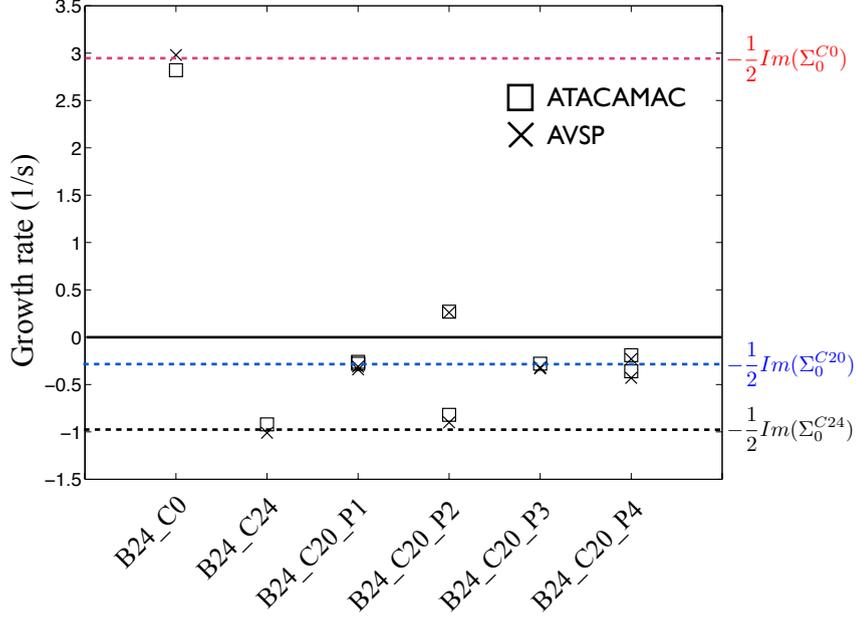
Figure 15: Growth rate of the first azimuthal mode ($p = 1$) for various asymmetry combination of burners with and without CBO: B24_C0 (24 noCBO burner), B24_C24 (24 CBO burners) and the four patterns B24_C20. **- - -** : Values of $-\frac{1}{2}I_m(\Sigma_0)$ depending on the configuration (C_0, C_{20} and C_{24})

However this pattern has a large splitting strength $\mathcal{S}_0$. Consequently it splits azimuthal modes into two singlets with different growth rates making the first azimuthal mode unstable. This case is an excellent example of how, for asymmetric circumferential patterns, one can use stable burners that match the condition $-\frac{1}{2}I_m(\Sigma_0) < 0$ and yet, due to the asymmetry term $\mathcal{S}_0$, have an unstable mode as shown in Fig. 12 (right).

- **B24_C20_P4:** As suggested by the strategy developed in Fig. 13, a solution to stabilize the mode is to find asymmetry patterns like $B24\_C20\_P4$ with a lower splitting strength $\mathcal{S}_0$ for which both singlets remain stable as mentioned in Fig. 12 (middle).

- **B24_C20_P1 and B24_C20_P3:** The pattern $B24\_C20\_P4$ induces a low splitting strength and stabilizes the mode. However, optimal

28
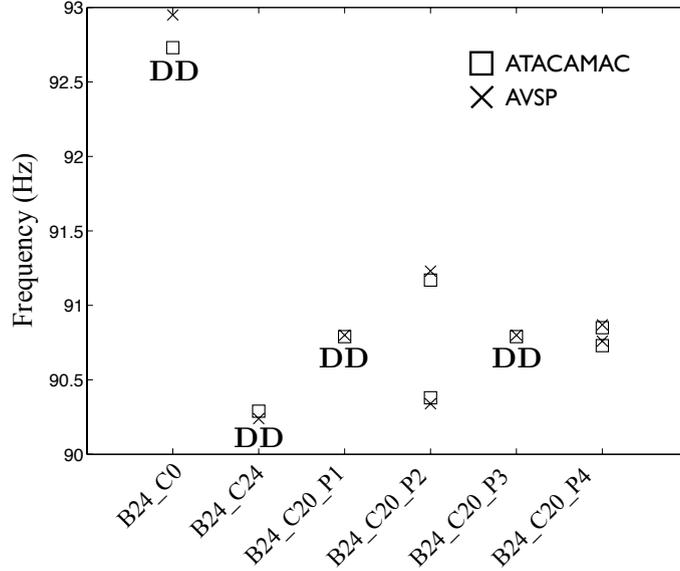
Figure 16: Frequencies of the first azimuthal mode ($p = 1$) for various asymmetry combination of burners with and without CBO: B24_C0 (24 noCBO burners), B24_C24 (24 CBO burners) and the four patterns B24_C20. **DD**: Degenerate Doublets.

asymmetry patterns can be found which lead to no or very low splitting and therefore ensure the mode stabilization. Patterns $B24\_C20\_P1$ and $B24\_C20\_P3$ are such patterns giving stable degenerate doublets. In these cases, $\mathcal{S}_0 = 0$ and therefore Eq. (35) becomes a necessary and sufficient condition for stability. The mode is stable: $Im(f^\pm) \simeq -0.25 \ s^{-1}$

- **B24_C24:** As explained in Fig. 13, the most efficient option to stabilize a mode is to symmetrize the annular combustor with burners which satisfy the necessary condition (Eq. (35)), i.e. 24 burners with a CBO. The mode is very stable: $Im(f^\pm) \simeq -1.0 \ s^{-1}$ (Fig. 15).

Considering the dashed-lines $(-\frac{1}{2}Im(\Sigma_0))$ in Fig. 15, it is interesting to notice that, independently of the asymmetry patterns, combining 20 CBOs and 4 noCBOs burners give potentially less stable modes than using 24 CBOs showing that breaking symmetry has a limited interest here compared to adding CBOs on all burners. Nevertheless, if for any reason (ignition, pollution, construction, etc.) one must keep the two types of burner, the present

29

analytical model offers an easy way to optimize the circumferential distribution of the burners by minimizing the imaginary part of the splitting strength $Im(\mathcal{S}_0)$ to stabilize the pth mode. To illustrate this idea, Figs. 17 and 18 display the effect of several asymmetry patterns on the splitting strength ($\mathcal{S}_0$) using a configuration with 20 CB0 - 4 noCBO burners. It is proved analytically that using two kinds of burners (with coupling parameters Γ_1^0 and Γ_2^0 respectively) yields a splitting strength of the form:

$$\mathcal{S}_0 = \overbrace{2\mathcal{K}}^{\text{Imposed by the pattern}} \underbrace{\left(\Gamma_1^0 - \Gamma_2^0\right)}_{\text{Imposed by the difference between burner types 1 and 2}} \tag{37}$$

where the reduced splitting strength $\mathcal{K}$ depends only on the asymmetry pattern (see Tab. 4 for the analytical expression of $\mathcal{K}$ for the four patterns studied). In Eq. (37), Γ_1^0 and Γ_2^0 are fixed by the burner characteristics so that minimizing $\mathcal{S}_0$ to increase stability is equivalent to minimizing $\mathcal{K}$.

Name	Asymmetry pattern	$\mathcal{K}$
P1	●●●●●●●●○○●●●●○○●●●●●●●	0
P2	●●●●●●●●●○○○○●●●●●●●●●●	$\frac{1}{2}\sqrt{3\sqrt{3}+6} \simeq 1.67$
P3	●●●●●○●●●●●○●●●●●○●●●●●○	0
P4	●●●●●○●●●●○●●●●●○●●●●●○	$\frac{1}{2}\sqrt{2-\sqrt{3}} \simeq 0.26$

Table 4: Analytical expressions of the reduced splitting strength $\mathcal{K}$ for the four patterns described in Tab. 3

Consequently, an optimization process appears as a promising approach to find patterns with the minimal value of the reduced splitting strength $\mathcal{K}$ which leads to a null or very low splitting and therefore ensure the stability of the pth azimuthal mode. This also highlights the potential of low-order models such as ATACAMAC to perform optimization processes at very-low costs.

In addition to their stability, symmetry breaking can also modify the dynamic nature of the acoustic modes. The modulus and phase of acoustic pressure of the first azimuthal mode ($p = 1$) [6] are plotted in Fig. 19 for the four studied patterns (Tab. 3), showing two distinct behaviors.

[6]Only one of the two components of a given azimuthal mode is shown in Fig. 19
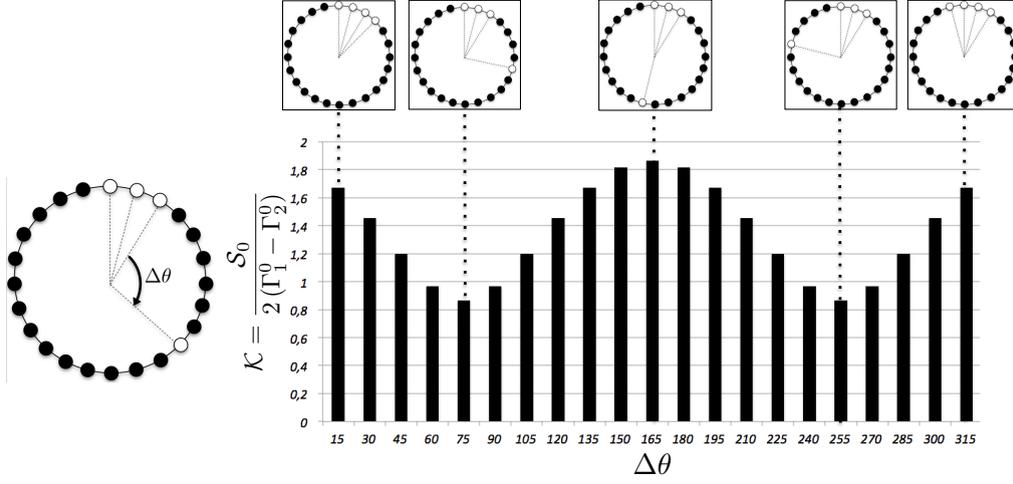
Figure 17: The reduced splitting strength ($\mathcal{K}$) for several patterns where three noCBO burners are kept together at the same place and the last noCBO burner's place is changed azimuthally. The splitting is then strongly affected by the asymmetry pattern.
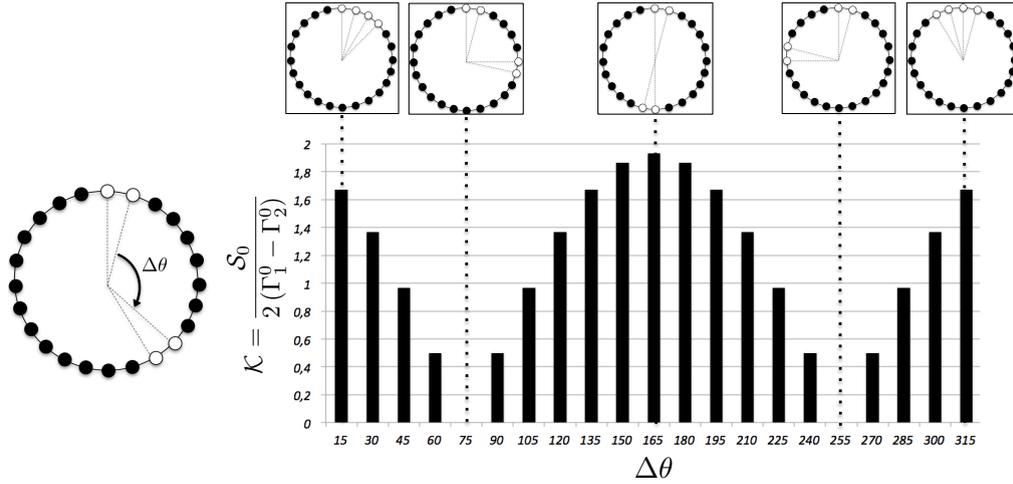

Figure 18: The reduced splitting strength ($\mathcal{K}$) for several patterns where two noCBO burners are kept together at the same place and the two other noCBO burner's places are changed azimuthally. The splitting is then strongly affected by the asymmetry pattern.

- **Patterns P1 and P3:** As expected, asymmetry patterns leading to degenerate doublets can be either spinning, standing or mixed. In this

31

case, P1 gives a mixed mode (——— in Fig. 19) while P3 gives a purely spinning mode (--- in Fig. 19). For these patterns, the two eigenwaves (V^+ and V^-) have the same frequency so that they can be combined to obtain either a spinning, a standing or a mixed mode.

- **Patterns P2 and P4:** On the other hand, patterns P2 and P4 give two standing modes (● and ○ respectively in Fig. 19) which are not degenerate ($\mathcal{S}_0 \neq 0$). The two eigenwaves V^+ and V^- oscillate in opposite phase with different (yet very close) frequencies (e.g. 90.3 Hz and 91.3 Hz for the pattern P2). As shown in Fig. 15, for the pattern P2, one wave is amplified whereas the other one is damped, resulting in an unstable standing mode.
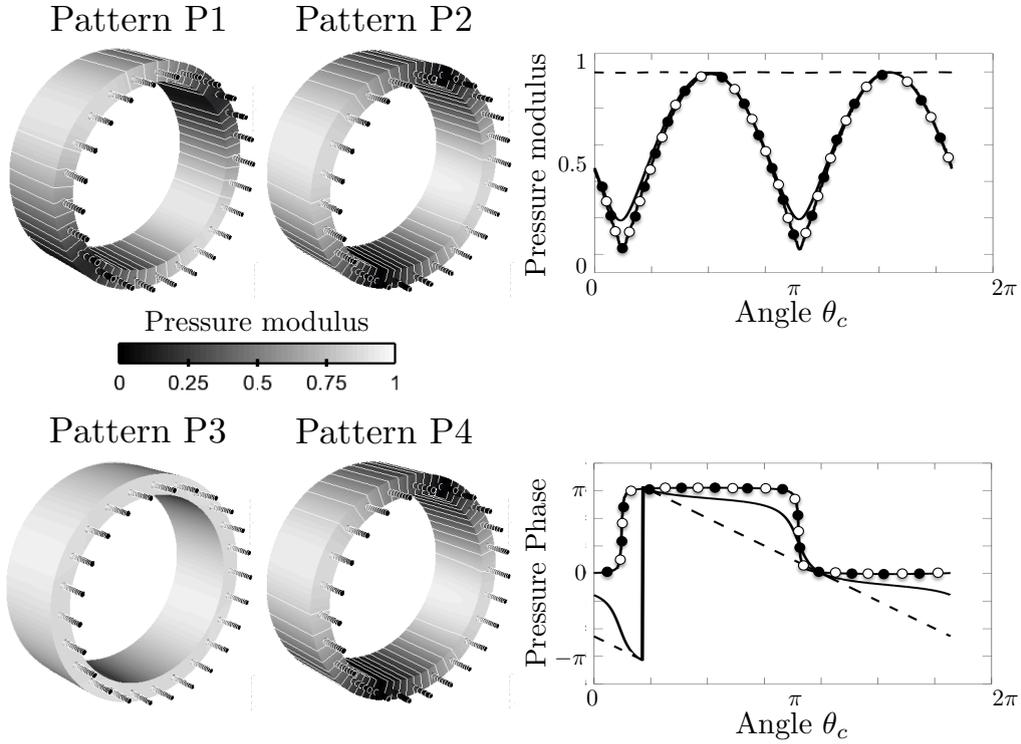

Figure 19: Effect of the asymmetry pattern on the azimuthal mode nature. 3D and isolines of the pressure modulus (left) and modulus and phase of the acoustic pressure over the circumference (right). ——: Pattern P1, ●: Pattern P2, --- : Pattern P3, ○: Pattern P4

32

7. Conclusion

The present work investigates analytically and numerically the effect of staging patterns on the nature and the stability of azimuthal modes in annular combustion chambers. The analytical model is based on a one-dimensional zero-Mach number formulation where N burners are connected to a downstream annular chamber. Flames are supposed to be compact and are modeled using a Flame Transfer Function, characterized by a coupling factor and a phase shift. Manipulation of the corresponding acoustic equations yields a simple dispersion relation which can be solved analytically in specific situations where coupling factors are small (weak coupling).

First, a symmetric configuration with N identical burners with null inlet impedances (i.e. $p' = 0$) is studied. Only two mode behaviors are observed: the degenerate doublets and the non-degenerate singlets, the latter being capable of generating warbles (low frequency oscillations due to a non-degenerate mode [15]). Then, a non-symmetric case was studied and symmetry breaking was proved to modify the azimuthal modes behavior in a simple case with only three burners in an annular chamber. The staging patterns can split nominally degenerate azimuthal modes (doublets) into non-degenerate pairs (singlets), a situation already mentioned in the literature and observed in recent Helmholtz simulations.

Finally, the effect of the asymmetry pattern was investigated in a $N = 24$ burners case representative of industrial gas turbines. A very good agreement is found for all cases between analytical and numerical results, obtained with a 3D Helmholtz solver. Results are compared to observations made in experiment where CBOs (Cylindrical Burner Outlet) are added to certain burners to control combustion instabilities. A simple criterion is derived to provide a necessary condition to stabilize an annular combustor. Since the asymmetry pattern does not appear in this criterion, it implies that symmetry breaking can modify the mode nature but has no real impact on controlling combustion instabilities in annular chambers. The best method to control a chamber with $N = 24$ sectors is to use 24 burners with FTF leading to stable azimuthal modes. However if keeping only one type of burner is not possible, a strategy to stabilize the mode is proposed: find an optimal pattern which leads to a low splitting of the corresponding azimuthal mode. The general character of this conclusion is limited by the low coupling assumption which implies no interaction between burners. Maybe strongly coupled situations where burners interfere [6, 7] would lead to an effect of the asymmetry pat-

tern on the overall stabilization of the annular engines. A second limit might be the use of an infinite impedance at the outlet (i.e. $u' = 0$), leading to purely azimuthal modes. Introducing mixed azimuthal/longitudinal modes in the chamber should be an interesting extension of the present study.

Appendix A. Summary of the analytical method providing the stability map of the pth azimuthal mode

This Section summarizes the analytical method to provide the stability map of the pth azimuthal mode of a chamber with N burners.

- **1)** Compute the coupling factors of each burner:

$$\Gamma_i^0 = -\frac{j}{2}\frac{S_i}{S_c}\frac{\mathbb{F}^0 C_{1-\alpha}^{k^0}[jS_\alpha^{k_u^0}Z + C_\alpha^{k_u^0}] + S_{1-\alpha}^{k^0}[jC_\alpha^{k_u^0}Z - S_\alpha^{k_u^0}]}{\mathbb{F}^0 S_{1-\alpha}^{k^0}[jC_\alpha^{k_u^0} - S_\alpha^{k_u^0}Z] + C_{1-\alpha}^{k^0}[C_\alpha^{k_u^0}Z + jS_\alpha^{k_u^0}]} \tag{A.1}$$

  where $\mathbb{F}^0 = \frac{c^0\rho^0}{c_u^0\rho_u^0}(1 + n_i e^{j\omega^0\tau_i})$, $C_x^y = cos(xyL_i)$, $S_x^y = sin(xyL_i)$, $k^0 = \omega^0/c^0$, $k_u^0 = \omega^0/c_u^0$, Z is the upstream impedance and $\omega^0 = \frac{p\pi c^0}{L_c}$.

- **2)** Compute the mean coupling factor $\frac{1}{N}\Sigma_0$ where $\Sigma_0 = \sum_{i=1}^N \Gamma_i^0$.

- **3)** Compute the splitting strength $\mathcal{S}_0$:

$$\mathcal{S}_0 = \sqrt{\sum_{i,j=1}^N \Gamma_i^0\Gamma_j^0 cos\left(\frac{4p\pi}{N}(j-i)\right)} \tag{A.2}$$

- **4)** The pth azimuthal mode is composed of two waves V^+ and V^- which have a wavenumber perturbation $\epsilon^\pm$ given by:

$$\epsilon^+ = -\frac{1}{2}(\Sigma_0 + \mathcal{S}_0) \quad \text{and} \quad \epsilon^- = -\frac{1}{2}(\Sigma_0 - \mathcal{S}_0) \tag{A.3}$$

- **5)** Then compute the complex frequency of the system from the definition of the wavenumber perturbation ($k^\pm L_c = \frac{2\pi f^\pm}{c^0}L_c = p\pi + \epsilon^\pm$) and Eq. (A.3):

$$f^\pm = \frac{pc^0}{2L_c} - \frac{c^0(\Sigma_0 \pm \mathcal{S}_0)}{4\pi L_c} \tag{A.4}$$

- **6)** Finally, the two waves composing the pth azimuthal mode can have different frequencies ($f^+ \neq f^-$, non-degenerate singlets) if $\mathcal{S}_0 \neq 0$ or the same frequencies ($f^+ = f^-$, degenerate doublets) if $\mathcal{S}_0 = 0$. The growth rate of each wave is obtained from the imaginary part of the complex frequency obtained in Eq. (A.4):

$$\text{Growth rate}^\pm = Im(f^\pm) = -\frac{c^0}{4\pi L_c}Im(\Sigma_0 \pm \mathcal{S}_0) \tag{A.5}$$

References

[1] T. Lieuwen, V. Yang, in: AIAA Prog. in Astronautics and Aeronautics , volume 210.

[2] B. Schuermans, V. Bellucci, C. Paschereit, in: International Gas Turbine and Aeroengine Congress & Exposition, ASME Paper, volume 2003-GT-38688.

[3] W. Krebs, P. Flohr, B. Prade, S. Hoffmann, Combust. Sci. Tech. 174 (2002) 99–128.

[4] W. C. Strahle, J. Sound Vib. 23 (1972) 113–125.

[5] J. Parmentier, P. Salas, P. Wolf, G. Staffelbach, F. Nicoud, T. Poinsot, Combustion and Flame 159 (2012) 2374–2387.

[6] M. Bauerheim, J. Parmentier, P. Salas, F. Nicoud, T. Poinsot, Combustion and Flame (2013 - under review) CNF–D–13–00088.

[7] N. Worth, J. Dawson, Proceedings of the Combustion Institute 34 (2013, in press) 3127–3134.

[8] N. Worth, J. Dawson, Combustion and Flame (2013, submitted).

[9] S. Evesque, W. Polifke, in: International Gas Turbine and Aeroengine Congress & Exposition, ASME Paper, volume GT-2002-30064.

[10] J. Kopitz, A. Huber, T. Sattelmayer, W. Polifke, in: Int'l Gas Turbine and Aeroengine Congress & Exposition, ASME GT2005-68797 , Reno, NV, U.S.A.

[11] G. Staffelbach, L. Gicquel, G. Boudier, T. Poinsot, Proc. Combust. Inst. 32 (2009) 2909–2916.

[12] S. R. Stow, A. P. Dowling, in: ASME Paper, New Orleans, Louisiana.

[13] S. Evesque, W. Polifke, C. Pankiewitz, in: 9th AIAA/CEAS Aeroacoustics Conference, volume AIAA paper 2003-3182.

[14] C. Sensiau, F. Nicoud, T. Poinsot, Int. Journal Aeroacoustics 8 (2009) 57–68.

[15] R. Perrin, T. Charnley, J. Sound Vib. 31 (1973) 411–418.

[16] J. C. Oefelein, V. Yang, J. Prop. Power 9 (1993) 657–677.

[17] S. R. Stow, A. P. Dowling, in: ASME Paper 2003-GT-38168, Atlanta, Georgia, USA.

[18] P. Berenbrink, S. Hoffmann, in: ASME Turbo Expo 2001. Paper 2001-GT-42.

[19] U. Krueger, J. Hueren, S. Hoffmann, W. Krebs, P. Flohr, D. Bohn, in: A. Paper (Ed.), ASME TURBO EXPO, Munich, Germany.

[20] F. E. C. Culick, P. Kuentzmann, Unsteady Motions in Combustion Chambers for Propulsion Systems, NATO Research and Technology Organization, 2006.

[21] J. Moeck, M. Paul, C. Paschereit, in: ASME Turbo Expo 2010 GT2010-23577.

[22] G. Gelbert, J. Moeck, C. Paschereit, R. King, Control Engineering Practice 20 (2012) 770–782.

[23] B. Schuermans, C. Paschereit, P. Monkewitz, in: 44th AIAA Aerospace Sciences Meeeting and Exhibit, volume AIAA paper 2006-0549.

[24] N. Noiray, M. Bothien, B. Schuermans, Combustion Theory and Modelling 15 (2011) 585–606.

[25] F. E. Marble, S. Candel, J. Sound Vib. 55 (1977) 225–243.

[26] P. Wolf, G. Staffelbach, A. Roux, L. Gicquel, T. Poinsot, V. Moureau, C. R. Acad. Sci. Mécanique 337 (2009) 385–394.

[27] J. O'Connor, T.Lieuwen, Journal of Engineering for Gas Turbines and Power 134 (2012).

[28] J.O'Connor, T.Lieuwen, Physics of fluids 24 (2012).

[29] J.O'Connor, T.Lieuwen, ASME TURBOEXPO 2012 (2012).

[30] J. Blimbaum, M. Zanchetta, T. Akin, V. Acharya, J.O'Connor, D. Noble, T. Lieuwen, International journal of spray and combustion dynamics 4 (2012) 275–298.

[31] A. P. Dowling, J. Sound Vib. 180 (1995) 557–581.

[32] T. Poinsot, D. Veynante, Theoretical and Numerical Combustion, Third Edition (www.cerfacs.fr/elearning), 2011.

[33] P. Palies, Dynamique et instabilités de combustion de flammes swirlées, Phd thesis, Ecole Centrale Paris, 2010.

[34] T. Schuller, D. Durox, P. Palies, S. Candel, Combustion and Flame 159 (2012) 1921–1931.

[35] L. Crocco, J. American Rocket Society 21 (1951) 163–178.

[36] F. Nicoud, L. Benoit, C. Sensiau, T. Poinsot, AIAA Journal 45 (2007) 426–441.

[37] A. D. Pierce, Acoustics: an introduction to its physical principles and applications, McGraw Hill, New York, 1981.

[38] F. Silva, P. Guillemain, J. Kergomard, B. Mallaroni, A. Norris, Journal of Sound and Vibration 322 (2009) 255–263.